DTU Fotonik
Institut for Fotonik

DTU

PhD Thesis

NONLINEAR OPTICAL PROPERTIES OF ULTRATHIN METAL LAYERS

by Oleg Lysenko

Supervisor:

Associate Professor Andrei Lavrinenko

Co-supervisor:

Associate Professor Morten Bache

Department of Photonics Engineering

Technical University of Denmark

June 2016

Abstract

This thesis presents experimental and theoretical studies of nonlinear propagation of ultrashort long-range surface plasmon polaritons in gold strip waveguides. The strip plasmonic waveguides are fabricated in house, and contain a gold layer, adhesion layers, and silicon dioxide cladding. The optical characterization of the plasmonic waveguides is performed using femtosecond and picosecond optical pulses. Two nonlinear optical effects in the strip plasmonic waveguides are experimentally observed and reported. The first effect is the nonlinear power transmission of the plasmonic mode, and the second effect is the spectral broadening of the plasmonic mode. A consistent theoretical model of the nonlinear optical effects in the strip plasmonic waveguides based on the third-order nonlinear susceptibility of the constituent materials is developed and reported. It is shown that the effective third-order nonlinear susceptibility of the plasmonic mode in the gold strip waveguides significantly depends on the metal layer thickness and laser pulse duration. This dependence is explained in detail in terms of the free-electron temporal dynamics in gold. The third-order nonlinear susceptibility of the gold layer has the dominant contribution to the effective third-order nonlinear susceptibility of the long-range surface plasmon polariton mode in the strip plasmonic waveguides. The spectral broadening of the plasmonic mode in the waveguides is determined by the real part of the third-order nonlinear susceptibility of the gold layer, and the nonlinear power transmission of the plasmonic mode is determined by the imaginary part of the third-order nonlinear susceptibility of the gold layer. The experimental values of the third-order nonlinear susceptibility of gold for ultrathin layers are presented. The pulse duration dependence of the third-order nonlinear susceptibility of gold is calculated in the broad range from tens of femtoseconds to tens of picoseconds using the two-temperature model of the free-electron temporal dynamics of gold, and shows the saturation of the third-order nonlinear susceptibility of gold for longer picoseconds pulses. The results are important for the development and applications of active plasmonic and nanophotonic components.

Resumé

Denne afhandling præsenterer eksperimentelle og teoretiske undersøgelser af ikke-lineær udbredelse af ultrakorte langtrækkende overflade plasmon polaritoner i guld bånd bølgeledere. De bånd plasmoniske bølgeledere er fremstillet her i huset, og indeholder et guld lag, vedhæftningslag, og siliciumdioxid beklædning. Den optiske karakterisering af plasmoniske bølgeledere udføres ved hjælp af femtosekund og picosekund optiske pulser. To ikke-lineære optiske effekter i bånd plasmoniske bølgeledere er eksperimentelt observeret og rapporteret. Den første effekt er den ikke-lineære transmission af plasmonisk mode power, og den anden effekt er den spektrale udvidelse af plasmoniske mode. En teoretisk model af de ikke-lineære optiske effekter i bånd plasmoniske bølgeledere baseret på tredje-ordens ikke-lineær susceptibilitet af materialesammensætning udvikles og rapporteres. Det er vist, at den effektive tredje-ordens ikke-lineær susceptibilitet plasmoniske tilstand i guld bånd bølgeledere afhænger væsentligt af metal lagets tykkelse og laser pulsens varighed. Denne afhængighed er forklaret i detaljer i form af de frie elektroners tidsmæssige dynamik i guld. Den tredje-ordens ikke-lineær susceptibilitet af guld laget er det dominerende bidrag til en effektiv tredje-ordens ikke-lineær susceptibilitet af langtrækkende overfladeplasmon polariton mode i bånd plasmoniske bølgeledere. Den spektrale udvidelse af plasmoniske tilstand i bølgelederne er bestemt af den reelle del af tredje ordens ikke-lineær susceptibilitet for guldlaget, og den ikke-lineære transmission af plasmonisk mode power er bestemt af den imaginære del af tredje ordens ikke-lineær susceptibilitet af guldlaget. De eksperimentelle værdier af tredje ordens ikke-lineær susceptibilitet af guld for ultratynde lag præsenteres. Pulsvarighedens afhængighed af tredje-ordens ikke-lineær susceptibilitet af guld beregnes i intervallet fra snesevis af femtosekunder til et tocifret antal picosekunder ved hjælp af to-temperatur modelen af de frie elektroners tidsmæssige dynamik i guld, og viser mætning af tredje ordens ikke-lineær susceptibilitet af guld for lange picosekund impulser. Resultaterne er vigtige for udvikling og anvendelse af aktive plasmoniske og nanofotoniske komponenter.

Preface and acknowledgements

This thesis is based on experimental and theoretical research on nonlinear optical properties of ultrathin metal layers performed during my PhD study in the Department of Photonics Engineering at Technical University of Denmark from June 2013 to June 2016. As part of the PhD study abroad, I also performed experimental research in the Department of Physics at King's College London from November 2015 to February 2016. The fabrication of the samples with ultrathin metal layers was performed in the National Center for Micro- and Nanofabrication in Denmark.

I would like to thank my supervisor Prof. Andrei Lavrinenko and my co-supervisor Prof. Morten Bache for their great help and support during the entire period of my PhD study at Technical University of Denmark.

I am also very grateful to Prof. Anatoly V. Zayats and Dr. Nicolas Olivier for their great help and excellent international collaboration during my external research stay at King's College London.

I would like to thank Prof. Gregory A. Wurtz for the valuable comments regarding the fabrication of the samples.

I also thank Dr. Radu Malureanu and Dr. Jesper Hanberg for the fruitful discussions and help with the fabrication of the samples in the National Center for Micro- and Nanofabrication in Denmark.

The PhD project was entirely funded by Technical University of Denmark. I also received some financial support from the Otto Mønsted Foundation for the participation in the SPIE International Conference Photonics Europe 2016 in Brussels.

Oleg Lysenko

June 2016

Publications and conferences

Journal publications:

[A] O. Lysenko, N. Olivier, M. Bache, A. V. Zayats, and A. Lavrinenko, “Nonlinear dynamics of long-range surface plasmon polaritons in gold strip waveguides”, (submitted).

[B] O. Lysenko, M. Bache, and A. Lavrinenko, “Nonlinear optical model for strip plasmonic waveguides”, J. Opt. Soc. Am. B **33**, 7, 1341 (2016).

[C] O. Lysenko, M. Bache, and A. Lavrinenko, “Third-order susceptibility of gold for ultrathin layers”, Opt. Lett. **41**, 2, 317 (2016).

Conferences:

[D] O. Lysenko, M. Bache, A. Zayats, and A. Lavrinenko, “Effective third-order nonlinearity of plasmonic waveguides for ultrashort laser pulses”, Danish Physical Society Annual Conference, Book of Abstracts, p. 27, June 6-7, 2016, Middelfart, Denmark.

[E] O. Lysenko, M. Bache, R. Malureanu, and A. Lavrinenko, “Nonlinear effects in propagation of long-range surface plasmon polaritons in gold strip waveguides”, Proceedings of SPIE International Conference Photonics Europe, vol. 9884, 988420, p. 1-12, April 3-7, 2016, Brussels, Belgium.

[F] O. Lysenko, M. Bache, R. Malureanu, and A. Lavrinenko, “Modeling of effective third-order nonlinearity for gold strip plasmonic waveguides”, Danish Optical Society Annual Conference, Book of Abstracts, p. 4, November 19-20, 2015, Odense, Denmark.

[G] A. Lavrinenko and O. Lysenko, “Modeling, fabrication and high power optical characterization of plasmonic waveguides”, Proceedings of IEEE International Conference on Electronics and Nanotechnology (ELNANO), pp. 245–248, April 21-24, 2015, Kiev, Ukraine.

[H] M. Bache, A. Lavrinenko, O. Lysenko, and R. Malureanu, “Nanoplasmonic solution for nonlinear optics”, DTU Sustain Conference, Book of Abstracts, p. 106, December 17, 2014, Kongens Lyngby, Denmark.

Contents

Chapter 1

Introduction

The optically controlled optical channel is considered as one of the main instruments in enhancing density of communication lines with reduced energy-per-bit consumption. All-optical signal processing is capable of achieving a signal modulation and transmission speeds beyond what is possible by their electronic counterparts. To optically modulate (or switch) signals in plasmonic waveguides (with one or several metal-dielectric interfaces) means that light induces changes in the real part or imaginary part of the dielectric functions of the constituent materials. These changes can occur either in a metal or in a dielectric, or in both. Most of the studies in nonlinear plasmonics are connected with the local field enhancement facilitated by metal nanoparticles [1].

So far the light-induced absorption modulation has been studied with the intrinsic metal nonlinearity [1]. The intrinsic nonlinearity of gold is related to the interband excitation of nonequilibrium electrons and results in small changes of the real part of the permittivity but in significant changes of the imaginary part of the permittivity. The associated relaxation time is on the picosecond scale, making THz-frequency modulation of signals in plasmonic gold waveguides possible. The relaxation time of the interband transitions in aluminum is much smaller and can provide even faster modulation speeds [2]. Thus, the optical nonlinearity in metals holds a potential that needs to be explored more. Results can be exploited for rapid optical switching and modulation by using strong excitation via an ultrafast laser pulse. This approach has opened a whole new field of active plasmonic systems [2].

This thesis presents theoretical and experimental studies in order to understand and ultimately exploit intrinsic metal nonlinearities in thin metal films. The current vision of possible nonlinear behavior in noble metals is that they occur

due to the Fermi smearing process. When a thin metal film is exposed to an ultrafast laser pulse, it absorbs the optical pulse which leads to rapid heating. The rise in the temperature of the material results in interband transitions and broadens the electronic distribution around the Fermi energy. This eventually causes significant change in the dielectric permittivity of metal [3]. Another possible mechanism is that a strong electric field in ultrashort laser pulses affects the distribution of free electrons. Such direct influence is preferable in terms of exploitation due to the fast electronic response and symmetric time scale of both phases of the nonlinear process: development and relaxation.

Plasmonic nanostructures represent a unique platform for many linear and nonlinear optical applications [4]. A great variety of plasmonic waveguides for integrated optics [5, 6], nanofocusing [7, 8], sensing [9, 10], lasing and amplification of light [11, 12] has been proposed. In particular, special attention has recently been paid to the nonlinear optical properties of plasmonic waveguides, hybrid plasmonic waveguides, and other elements important for future nanophotonic communication approaches [13-16]. Bulk metals, thin metal layers, and plasmonic metamaterials have been investigated in the nonlinear regime [17-20].

The nonlinear propagation of surface plasmon polaritons (SPPs) in plasmonic waveguides can be studied in terms of either the second-order nonlinearity [21, 22] or the third-order nonlinearity [23, 24]. The latter is particularly important because it is present in all materials and in metals arises due to changes of the intrinsic electronic temperature after the absorption of incident light. A novel approach in the field of nonlinear optics with metals has been introduced by Conforti and Della Valle in [23], where the third-order nonlinear susceptibility for gold was derived from the two-temperature model of electron temporal dynamics. In Ref. [24] Marini and coworkers reported a consistent nonlinear model for plasmonic modes, formulated in terms of the classical nonlinear fiber optics formalism.

The majority of the experimental data on the third-order nonlinear susceptibility of Au were collected near the interband transitions in a wavelength range of 532-630 nm for pulse durations between 100 fs and 1 ns [25]. Most of the results were obtained with the z-scan method, reporting very high values of the third-order nonlinear susceptibility in the range of 10^{-16}-10^{-15} m^2/V^2 [26-29]. However, the linear losses in plasmonic waveguides, which are also related to the same interband transitions in gold, are very high (approximately 30-40 dB/mm) in this wavelength range [30, 31].

On the other hand, nanophotonic and plasmonic devices are extensively exploited in the infrared (IR) range [5,6]. The propagation losses of long-range surface plasmon polaritons (LRSPPs) in Au-based waveguides can be approximately 2-5 dB/mm at the telecommunication wavelengths. However, the third-order nonlinear susceptibility of gold, $\chi_{Au}^{(3)}$, in the IR range arises mainly from intraband electron transitions and is much smaller than in the visible range [24, 25], so that a conventional z-scan method may be not sensitive enough for measurements of $\chi_{Au}^{(3)}$ in ultrathin gold layers. Nevertheless, the values of $\chi_{Au}^{(3)}$ can be quite large to affect the signal propagation in a LRSPP waveguide due to the field localization near the metal interfaces and long propagation distance L_{SPP}.

By the virtue of its origin and the SPPs field localization, the effective third-order nonlinear susceptibility of a gold strip waveguide must depend on the pulse duration and thickness of the constituent gold layer. One of the goals of this thesis is to quantify such dependences adopting experimental and theoretical results on nonlinear propagation of the LRSPP mode in gold strip waveguides conditioned by the third-order nonlinear susceptibility [Paper A].

This thesis present new experimental data on the third-order nonlinear susceptibility of gold for 200-fs laser pulses at a wavelength of 1030 nm, and for 3-ps laser pulses at a wavelength of 1064 nm. The experimental data can be compared to obtain an experimental dependence of the third-order nonlinear susceptibility on the gold layer thickness and pulse duration in the femtosecond-

picosecond range. The obtained dependences confirm a significant increase in nonlinearity for picosecond pulses over femtosecond ones due to their better temporal overlap with the transient profile of electronic temperature variation in gold. The theoretical pulse duration dependences of $\chi_{\mathrm{Au}}^{(3)}$ are extrapolated over the broad range from tens of femtoseconds to tens of picoseconds. It is also confirmed experimentally that the effective enhancement of the third-order nonlinear susceptibility of the gold strip waveguides inversely proportional to the gold layers thickness. A theoretical dependence of the third-order nonlinear susceptibility of the gold strip waveguides on the metal layer thickness is derived and presented in [Paper B]

The LRSPP waveguides studied here were fabricated in house [Paper C]. They contain a thin gold layer of different thickness *t* (22, 27 and 35 nm) sandwiched between tantalum pentoxide adhesion layers and silicon dioxide cladding. A schematic diagram of the LRSPP waveguides is shown in Fig. 1.1. This symmetric arrangement provides a substantial effective propagation length of LRSPPs of about 0.5-1 mm at a wavelength of 1030 nm depending on *t*.

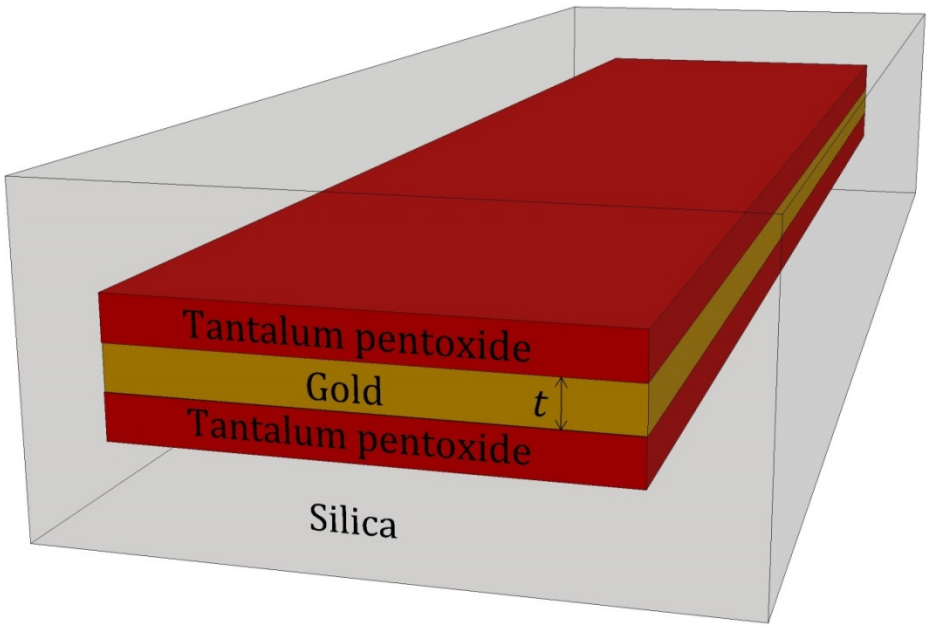

Figure 1.1. Sketch of the strip plasmonic waveguides.

The thesis has the following structure. Chapter 2 presents nonlinear optical model for the LRSPP waveguides, and, in particular, dependence of the third-order nonlinear susceptibility of gold on the layer thickness and laser pulse duration. Chapter 3 describes the fabrication process of the samples with the strip plasmonic waveguides. Chapter 4 is devoted to experimental studies of nonlinear optical effects in the LRSPP waveguides, and also presents the experimental values of the third-order nonlinear susceptibility of gold for different values of the layer thickness and laser pulse duration.

Chapter 2

Theoretical research

2.1. Optical properties of materials

The modeling of the strip plasmonic waveguides starts from consideration of optical properties of the constituent materials. These materials are gold (Au), tantalum pentoxide (Ta_2O_5), and silicon dioxide (SiO_2). The dielectric permittivity ε_{SiO_2} for silicon dioxide (also called as silica) is described by the following Sellmeier equation [32]:

$$\varepsilon_{SiO_2} = 1 + \frac{0.6961663\lambda^2}{\lambda^2 - (0.0684043)^2} + \frac{0.4079426\lambda^2}{\lambda^2 - (0.1162414)^2} + \frac{0.8974794\lambda^2}{\lambda^2 - (9.896161)^2}, \qquad \textbf{(2.1)}$$

where λ is the light wavelength in micrometers. The dielectric permittivity ε_{TPO} for tantalum pentoxide (amorphous dielectric) is given by the following equation [33]:

$$\varepsilon_{TPO} = \varepsilon_\infty - \frac{\omega_{p,0}^2}{\omega^2 + i\gamma_0\omega} + \sum_{j=1}^{6} \frac{\omega_{p,j}^2}{\omega_j^2 - \omega^2 - i\gamma\omega}. \qquad \textbf{(2.2)}$$

Here $\omega = 2\pi c / \lambda$ is the light angular frequency, c is the speed of light in vacuum, $\varepsilon_\infty = (A + B/\lambda^2)^2$ is the dielectric permittivity of amorphous Ta_2O_5 following the Cauchy dispersion formula [33] with the parameters A = 2.06 and B = 0.025 μm^2; $\omega_{p,0}$ = 6490 cm^{-1} and γ_0 = 6.5 × 10^{-5} cm^{-1} are the Drude plasma frequency and scattering rate for Ta_2O_5, and $\omega_{p,1}$ = 1040 cm^{-1}, $\omega_{p,2}$ = 573 cm^{-1}, $\omega_{p,3}$ = 634 cm^{-1}, $\omega_{p,4}$ = 408 cm^{-1}, $\omega_{p,5}$ = 277 cm^{-1}, $\omega_{p,6}$ = 373 cm^{-1}, γ_1 = 188 cm^{-1}, γ_2 = 112 cm^{-1}, γ_3 = 88 cm^{-1}, γ_4 = 43 cm^{-1}, γ_5 = 113 cm^{-1}, and γ_6 = 652 cm^{-1} are the

experimental parameters for the Lorentz oscillators taken from Ref. [33]. The linear refractive index for silica is $n_{SiO_2} = \sqrt{\varepsilon_{SiO_2}}$, and the linear refractive index for tantalum pentoxide is $n_{TPO} \approx \sqrt{\mathrm{Re}[\varepsilon_{TPO}]}$. The linear refractive indices n_{SiO_2} and n_{TPO} were calculated in the wavelength range from 350 to 1800 nm, according to Eq. (2.1) and Eq. (2.2), respectively, and shown in Fig. 2.1(a). The obtained dependences $n_{SiO_2}(\lambda)$ and $n_{TPO}(\lambda)$ have two main features. The first feature is that tantalum pentoxide has somewhat greater values of the linear refractive index. In particular, at the wavelength 1064 nm, the refractive index n_{SiO_2} for silica is approximately 1.45, and the refractive index n_{TPO} for tantalum pentoxide is approximately 2.07. The second feature is related to the zero dispersion wavelength (ZDW) values. The dispersion parameter for silica is $D_{SiO_2} = -(\lambda / c)(d^2 n_{SiO_2} / d\lambda^2)$ and changes sign at the wavelength approximately 1.27 μm [34], and the dispersion parameter for tantalum pentoxide is $D_{TPO} = -(\lambda / c)(d^2 n_{TPO} / d\lambda^2)$ and changes sign at the wavelength approximately 1.8 μm [35]. The ZDW values of the materials are important in nonlinear optics applications [34-37]. In fact, it will be shown further that the ZDW value of the long-range surface plasmon polariton mode in the strip plasmonic waveguides significantly depends on the thickness of the gold layer, and is somewhat different than the ZDW values of the constituent materials.

The dielectric permittivity ε_{Au} of a thin gold layer is calculated based on the classical Drude model [30, 31, 38], but also with accounting for an electron confinement factor. For a metal nanosphere the collision frequency of electrons γ_f depends on the radius *r* [39, 40]. In the same way of arguing as in [40], where a 1/*r* dependence reflects the ratio of surface area to volume, one can proceed by assuming that for a thin gold stripe with the thickness *t* one can take:

$$\mathrm{Re}[\varepsilon_{Au}] = 1 - \frac{\omega_p^2}{\gamma_f^2 + \omega^2}, \qquad \textbf{(2.3)}$$

$$\mathrm{Im}\left[\varepsilon_{\mathrm{Au}}\right]=\frac{\gamma_{\mathrm{f}}\omega_{\mathrm{p}}^{\,2}}{\omega(\gamma_{\mathrm{f}}^{\,2}+\omega^{2})}, \tag{2.4}$$

$$\gamma_{\mathrm{f}}=\gamma_{\infty}+\frac{\upsilon_{\mathrm{F}}}{t}, \tag{2.5}$$

where $\omega_{\mathrm{p}}=\sqrt{ne^{2}/\varepsilon_{0}m_{\mathrm{e}}}$ is the plasma frequency for gold, e is the electron charge, ε_{0} is the vacuum permittivity, n is the electron density, m_{e} is the electron mass, γ_{∞} = 3.3 × 10^{13} s^{-1} is the collision frequency of electrons for bulk gold, and υ_{F} is the Fermi velocity of electrons. As the layer thickness t approaches nanoscale values, free electrons start to feel the layer boundaries and the second term in Eq. (2.5) accounts for this increment of the electrons collisions frequency, while the plasma frequency stays the same [31]. The local Drude model may not be applicable for metal layers with the thickness below 10 nm [41]. Also there is an intensive clustering process for thin metal layers [40], and their fabrication, especially with thicknesses below 10 nm, is still challenging [42]. Therefore, the present model will focus on the strip plasmonic waveguides with the metal thickness values above the clustering threshold. Constraining the layer thickness t by 10 nm it is straightforward to show that Eq. (2.4) can be simplified as follows:

$$\mathrm{Im}[\varepsilon_{\mathrm{Au}}]\approx(\mathrm{Im}[\varepsilon_{\mathrm{Au}}])_{\infty}+\frac{\omega_{\mathrm{p}}^{\,2}\upsilon_{\mathrm{F}}}{\omega(\gamma_{\infty}^{\,2}+\omega^{2})t}, \tag{2.6}$$

where $(\mathrm{Im}[\varepsilon_{\mathrm{Au}}])_{\infty}$ is the imaginary part of the dielectric permittivity for bulk gold. The real part and imaginary part of the dielectric permittivity function $\varepsilon_{\mathrm{Au}}(t)$ for thin gold layers were calculated at the wavelength 1064 nm, and for the layers thickness t in the range from 10 to 60 nm. The dependences $\mathrm{Re}[\varepsilon_{\mathrm{Au}}(t)]$ and $\mathrm{Im}[\varepsilon_{\mathrm{Au}}(t)]$ are shown in Fig. 2.1(b). The real part $\mathrm{Re}[\varepsilon_{\mathrm{Au}}]$ is negative and changes insignificantly by only approximately 0.9%. This is because the collision

frequency of electrons γ_f is much less than telecom optical frequencies: γ_f is approximately 17.2 × 10^{13} s^{-1} at the thickness t = 10 nm and decreases to approximately 5.6 × 10^{13} s^{-1} at the thickness t = 60 nm. In contrary, the imaginary part $\mathrm{Im}[\varepsilon_{Au}]$ changes by an order of magnitude. The calculated values of the linear refractive index n_{SiO_2} for silicon dioxide, the linear refractive index n_{TPO} for tantalum pentoxide, and the dielectric permittivity ε_{Au} for thin gold layers are used for the modeling of the long-range surface plasmon polaritons propagation in the strip plasmonic waveguides.

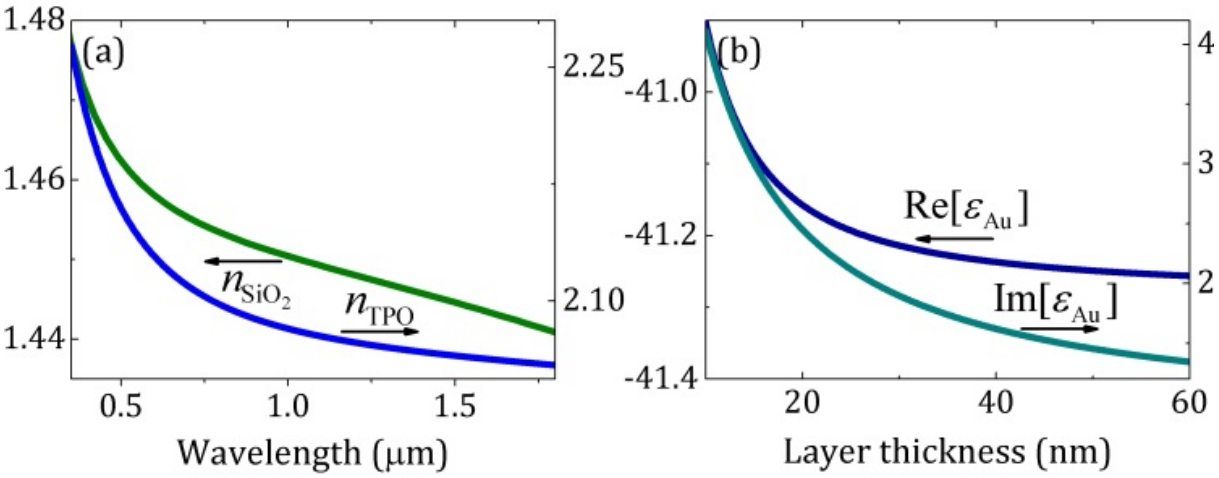

Figure 2.1. (a) Linear refractive indices n_{SiO_2} for silicon dioxide and n_{TPO} for tantalum pentoxide versus wavelength. (b) Real part and imaginary part of the dielectric permittivity ε_{Au} for gold layers with different thickness at the wavelength 1064 nm.

2.2. Strip plasmonic waveguides

The designed geometry of the strip plasmonic waveguides is shown in Fig. 2.2. It contains the gold core with the thickness t, tantalum pentoxide layers with thickness t_1, and thick silica cladding. The waveguide has the microscale width w and millimeter scale length l. The thickness of the SiO_2 cladding is large enough to cover the long-range surface plasmon polariton mode distribution in the yz-plane. The propagation constant β of the plasmonic mode in this multilayer configuration can be calculated by using the effective refractive index method [43]. This method is well-known and often applied for the modal analysis of multilayer waveguides. The first step here is to calculate the propagation constant β_∞ of the long-range surface plasmon polariton mode in the symmetric slab waveguide with five layers of materials (silica, tantalum pentoxide, gold, tantalum pentoxide, and silica), assuming the infinitely large width of the layers, namely $w = \infty$.

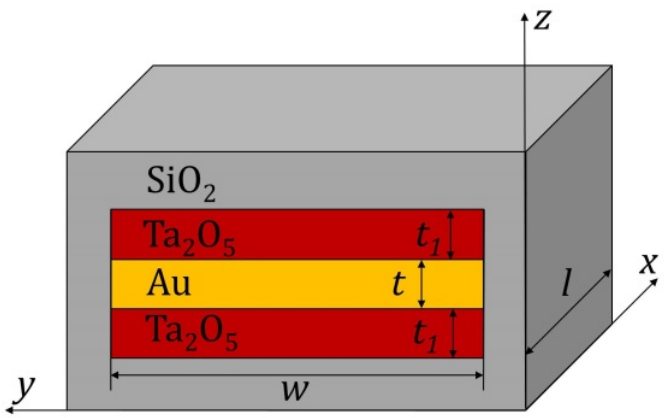

Figure 2.2. Geometry of the strip plasmonic waveguide.

By using Maxwell's equations and boundary conditions [44, 45] it is straightforward to show that the dispersion equation for the propagation constant β_∞ in the symmetric five-layer system is given by:

$$\frac{k_3}{\varepsilon_3}\tanh\left(\frac{t}{2}k_3\right)=-\frac{k_2}{\varepsilon_2}\frac{\left(\frac{k_2}{\varepsilon_2}+\frac{k_1}{\varepsilon_1}\right)e^{k_2t_1}-\left(\frac{k_2}{\varepsilon_2}-\frac{k_1}{\varepsilon_1}\right)e^{-k_2t_1}}{\left(\frac{k_2}{\varepsilon_2}+\frac{k_1}{\varepsilon_1}\right)e^{k_2t_1}+\left(\frac{k_2}{\varepsilon_2}-\frac{k_1}{\varepsilon_1}\right)e^{-k_2t_1}}. \quad \textbf{(2.7)}$$

Here $k_j=\sqrt{\beta_\infty^2-\varepsilon_j\omega^2/c^2}$ (j = 1, 2, 3) are the wave vectors for silica, tantalum pentoxide and gold, respectively. This dispersion equation is solved numerically for β_∞, and the effective linear refractive index of the LRSPP mode is $n_{\text{eff}}=\beta_\infty c/\omega$. Then, the effective linear refractive index n_{eff} of the slab waveguide is used to determine the propagation constant β of the long-range surface plasmon polariton mode in the finite-width strip waveguide by solving the standard dispersion equation [43]:

$$\sqrt{\frac{\omega^2 {n_{\text{eff}}}^2}{c^2}-\beta^2}\tan\left(\frac{w}{2}\sqrt{\frac{\omega^2 {n_{\text{eff}}}^2}{c^2}-\beta^2}\right)=\sqrt{\beta^2-\frac{\omega^2 {n_{\text{SiO}_2}}^2}{c^2}}. \quad \textbf{(2.8)}$$

The normalized propagation constant $\overline{\beta}=\beta c/\omega=n_{\text{eff1}}$ corresponds to the effective linear refractive refractive index of the LRSPP mode. Equation (2.8) has several roots, which correspond to different LRSPP spatial modes. The fundamental LRSPP mode has the largest value of the effective linear refractive index n_{eff} [43], and the effective refractive indices of other roots are in the range $n_1<n_{\text{eff1}}<n_{\text{eff}}$. The present work will focus further on the fundamental LRSPP mode, which is a transverse magnetic (TM) mode with the magnetic field pointed along the *y*-direction, and the electric field pointed along the *z*- and *x*-directions. The real part of the effective linear refractive index $\text{Re}[n_{\text{eff1}}]$ and the linear absorption parameter $\alpha=2\,\text{Im}[\beta]$ were calculated in the wavelength range from 800 to 1550 nm, and for the gold layer thickness t = 22, 27, and 35 nm (Fig. 2.3). These specific values of the thickness were selected mainly to follow the recent experimental studies [Paper A, Paper C]. These values of the

thickness are above the clustering threshold, that is approximately 10 nm, and they are small enough to provide low-loss propagation of the LRSPP mode. Figure 2.3 shows that the linear propagation loss of the LRSPP mode is smaller (and the characteristic propagation distance is larger) for the strip plasmonic waveguides with thinner gold layers. In terms of the linear propagation loss, the IR wavelength range (in particular, the telecom wavelength range) is more often used than the visible range, as the values of the propagation loss in the strip plasmonic waveguides change by approximately one order of magnitude. In the calculation the thickness of the tantalum pentoxide layer t_1 = 26 nm, and the width of the layers w = 10 μm. These specific values of the width w and thickness t_1 were also selected mainly to follow the fabrication of the samples and experimental results, which are presented in [Paper C].

The transverse electric field component E_z of the LRSPP mode has the dominant contribution to the plasmonic mode intensity and will be considered in detail further. The normalized electric field intensity distribution function $|E_z(y,z)|^2$ of the LRSPP mode was calculated in the transverse sections of the strip plasmonic waveguide, and for the gold layer thickness t = 22, 27, and 35 nm (Fig. 2.4). Figure 2.4(a) shows the distribution function $|E_z|^2$ in the transverse *xy*-plane and in the micrometer range. In fact, it determines the necessary thickness of the silica cladding to completely cover the LRSPP mode distribution. It is easy to see that the distribution function $|E_z|^2$ of the fundamental LRSPP mode significantly decays after approximately 1 μm, therefore around 3-5 μm thickness of the silica cladding is usually enough during the fabrication of the samples. Figure 2.5(c) shows the distribution function $|E_z|^2$ in the transverse *xy*-plane and in the nanometer range. The distribution function $|E_z|^2$ experiences a step-like behavior at the interface of gold and tantalum pentoxide, and at the interface of tantalum pentoxide and silica, as expected from the boundary conditions [30, 45]. The gold layer

thickness t does not affect the intensity distribution function $|E_z|^2$ in the z-plane [Fig. 2.4(b)]. The two-dimensional distribution function $|E_z(y,z)|^2$ of the fundamental LRSPP mode with a good accuracy can be expressed in terms of a product of the one-dimensional distribution functions: $E_z(y,z) = E_z(y)E_z(z)$. In fact, the value of the propagation constant β_∞ for the infinitely wide slab waveguide differs by less than one percent from the value of the propagation constant β of the finite-width strip waveguide, thus justifying the variables y and z separation in the expression for the two-dimensional distribution function $E_z(y,z)$. This important property of the distribution function $E_z(y,z)$ will be used further in the calculation of the field integrals for the constituent materials of the strip plasmonic waveguide.

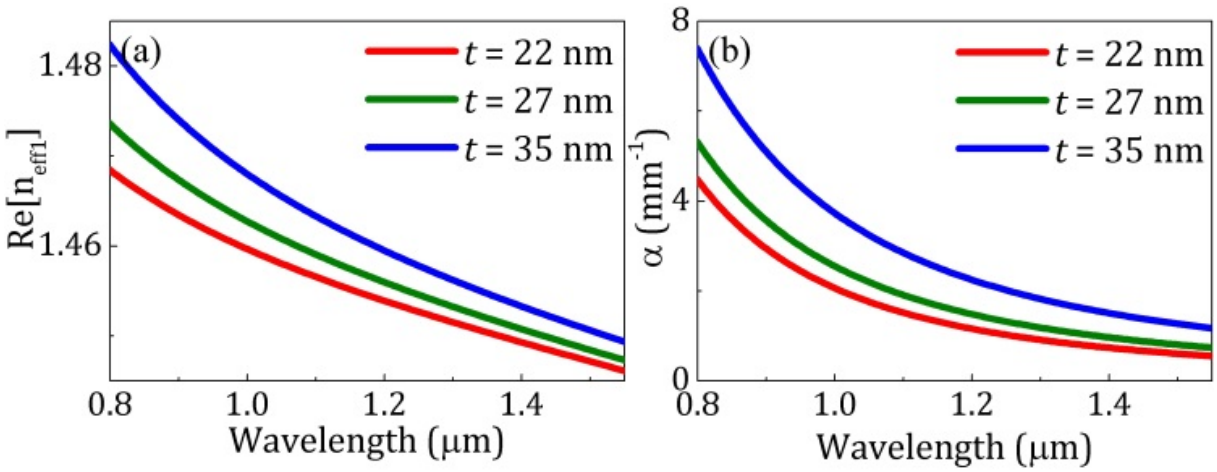

Figure 2.3. Real part of the effective linear refractive index n_{eff} (a) and linear propagation loss coefficient α (b) of the fundamental LRSPP mode in the strip plasmonic waveguides for the gold layer thickness t = 22, 27, and 35 nm versus wavelength.

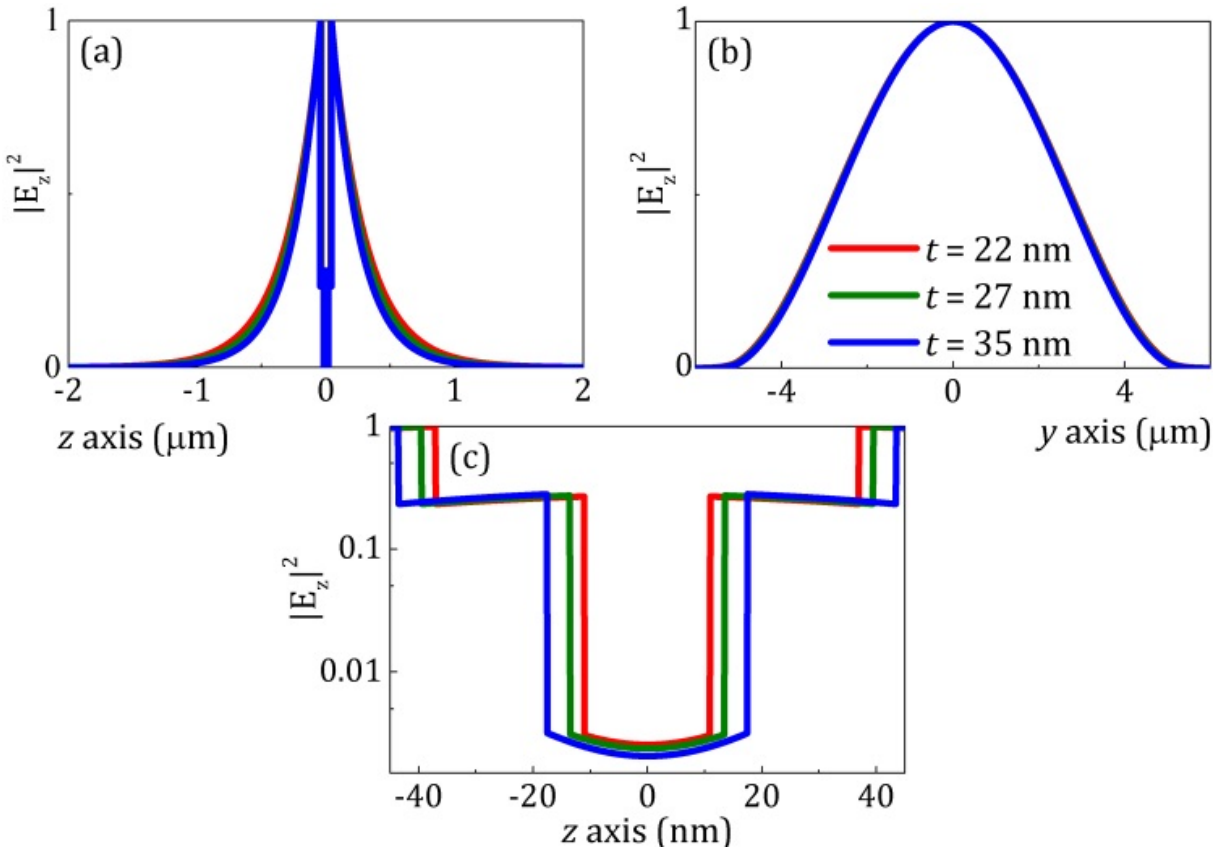

Figure 2.4. Intensity distribution function $|E_z(y,z)|^2$ of the fundamental LRSPP mode in the strip plasmonic waveguides for the gold layer thickness t = 22, 27, and 35 nm versus (a) z-axis in the micrometer range, (b) y-axis in the micrometer range, and (c) z-axis in the nanometer range.

2.3. Chromatic dispersion

The first and second derivatives of the real part of the propagation constant β determine the chromatic dispersion parameters of the long-range surface plasmon polariton mode in strip plasmonic waveguides. The first dispersion derivative $\beta_1 = d\beta / d\omega$ is related to the group velocity υ_g and the group linear refractive index n_g of the LRSPP mode by the following expression [34]:

$$\beta_1 = \frac{1}{\upsilon_g} = \frac{n_g}{c}. \qquad \textbf{(2.9)}$$

The second dispersion derivative $\beta_2 = d^2\beta / d\omega^2$, which is also referred as the group velocity dispersion (GVD) parameter, is related to the characteristic dispersion length L_D of the LRSPP mode as follows [34]:

$$L_D = \frac{T_0^2}{|\beta_2|}, \qquad \textbf{(2.10)}$$

where T_0 is the half-width (1/e-intensity value) in the case of Gaussian shape of optical pulses in the strip plasmonic waveguides. In practice, it is also convenient to use the full width at half maximum (FWHM). For a Gaussian pulse, these parameters are related by the following formula [34]:

$$T_{FWHM} = 2\sqrt{\ln 2}T_0. \qquad \textbf{(2.11)}$$

The FWHM parameter of Gaussian pulses is often referred simply as the pulse duration. The group linear refractive index n_g and the GVD parameter β_2 of the LRSPP mode in the strip plasmonic waveguides were calculated in the wavelength range from 800 to 2000 nm and for the gold layer thickness t = 22, 27, and 35 nm [Fig. 2.5(a) and 2.5(b)]. The normalized group velocity υ_g and the

characteristic dispersion length L_D of the LRSPP mode were calculated in the wavelength range from 800 to 1550 nm and for the same values of the gold layer thickness [Fig. 2.5(c) and 2.5(d)]. The average value of the group velocity υ_g at the wavelength 1064 nm is approximately 67 percent of the speed of light in vacuum. The ZDW values of the LRSPP mode in the strip plasmonic waveguides are approximately 1.7 μm, 1.8 μm, and 1.93 μm for the gold layer thickness 22, 27, and 35 nm, respectively. Meanwhile, the ZDW value of the LRSPP mode at the telecom wavelength 1.55 μm can be achieved in plasmonic waveguides with the gold layer thickness 15 nm. This thickness is above the clustering threshold [40] and it can be interesting to fabricate the waveguides with thinner gold layers and implement the anomalous-dispersion regime (when $\beta_2 < 0$) in propagation of the optical pulses. The magnitude of the GVD parameter β_2 is approximately ten times greater (~10^{-4} ps^2/mm=10^2 ps^2/km) than typical GVD values for single-mode optical fibers (~10 ps^2/km) [34-36]. The characteristic dispersion length L_D for optical pulses with the Gaussian shape and the pulse duration T_{FWHM} = 3 ps (also simply referred as 3-ps pulses) is in the range from 200 to 1000 mm, and is significantly greater than the physical length of the strip plasmonic waveguides l (which is usually in the millimeter range). Therefore, the chromatic dispersion has a very small effect on the propagation of the picosecond long-range surface plasmon polaritons in the strip plasmonic waveguides. Nevertheless, the calculation of the chromatic dispersion parameters of the LRSPP mode is important and can be used in the case of very short (tens of femtoseconds) optical pulses, when the characteristic dispersion length is comparable or shorter than the physical length of the waveguides.

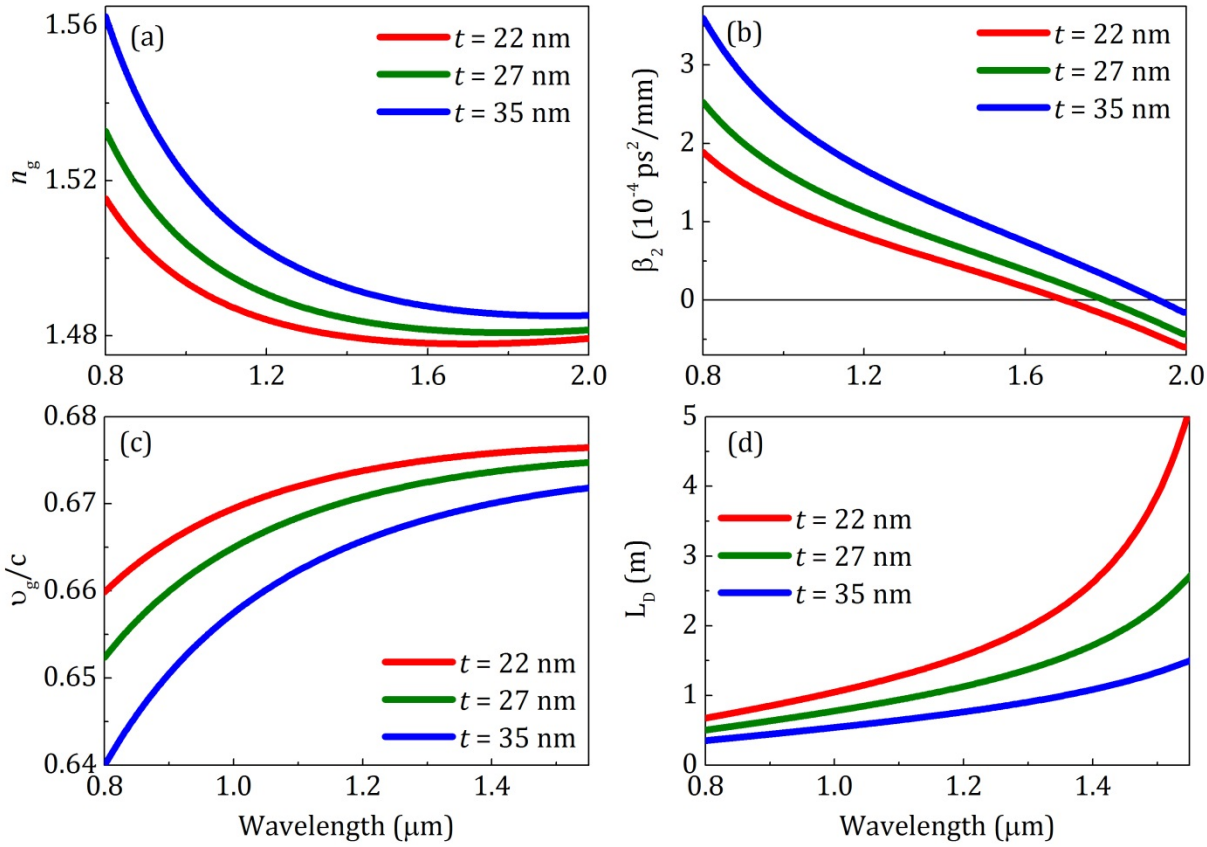

Figure 2.5. Chromatic dispersion parameters of the LRSPP mode in the strip plasmonic waveguides for the gold layer thickness t = 22, 27, and 35 nm: (a) group linear refractive index n_g, (b) group velocity dispersion parameter β_2, (c) normalized group velocity υ_g / c, and (d) characteristic dispersion length L_D for 3-ps optical pulses versus wavelength.

2.4. Nonlinear parameters

For the quantitative analysis of effective nonlinear properties of the fundamental long-range surface plasmon polariton mode in the strip plasmonic waveguide, one can calculate the field integrals of the plasmonic mode in the constituent materials, according to the following expressions:

$$\theta_{\mathrm{Au}} = \frac{\int_{-t/2}^{t/2} |E_z|^2 \, dz}{\int_{-\infty}^{+\infty} |E_z|^2 \, dz}, \tag{2.12}$$

$$\theta_{\mathrm{Ta_2O_5}} = \frac{2\int_{t/2}^{t/2+t_1} |E_z|^2 \, dz}{\int_{-\infty}^{+\infty} |E_z|^2 \, dz}, \tag{2.13}$$

$$\theta_{\mathrm{SiO_2}} = \frac{2\int_{t/2+t_1}^{+\infty} |E_z|^2 \, dz}{\int_{-\infty}^{+\infty} |E_z|^2 \, dz} = 1 - \theta_{\mathrm{Au}} - \theta_{\mathrm{Ta_2O_5}}. \tag{2.14}$$

The initial two-dimensional integrals over the plasmonic mode area in the *yz*-plane were reduced to one-dimensional integrals over the *z*-coordinate by applying the variables separation justified above: $E_z(y,z) = E_z(y)E_z(z)$. In fact, the one-dimensional integrals over the *y*-coordinate have the same values in the numerator and denominator and are canceled due to the waveguide symmetry.

The real and imaginary parts of effective third-order nonlinear susceptibility $\chi^{(3)}$ of the long-range surface plasmon polariton mode in the strip plasmonic waveguides are expressed by the following expression:

$$\mathrm{Re}\left[\chi^{(3)}\right] = \theta_{\mathrm{Au}} \mathrm{Re}\left[\chi_3^{(3)}\right] + \theta_{\mathrm{Ta_2O_5}}\chi_2^{(3)} + \theta_{\mathrm{SiO_2}}\chi_1^{(3)}, \tag{2.15}$$

$$\mathrm{Im}\left[\chi^{(3)}\right]=\theta_{\mathrm{Au}}\,\mathrm{Im}\left[\chi_3^{(3)}\right]. \tag{2.16}$$

Here $\chi_1^{(3)}$ is the third-order nonlinear susceptibility for the silicon dioxide cladding [46], $\chi_2^{(3)}$ is the third-order nonlinear susceptibility for the tantalum pentoxide layers [47] and $\chi_3^{(3)}$ is the third-order nonlinear susceptibility of the gold layer. The third-order nonlinear susceptibility of bulk gold $\chi_\infty^{(3)}$ is given by the following formula [24]:

$$\chi_\infty^{(3)}=\frac{1}{2}\varepsilon_0\omega\mathrm{Im}[\varepsilon_{\mathrm{Au}}]\tau_{\mathrm{r}}\tau_{\mathrm{th}}\left(\frac{\gamma_{\mathrm{e}}}{C_{\mathrm{e}}}-\frac{\gamma_{\mathrm{lat}}}{C_{\mathrm{lat}}}\right)\frac{\partial\varepsilon_{\mathrm{inter}}}{\partial T_{\mathrm{e}}}, \tag{2.17}$$

where $C_{\mathrm{e}} \approx 2.1\times10^4$ J/(m^3·K) is the electronic heat capacity per unit volume of gold [48], $C_{\mathrm{lat}} \approx 2.5\times10^6$ J/(m^3·K) is the lattice heat capacity per unit volume of gold [48], $\gamma_{\mathrm{e}} \approx 2$ THz is the electron thermalization rate [49], $\gamma_{\mathrm{lat}} \approx 1$ THz is the lattice thermalization rate [49], $G \approx 20$ PHz is the electron-photon coupling coefficient [48], $\tau_{\mathrm{th}}=1/(\gamma_{\mathrm{e}}+\gamma_{\mathrm{lat}}) \approx 300$ fs is the decay time for nonthermalized electrons [24], $\tau_{\mathrm{r}}=C_{\mathrm{e}}C_{\mathrm{lat}}/[G(C_{\mathrm{e}}+C_{\mathrm{lat}})] \approx 1$ ps is the decay time for thermalized electrons [24], and $\partial\varepsilon_{\mathrm{inter}}/\partial T_{\mathrm{e}}$ is the complex value of the interband thermo-modulational derivative [24].

To calculate the thickness dependent third-order nonlinear susceptibility of gold layer $\chi_3^{(3)}(t)$, one can substitute the thickness dependent permittivity $\varepsilon_{\mathrm{Au}}(t)$ from Eq. (2.6) into Eq. (2.17) and obtain the following expression:

$$\chi_3^{(3)}=\chi_\infty^{(3)}\left(1+\frac{\upsilon_{\mathrm{F}}}{\gamma_\infty t}\right). \tag{2.18}$$

In the derivation of Eq. (2.18) all parameters in the two-temperature model were assumed thickness independent, except the dielectric permittivity of gold layer $\varepsilon_{\mathrm{Au}}$. For very small values of the gold layer thickness *t*, the model of the third-

order nonlinear susceptibility must be revised by using nonlocal and quantum approaches [41, 50]. The real and imaginary parts of the third-order nonlinear susceptibility $\chi_3^{(3)}$ were calculated at the wavelength 1064 nm, and for the gold layer thickness *t* in the range from 10 to 60 nm. The obtained dependences are shown in Fig. 2.6, and indicate the effective enhancement of the third-order nonlinear susceptibility $\chi_3^{(3)}$ in approximately 3 times as the layer thickness *t* decreases from 60 nm to 10 nm. The horizontal asymptotes in Fig. 2.6(a) and 2.6(b) correspond to the values of the real part and imaginary part of the third-order nonlinear susceptibility $\chi_\infty^{(3)}$ of bulk gold at the wavelength 1064 nm, respectively [24]. The value of the real part of the third-order susceptibility $\chi_\infty^{(3)}$ is approximately 4.6×10^{-17} m^2/V^2, and the values of the imaginary part of the third-order susceptibility $\chi_\infty^{(3)}$ is approximately 4.8×10^{-18} m^2/V^2. The real part of the third-order susceptibility $\mathrm{Re}[\chi_3^{(3)}]$ is around 10 times greater in magnitude than the imaginary part of the third-order susceptibility $\mathrm{Im}[\chi_3^{(3)}]$ for the same values of the layer thickness *t*. Figure 2.6 also shows the thickness limitations. The classical Drude model based on Eq. (2.3)-(2.5) cannot be completely applicable in the case of gold layers with the thickness *t* below approximately 10-15 nm due to possible quantum effects [50], nonlocal effects [41], and also clustering of the metal layer [40]. On the other hand, the coupled long-range surface plasmon polariton mode breaks down in the case of gold layers with the thickness *t* above approximately 50-60 nm due a small penetration depth of surface electromagnetic waves in the metal [51, 52]. Therefore, the effective range of the gold layer thickness *t* is approximately from 15 to 50 nm for experimental studies of nonlinear propagation of the LRSPP mode in the strip plasmonic waveguides.

The literature values of the third-order nonlinear susceptibility $\chi_\infty^{(3)}$ of bulk gold at the wavelength 1550 nm are approximately the same as the ones at the wavelength 1064 nm [24], however the values of the linear propagation loss

parameter α of the LRSPP mode in the strip plasmonic waveguides are significantly smaller at the wavelength 1550 nm [Fig. 2.3(b)]. Thus, the wavelength 1550 nm can be a good option for an experimental study of nonlinear plasmonic effects in the gold strip waveguides. Depending on the fabrication process, in the case of continuous gold layers with the thickness t approximately 10-15 nm, an anomalous-dispersion regime of propagation of the LRSPP mode in the strip plasmonic waveguides can be realized at the telecom C-band wavelengths. This opens up a possibility to excite solitons in the strip plasmonic waveguides.

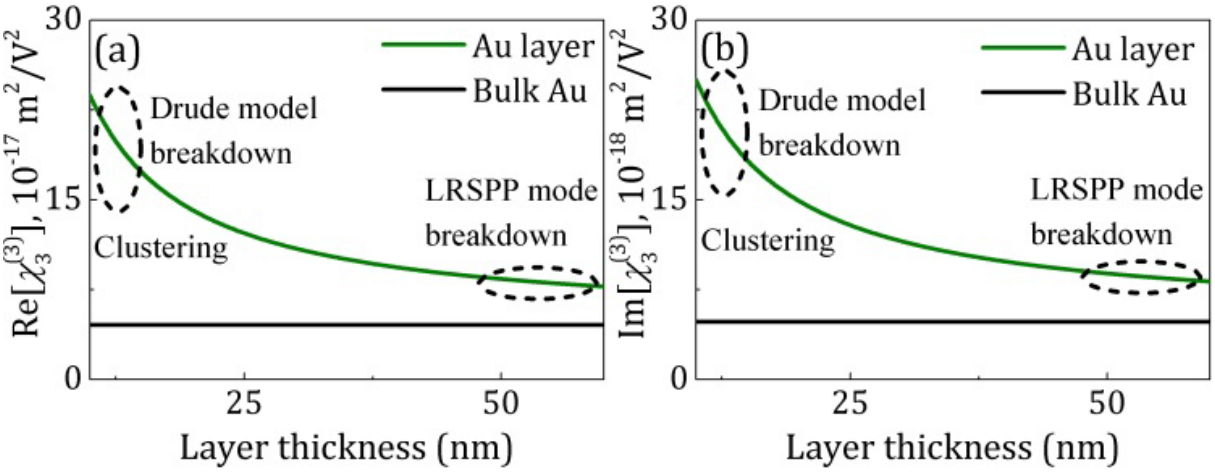

Figure 2.6. (a) Real part and (b) imaginary part of the third-order nonlinear susceptibility $\chi_3^{(3)}$ of bulk gold (black lines) and thin gold layers (green lines) at the wavelength 1064 nm.

For the wavelength 800 nm, the value of the real part of the third-order nonlinear susceptibility of bulk gold $\chi_\infty^{(3)}$ is approximately 40 percent greater, and the value of the imaginary part of the third-order nonlinear susceptibility of bulk gold $\chi_\infty^{(3)}$ is approximately 5 times greater than the ones at the wavelength 1064 nm. Therefore, in this case, the nonlinear absorption has a more dominant effect on nonlinear dynamics of the LRSPP mode in the strip plasmonic waveguides. The values of the linear propagation loss parameter α of the LRSPP

mode are significantly larger than at the wavelength 1064 nm [Fig. 2.3(b)]. Depending on the experimental equipment, in particular, the laser source and detection device, the wavelength 800 nm is possible for experimental studies of the LRSPP mode in the strip plasmonic waveguides. The physical length l of the waveguides should as small as possible, for instance, 1 mm or even less. In one of the recent experiments, Baron *et al.* [53] measured the imaginary component of the third-order nonlinear susceptibility for bulk gold by studying nonlinear propagation of SPPs at a single air/metal interface at the wavelength 800 nm.

The effective nonlinear refractive index $n_{2\mathrm{eff}}$, nonlinear absorption coefficient β and nonlinear parameter γ of the LRSPP mode in the strip plasmonic waveguides are given by the following expressions [34, 54]:

$$n_{2\mathrm{eff}} = \frac{3}{4\varepsilon_0 c n_0^2}\mathrm{Re}[\chi^{(3)}], \tag{2.19}$$

$$\beta = \frac{\beta_{\mathrm{c}}}{A_{\mathrm{eff}}} = \frac{3\omega}{2\varepsilon_0 c^2 n_0^2 A_{\mathrm{eff}}}\mathrm{Im}[\chi^{(3)}], \tag{2.20}$$

$$\gamma = \frac{\omega}{c}\frac{n_{2\mathrm{eff}}}{A_{\mathrm{eff}}}. \tag{2.21}$$

Here β_{c} is the conventional definition of the nonlinear absorption coefficient [54], and A_{eff} is the effective area of the fundamental LRSPP mode calculated by the following formula [34]:

$$A_{\mathrm{eff}} = \frac{\left(\int_{-\infty}^{+\infty}\int_{-\infty}^{+\infty}|E_{\mathrm{z}}(y,z)|^2\,dydz\right)^2}{\int_{-\infty}^{+\infty}\int_{-\infty}^{+\infty}|E_{\mathrm{z}}(y,z)|^4\,dydz}. \tag{2.22}$$

The parameters of the fundamental LRSPP mode, namely the field integrals θ_{Au}, $\theta_{Ta_2O_5}$, θ_{SiO_2}, effective area A_{eff}, linear refractive index n_{eff}, nonlinear absorption coefficient β, and nonlinear coefficient γ were calculated for the gold layer thickness t = 22, 27 and 35 nm, and presented in Table 2.1. And the values of the third-order nonlinear susceptibility $\chi_3^{(3)}$, and the linear refractive index n_{Au} of the gold layers with the thickness t = 22, 27 and 35 nm are also shown in Table 2.1. The variations of the obtained values were calculated by changing the gold layer thickness t by 1 nm. The same values of the tantalum pentoxide layer thickness t_1 = 26 nm, layers width w = 10 μm, and the wavelength 1064 nm were used, mainly to follow the fabrication of the samples and experimental results, which are presented in [Paper C].

The literature value of the third-order susceptibility $\chi_1^{(3)}$ for silica is approximately 2.07×10^{-22} m^2/V^2 [46], and the literature value of the third-order susceptibility $\chi_2^{(3)}$ for tantalum pentoxide is approximately 1.12×10^{-20} [47]. The calculated values of the field integrals indicate that the most of the electric field of the fundamental LRSPP mode (around 97%) is localized in the silica cladding. However, the specific contributions from tantalum pentoxide $\theta_{Ta_2O_5}\chi_2^{(3)}$ and silica $\theta_{SiO_2}\chi_1^{(3)}$ to the real part of the effective third-order nonlinear susceptibility $\chi^{(3)}$ of the LRSPP mode are of the same order of magnitude (~3×10^{-22} m^2/V^2 and ~2×10^{-22} m^2/V^2, respectively). The specific contribution from the gold layer is approximately two orders of magnitude greater (~2×10^{-20} m^2/V^2), and is therefore dominating. The imaginary part of the effective third-order nonlinear susceptibility $\chi^{(3)}$ is solely determined by the imaginary part of the third-order nonlinear susceptibility $\chi_3^{(3)}$ of the gold layer. The dielectrics have only the real component of the third-order nonlinear susceptibility because the photon energy at 1064 nm is far below half of the bandgap energy for silica and tantalum pentoxide. Thus, the dominant role of the third-order nonlinearity of the gold layer in the effective third-order nonlinearity of the LRSPP mode in

the strip plasmonic waveguides is confirmed. This conclusion about the dominant role of the metal nonlinearity is in accordance with the recent theoretical results published by Baron *et al.* for other plasmonic systems [53].

Table 2.1. Parameters of the fundamental LRSPP mode in the strip plasmonic waveguides: the field integrals θ_{Au}, $\theta_{Ta_2O_5}$, θ_{SiO_2}, effective area A_{eff}, linear refractive index n_{eff}, nonlinear absorption coefficient β, nonlinear coefficient γ, and the values of the third-order nonlinear susceptibility $\chi_3^{(3)}$ and the linear refractive index n_{Au} of the gold layers with the thickness t = 22, 27 and 35 nm and at the wavelength 1064 nm.

t, nm	35 ± 1	27 ± 1	22 ± 1
θ_{Au}, 10^{-3}	0.1872 ± 0.0055	0.1397 ± 0.0062	0.1084 ± 0.0063
$\theta_{Ta_2O_5}$	0.0298 ± 0.0004	0.0263 ± 0.0004	0.0239 ± 0.0005
θ_{SiO_2}	0.9701 ± 0.0005	0.9736 ± 0.0005	0.9760 ± 0.0005
Re[n_{eff1}]	1.4649 ± 0.0003	1.4603 ± 0.0003	1.4576 ± 0.0003
Im[n_{eff1}], 10^{-2}	0.0265 ± 0.0009	0.0179 ± 0.0009	0.0143 ± 0.0009
Re[n_{Au}]	0.1352 ± 0.0020	0.1570 ± 0.0034	0.1786 ± 0.0050
Im[n_{Au}]	6.4223 ± 0.0001	6.4208 ± 0.0003	6.4192 ± 0.0004
A_{eff}, μm^2	9.17 ± 0.11	10.24 ± 0.16	11.15 ± 0.20
β, 1/(W·m)	0.139 ± 0.005	0.095 ± 0.005	0.069 ± 0.005
γ, 1/(W·m)	0.77 ± 0.03	0.52 ± 0.03	0.38 ± 0.03
Re[$\chi_3^{(3)}$], m^2/V^2	10.03×10^{-17}	11.65×10^{-17}	13.27×10^{-17}
Im[$\chi_3^{(3)}$], m^2/V^2	10.58×10^{-18}	12.29×10^{-18}	14.00×10^{-18}

2.5. Pulse propagation equation

Once the linear and nonlinear optical parameters of the fundamental LRSPP mode in the strip plasmonic waveguide are known, the propagation dynamics of the mode is well described by the pulse propagation equation, which is often referred as the nonlinear Schrödinger equation [34]:

$$\frac{\partial A}{\partial x} = i\gamma |A|^2 A - \frac{\alpha}{2} A - \frac{\beta}{2} |A|^2 A, \tag{2.23}$$

where $A(x,T)$ is the complex amplitude of an optical pulse, x is the propagation coordinate, T is the time coordinate in the co-moving frame of the input pulse. The first and third term correspond to the self-phase modulation (SPM) and nonlinear absorption, respectively. The chromatic dispersion has been neglected, which is a good approximation as dispersion length L_D for picosecond optical pulses in the strip plasmonic waveguides is significantly larger than the physical length l of the waveguides. The formal solution to Eq. (2.23) is the following [34]:

$$A(x,T) = \sqrt{P(x,T)} \exp[i\phi_{NL}(x,T)], \tag{2.24}$$

where $P(x,T)$ is the pulse power amplitude and $\phi_{NL}(x,T)$ is the pulse nonlinear phase. Substituting this solution in Eq. (2.23) gives the following system of differential equations:

$$\begin{cases} \dfrac{\partial P(x,T)}{\partial x} = -\alpha P(x,T) - \beta |P(x,T)|^2, \\ \dfrac{\partial \phi_{NL}(x,T)}{\partial x} = \gamma P(x,T). \end{cases} \tag{2.25}$$

The system is straightforward to solve for the Gaussian pulse initial conditions: $P(0,T) = P_0 \exp(-T^2 / T_0^2)$ and $\phi_{\mathrm{NL}}(0,T) = 0$:

$$\begin{cases} P(x,T) = \dfrac{P_0 e^{-\frac{T^2}{T_0^2}} e^{-\alpha x}}{1 + \beta P_0 e^{-\frac{T^2}{T_0^2}} (1 - e^{-\alpha x}) / \alpha}, \\ \phi_{\mathrm{NL}}(x,T) = \dfrac{\gamma}{\beta} \ln\left[1 + \beta P_0 e^{-\frac{T^2}{T_0^2}} \dfrac{(1 - e^{-\alpha x})}{\alpha} \right]. \end{cases} \tag{2.26}$$

These solutions describe how the peak power $P(x,T)$ and nonlinear phase $\phi_{\mathrm{NL}}(x,T)$ of optical pulses in the strip plasmonic waveguides change in the time domain upon propagation. For practical purposes, the formula for the peak power $P(x,T)$ can be modified to obtain a formula for the average values of the power $\bar{P}$ of light at the input and output of the plasmonic waveguides, which are the observable and directly measurable physical values. The equation for the pulse energy $E(x)$ is expressed as:

$$E(x) = \int_{-\infty}^{+\infty} |A(x,T)|^2 \, dT = \int_{-\infty}^{+\infty} \frac{P_0 T_0 e^{-\alpha x} e^{-\frac{T^2}{T_0^2}}}{1 + \beta P_0 e^{-\frac{T^2}{T_0^2}} (1 - e^{-\alpha x}) / \alpha} d\left(\frac{T}{T_0} \right). \tag{2.27}$$

It is straightforward to show that if the integral in Eq. (2.27) is expanded in the Taylor series up to the second order term, the equation for the pulse energy can be simplified to the following form:

$$E(x) = P_0 T_0 e^{-\alpha x} \left(\sqrt{\pi} - \frac{\sqrt{\pi} \beta P_0}{\sqrt{2}} \frac{1 - e^{-\alpha x}}{\alpha} \right), \tag{2.28}$$

where $E(x) = \bar{P}(x) / f_{\text{rep}}$ is the optical pulse energy in the plasmonic waveguides expressed in terms of the average power $\bar{P}(x)$, and the laser repetition rate f_{rep}. The peak power P_0 is related to the average input power $\overline{P_0}$ as follows:

$$P_0 = \frac{\overline{P_0}}{\sqrt{\pi} T_0 f_{\text{rep}}}. \qquad \textbf{(2.29)}$$

By substituting the expression for the pulse energy $E(x)$ and the pulse peak power $\overline{P_0}$ in Eq. (2.28), and accounting that $e^{-\alpha x} << 1$ at the output of the plasmonic waveguide ($x = l$) because of the high values of the linear propagation loss parameter α [Fig. 2.3(b)], the following equation for the average output power $\bar{P}(l)$ is obtained:

$$\bar{P}(l) = \overline{P_0} e^{-\alpha l} - \frac{\sqrt{\pi} \beta \overline{P_0}^2}{\sqrt{2} \alpha T_0 f_{\text{rep}}} e^{-\alpha l}. \qquad \textbf{(2.30)}$$

This equation can be used for practical applications since the average input and output power of light are the directly measurable by experimental equipment. This equation shows that the average output power $\bar{P}(l)$ of optical pulses after propagation in the strip plasmonic waveguides with the length l depends nonlinearly on the average input power $\overline{P_0}$, and an asymptotic saturation of dependency $\bar{P}(l)\{\overline{P_0}\}$ is expected at high values of $\overline{P_0}$. The nonlinear transmission trends $\bar{P}(l)\{\overline{P_0}\}$ depends on the linear propagation loss coefficient α, laser repetition rate f_{rep}, pulse half-width T_0 (or pulse duration T_{FWHM}, respectively), nonlinear absorption parameter β of the LRSPP mode, and also the physical length l of the strip plasmonic waveguides. The calculated power trends $\bar{P}(l)\{\overline{P_0}\}$ for the gold layer thickness t = 22, 27 and 35 nm (Fig. 2.7) confirm the expected nonlinear behavior. The second term in Eq. (2.30)

becomes important at values of the average input power $\overline{P_0}$ above approximately 0.15-0.2 W. The possible saturation of the output power $\overline{P}(l)$ can be achieved at values of the input power $\overline{P_0}$ above approximately 0.5 W. The obtained nonlinear transmission trends $\overline{P}(l)\{\overline{P_0}\}$ significantly depend on the gold layer thickness *t*, and the power saturation is achieved faster for the strip plasmonic waveguides with thinner gold layers. Therefore, it confirms a conclusion that the gold layer thickness *t* is one of the main parameters for the third-order nonlinear optical properties of the LRSPP mode in the strip plasmonic waveguides. In the calculation the thickness of the tantalum pentoxide layer t_1 = 26 nm, the width of the layers w = 10 μm, the physical length of the waveguides l = 3 mm, the laser peak wavelength 1064 nm, the laser repetition rate f_{rep} = 78 MHz, and the pulse duration T_{FWHM} = 3 ps were used. These specific values of the waveguides geometry parameters, and the laser parameters were selected mainly to follow the fabrication of the samples and experimental results, which are presented in detail in [Paper C].

The second nonlinear effect is related to spectral features of the LRSPP mode in the strip plasmonic waveguides. The power spectral density (PSD) of optical pulses in W/Hz is given by the squared Fourier transform of pulse amplitude $A(x,T)$ as follows [34]:

$$\text{PSD}(x,\omega) = f_{\text{rep}} \left| \int_{-\infty}^{+\infty} A(x,T) e^{i\omega T} dT \right|^2 . \qquad \textbf{(2.31)}$$

By substituting the expressions for the pulse power amplitude $P(x,T)$ and nonlinear phase $\phi_{\text{NL}}(x,T)$ of optical pulses in Eq. (2.31), the final formula for the PSD is obtained:

$$\mathrm{PSD}(l,\omega) = f_{\mathrm{rep}} \left| \int_{-\infty}^{+\infty} \left(\frac{P_0 e^{-\frac{T^2}{T_0^2}} e^{-\alpha l}}{1+\beta P_0 e^{-\frac{T^2}{T_0^2}} L_{\mathrm{eff}}} \right)^2 e^{i\frac{\gamma}{\beta}\ln\left[1+L_{\mathrm{eff}}\beta P_0 e^{-\frac{T^2}{T_0^2}}\right]} e^{i(\omega-\omega_c)T} dT \right|^2, \qquad \textbf{(2.32)}$$

where $\omega_c = 2\pi c/\lambda$ is the carrier frequency, which corresponds to the wavelength 1064 nm, and $L_{\mathrm{eff}} = (1-e^{-\alpha l})/\alpha$ is the effective length of the LRSPP mode. The numerical modeling based on Eq. (2.32) for the gold layer thickness t = 22 nm (Fig. 2.8) shows that the nonlinear spectral broadening and splitting of the Gaussian input pulse significantly depends on the average input power $\overline{P_0}$. The pulse splitting occurs at values of the average power $\overline{P_0}$ around 0.2 W. This nonlinear spectral effect was observed in one of the recent experiments [Paper C]. The further increase of the average input power $\overline{P_0}$ leads to the splitting and formation of more self-phase modulation peaks. The cases of other thickness values (27 nm and 35 nm) and other wavelength values (800 nm and 1550 nm) are qualitatively the same. The splitting occurs at the average input power $\overline{P_0}$ around 0.1 W at the wavelength 1550 nm, and at the average input power $\overline{P_0}$ around 1.2 W at the wavelength 800 nm.

The obtained spectral features of the fundamental LRSPP mode in the strip plasmonic waveguides are in accordance with the theoretical results for nonlinear properties of optical pulses in silicon waveguides [56-61]. The principal difference here is that the plasmonic waveguides have significantly larger values of the linear propagation loss parameter α and shorter physical length l than ordinary silicon waveguides. And comparable nonlinear spectral effects can be achieved. In the case of optical fibers, the required waveguide length l can reach hundreds of meters or more to receive the necessary nonlinear features. In this sense, strip plasmonic waveguides or silicon waveguides provide the same nonlinear optical functionality, can be integrated on-chip, and

used for different nonlinear applications with even very short propagation lengths.

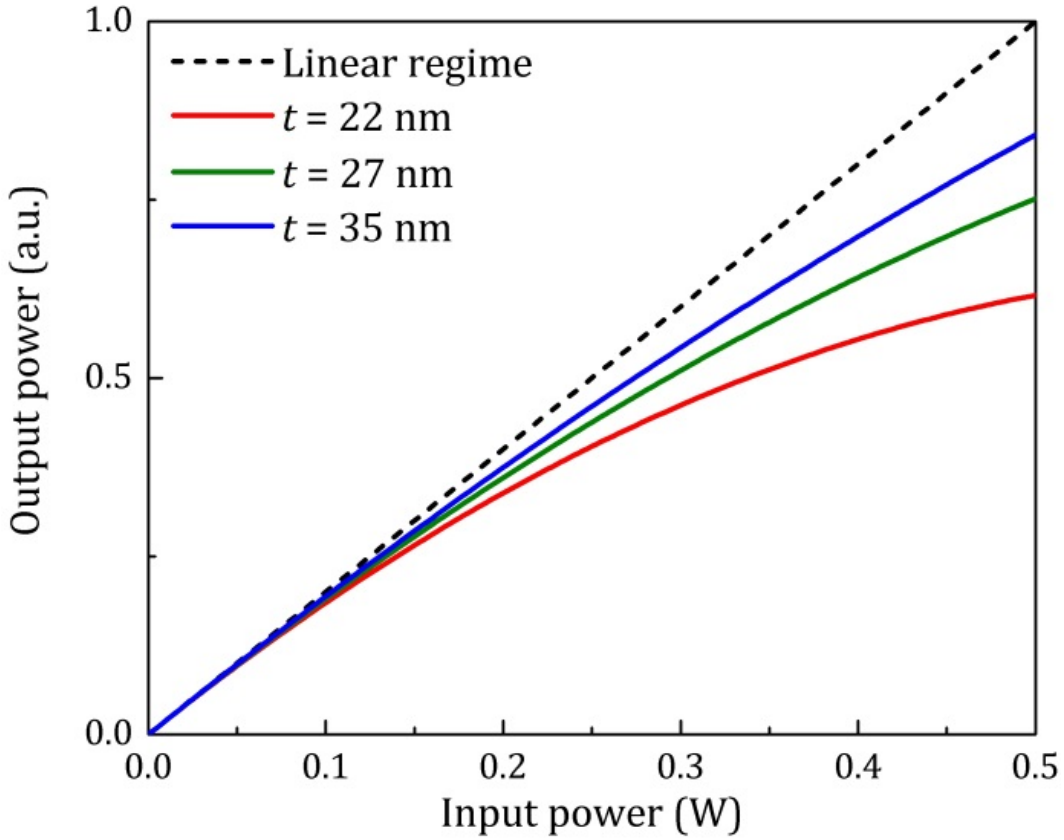

Figure 2.7. Nonlinear power transmission $\overline{P}(l)\{\overline{P_0}\}$ of the LRSPP mode in the strip plasmonic waveguides for the gold layer thickness t = 22, 27, and 35 nm and at the peak wavelength 1064 nm. Black line indicates the linear propagation regime.

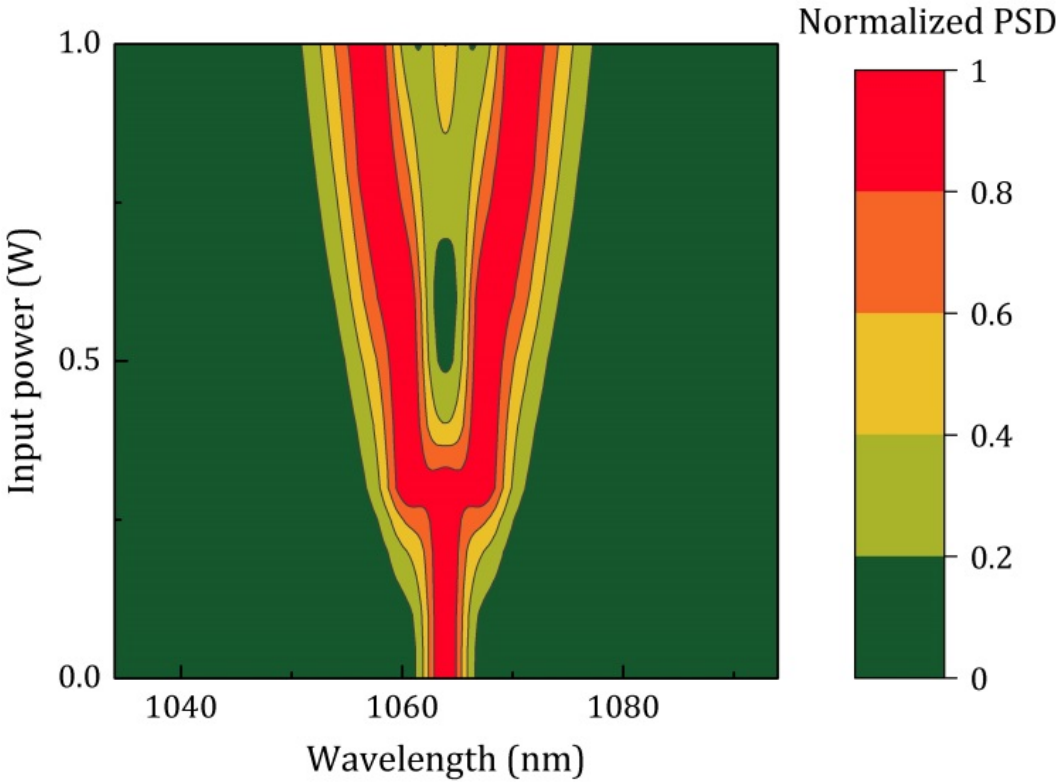

Figure 2.8. Self-phase modulation broadening of a 3-ps input Gaussian pulse with the peak wavelength 1064 nm in the strip plasmonic waveguides with the gold layer thickness t = 22 nm.

2.6. Electron temporal dynamics in gold

To model the pulse duration dependence of the third-order nonlinear susceptibility of gold, one can apply the two-temperature model of electron temporal dynamics [23, 24]. At first let us consider an ultrashort optical pulse with the Gaussian electric field profile [34]:

$$E(t) = E_0 e^{-t^2/(2T_0^2)} e^{-i\omega t}, \qquad \textbf{(2.33)}$$

where E_0 is the electric field amplitude, $\omega = 2\pi c/\lambda$ is the light angular frequency, t is the time coordinate, $T_0 = \Delta T/(2\sqrt{\ln(2)})$ is the pulse half-width, ΔT

is the pulse duration or the FWHM parameter. The mean absorbed power per unit volume of gold $P_{\mathrm{A}}(t)$ is given by the following formula [24, 62]:

$$P_{\mathrm{A}} = \frac{\varepsilon_0 \omega |E_0|^2}{2} \mathrm{Im}[\varepsilon_{\mathrm{Au}}] e^{-t^2/T_0^2} - \frac{t\varepsilon_0 |E_0|^2}{2T_0^2} e^{-t^2/T_0^2} \left(1 + \frac{\omega_{\mathrm{p}}^2(\omega^2 - \gamma^2)}{(\omega^2 + \gamma^2)^2}\right), \tag{2.34}$$

where $\omega_{\mathrm{p}} = \sqrt{ne^2/\varepsilon_0 m_{\mathrm{e}}}$ is the plasma frequency for gold, e is the electron charge, ε_0 is the vacuum permittivity, n is the electron density, m_{e} is the electron mass, γ is the collision frequency of electrons for bulk gold, $\varepsilon_{\mathrm{Au}}$ is the dielectric permittivity for bulk gold. Equation 2.34 can be simplified for the wavelength range far from the interband transitions in gold, specifically, for the peak wavelengths 1030 nm and 1064 nm, as follows [63]:

$$P_{\mathrm{A}} \approx \frac{1}{2} \varepsilon_0 \omega |E_0|^2 \mathrm{Im}[\varepsilon_{\mathrm{Au}}] e^{-t^2/T_0^2}. \tag{2.35}$$

Then this expression for the mean absorbed power per unit volume of gold is used to solve the equations of the electron temporal dynamics [24, 25]:

$$\begin{cases} \dfrac{\partial N}{\partial t} = -(\gamma_{\mathrm{e}} + \gamma_{\mathrm{lat}})N + P_{\mathrm{A}}, \\ C_{\mathrm{e}} \dfrac{\partial T_{\mathrm{e}}}{\partial t} = G(T_{\mathrm{lat}} - T_{\mathrm{e}}) + \gamma_{\mathrm{e}} N, \\ C_{\mathrm{lat}} \dfrac{\partial T_{\mathrm{lat}}}{\partial t} = G(T_{\mathrm{e}} - T_{\mathrm{lat}}) + \gamma_{\mathrm{lat}} N, \end{cases} \tag{2.36}$$

where $C_{\mathrm{e}} \approx 2.1 \times 10^4$ J/(m^3·K) is the electronic heat capacity per unit volume of gold [48], $C_{\mathrm{lat}} \approx 2.5 \times 10^6$ J/(m^3·K) is the lattice heat capacity per unit volume of gold [48], $\gamma_{\mathrm{e}} \approx 2$ THz is the electron thermalization rate [49], $\gamma_{\mathrm{lat}} \approx 1$ THz is the lattice thermalization rate [49], $G \approx 20$ PHz is the electron-photon coupling coefficient [48],

and $N(t)$ is the energy density stored in the nonthermalized part of the electronic distribution.

These equations of electron temporal dynamics can be solved directly in the time domain. It is convenient to define the initial thermal equilibrium of the electrons and lattice at the time t = 0. Therefore, the initial condition for the energy density of nonthermalized electrons is $N(t)$ = 0, and the initial condition for the electronic and lattice temperatures is $T_{\mathrm{e}}(0)=T_{\mathrm{lat}}(0)$. The first step is to substitute the formula for the mean absorbed power $P_{\mathrm{A}}(t)$ to the first equation in Eq. (2.36) and solve the differential equation for $N(t)$, using the initial condition $N(t)$ = 0. The solution for the energy density of nonthermalized electrons is given by the following expression:

$$N(t)=Ae^{-(t+4T_0)/\tau_{\mathrm{th}}}\left[\mathrm{erf}\left(\frac{T_0}{2\tau_{\mathrm{th}}}+4\right)-\mathrm{erf}\left(\frac{T_0}{2\tau_{\mathrm{th}}}-\frac{t}{T_0}\right)\right]. \qquad \textbf{(2.37)}$$

Here $\tau_{\mathrm{th}}=1/(\gamma_{\mathrm{e}}+\gamma_{\mathrm{lat}})\approx 300$ fs is the characteristic decay time for nonthermalized electrons, and $A=(\sqrt{\pi}\varepsilon_0/4)\left|E_0\right|^2\mathrm{Im}[\varepsilon_{\mathrm{Au}}]\omega T_0\exp(T_0(T_0+16\tau_{\mathrm{th}})/4\tau_{\mathrm{th}}^2)$ is the time independent constant. The second step is to substitute the obtained solution for the energy density of nonthermalized electrons to the second and third equations in Eq. (2.36). It is also convenient to define the electronic temperature variation, $\Delta T_{\mathrm{e}}(t)=T_{\mathrm{e}}(t)-T_{\mathrm{lat}}(t)$, and the initial condition for the temperature variation function is $\Delta T_{\mathrm{e}}(0)$ = 0, that means the electrons and the lattice have the same equilibrium temperature. The solution for the electronic temperature variation $\Delta T_{\mathrm{e}}(t)$ from the second and third equations in Eq. (2.36) is given by the following formula:

$$\begin{aligned}\Delta T_{\mathrm{e}}(t)=Be^{-(t+4T_0)/\tau_{\mathrm{th}}}&\left\{\frac{T_0}{\sqrt{\pi}}\left(e^{-\left(T_0/(2\tau_{\mathrm{th}})-t/T_0\right)^2}-e^{-\left(T_0/(2\tau_{\mathrm{th}})+4\right)^2}\right)\right.\\&\left.+\left[\mathrm{erf}\left(\frac{T_0}{2\tau_{\mathrm{th}}}+4\right)-\mathrm{erf}\left(\frac{T_0}{2\tau_{\mathrm{th}}}-\frac{t}{T_0}\right)\right]\left(t-\frac{T_0^2}{2\tau_{\mathrm{th}}}\right)\right\},\end{aligned} \qquad \textbf{(2.38)}$$

where $B = A(\gamma_e C_{lat} - \gamma_{lat} C_e)/(C_e C_{lat})$ is also the time independent constant. Let us consider the dynamics of the input pulse intensity $I(t) = |E_0|^2 e^{-t^2/T_0^2}$, the mean absorbed power $P_A(t)$, the electronic temperature variation $\Delta T_e(t)$, and the energy density stored in the nonthermalized part of the electronic distribution $N(t)$ for the incident pulse duration T_{FWHM} = 200 fs and 3 ps. The normalized functions are shown in Fig. 2.9 in the time domain and in Fig. 2.10 in the Fourier domain. They illustrate how ultrashort laser pulses interact with nonthermalized (out of equilibrium hot electrons, which cannot be described by the electron temperature) and thermalized (described by the elevated electron temperature) electrons in gold. At first the pulse energy is absorbed by the metal (indicated by $P_A(t)$, red curve) and the nonthermalized electron density $N(t)$ increases (blue curve). There is a clear difference in the two cases: as in the case of 200-fs pulses at the trailing edge of the pump pulse a delayed response of the nonthermalized electron density $N(t)$ is observed, while in the case of 3-ps pulses the nonthermalized electron density $N(t)$ follows the shape of the pump pulse almost exactly with only a small time delay. The next step is that electronic temperature variation $\Delta T_e(t)$ increases as the nonthermalized electrons transfer their energy to other electrons and the lattice. In the case of 200-fs pulses there is an asymmetric shape due to the delayed nonthermalized electron density $N(t)$ on the trailing edge of the pulse, while in the case of 3-ps pulse the shape of the electronic temperature variation $\Delta T_e(t)$ is Gaussian. The increased electronic temperature variation $\Delta T_e(t)$ dissipates during approximately 6-7 ps until the final thermal equilibrium of the electrons and the lattice is reached. The total thermalization rate in gold is significantly greater than typical values of the laser repetition rate (the repetition rate of the picosecond laser is 78 MHz, and the repetition rate of the femtosecond laser is 200 kHz). This implies that every laser pulse interacts with gold individually. In the case of pulse durations T_{FWHM} longer than the electron-electron scattering rate (approximately above 10 fs), the

third-order nonlinear susceptibility of metal originates from the interaction of the optical pulse with the thermalized gas of electrons.

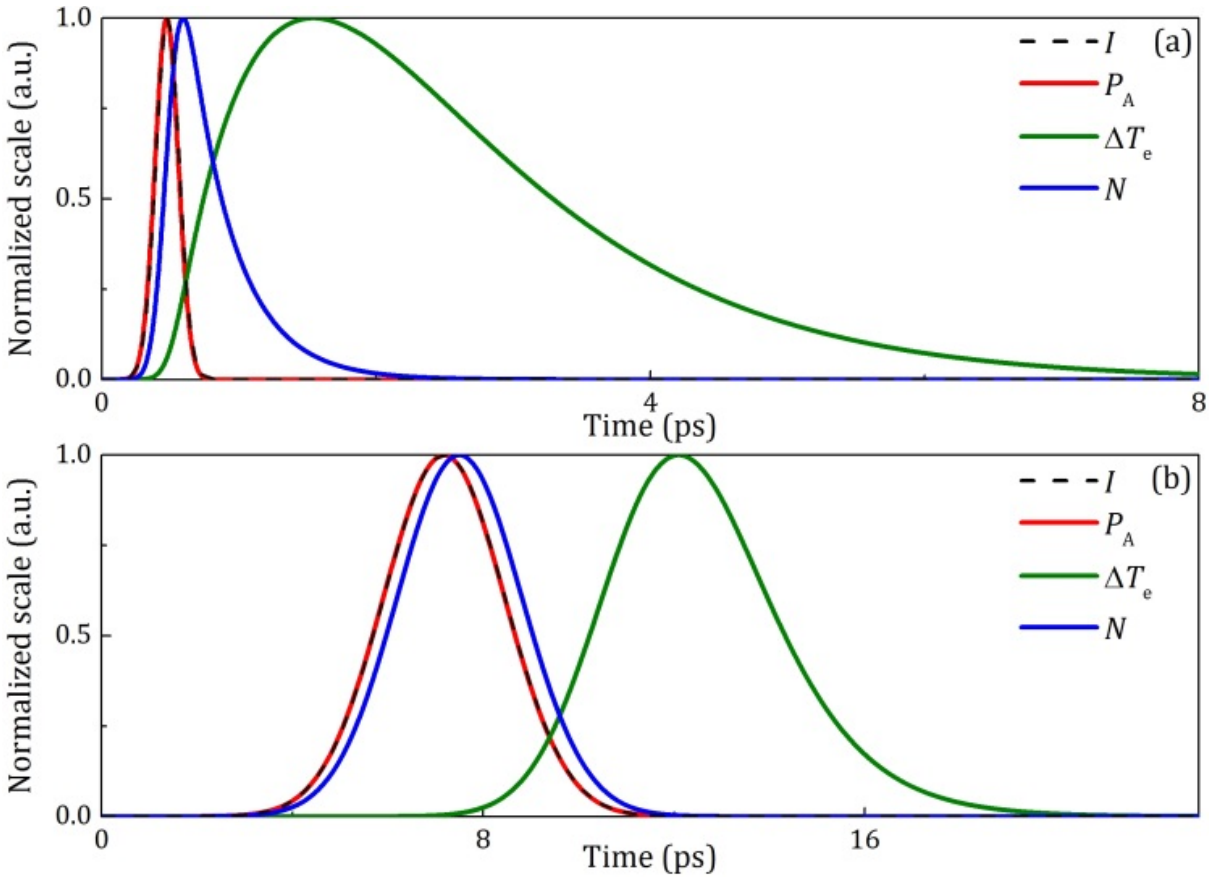

Figure 2.9. Two-temperature model simulations of electron temporal dynamics in bulk gold for (a) 200-fs pulses at 1030 nm and (b) 3-ps pulses at 1064 nm. The mean absorbed power P_A is almost exactly identical to the shape of the input pulse intensity I. For convenience, the input pulses are centered at the time $t = 4T_0$ (notice the different scales on the x-axes).

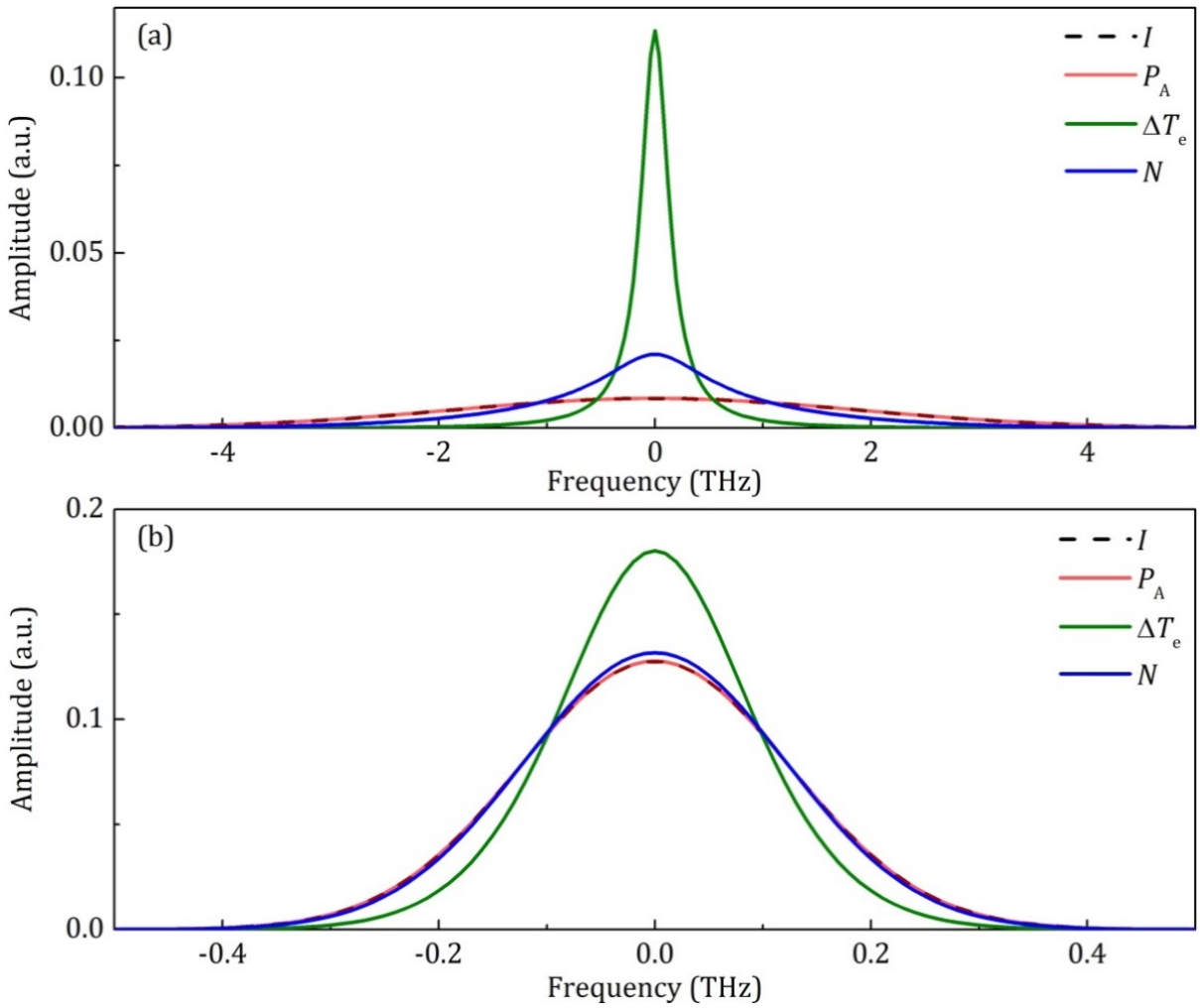

Figure 2.10. Fourier transform of the input pulse intensity function I, mean absorbed power P_A, electronic temperature variation ΔT_e, and energy density stored in the nonthermalized part of electronic distribution $N(t)$ for (a) 200-fs pulses at 1064 nm and (b) 3-ps pulses at 1064 nm.

The equations of electron dynamics [Eq. (2.36)] can be also solved in the Fourier domain [24]. Specifically, the electronic temperature variation $\Delta T_e(t)$ can be also obtained via the convolution of the mean absorbed power $P_A(t)$ and the response function $h_T(t)$ of gold. In this approximation, the time derivative of the nonthermalized electron density is $\partial N / \partial t = 0$, that is equivalent to instantaneous

energy transfer from the nonthermalized electrons to thermalized electrons. The response function of gold is given by the following formula [24, 25]:

$$h_{\mathrm{T}}(t)=\frac{\theta(t)}{\tau_{\mathrm{th}}-\tau_{\mathrm{r}}}\left(e^{-t/\tau_{\mathrm{th}}}-e^{-t/\tau_{\mathrm{r}}}\right), \qquad \textbf{(2.39)}$$

where $\tau_{\mathrm{r}}=C_{\mathrm{e}}C_{\mathrm{lat}}/[G(C_{\mathrm{e}}+C_{\mathrm{lat}})] \approx 1$ ps is the characteristic decay time for the thermalized electrons, and $\theta(t)$ is the Heaviside step function. The function $h_{\mathrm{T}}(t)$ is shown in Fig. 2.11. The response function of gold reaches its maximum value at the time t approximately 600 fs, and then decays during approximately 5-6 ps. In the present work, and the equations of the electron dynamics were solved analytically in the time domain, and Eq. (2.38) represents the solution for the electronic temperature variation $\Delta T_{\mathrm{e}}(t)$.

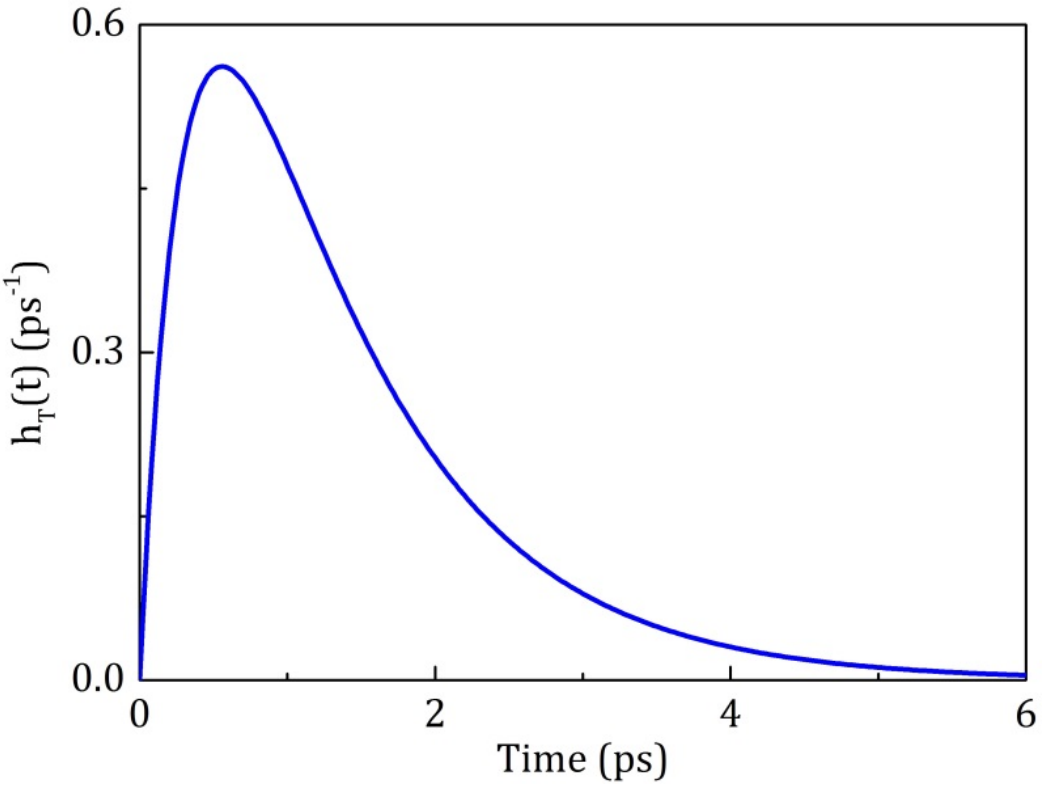

Figure 2.11. Temporal response function $h_{\mathrm{T}}(t)$ of gold.

Further the formulas for the mean absorbed power $P_A(t)$ and the electronic temperature variation $\Delta T_e(t)$ can be used to calculate the scaling of the third-order nonlinear susceptibility $\chi^{(3)}_{Au}$ for bulk gold (as well as thin gold layers), for different values of the incident pulse duration T_{FWHM}. The obtained theoretical dependences of the third-order nonlinear susceptibility $\chi^{(3)}_{Au}$ for thin gold layers explain well the experimental results on the imaginary part of the third-order nonlinear susceptibility $\chi^{(3)}_{Au}$ for thin gold layers and for the pulse duration T_{FWHM} = 200 fs and 3 ps [Paper A, Paper C]. The pulse duration dependences for the real part of the third-order nonlinear susceptibility $\chi^{(3)}_{Au}$ are also calculated based on the experimental results on the third-order nonlinear susceptibility $\chi^{(3)}_{Au}$ for the pulse duration T_{FWHM} = 3 ps [Paper C].

2.7. Pulse duration dependence of the third-order nonlinear susceptibility of gold

The third-order nonlinear susceptibility $\chi^{(3)}_{Au}$ of gold originates from the interaction of the ultrafast optical pulses with the excited gas of free electrons in gold. The pulse dynamics is characterized by the intensity function $I(t)$, and the mean absorbed power per unit volume of gold $P_A(t)$. The excited gas of free electrons is characterized by the electronic temperature deviation function $\Delta T_e(t)$. By solving the two-temperature model of electron temporal dynamics and the nonlinear Schrödinger equation [64] one can obtain the pulse duration dependence of the third-order nonlinear susceptibility of gold. The theoretical trends are shown in Fig. 2.12. The known values of the third-order nonlinear susceptibility $\chi^{(3)}_{Au,\tau_2}$ for the pulse duration 3 ps [Paper C] and the theoretical trends were used to calculate the values of the third-order nonlinear susceptibility $\chi^{(3)}_{Au,\tau_1}$ for the pulse duration 200 fs. The experimental values of the imaginary part of the third-order nonlinear

susceptibility $\chi^{(3)}_{\mathrm{Au},\tau_1}$ of gold [Paper A] obtained for the pulse duration 200 fs at the wavelength 1030 nm, and the experimental values of the real part and imaginary part of the third-order nonlinear susceptibility $\chi^{(3)}_{\mathrm{Au},\tau_2}$ of gold [Paper C] obtained for the pulse duration 3 ps are also presented in Fig. 2.12. The direct comparison of the values of the nonlinear susceptibility of gold from both experiments can be justified by the fact that the wavelengths 1030 nm and 1064 nm are far from the interband transitions in gold [24]. The obtained theoretical dependences agree well with the experimental values of the third-order nonlinear susceptibility $\chi^{(3)}_{\mathrm{Au}}$ for the pulse durations 200 fs and 3 ps. Figure 2.12(b) shows that the imaginary part of the third-order nonlinear susceptibility $\chi^{(3)}_{\mathrm{Au}}$ decreases by approximately one order of magnitude as the pulse duration decreases from 3 ps to 200 fs. The theoretical trends on Fig. 2.12 (a) show the expected values of the third-order nonlinear susceptibility of bulk gold and thin gold layers in the wide range of the pulse duration T_{FWHM} from 10 fs to 10 ps [Paper A]. The obtained theoretical trends show the characteristic saturation of the third-order nonlinear susceptibility of gold for longer (above approximately 10 ps) optical pulses.

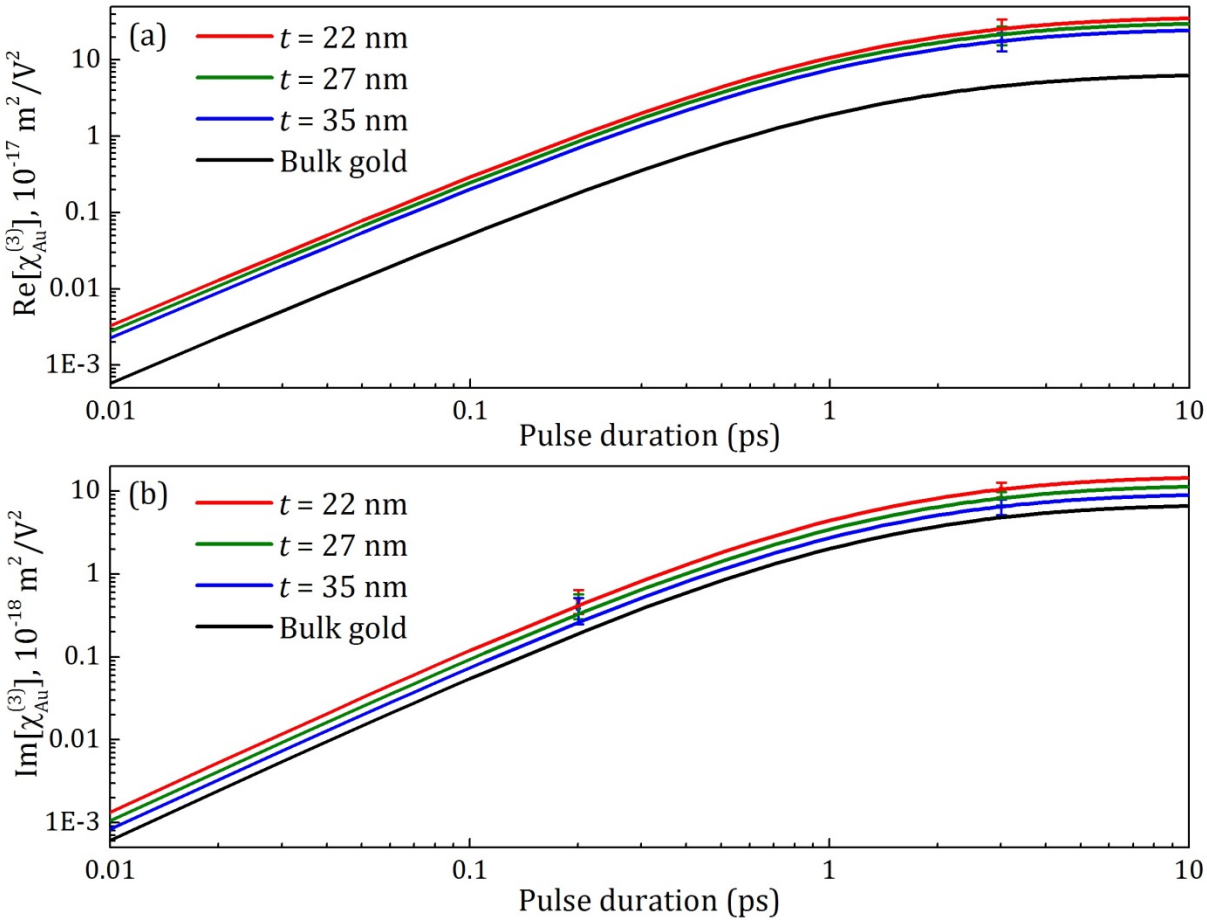

Figure 2.12. Pulse duration dependence of (a) real part and (b) imaginary part of the third-order nonlinear susceptibility $\chi^{(3)}_{\mathrm{Au}}$ of bulk gold and gold layers with the thickness t = 22, 27, and 35 nm. The experimental results on the third-order nonlinear susceptibility $\chi^{(3)}_{\mathrm{Au}}$ of thin gold layers are presented for the pulse duration 200 fs and the wavelength 1030 nm [Paper A], and for the pulse duration 3 ps and the wavelength 1064 nm [Paper C]. The theoretical lines were calculated from the two-temperature model and the nonlinear Schrödinger equation [64].

Chapter 3

Fabrication of samples

3.1. Preparation and selection of wafers

The first step in the fabrication of the samples with the strip plasmonic waveguides was to design a mask for a standard ultraviolet (UV) lithography process, and also to select a proper wafer as a substrate. The design of the photolithographic mask was done by using the specialized layout editor for micro- and nanotechnology CleWin 5 [65]. This layout editor was used to design the length and width of the strip plasmonic waveguides in the *xy*-plane (Fig 2.2). The values of the thickness of the gold layer, tantalum pentoxide layers, and silicon dioxide cladding in the strip plasmonic waveguides were determined by the deposition times during the further steps in the fabrication of samples. It was important to determine the necessary values for the width and length of the waveguides before ordering of the photolithographic mask. Thus, the plasmonic waveguides were designed as strips of different width, ranging from 10 μm to 100 μm in one series, and from 1 μm to 10 μm in another series. The distance between the neighbor strips was designed as 100 μm, so it was convenient to observe and select in a microscope the strips of different widths. The characteristic decay of the LRSPP mode in the silica cladding near the strip plasmonic waveguides is approximately 1-2 μm (Fig. 2.4), thus, it was also convenient to investigate propagation the LRSPP mode in every plasmonic waveguide independently. An example of a series of the strip plasmonic waveguides, which were designed in the physical layout editor CleWin 5, is shown in Fig. 3.1. The purple strips are the designed plasmonic waveguides with the width values in the range from 10 μm to 100 μm and the white background

is the 100 μm spacing of silica. The photolithographic mask was ordered and shipped from Delta Mask B. V. (Netherlands).

Then several wafers with a thick (approximately 6.5 μm) pre-made layer of silica were selected. The geometry of the selected wafers is standard: the thickness of silicon is approximately 525 μm, and the diameter is 4 inch (or approximately 10 cm). It was convenient to use the wafers with the pre-made cladding layer of silica because this layer was used as a bottom cladding layer for the strip plasmonic waveguides. A sketch of the selected wafer is shown in Fig. 3.2.

Figure 3.1. Strip plasmonic waveguides with different width ranging from 10 to 100 μm in the layout editor CleWin 5. The distance between waveguides is 100 μm.

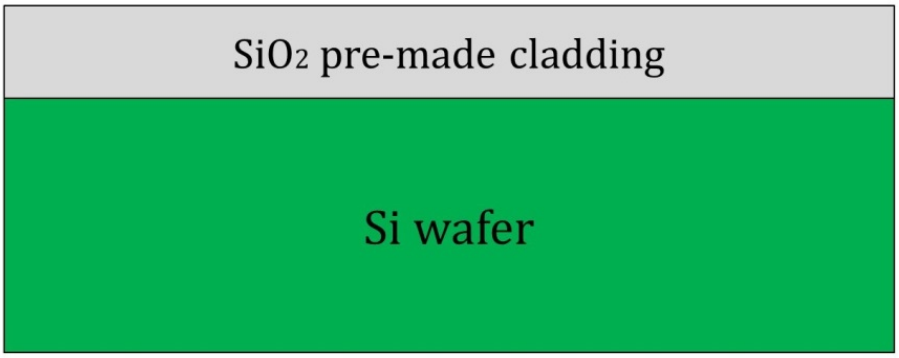

Figure 3.2. Sketch of the selected wafers with the pre-made layer of silica.

3.2. Ultraviolet lithography

The second step in the fabrication of the samples was the UV lithography process [66]. At first the selected wafers were pre-baked by using a standard hexamethyldisilazane (HMDS) oven. A photograph of the oven is shown in Fig. 3.3(a). Then a photoresist layer was deposited on top of the wafers by using the coater system Spin Track 1+2 [67]. A photograph of the coater is shown in Fig. 3.3(b). The thermally-stable negative photoresist AZ nLOF 2020 was selected for the ultraviolet lithography process. The ultraviolet exposure was performed by using the KS Aligner (SUSS MicroTec) [68]. A photograph of the KS Aligner is shown in Fig. 3.3(c). The development process was performed by using the tetramethylammonium hydroxide (TMAH) UV-lithography Developer (SUSS MicroTec) [68]. A photograph of the Developer is shown in Fig. 3.3(d). The quality of the UV lithography process was verified by using the optical microscope ECLIPSE L200 (Nikon) [69]. An example of a pattern of the strip plasmonic waveguides after the UV lithography process is shown in Fig. 3.4. The strips here correspond to the plasmonic waveguides and the background area is covered by the photoresist layer. And a sketch of the wafer after the ultraviolet lithography process is shown in Fig. 3.5. The obtained UV

lithography pattern agrees well with the strip waveguides pattern that was designed in the layout editor CleWin 5 (Fig. 3.1).

Figure 3.3. Equipment for the UV lithography process: (a) HMDS oven, (b) Spin Track 1+2, (c) KS Aligner, and (d) TMAH UV-lithography Developer.

Figure 3.4. Pattern of the strip plasmonic waveguides in the optical microscope Nikon ECLIPSE L200 after the UV lithography process.

Figure 3.5. Sketch of the wafer after the UV lithography process with the photoresist pattern.

3.3. Deposition of thin layers of metal and dielectrics

The third step in the fabrication of the samples was a sputter deposition of thin layers of gold and tantalum pentoxide. The deposition process was performed by using the Lesker CMS 18 sputter system (Kurt J. Lesker Company) [70]. A photograph of the Lesker sputter system is shown in Fig. 3.6. At first the wafers were loaded in the transfer cassette (Fig. 3.6, left side). Then the sputter system took the wafers and transferred them to the vacuum chamber for the deposition process (Fig. 3.6, center). The machine has several channels (guns) for independent deposition of different materials. In this particular case, three materials were used: gold, tantalum pentoxide, and silicon dioxide. The sputter system was controlled by the internal computer (Fig. 3.6, right side). The program of the deposition process was configured by setting the deposition times of the standard recipes for different materials: radio frequency (RF) sputter deposition of the bottom layer of tantalum pentoxide, direct current (DC) sputter deposition of the central layer of gold, radio frequency sputter deposition of the top layer of tantalum pentoxide, and also reactive deposition of a small protection layer of silica. The main parameters of the deposition process for two wafers are shown in Table 3.1. The layers of different materials were deposited one after another in one sputtering program, and the known deposition times and rates were used to calculate the layers thickness values. During the deposition process the wafers were rotated in the vacuum chamber to ensure uniform deposition all over the surface. At the end of the process the sputter system moved back the ready wafers to the transfer cassette. A sketch of the wafer after the deposition process is shown in Fig. 3.7.

Then the lift-off procedure was performed. The wafers were placed in a chemical solution (Piranha) and the chemical solution easily removed the photoresist layer. A sketch of the wafer after the lift-off procedure is shown in Fig. 3.8. Also the quality of the adhesion layers of tantalum pentoxide was verified by using an ordinary scotch tape. The tape was placed on the wafer

surface on top of the ridge plasmonic waveguides, and then removed. The layers remained the same on the wafer surface and, thus, the adhesion quality of tantalum pentoxide is very good.

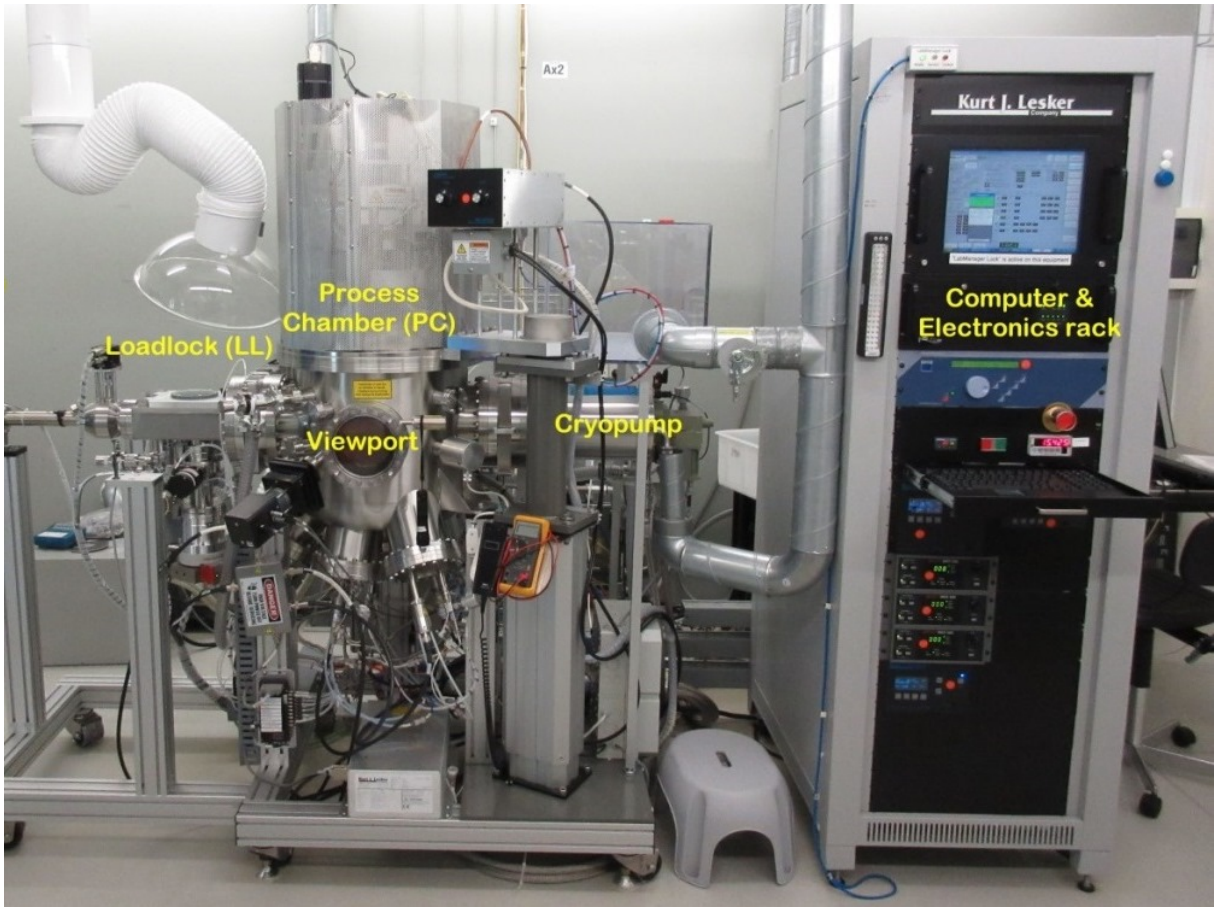

Figure 3.6. Lesker sputter system for thin films deposition.

Table 3.1. Parameters of the deposition process in the Lesker sputter system.

Line	Recipe	Time (s)	Gas	Pressure (mtorr)	Gun	Power (W)	Voltage (V)	Target
1	RF sputter Ta_2O_5	660	Ar	3.5	5	157	2	Ta_2O_5
2	Source 4 DC	165	Ar	3	4	110	450	Au
3	RF sputter Ta_2O_5	660	Ar	3.5	5	157	2	Ta_2O_5
4	SiO_2 reactive O_2 ratio 10	600	10% O_2 in Ar	3	1	90	610	Si
5	RF sputter Ta_2O_5	660	Ar	3.5	5	157	2	Ta_2O_5
6	Source 4 DC	82	Ar	3	4	110	450	Au
7	RF sputter Ta_2O_5	660	Ar	3.5	5	157	2	Ta_2O_5
8	SiO_2 reactive O_2 ratio 10	600	10% O_2 in Ar	3	1	90	610	Si

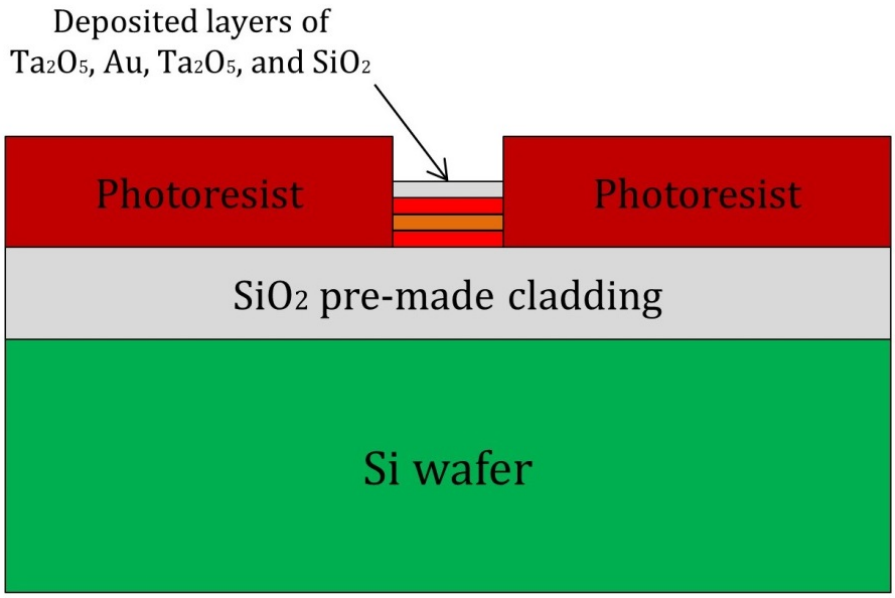

Figure 3.7. Sketch of the wafer after the deposition process with the layers of gold, tantalum pentoxide, and silica.

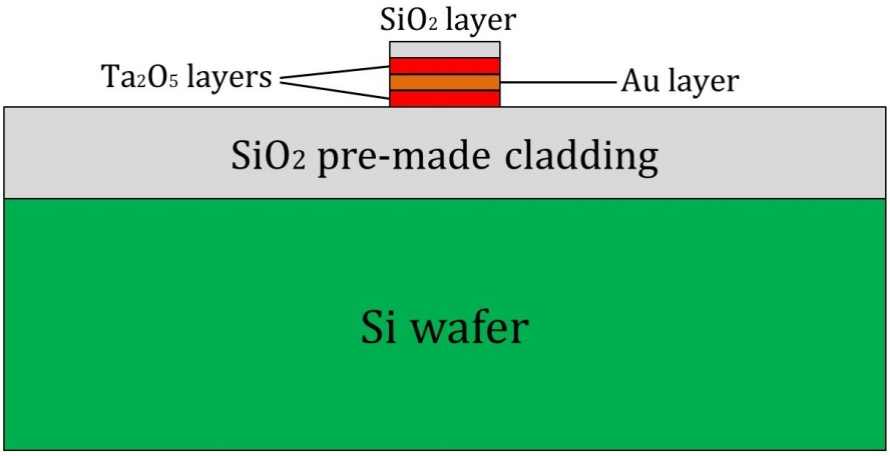

Figure 3.8. Sketch of the wafer after the lift-off procedure with the ridge strip plasmonic waveguides.

3.4. Plasma-enhanced chemical vapor deposition

The forth step in the fabrication of the samples was the plasma-enhanced chemical vapor deposition (PECVD) of the top cladding layer of silica. The wafers were placed in the deposition system STS Multiplex PECVD3. A photograph of the deposition machine is shown in Fig. 3.9. The wafers with the ridge plasmonic waveguides were placed in the transfer cassette (Fig. 3.9, left side). Then the wafers were moved to the PECVD deposition section, which is situated next to the transfer cassette (Fig. 3.9). The deposition program and all system parameters were controlled by the computer (Fig. 3.9, right side). The PECVD3 is used, in particular, to deposit thick layers of silica in the micrometer range. It has significantly higher speed of the silica deposition than the Lesker sputter system, but can deposit only silica, among the necessary constituent materials for the strip plasmonic waveguides.

A standard program for the deposition of silica was selected, and the known deposition rate and time were used to calculate the expected thickness of the silica cladding. Taking into account the characteristic decay length of the plasmonic mode intensity distribution in the silica cladding (Fig. 2.4),

approximately 5 micrometers of the cladding layer of silica were deposited on top of the wafers with the strip plasmonic waveguides. Thus, the samples were ready. A sketch of the wafer after the PECVD deposition procedure is shown in Fig. 3.10. The quality of the fabrication of samples was verified by using several characterization devices, which are described below.

Figure 3.9. Plasma-enhanced chemical vapor deposition machine STS Multiplex PECVD3.

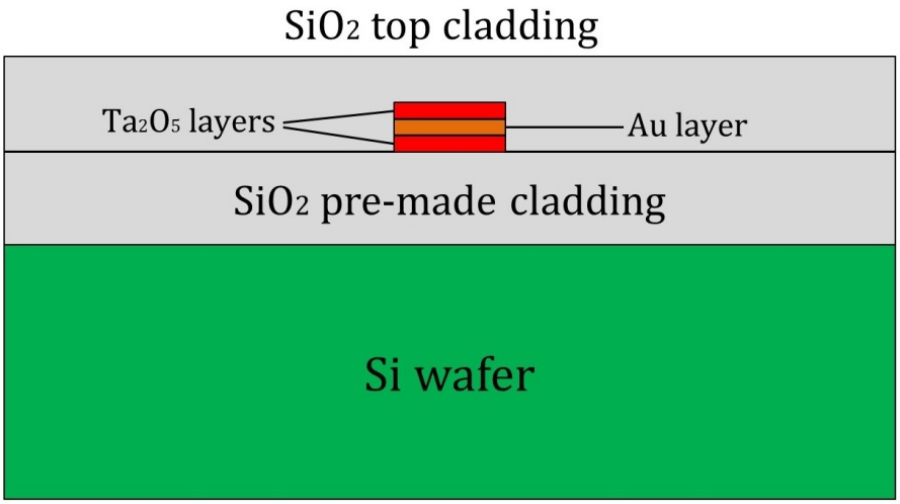

Figure 3.10. Sketch of the wafer after the PECVD deposition process with the strip plasmonic waveguides.

3.5. Scanning electron microscope characterization

The first verification of the quality of the samples was performed by using the scanning electron microscopes (SEM) LEO and SUPRA (Carl Zeiss) [71, 72]. A photograph of the SEM-LEO microscope is shown in Fig. 3.11. The ready wafers were placed in the vacuum chamber (Fig. 3.11, left side). The system calibration and all measurements were controlled by the computer (Fig. 3.11, right side). This quality verification was done before the PECVD deposition of the top cladding of silica, because thick oxide layers shield the strip plasmonic waveguides and the electron beam microscope can image only the ridge nanostructures. An example of the imaging of the strip plasmonic waveguides using the SEM-LEO microscope is shown in Fig. 3.12. Here the optical magnification is approximately x1000. The strips correspond to the plasmonic waveguides and the background area is the bottom cladding of silica. The distance between the neighbor plasmonic waveguides is 100 μm, and their pattern agrees well with the designed pattern in the layout editor CleWin 5.

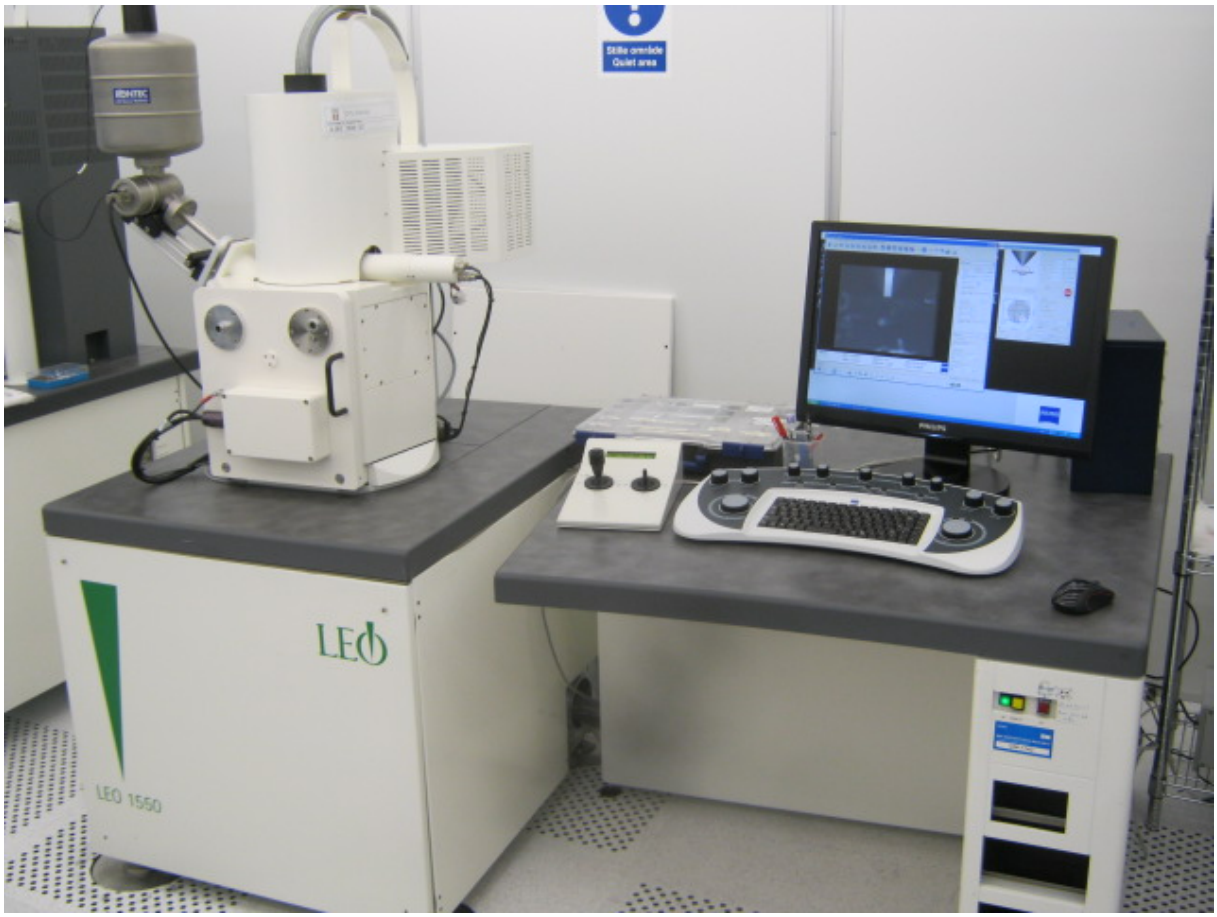

Figure 3.11. Scanning electron microscope LEO.

To verify the quality of the deposited metal and adhesion layers, a separate test wafer was prepared. A silicon wafer with a thick (approximately 800 nm) layer of silica was used as a substrate. A gold layer and a tantalum pentoxide layer were deposited in the Lesker sputter system by the same procedure, but in different parts of the wafer. The surfaces of the deposited gold layer and tantalum pentoxide layer were imaged by the SEM-LEO microscope, and shown in Fig. 3.13. The gold surface has many bright dots related to the roughness spikes [Fig. 3.13(a)], and the tantalum pentoxide surface is smooth and free from any particles [Fig. 3.13(b)]. The imaging showed that both layers are continuous and of high quality. The gold surface was also imaged by the SEM-SUPRA microscope, and shown in Fig. 3.14. Here the optical magnification is approximately x250000. This verification of the layers quality by the SEM

microscopes is important to ensure that the Lesker deposition process provided continuous layers of metal. Thus, no clustering process was happened during the layers deposition, and the Drude model based on Eq. (2.3)-(2.5) is well applicable to the deposited layers of gold [40].

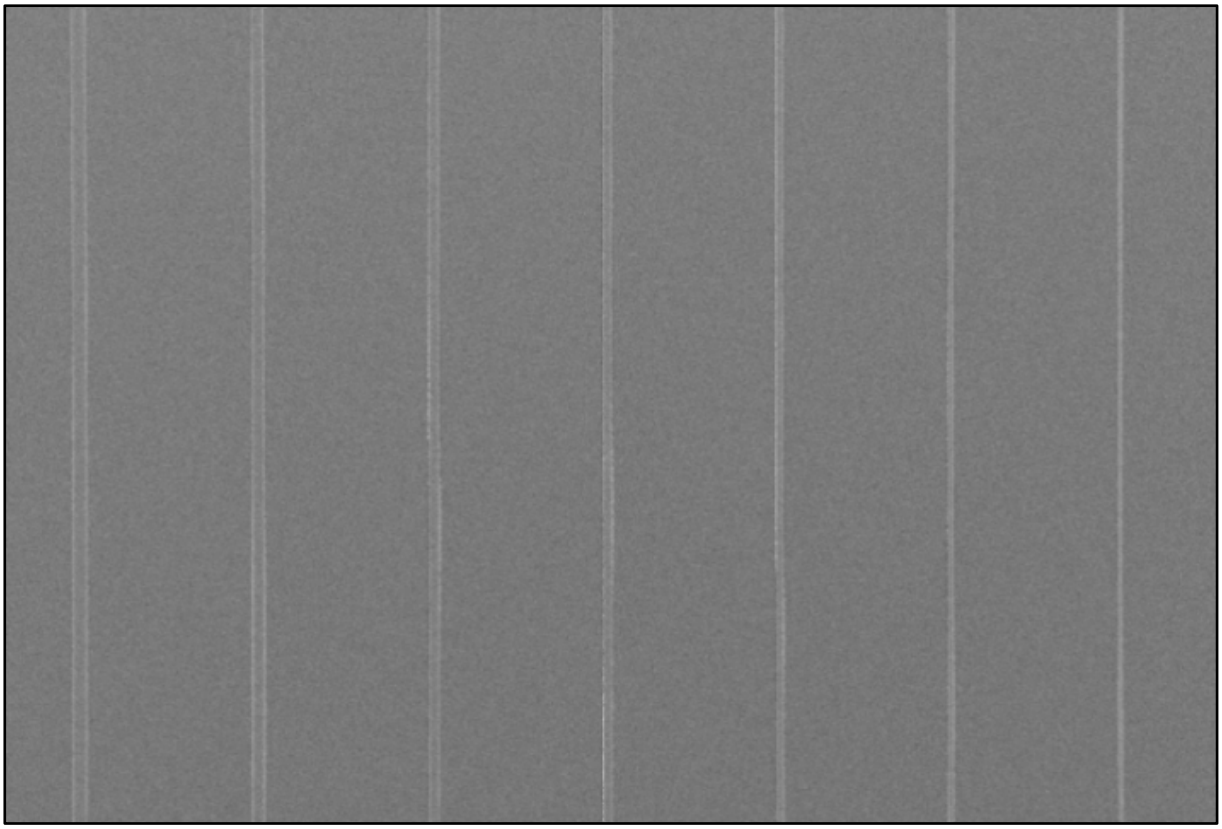

Figure 3.12. SEM-LEO image of the strip plasmonic waveguides after the lift-off procedure.

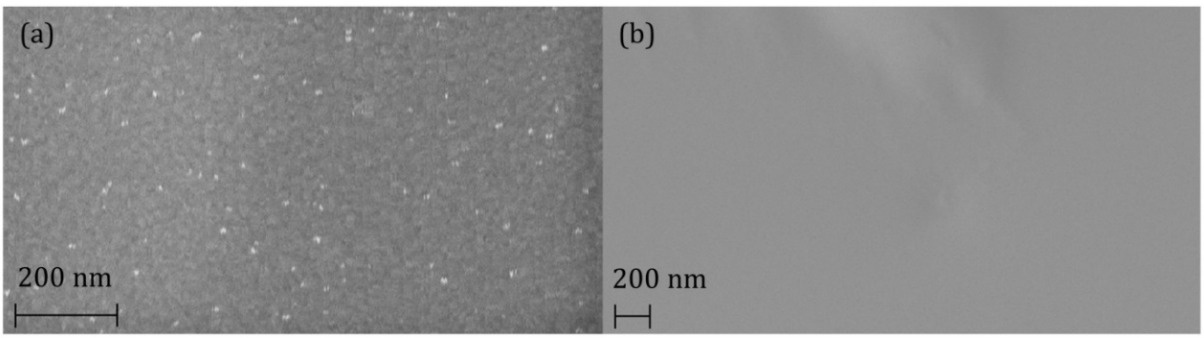

Figure 3.13. SEM-LEO images of the (a) gold surface and (b) tantalum pentoxide surface.

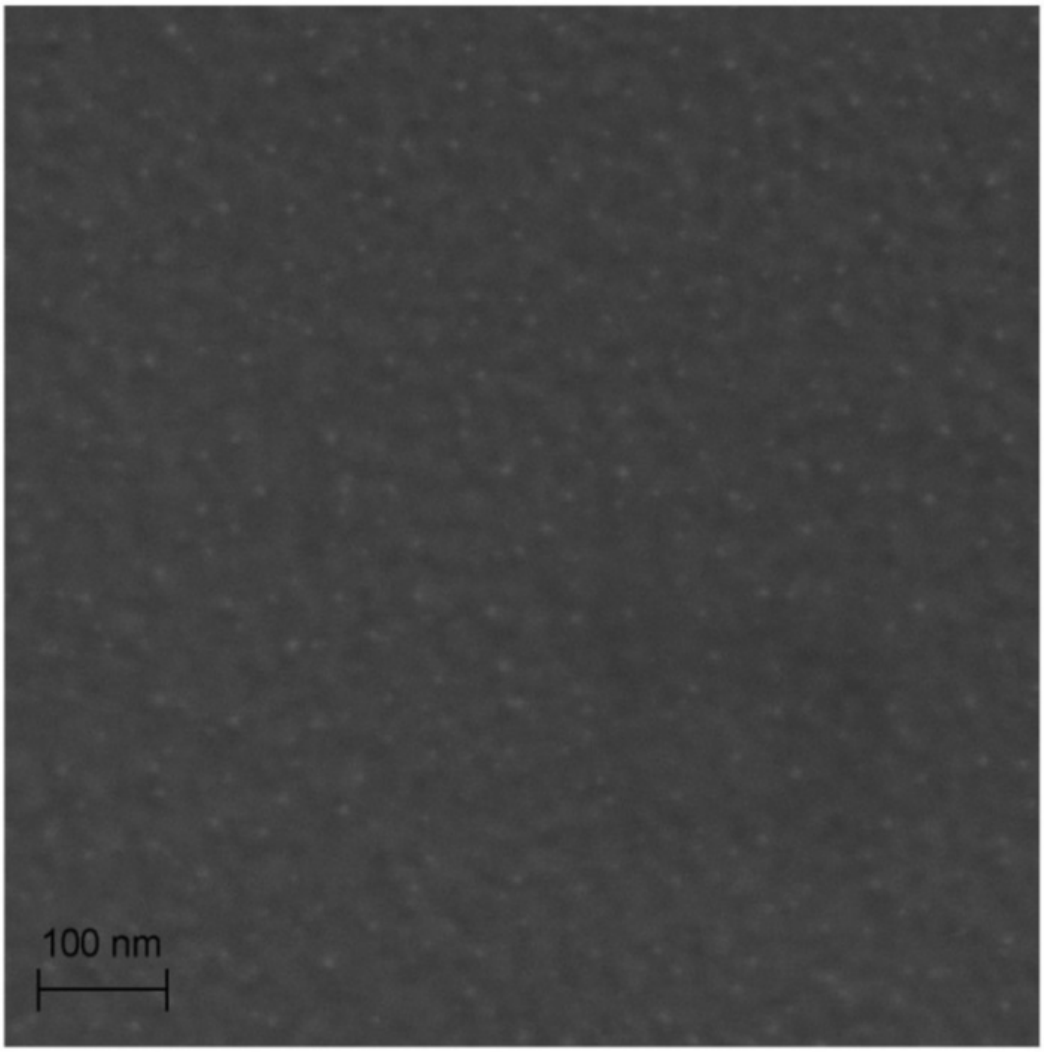

Figure 3.14. SEM-SUPRA image of the gold surface.

3.6. Atomic force microscope characterization

The second verification of the quality of the samples was performed by using the atomic force microscope (AFM) Dimension Icon (Bruker) [73, 74]. A photograph of the AFM microscope is shown in Fig. 3.15. The ready wafer was transferred to the measurement platform in the chamber (Fig. 3.15, right side). The system calibration and all measurements were controlled by the personal computer (Fig. 3.15, left side). This quality verification was also done before the PECVD deposition of the top cladding of silica. At first the multilayer profile of

the strip plasmonic waveguides and surface roughness of the metal layer were investigated. An example of the imaging of the strip plasmonic waveguide using the AFM microscope is shown in Fig. 3.16(a). The waveguides profile contained four layers: a bottom layer of tantalum pentoxide (approximately 26 nm), gold layer (approximately 27 nm), top layer of tantalum pentoxide (approximately 26 nm), and small layer of silica (approximately 21 nm). The sharp edges on the waveguide profile are the usual artifacts after the lift-off procedure [75]. Usually they do not contribute significantly to the propagation losses as the LRSPP mode intensity is close to zero at the waveguide edges [30]. The width of the waveguide also well agrees with the nominal width w = 10 μm, that was designed in the physical layout editor CleWin 5.

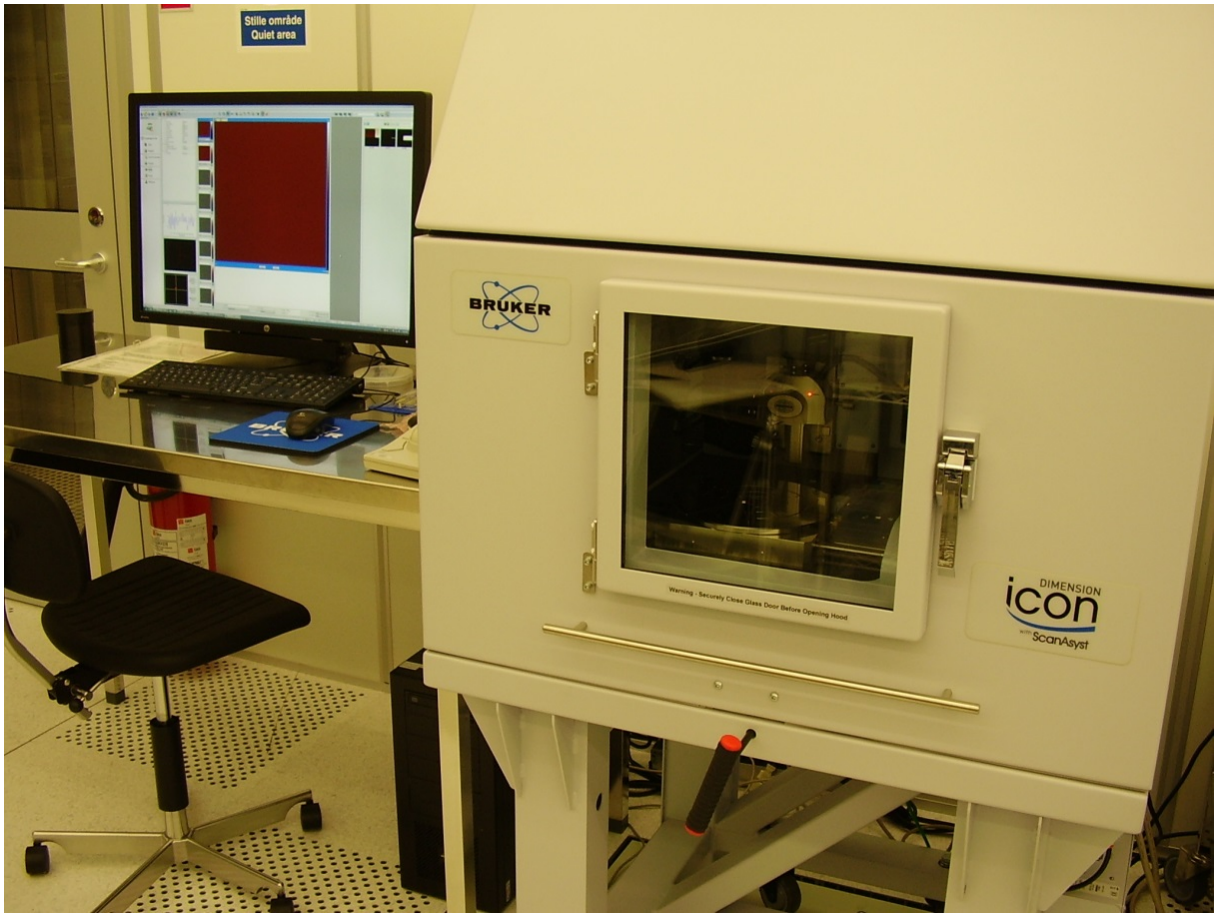

Figure 3.15. Atomic force microscope Dimension Icon.

Then the surface measurements were performed [76, 77]. An example of the roughness measurements of the metal surface using the AFM microscope is shown in Fig. 3.16(b). It shows the spikes with the maximum height values of approximately 2 nm. The root mean square (RMS) value for the roughness of the deposited metal layers is approximately 0.67 nm. The 2D roughness profile of the deposited gold surface is shown in Fig. 3.17. The AFM has the maximum resolution 512 points per line, and the standard approach here is to measure a surface area with the length 2 μm, and width 2 μm. Thus, the resolution of the measurement is 4 nm per point. The bright dots in Fig. 3.17 correspond to the roughness spikes with the height approximately 2 nm. And the RMS value of the roughness is calculated all over the measured surface. The AFM measurement of the gold surface (Fig. 3.17) is in agreement with the previous imaging by using the SEM-SUPRA microscope (Fig. 3.14). So the AFM measurements and SEM imaging are complementary to verify the quality of the metal surface and the strip plasmonic waveguides. Also the roughness of the original pre-made cladding layer of silica with the thickness 6.5 μm was verified by using the same procedure. The RMS value for the roughness of the bottom silica cladding is approximately 0.23 nm.

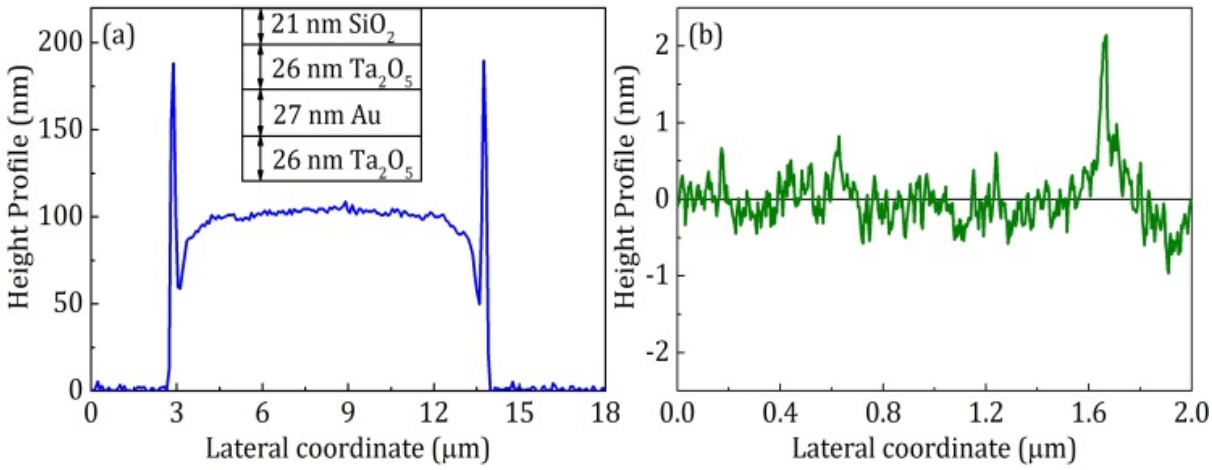

Figure 3.16. AFM measurements: (a) waveguide profile and layers scheme, and (b) metal layers roughness.

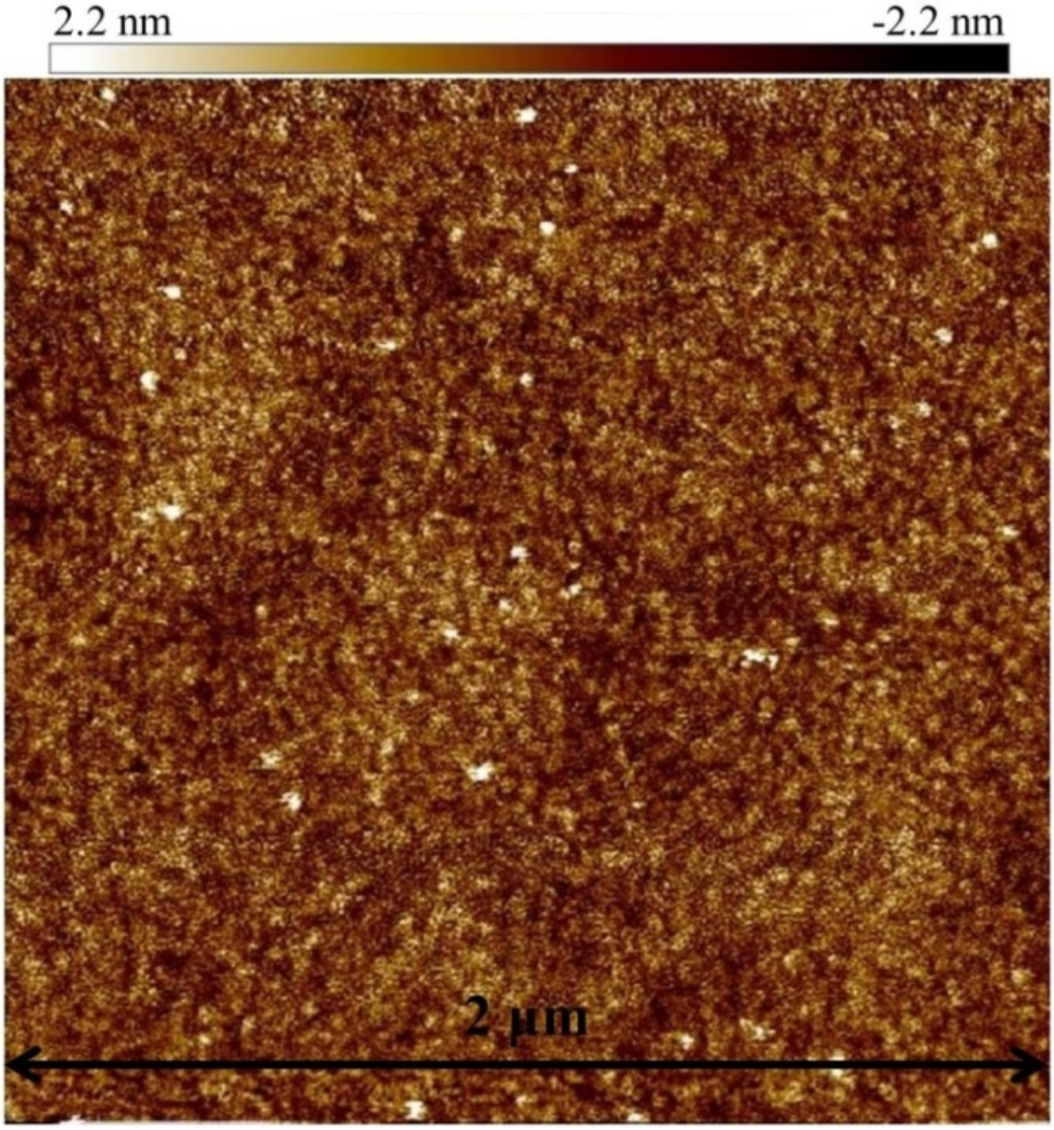

Figure 3.17. AFM measurement of the gold surface roughness**.**

3.7. Multiple-angle reflectometer characterization

The third verification of the quality of the samples was performed by using the multiple-angle reflectometer FilmTek 4000 and the ellipsometer VASE (John A. Woollam Company) [78]. A photograph of the FilmTek is shown in Fig. 3.18, and a photograph of the ellipsometer VASE is shown in Fig. 3.19. The ready wafer was placed on the measurement platform (Fig. 3.18, right side, and Fig. 3.19, left side). The system calibration and all measurements were controlled by

the personal computer (Fig. 3.18, left side, and Fig. 3.19, right side). This quality verification was done after the PECVD deposition of the top cladding of silica. The characterization systems measure the thickness and linear refractive index of the silica cladding. An example of the thickness measurement of the silica cladding by using the FilmTek is shown in Fig. 3.20. The program selected five different points on the wafer surface and measured the thickness. The average thickness of the silica cladding is approximately 11.5 μm. The program took into account the whole thickness of silica on the wafer that is approximately 6.5 μm of the pre-made cladding layer and approximately 5 μm of the deposited top cladding layer. The measurement also showed that the surface of the ready wafer is not strictly flat, and the height at the center of the wafer is approximately 2 percent greater than the height at the wafer edges.

Figure 3.18. Multiple-angle reflectometer FilmTek 4000.

The linear refractive index of the silica cladding was measured by using the ellipsometer VASE (Variable Angle Spectroscopic Ellipsometry) [79]. The operating principle of both characterization devices is the same, but the ellipsometer VASE has somewhat broader NIR wavelength range than FilmTek 4000. The linear refractive index for the deposited silica is approximately 1.456 at the wavelength 1064 nm.

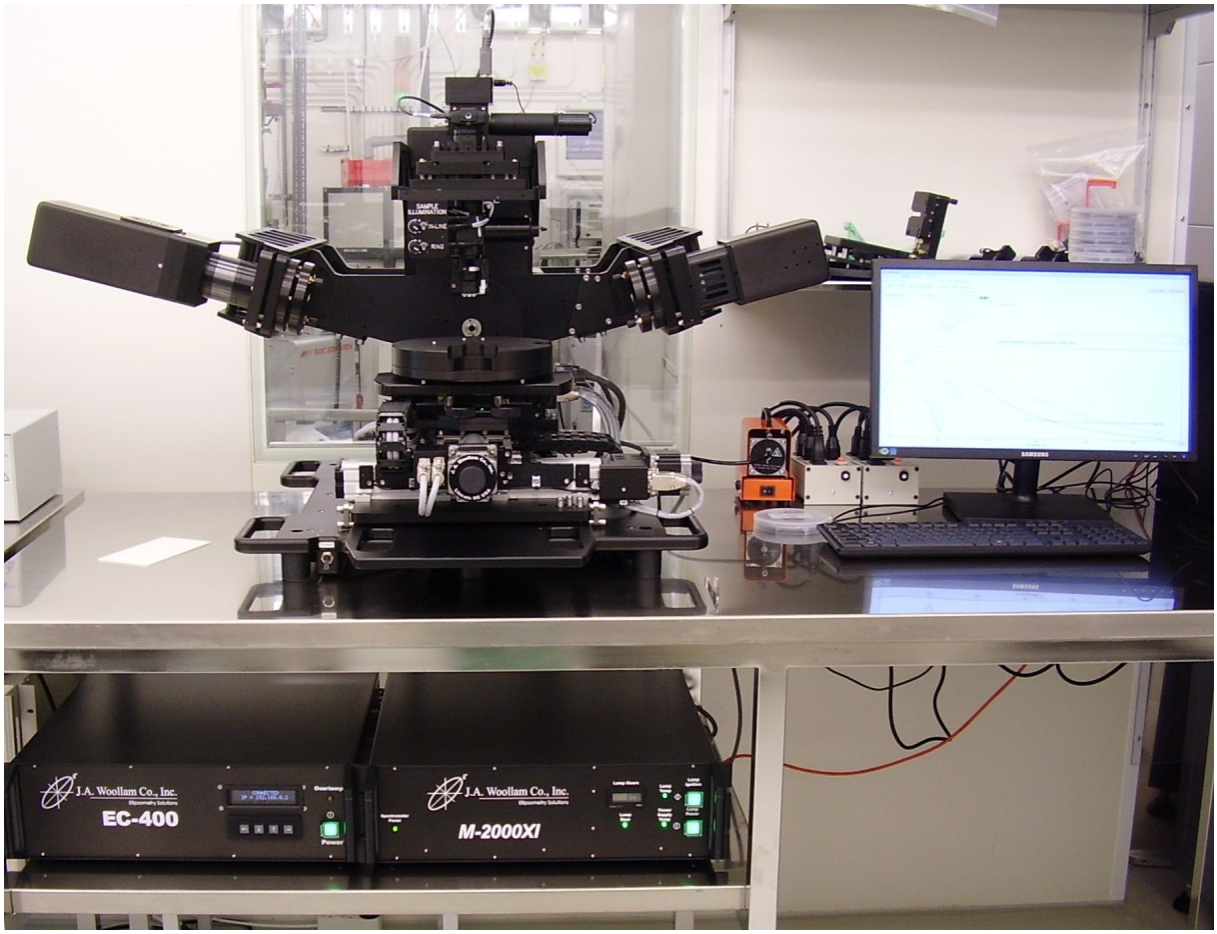

Figure 3.19. Ellipsometer VASE.

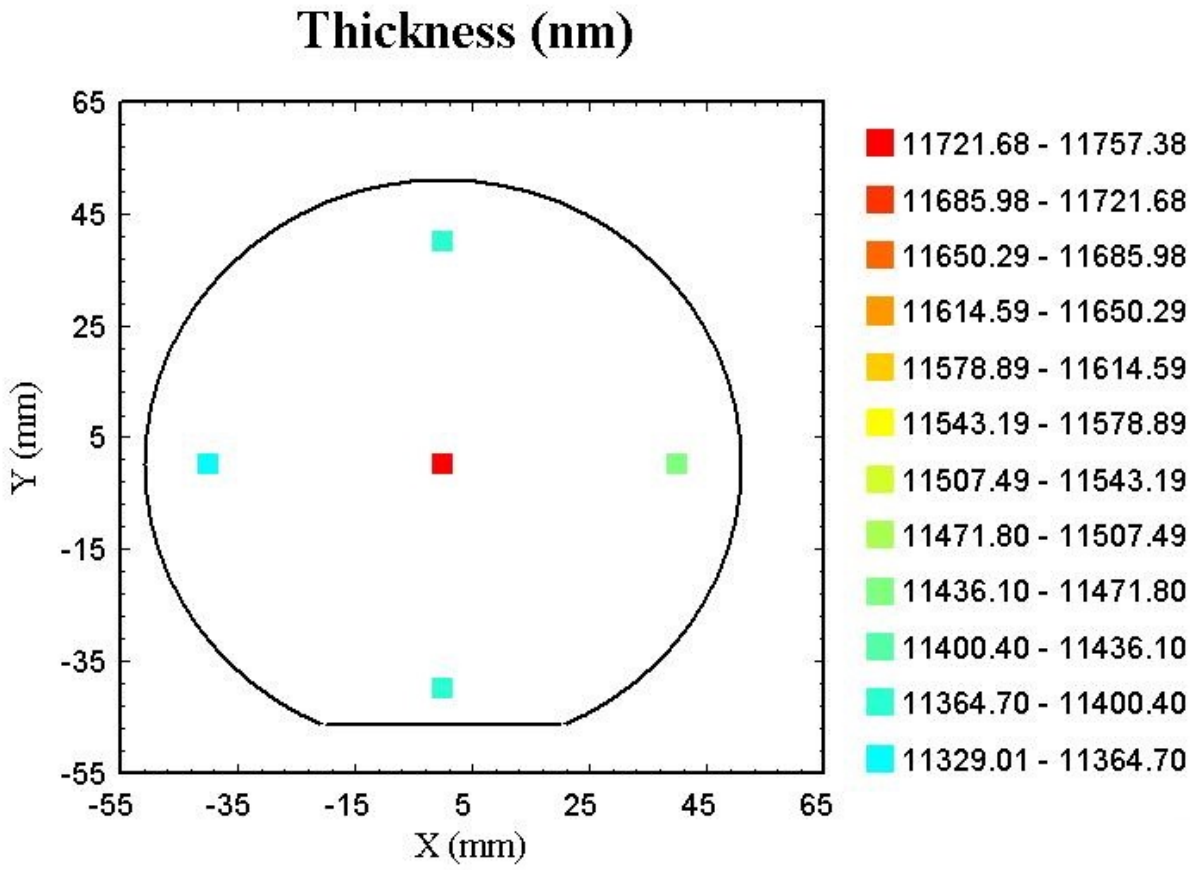

Figure 3.20. Thickness measurement of the silica cladding by the multiple-angle reflectometer FilmTek 4000 at five different points on the wafer surface after the PECVD deposition.

3.8. Optical microscope characterization

The ready strip plasmonic waveguides were also imaged by using the optical microscope ECLIPSE L200 (Nikon) [69]. An example of the waveguides pattern in the optical microscope is shown in Fig. 3.21. Here the optical magnification is x20. The gold strip waveguides with different width values are clearly seen as well as the silica background. The distance between waveguides is 100 μm. The pattern of the strip plasmonic waveguides agrees well with the designed pattern in the layout editor CleWin 5 (Fig. 3.1).

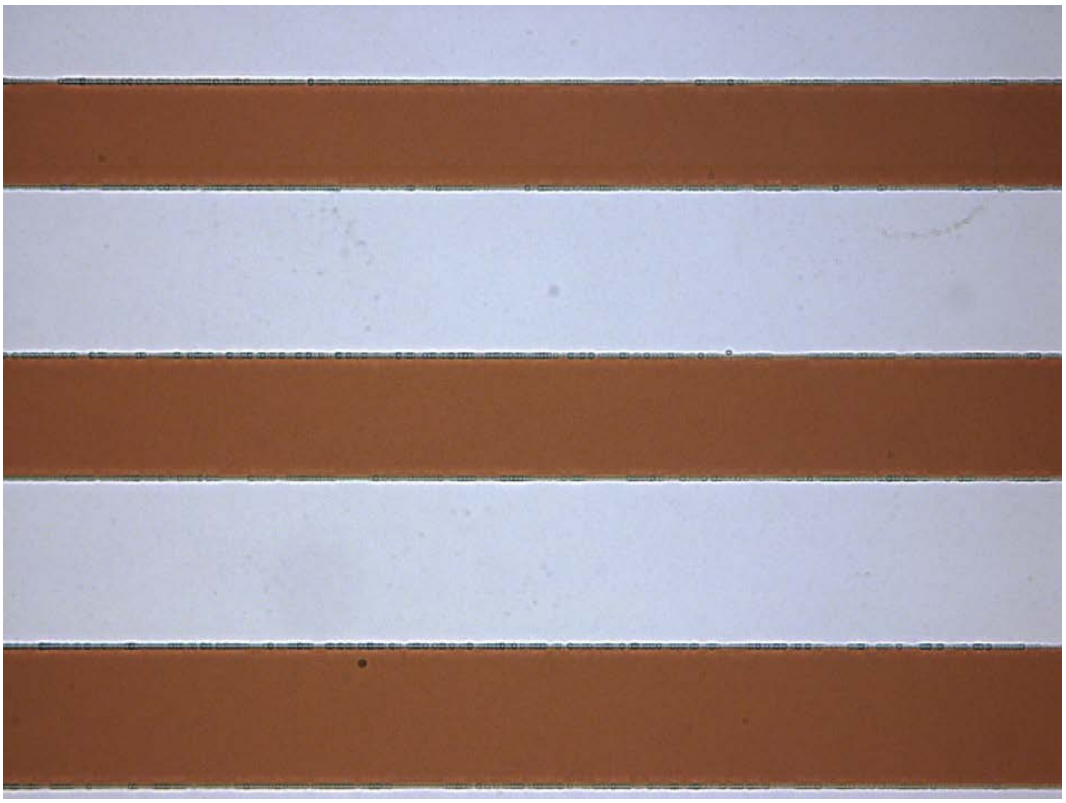

Figure 3.21. Optical microscope image of the strip plasmonic waveguides.

3.9. Dicing of wafers

The final step in the fabrication of samples was dicing of the ready wafers into rectangular parts with the strip plasmonic waveguides of different width and length. At first the dicing diagram for the wafers was prepared by using the physical layout editor CleWin 5. The complete wafer with the designed lines for the dicing process is shown in Fig. 3.22. The central part of the wafer contains three areas with the deposited nanostructures. The top part of the wafer has five series of the strip plasmonic waveguides. Every series contains ten plasmonic waveguides with the width values 10 μm, 20 μm, 30 μm, 40 μm, 50 μm, 60 μm, 70 μm, 80 μm, 90 μm, and 100 μm. The central part of the wafer has ten series of the strip plasmonic waveguides. Every series contains ten plasmonic waveguides with the width values 1 μm, 2 μm, 3 μm, 4 μm, 5 μm, 6 μm, 7 μm, 8

μm, 9 μm, and 10 μm. The bottom part of the wafer contains one continuous area of the deposited layers. A photograph of the prepared wafer before the dicing process is shown in Fig. 3.23.

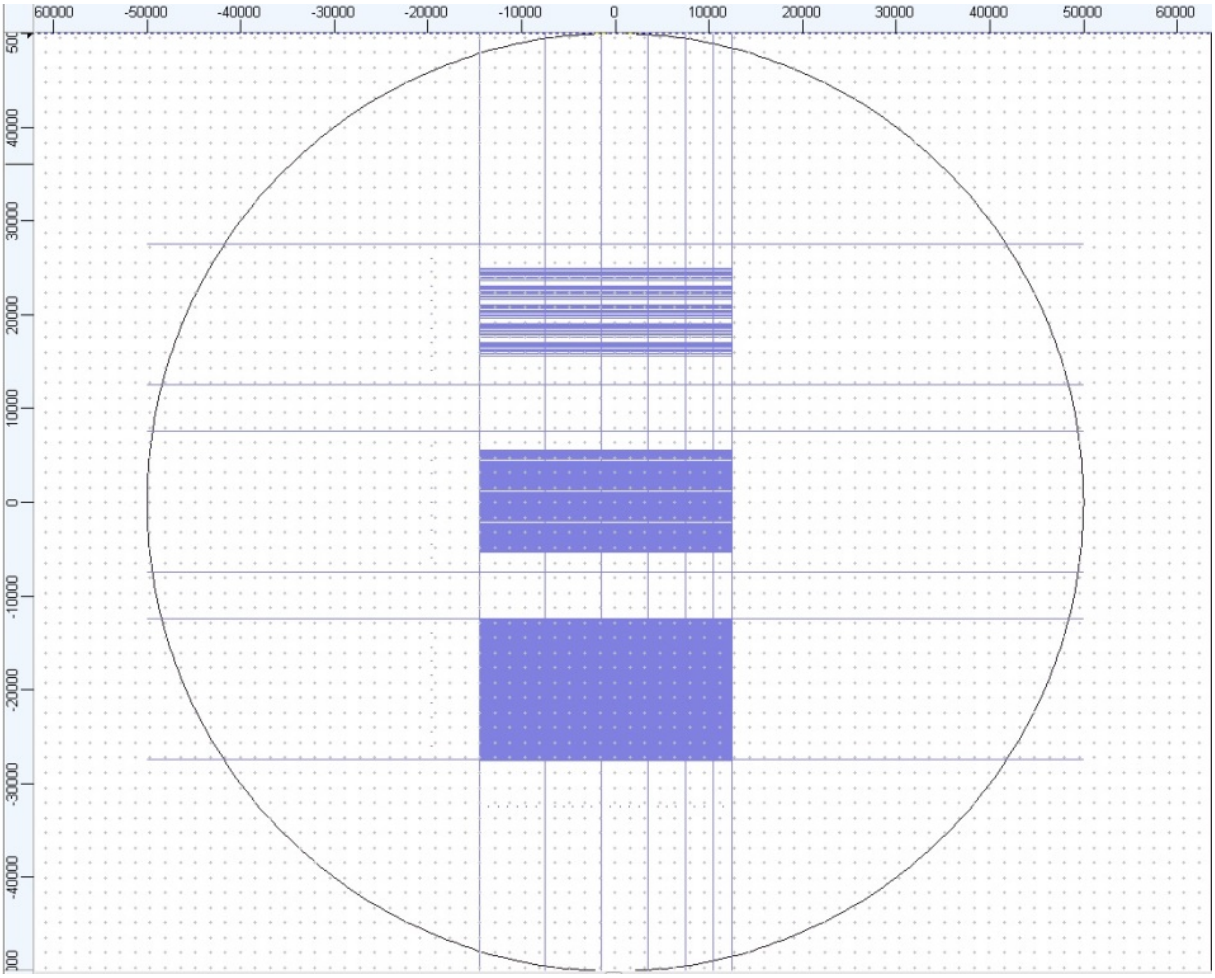

Figure 3.22. Dicing diagram of the wafer with the strip plasmonic waveguides in the layout editor CleWin5.

The wafers were diced, according to the dicing diagram, and by using the automatic dicing saw Disco DAD-321. A photograph of the dicing machine is shown in Fig. 3.24. The wafer was placed on the dicing platform in the machine (Fig. 3.24, right side). The system calibration and the dicing process were controlled by the embedded computer system (Fig. 3.24, left side). The wafer was diced into 18 rectangular samples with the length values 2, 3, 4, 5, 6, and 7

mm, and with the same width value 1.5 cm. The rectangular samples were collected and placed in a rectangular box. A photograph of the ready samples is shown in Fig. 3.25. The samples were classified, according to the length and width values of the strip plasmonic waveguides. Thus, these rectangular samples are completely ready for the optical characterization in the laboratory.

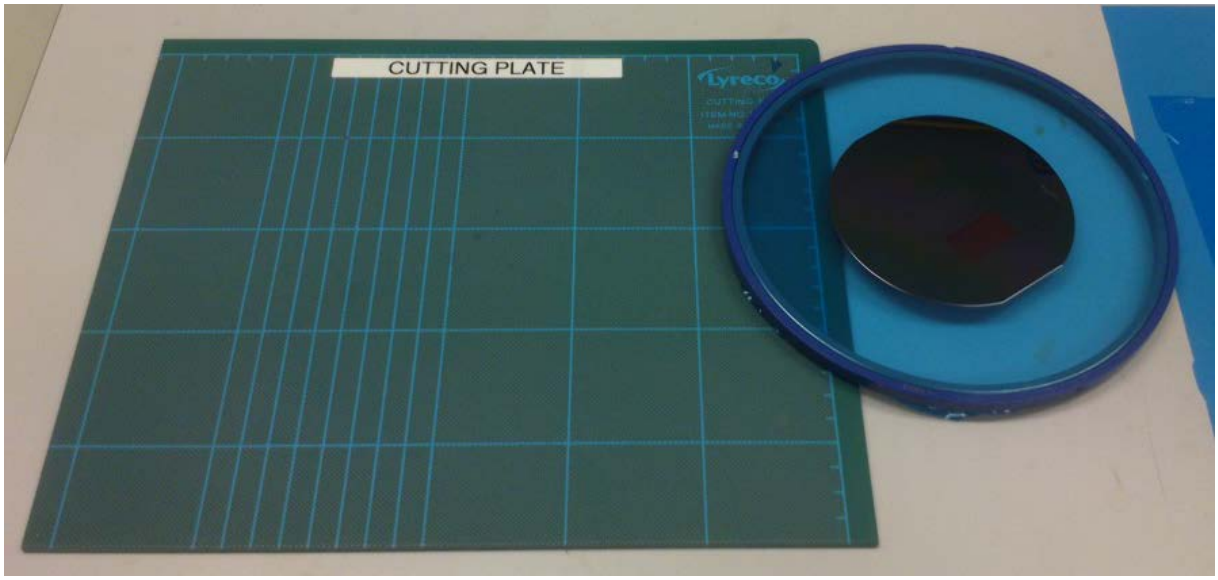

Figure 3.23. Prepared wafer before the dicing process.

Figure 3.24. Automatic dicing machine Disco DAD-321.

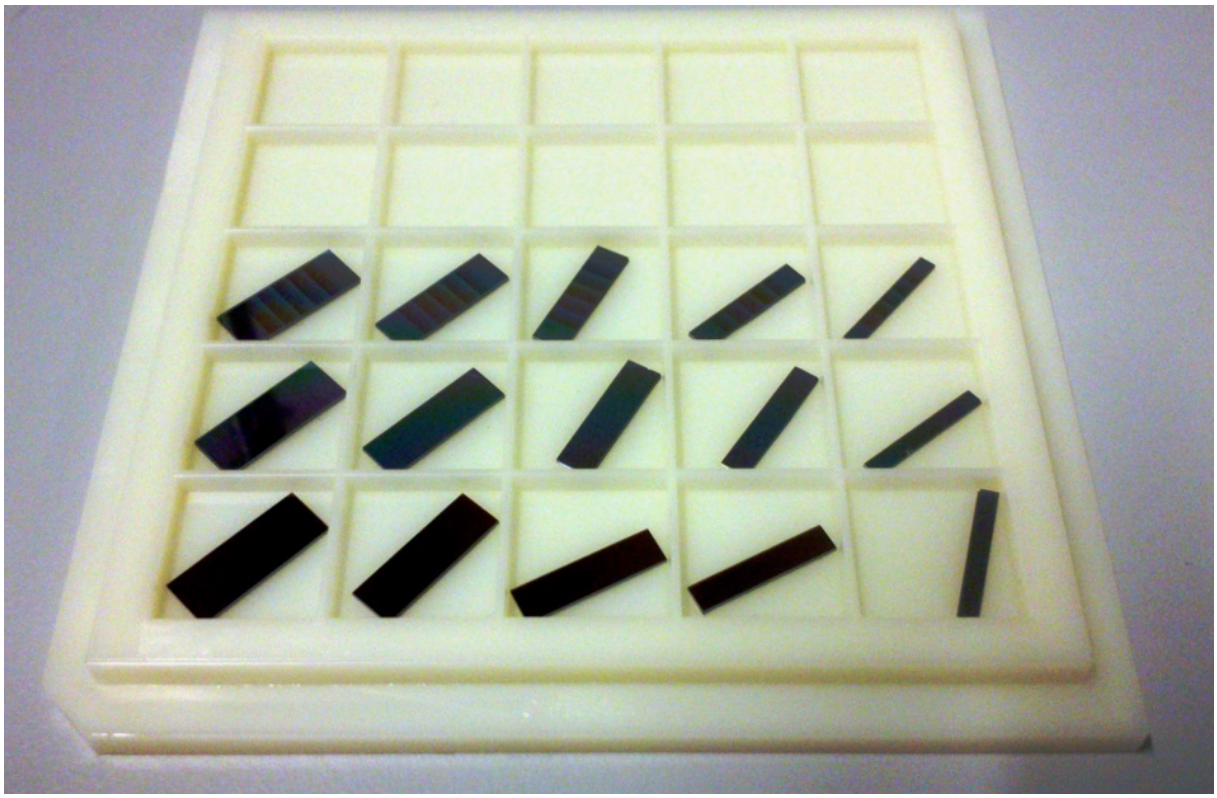

Figure 3.25. Ready samples with the strip plasmonic waveguides.

Chapter 4

Experimental research

4.1. Experimental setup at Technical University of Denmark

The experimental setup for linear and nonlinear optical characterization of the samples with the strip plasmonic waveguides was prepared in the optical laboratory at Technical University of Denmark (DTU). A schematic diagram of the experimental setup is shown in Fig. 4.1. A photograph of the experimental setup in the optical laboratory is shown in Fig. 4.2. This original experimental setup was used earlier by A. Boltasseva for linear optical characterization of plasmonic waveguides [80-83]. The laser source is the picosecond pump source for the SuperK EXTREME, model EXR-15 (NKT Photonics) [84]. The laser source (Fig. 4.3) provides a free-space laser beam in the average power range up to approximately 15 W. The average power of the laser source was controlled by using a personal computer with a USB interface connection. The repetition rate of the laser is 78 MHz. The peak wavelength of the laser is approximately 1064 nm, and the pulse duration is approximately 3 ps. At first the free-space beam from the laser source was linearly polarized by using a standard polarizer (Thorlabs) [85]. Then the laser beam was shaped by a Gaussian filter (model 10LF04-1064, FWHM parameter 3.5 nm, Newport) [86]. Afterwards the free-space beam was attenuated by a set of neutral-density filters. At the end of the free-space propagation line (Fig. 4.2, center) the laser beam was coupled to a polarization-maintaining fiber (LMA-PM-10, NKT Photonics) [84], and at last delivered to the sample with the strip plasmonic waveguides (Fig. 4.2, right side). The linear polarization of the free-space laser beam was aligned to match the fast axis of the polarization-maintaining fiber, and to match the transverse

magnetic polarization of the long-range surface plasmon polariton mode in the strip plasmonic waveguides [87-89].

The samples with the strip plasmonic waveguides were placed on the measurement platform (Fig. 4.2, right side), and their positioning was controlled by using the optical microscope Axiotech vario (Carl Zeiss) [71]. A photograph of the sample on the measurement platform is also shown in Fig. 4.4. The holder with the polarization-maintaining fiber was placed on the XYZ positioner (Fig. 4.3, left side). The end-fire coupling method was used to excite the long-range surface plasmon polariton mode in the strip plasmonic waveguides [90]. A single mode fiber (LMA-10, NKT Photonics) collected and delivered the transmitted optical flux to the optical spectrum analyzer (OSA) AQ6315E (Yokogawa) [91]. The end-fire coupling alignment was also controlled by the optical microscope Axiotech vario. Before the transmission measurements, the long-range surface plasmon polariton mode in every waveguide was imaged by using a lens (Fig. 4.4, right side) and a camera beam profiler (Thorlabs), and the transverse magnetic polarization of the plasmonic mode was verified by the linear polarizer. This polarization check verifies coupling to the long-range surface plasmon polariton mode in every plasmonic waveguide [92-95].

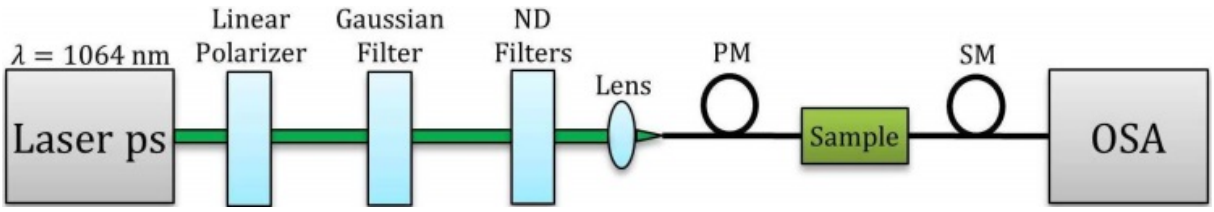

Figure 4.1. Experimental setup for picosecond optical characterization of the samples with the strip plasmonic waveguides.

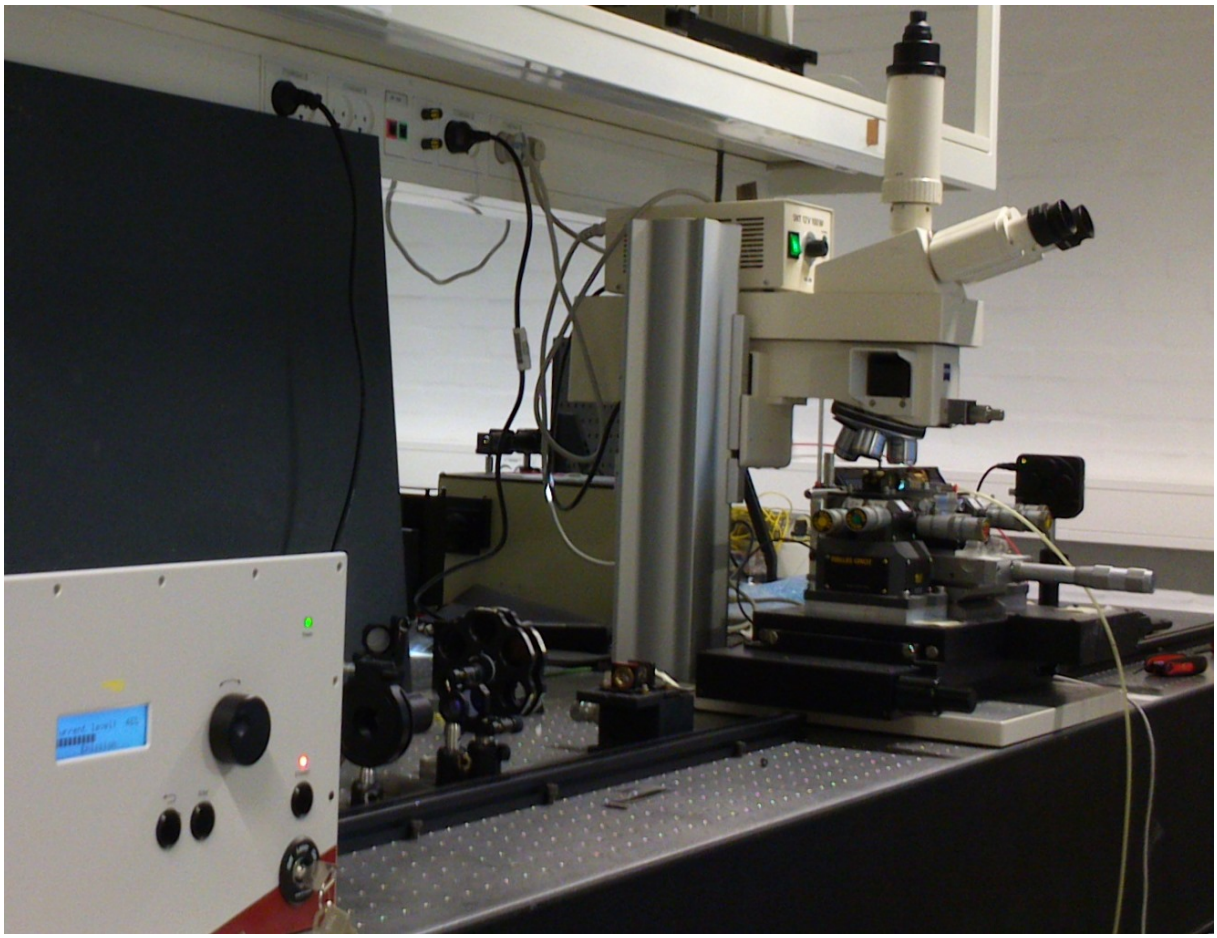

Figure 4.2. Experimental setup in the optical laboratory at DTU.

Figure 4.3. Picosecond laser SuperK EXTREME.

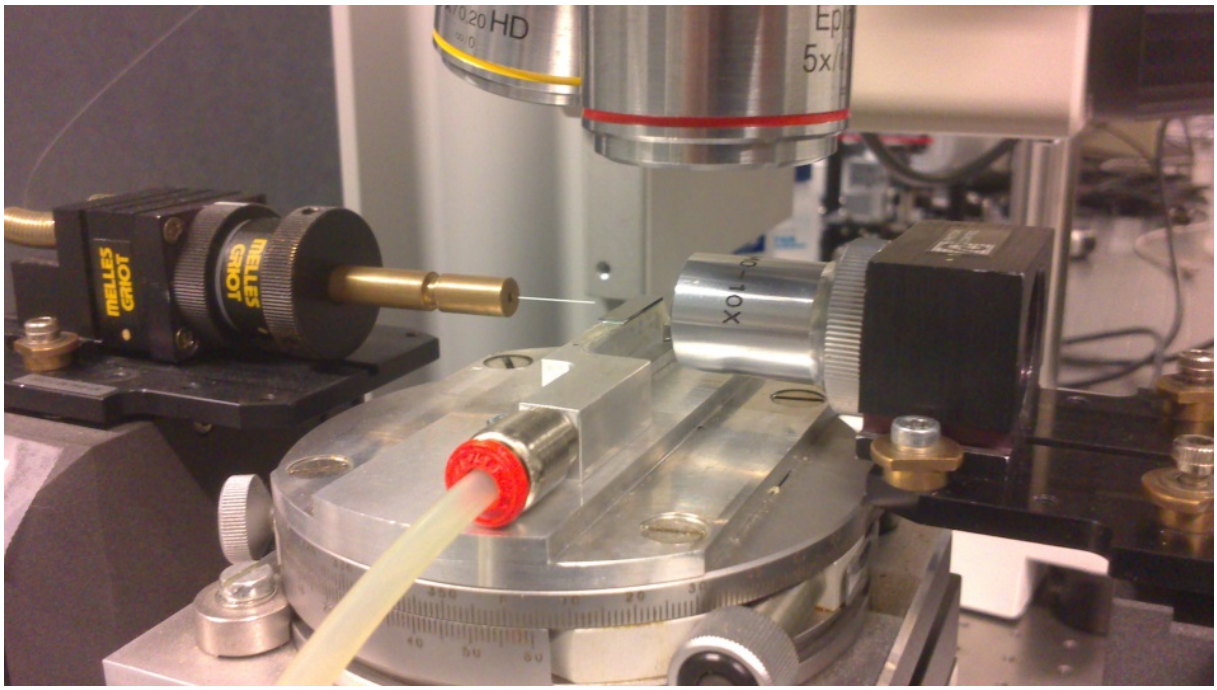

Figure 4.4. Sample on the platform controlled by the optical microscope.

4.2. Linear characterization

The first step in the experimental study of the strip plasmonic waveguides was the linear optical characterization. The average power of the laser source was tuned to a small value (less than 1 mW). The transmitted power from the strip plasmonic waveguides was measured by using the optical spectrum analyzer, according to the experiment scheme shown in Fig. 4.1. The strip plasmonic waveguides with the lengths l = 2, 3, and 4 mm, and the gold layer thickness t = 22, 27, and 35 nm were selected for the linear optical characterization. The linear propagation loss α per unit length of the waveguides, and the coupling loss C per two facets of the waveguides were experimentally obtained for different values of the gold layer thickness t. A standard approach for the linear optical characterization of the waveguides is to use the insertion loss graphs [94, 95]. These graphs are shown in Fig. 4.5. For every value of the waveguide length and gold layer thickness the measurements of five identical strip

plasmonic waveguides were averaged, and the linear fit was calculated by the least squares method. The coupling loss C per two facets is obtained as the intersection of the fitted lines with the vertical axis. The linear propagation loss α per unit length is calculated as the slope angle to the fitting lines.

The calculated values for the propagation loss α and the coupling loss C, with the calculation errors are presented in Table 4.1. The obtained experimental values show that the linear propagation loss per unit length increases by approximately 1.8 times as the gold layer thickness increases from 22 nm to 35 nm. The coupling loss per two facets varies by approximately 10 percent, and is completely within the calculation errors. This conclusion is in accordance with the previous measurements of the similar strip plasmonic waveguides [94]. The obtained values for the linear propagation loss are approximately 2-3 times greater than the results published by Berini and co-workers [94], and there are several possible reasons to explain this. First, the maximum values of the roughness spikes of the gold layers are approximately 2 nm (Fig. 3.17) in comparison with approximately 1 nm in Ref. [94]. Second, the peak wavelength 1550 nm used in Ref. [94] provides lower attenuation of the long-range surface plasmon polariton mode in the strip plasmonic waveguides than the peak wavelength 1064 nm used in the present experiment [Fig. 2.3 (b)]. Meanwhile, it is expected that the sharp edges on the waveguide profile in Fig. 3.16(a) do not contribute significantly to the propagation losses. This is because the intensity distribution function of the long-range surface plasmon polariton mode in the studied plasmonic waveguides is close to zero at the waveguide edges [96-98] (Fig. 2.4).

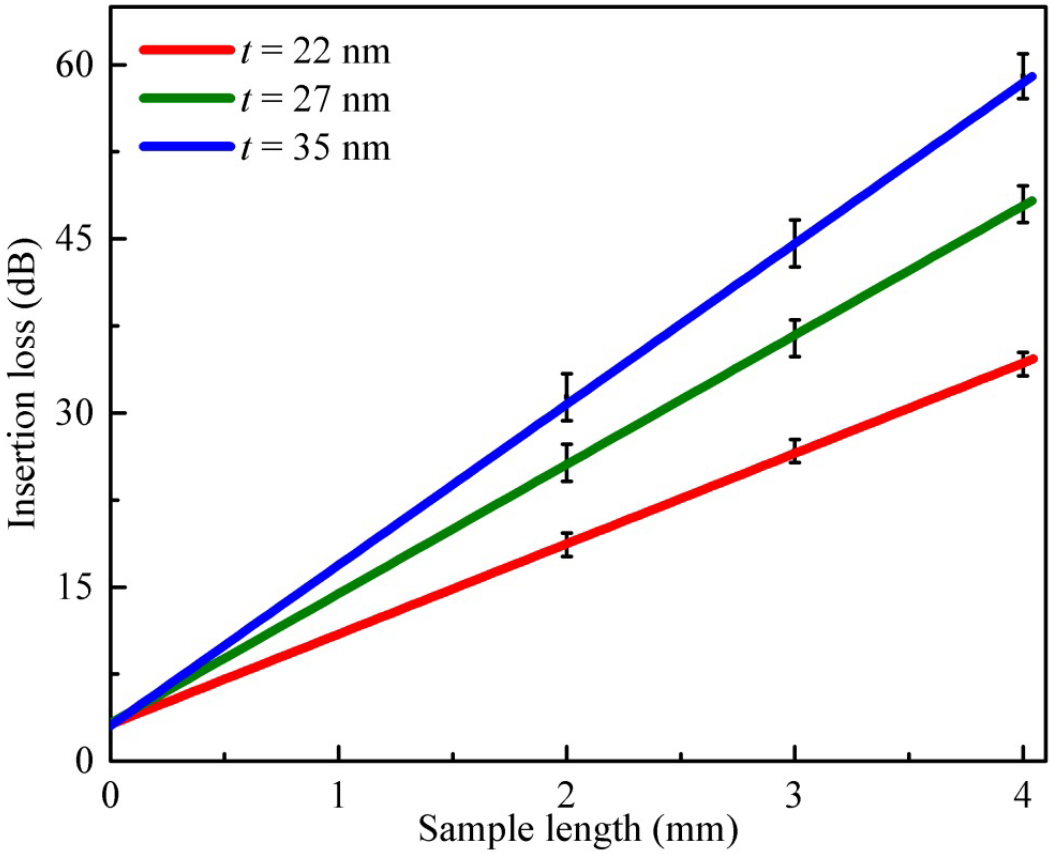

Figure 4.5. Linear characterization of the strip plasmonic waveguides: experimental determination of the linear loss parameter α, and the coupling loss C for the gold layer thickness t = 22, 27, and 35 nm.

Table 4.1. Experimental values of the propagation loss α and coupling loss C for plasmonic waveguides with different thicknesses.

t (nm)	α (dB/mm)	C (dB)
22	7.8 ± 0.2	3.2 ± 0.5
27	11.1 ± 0.2	3.3 ± 0.8
35	13.8 ± 0.3	3.5 ± 1.0

4.3. Nonlinear power characterization

The second step in the experimental study of the strip plasmonic waveguides was the nonlinear power characterization. The average power delivered to the strip plasmonic waveguides was varied by either changing the neutral density filters or changing the original average power of the laser source, in order to obtain the necessary amount of measurements. The transmitted power from the strip plasmonic waveguides was measured by using the optical spectrum analyzer. The waveguides with the length l = 3 mm, and the gold layer thickness t = 22, 27, and 35 nm were selected for the nonlinear optical characterization.

The obtained dependences of the transmitted power P_{out} from the waveguides with respect to the delivered power P_{in} to the waveguides have several interesting features, and are shown in Fig. 4.6. The first feature is the nonlinear trends of dependencies $P_{\text{out}}(P_{\text{in}})$ at high values of input power P_{in}. The second feature is that these nonlinear trends significantly depend on the gold layers thickness *t*. The strip plasmonic waveguides with thinner gold layers have more pronounced relative deviation from the linear power dependency at the same values of the input power P_{in}. For every value of the gold layer thickness *t* the measurements of five identical strip plasmonic waveguides were averaged and the nonlinear curve fit was calculated as follows:

$$P_{\text{out}} = aP_{\text{in}} - bP_{\text{in}}^{\,2}, \qquad \textbf{(4.1)}$$

where *a* and *b* are the fitting coefficients, and the input and output powers are corrected for the coupling loss *C* at the end facets. The calculated values for the parameters *a* and *b*, with the calculation errors are presented in Table 4.2. The parameter *a* is related to the linear propagation loss α of the long-range surface plasmon polariton mode in the strip plasmonic waveguides as $a = e^{-\alpha l}$, where *l* is the waveguide length. The calculated values of α are 2.031 ± 0.001 mm^{-1}, 2.766

± 0.001 mm^{-1}, and 3.980 ± 0.002 mm^{-1} for the gold layer thickness t = 22, 27, and 35 nm, respectively. These values of the linear loss parameter α are somewhat higher than the values of the linear propagation loss at low power characterization; an explanation could be that the strip plasmonic waveguides were significantly heated at high pump powers.

The coefficient b is related to the nonlinear absorption parameter β of the LRSPP mode. In terms of the nonlinear susceptibility for the constituent materials in the strip plasmonic waveguides (gold, tantalum pentoxide, and silica), gold has the dominant contribution to the effective third-order nonlinear susceptibility $\chi_{\text{eff}}^{(3)}$ of the plasmonic mode [Paper B]. The effective third-order nonlinear susceptibility $\chi_{\text{eff}}^{(3)}$ is related to the nonlinear absorption coefficient β of the LRSPP mode as follows [54]:

$$\beta = \frac{\beta_{\text{c}}}{A_{\text{eff}}} = \frac{3\omega}{2\varepsilon_0 c^2 n_0^2 A_{\text{eff}}} \text{Im}[\chi_{\text{eff}}^{(3)}]. \qquad \textbf{(4.2)}$$

Here β_{c} is the conventional definition of the nonlinear absorption coefficient [54], $\omega = 2\pi c / \lambda$ is the light angular frequency, c is the speed of light in vacuum, ε_0 is the vacuum permittivity, n_0 is the effective linear refractive index of the LRSPP mode, n_2 is the effective nonlinear refractive index of the LRSPP mode, and A_{eff} is the effective area of the LRSPP mode. The nonlinear coefficient b depends on both the nonlinear parameters of the LRSPP mode in the strip plasmonic waveguides and the characteristic parameters of the laser source. By considering the pulse propagation equation [Paper B], it is straightforward to show that the ratio of the nonlinear and linear parameters is given by:

$$\frac{b}{a} \approx \frac{\beta}{\alpha T f_{\text{rep}}}, \qquad \textbf{(4.3)}$$

where T is the laser pulse duration (FWHM parameter), and f_{rep} is the repetition rate of the laser source. In Chapter 2 the structure of the strip plasmonic waveguides was analyzed in detail, and it was also shown that the specific contribution from the gold layer has the dominant contribution to the effective third-order nonlinear susceptibility of the LRSPP mode. In fact, the contribution from the gold layer is two orders of magnitude greater (around 10^{-20} $\mathrm{m}^2/\mathrm{V}^2$) than the one from the tantalum pentoxide layer (around 10^{-22} $\mathrm{m}^2/\mathrm{V}^2$), although the latter has a quite large cubic nonlinearity [47]. The calculated value of the real part of the effective linear refractive index of the LRSPP mode $\mathrm{Re}[N_{\mathrm{eff}}]$ is approximately 1.47, and is significantly greater than the value of the imaginary part of the effective linear refractive index $\mathrm{Im}[N_{\mathrm{eff}}]$, which is less than 0.01. Therefore the following formula can be taken as a good approximation for the nonlinear absorption coefficient:

$$\beta \approx \frac{3\omega\theta_{\mathrm{Au}}\,\mathrm{Im}[\chi^{(3)}_{\mathrm{Au}}]}{2\varepsilon_0 c^2 n_0^2 A_{\mathrm{eff}}}, \qquad \textbf{(4.4)}$$

where $\chi^{(3)}_{\mathrm{Au}}$ is the third-order susceptibility of the gold layers. Thus, the obtained coefficients a and b were used to experimentally determine the values of the imaginary part of the third-order nonlinear susceptibility $\chi^{(3)}_{\mathrm{Au}}$ of the gold layers with the thickness t = 22, 27, and 35 nm.

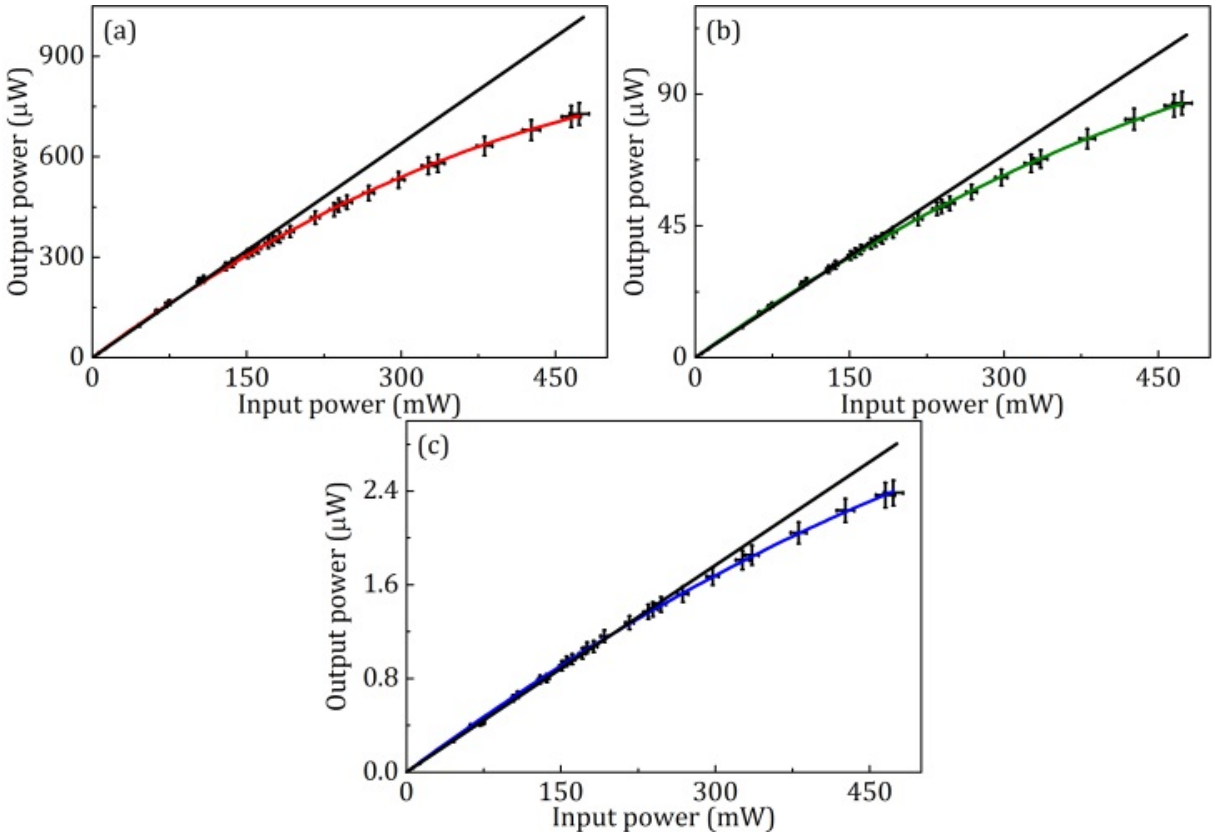

Figure 4.6. Nonlinear power transmission for the strip plasmonic waveguides with the gold layer thickness (a) t = 22 nm, (b) t = 27 nm, and (c) t = 35 nm. Black lines on each graph correspond to the fitted linear trend.

Table 4.2. Experimental parameters a and b of the LRSPP mode in the strip plasmonic waveguides with the gold layer thickness t = 22, 27, and 35 nm.

t (nm)	a	b (1/W)
22	$(2.26 \pm 0.01) \times 10^{-3}$	$(1.54 \pm 0.02) \times 10^{-3}$
27	$(2.49 \pm 0.01) \times 10^{-4}$	$(1.38 \pm 0.02) \times 10^{-4}$
35	$(6.53 \pm 0.03) \times 10^{-6}$	$(3.09 \pm 0.08) \times 10^{-6}$

4.4. Nonlinear spectral characterization

The third step in the experimental study of the strip plasmonic waveguides was the nonlinear spectral characterization. The strip plasmonic waveguides with the length l = 3 mm, and the gold layer thickness t = 22, 27, and 35 nm were also selected for the nonlinear spectral measurements. The spectra of the transmitted optical flux from the strip plasmonic waveguides were measured by using the optical spectrum analyzer in the wavelength range 1058-1069 nm (Fig. 4.7). The spectral broadening and splitting are observed – a clear sign of self-phase modulation (SPM) effect influenced by two-photon absorption from the real part and imaginary part of the effective third-order susceptibility $\chi^{(3)}$ of the LRSPP mode, respectively [34, 56, 57]. This was confirmed with numerical simulations of the nonlinear Schrödinger equation, giving almost identical spectra as those in Fig. (4.7), where the experimental input pulse was used and no free parameters were adopted – all linear and nonlinear parameters were those calculated via the waveguide analysis or measured experimentally). Another feature is that the spectral broadening and splitting in the output spectra differ slightly for every case. The values of the effective spectral width were compared for the input pulse and output pulses at the splitting level (approximately 0.05), where for simplicity the side peaks with lower intensities (approximately 0.01-0.03) were neglected. To do an analytical estimate, the input pulse was approximated with a Gaussian one, and the nonlinear spectral broadening factor (SBF) was calculated by comparing it to a Gaussian fit to the two distinct self-phase modulation peaks. Then the SBF parameter is related to the effective nonlinear coefficient γ and effective nonlinear refractive index $n_{2\text{eff}}$ the LRSPP mode in the strip plamonic waveguides by the following expressions [34]:

$$\text{SBF} \approx 0.86\gamma P_0 \frac{1-e^{-\alpha l}}{\alpha}, \qquad \textbf{(4.5)}$$

$$\gamma = \frac{\omega}{c}\frac{n_{2\text{eff}}}{A_{\text{eff}}}, \tag{4.6}$$

where P_0 is the peak power of an input pulse, and *l* is the physical length of the strip plasmonic waveguides. This result assumes a purely Gaussian input pulse, which is transform limited (no chirp across the pulse). Although the input pulse in the experiment was not transform limited and its spectrum had multiple modulated peaks, this expression serves as a rough estimate of the effective nonlinearity γ of the long-range surface plasmon polariton mode in the strip plasmonic waveguides. Such an approach is also justified by the close agreement with the numerical simulations. From Eq. (4.6) and using the relation between the effective nonlinear refractive index $n_{2\text{eff}}$ and the real part of the effective third-order susceptibility $\text{Re}[\chi^{(3)}_{\text{eff}}]$ the following formula is realized:

$$\gamma \approx \frac{3\omega\theta_{\text{Au}}\,\text{Re}[\chi^{(3)}_{\text{Au}}]}{4\varepsilon_0 c^2 n_0^2 A_{\text{eff}}}, \tag{4.7}$$

since as argued above for the nonlinear loss, the dominating contribution comes from the gold layer in the strip plasmonic waveguides. The experimental values of the spectral broadening factor are used to extract the real part of the third-order susceptibility of the gold layers showing its dependence on the layer thickness *t*.

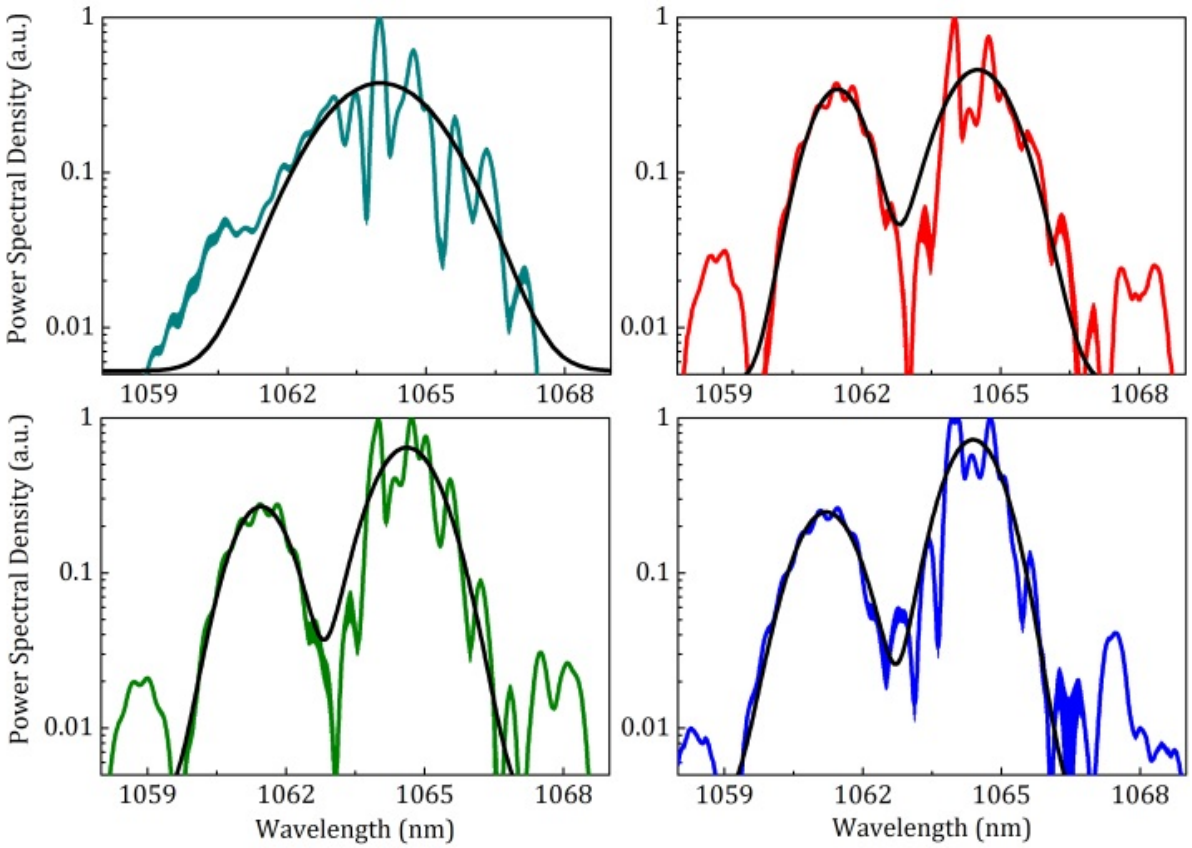

Figure 4.7. (a) Input pulse spectrum, and output pulse spectra for the strip plasmonic waveguides at the maximum input power (approximately 480 mW) with the gold layer thickness (b) t = 22 nm, (c) t = 27 nm, and (d) t = 35 nm. Black lines on graph show a Gaussian fit to the measured spectra.

4.5. Experimental setup at King's College London

The second experimental setup for optical characterization of the samples with the strip plasmonic waveguides was assembled in the optical laboratory at King's College London. A schematic diagram of the experimental setup is shown in Fig. 4.8. A photograph of the experimental setup in the optical laboratory is shown in Fig. 4.9. The laser source is the femtosecond laser amplifier PHAROS (Light Conversion) [99], and is shown in Fig. 4.10. The laser source provides a free-space laser beam in the average power range up to

approximately 7 W. The laser source was controlled remotely by using a laptop. The repetition rate of the laser source was tunable and was selected as 200 kHz. The peak wavelength of the laser is approximately 1030 nm, and the pulse duration is approximately 200 fs.

At first the average power of the free-space laser beam was attenuated by several neutral density (ND) filters. Then the linear polarization of the laser beam was aligned by using a standard half-wave plate (Thorlabs) and linear polarizer (Thorlabs) [85] (Fig. 4.9, right side) to match the transverse magnetic polarization of the long-range surface plasmon polariton mode in the strip plasmonic waveguides. The samples with the strip plasmonic waveguides were placed on the platform (Fig. 4.9, center). This platform was mounted to the vertical XYZ stage, and the input and output NIR lens were situated on the XYZ stages. The end-fire coupling method was used to excite the LRSPP modes [90] in the strip plasmonic waveguides. Then an iris diaphragm was placed to eliminate the scattered light and to transmit the LRSPP mode optical flux to the power meter S132C (Thorlabs) [85] (Fig. 4.9, left side). The end-fire coupling alignment was controlled by using the digital color camera WAT-221S (Watec) [101]. Before the power transmission measurements were taken, the LRSPP mode in every waveguide was imaged by the digital camera and the transverse magnetic polarization of the plasmonic mode was verified using the half-wave plate and linear polarizer [87, 102]. This polarization check verified coupling to the LRSPP mode in every plasmonic waveguide.

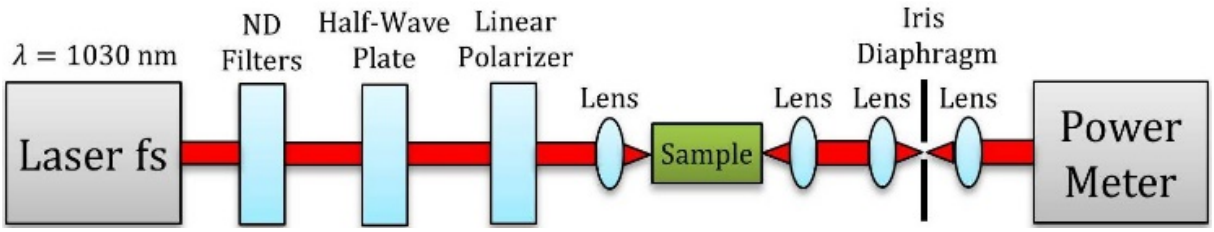

Figure 4.8. Experimental setup for femtosecond optical characterization of the samples with the strip plasmonic waveguides.

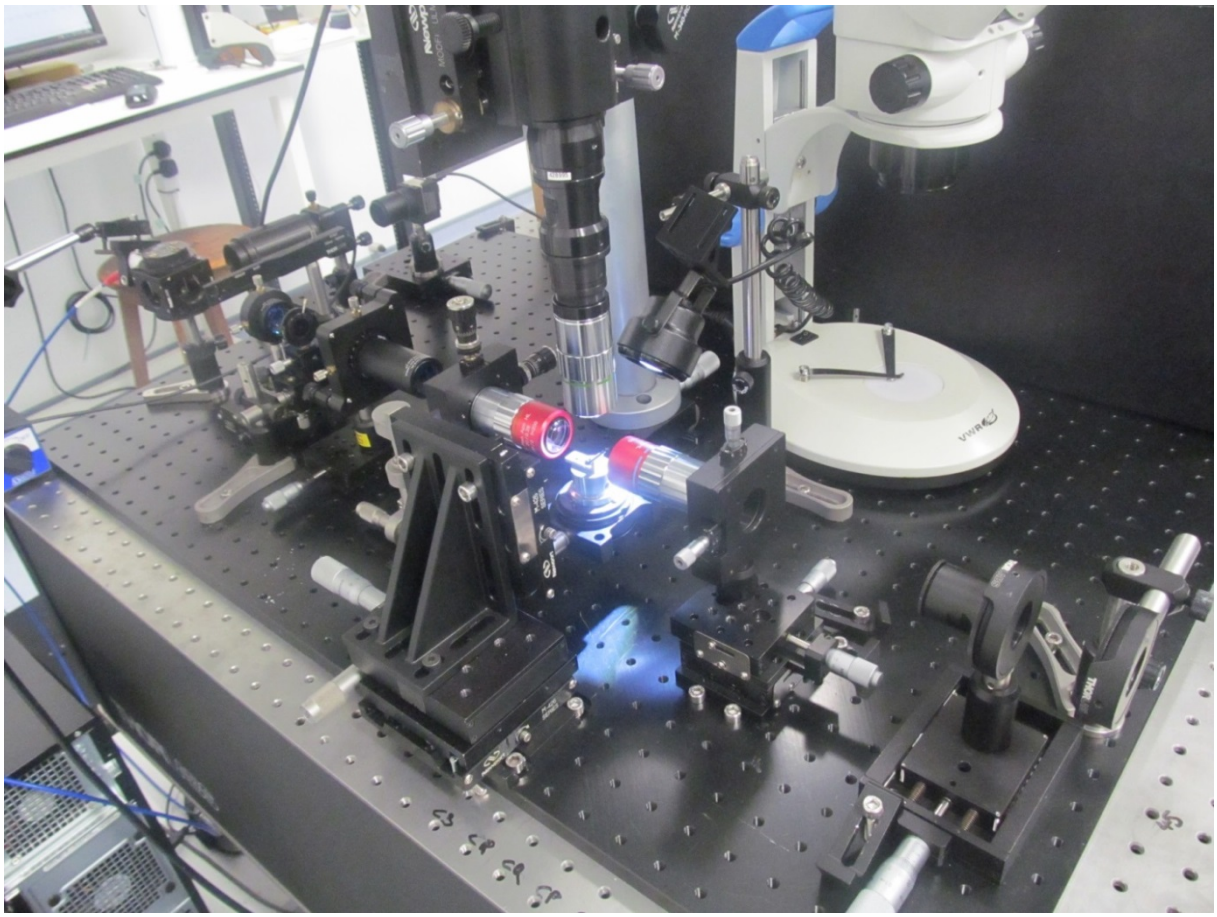

Figure 4.9. Experimental setup in the optical laboratory at KCL.

Figure 4.10. Femtosecond laser amplifier PHAROS.

4.6. Linear and nonlinear power characterization

By using the experimental setup described above, the optical characterization of the samples with the strip plasmonic waveguides was performed. At first the free-space laser beam was attenuated to a small average power (approximately 1 mW). The linear optical characterization of the strip plasmonic waveguides was performed for the gold layer thickness t = 22, 27, and 35 nm, and the length l = 2, 3, and 4 mm. The linear propagation loss α per unit length, and the coupling loss C per two facets were calculated by using the insertion loss graphs and the same procedure as described earlier for the 3-ps pulses experiment. The obtained values of the propagation loss and coupling loss are presented in Table 4.3. The linear propagation loss α increases by approximately 1.85 times as the gold layer thickness t increases from 22 nm to 35 nm. This agrees well with the tendency for the linear propagation loss that was found earlier by using 3-ps laser pulses at the wavelength 1064 nm [Paper C]. At the same time, the values of the end-fire coupling loss C per two facets are approximately 7 dB and change a little for the strip plasmonic waveguides with the thickness t = 22, 27, and 35 nm. The obtained values of the propagation loss α per unit length at the wavelength 1030 nm are approximately 10 percent greater than the obtained values of the linear propagation loss per unit length obtained previously at the wavelength 1064 nm. This confirms the expected tendency of the increase of the linear propagation loss for shorter wavelengths [Fig. 2.3(b)]. Although the values of the coupling loss C for the free-space lens coupling are approximately 3 dB greater than the values of the coupling loss C obtained previously by using the fiber coupling setup (Fig. 4.4), this free-space coupling scheme is preferred to exclude dispersion effects when operating with femtosecond laser pulses.

The nonlinear optical characterization of the samples with the strip plasmonic waveguides was performed by tuning the input average power before the waveguides from approximately 1 mW (5 nJ) to approximately 55 mW (275 nJ). The strip plasmonic waveguides with the length l = 2 mm were selected for the

nonlinear optical characterization. The values of the coupling loss C (approximately 3.5 dB per facet) were used to calculate the corresponding values of the pulse energy and peak power inside the strip plasmonic waveguides, which were therefore in the range 1-55 nJ and 5-275 kW, respectively. The further increase of the average input power caused significant heating and melting of the waveguide structures. The fit to experimental data was calculated by using the following nonlinear formula [Paper B] $P_{\text{out}}/(aP_{\text{in}}) = 1/[1+(\beta L_{\text{eff}} P_{\text{in}} e^{-C/2})/(\sqrt{\pi} T_0 f_{\text{rep}})]$, where P_{out} is the average output power right after the waveguides, $L_{\text{eff}} = [1-\exp(-\alpha l)]/\alpha$ is the effective propagation length, l is the physical length of the waveguides, T_0 is the pulse duration, f_{rep} is the laser repetition rate, and $a = e^{-(\alpha L + C)}$ is the experimental coefficient that contains the linear propagation loss α and coupling loss C (Table 4.3). The nonlinear dependences of transmitted power P_{out} with respect to input power P_{in} for the waveguides with the length l = 2 mm, and the gold layer thickness t = 22, 27, and 35 nm are shown in Fig. 4.11. The deviation from the horizontal line (where $P_{\text{out}} = aP_{\text{in}}$) is an indication of the two-photon absorption effect and determined by the nonlinear parameter β. The nonlinear curve fits were obtained by using only one free parameter β and starting from unity at P_{in} = 0 for consistency of the linear and nonlinear regimes.

Table 4.3. Experimental values of the propagation loss α per unit length, coupling loss C per two facets, and parameter a for strip plasmonic waveguides with the gold layer thickness t = 22, 27, and 35 nm.

t (nm)	α (dB/mm)	C (dB)	a
22	8.7 ± 0.1	6.8 ± 0.4	3.6×10^{-3}
27	11.8 ± 0.2	6.9 ± 0.5	8.6×10^{-4}
35	15.3 ± 0.4	7.0 ± 0.8	2.0×10^{-4}

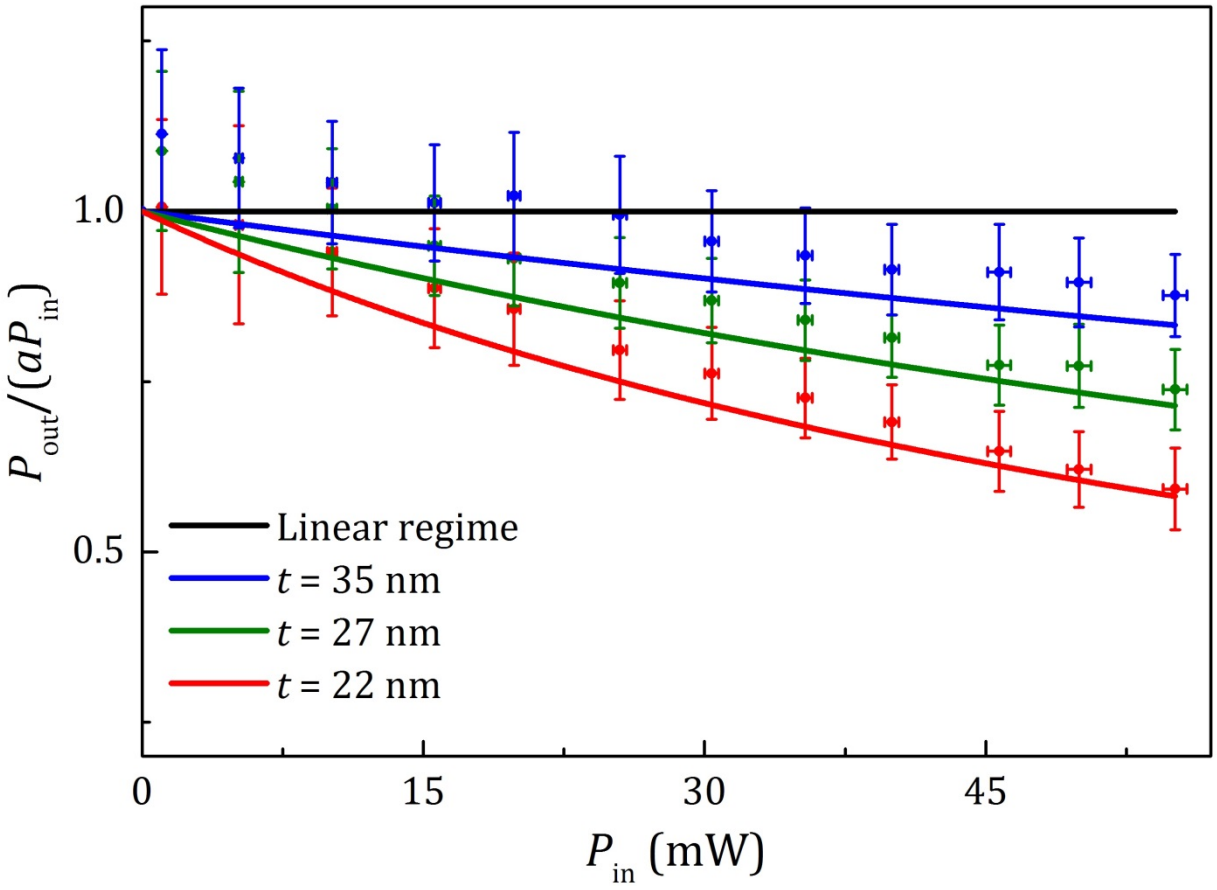

Figure 4.11. Nonlinear transmission dependences for 200-fs pulses at a wavelength of 1030 nm for plasmonic waveguides with the gold layer thickness t = 22, 27, and 35 nm. The black line corresponds to the linear regime and the color lines are fits to the experimental data.

The only contribution to the nonlinear loss in the waveguides comes from the gold layer because the photon energy at 1030 nm is far below half of the bandgap energy for silica and tantalum pentoxide. Thus, the nonlinear parameter β is directly connected to the imaginary part of the third-order susceptibility $\chi^{(3)}_{\mathrm{Au}}$ of the gold layers as $\beta \approx (3\omega\theta_{\mathrm{Au}}\,\mathrm{Im}[\chi^{(3)}_{\mathrm{Au}}])/(2\varepsilon_0 c^2 n_0^2 A_{\mathrm{eff}})$, where $\omega = 2\pi c/\lambda$ is the light angular frequency, c is the vacuum speed of light, ε_0 is the vacuum permittivity, n_0 is the effective linear refractive index of the LRSPP mode, θ_{Au} is the field localization parameter of the gold layer, and A_{eff} is the effective area of the LRSPP mode [Paper A, Paper B]. Thus, the values of the imaginary part

of the third-order nonlinear susceptibility $\chi^{(3)}_{Au}$ of the gold layers with the thickness t = 22, 27, and 35 nm were experimentally obtained for 200-fs laser pulses.

4.7. Thickness dependence of the third-order nonlinear susceptibility of gold

By using the obtained experimental results from two experiments with 3-ps optical pulses, and 200-fs optical pulse, the thickness dependence of the values of the third-order nonlinear susceptibility $\chi^{(3)}_{Au}$ of gold for ultrathin gold layers was obtained.

The calculated values of the real part and imaginary part of the third-order nonlinear susceptibility $\chi^{(3)}_{Au}$ from the first experiment using 3-ps optical pulses are shown in Fig. 4.12. The values of the third-order susceptibility $\chi^{(3)}_{Au}$, and the calculation errors are also presented in Table 4.4. The real and imaginary parts of the third-order nonlinear susceptibility $\chi^{(3)}_{Au}$ decrease as the gold layer thickness t increases. The nonlinear curve fit was calculated according to the following formula:

$$\chi^{(3)}_{Au} = \chi^{(3)}_{\infty} + \frac{C}{t}, \qquad \textbf{(4.8)}$$

where $\chi^{(3)}_{\infty}$ is value of the third-order nonlinear susceptibility for bulk gold [24], t is the gold layer thickness, and C is the experimental coefficient. The fitting $1/t$ is done by following the discussion described for the theoretical thickness dependency of $\chi^{(3)}_{\infty}$ [Paper B]. The value for the real part of the fitting coefficient is Re[C] = (5.82 ± 0.15) × 10^{-24} m^3/V^2, and the value for the imaginary part of the experimental coefficient is Im[C] = (9.34 ± 1.79) × 10^{-26} m^3/V^2. The theoretical value of the third-order susceptibility for bulk gold $\chi^{(3)}_{\infty}$ =

$(4.56 + 0.48i) \times 10^{-17}$ m^2/V^2 [24] is also shown in Fig. 4.11. The obtained experimental results confirm the effective enhancement of the third-order nonlinear susceptibility in the gold layers with nanoscale thickness. The values of the real part of the third-order susceptibility are approximately 4-5 times greater than the value of the real part of the third-order susceptibility for bulk gold at the wavelength 1064 nm [24]. The values of the imaginary part of the third-order susceptibility are approximately 1.5-2 times greater than the value of the imaginary part of the third-order susceptibility for bulk gold at the wavelength 1064 nm. Figure 4.12 also shows the limitations for experimental study of the third-order susceptibility $\chi_{Au}^{(3)}$ by using the method of the long-range surface plasmon polaritons. The standard Drude model based on Eq. (2.3)-(2.5) breaks down in the gold layers with the thickness below approximately 10 nm due to possible nonlocal effects [103-106], quantum effects [107-109], and the layers clustering [39, 40]. On the other side, the long-range surface plasmon polariton mode in the strip plasmonic waveguides breaks down at the gold layers thickness t above approximately 50-60 nm due to the small penetration depth of the electromagnetic field in the metal [110-112]. Therefore, the values of the gold layer thickness t applicable for experimental study of the third-order nonlinear susceptibility $\chi_{Au}^{(3)}$ of the gold layers are approximately in the range from 15 to 50 nm.

Table 4.4. Experimental values of the third-order susceptibility $\chi_{Au}^{(3)}$ of the gold layers with the thickness t = 22, 27, and 35 nm for 3-ps optical pulses at the wavelength 1064 nm.

t (nm)	Re[$\chi_{Au}^{(3)}$] (m^2/V^2)	Im[$\chi_{Au}^{(3)}$] (m^2/V^2)
22	$(2.57 \pm 0.84) \times 10^{-16}$	$(10.50 \pm 2.08) \times 10^{-18}$
27	$(2.18 \pm 0.61) \times 10^{-16}$	$(8.22 \pm 1.49) \times 10^{-18}$
35	$(1.79 \pm 0.48) \times 10^{-16}$	$(6.51 \pm 1.38) \times 10^{-18}$

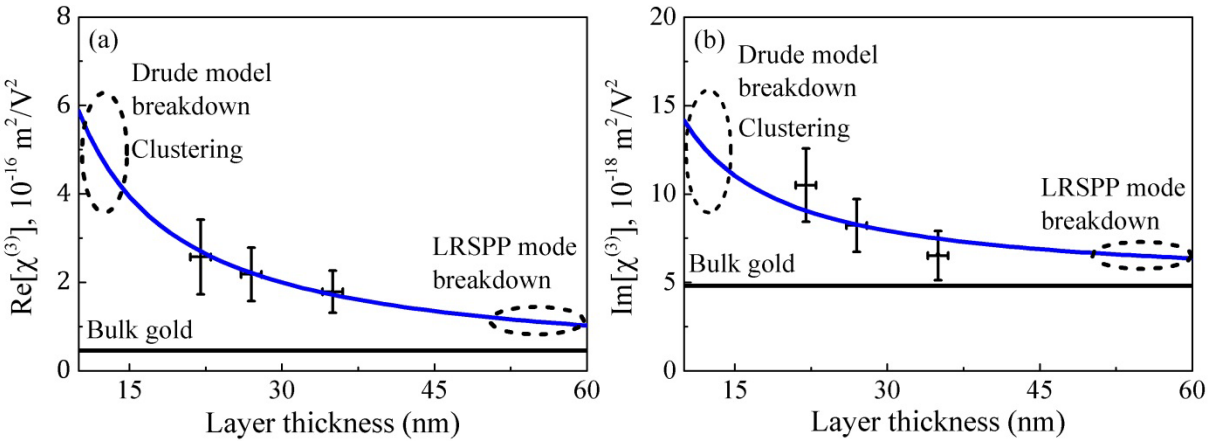

Figure 4.12. The real part (a) and imaginary part (b) of the third-order susceptibility $\chi^{(3)}_{\mathrm{Au}}$ of the gold layers with the thickness t = 22, 27, and 35 nm. The blue curves indicate the nonlinear curves fitting to the experimental data, according to Eq. (4.8). The black lines indicate the values of third-order susceptibility for bulk gold.

Figure 4.13 shows the obtained values of the imaginary part of the third-order susceptibility $\chi^{(3)}_{\mathrm{Au}}$ of gold for 200-fs laser pulses [Paper A], which are approximately one order of magnitude smaller than the values of the imaginary part of the third-order susceptibility $\chi^{(3)}_{\mathrm{Au}}$ of gold obtained earlier for 3-ps laser pulses [Paper C]. The experimental results also confirm the effective enhancement of the third-order nonlinear susceptibility for thinner gold layers: the values of the third-order susceptibility $\chi^{(3)}_{\mathrm{Au}}$ increase when the thickness t of the gold layers decreases (Table 4.5). The thickness dependence can be phenomenologically fitted, according to Eq. (4.8) as follows $\mathrm{Im}[\chi^{(3)}_{\mathrm{Au}}] = \mathrm{Im}[\chi^{(3)}_{\infty}] + D/t$, where $\mathrm{Im}[\chi^{(3)}_{\infty}]$ = 2.2 × 10^{-19} m^2/V^2 is the third-order nonlinear susceptibility for bulk gold at the wavelength 1030 nm, and for 200-fs laser pulses (Fig. 4.13, black line), and D = (5.8 ± 0.1) × 10^{-27} m^3/V^2 is the fitting coefficient. The value of the imaginary part of the third-order susceptibility $\mathrm{Im}[\chi^{(3)}_{\infty}]$ of bulk gold for 200-fs laser pulses was obtained by using the value of the imaginary part of the third-order susceptibility $\mathrm{Im}[\chi^{(3)}_{\infty}]$ of bulk gold for 3-ps

laser pulses and the theoretical pulse duration dependence [64]. The theoretical values of the third-order susceptibility $\chi^{(3)}_{Au}$ of the gold layers with the thickness t = 22, 27, and 35 nm, for 200-fs laser pulses and the wavelength 1030 nm are presented in Table 4.6. These values were obtained by using the experimental values of the third-order nonlinear susceptibility of the gold layers for 3-ps pulses [Paper C], and the theoretical pulse duration dependence (Fig. 2.12). The obtained theoretical values of the imaginary part of the third-order nonlinear susceptibility $\chi^{(3)}_{Au}$ agree well, within the measurement errors, with the obtained experimental results (Table 4.4), thus confirming the theoretical model.

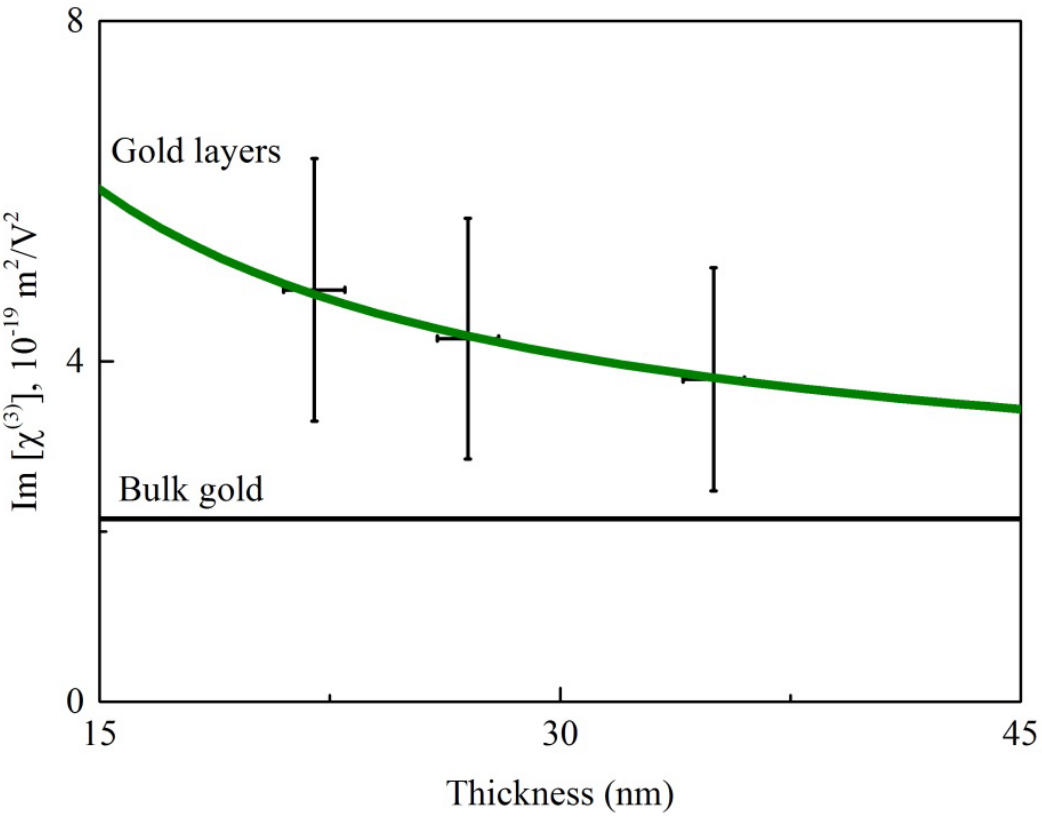

Figure 4.13. Imaginary part of the third-order susceptibility $\chi^{(3)}_{Au}$ of the gold layers with the thickness t = 22, 27, and 35 nm at the wavelength 1030 nm, and for 200-fs laser pulses. The green curve indicates the nonlinear curve fit to experimental data. The black line indicates the value of the third-order susceptibility for bulk gold.

Table 4.5. Experimental values of the imaginary part of the third-order susceptibility $\chi^{(3)}_{Au}$ of the gold layers with the thickness t = 22, 27, and 35 nm for 200-fs laser pulses at the wavelength 1030 nm.

t (nm)	Im[$\chi^{(3)}_{Au}$] (m^2/V^2)
22	$(4.8 \pm 1.6) \times 10^{-19}$
27	$(4.3 \pm 1.4) \times 10^{-19}$
35	$(3.8 \pm 1.3) \times 10^{-19}$

Table 4.6. Theoretical values of the third-order susceptibility $\chi^{(3)}_{Au}$ of the gold layers with the thickness t = 22, 27, and 35 nm for 200-fs laser pulses at the wavelength 1030 nm.

t (nm)	Re[$\chi^{(3)}_{Au}$] (m^2/V^2)	Im[$\chi^{(3)}_{Au}$] (m^2/V^2)
22	10.8×10^{-18}	4.4×10^{-19}
27	9.2×10^{-18}	3.5×10^{-19}
35	7.5×10^{-18}	2.7×10^{-19}
Bulk gold	1.9×10^{-18}	2.2×10^{-19}

Chapter 5

Conclusions and outlook

In this thesis the experimental and theoretical studies on nonlinear propagation of the long-range surface plasmon polaritons in the strip plasmonic waveguides have been presented. The effective third-order nonlinear susceptibility $\chi^{(3)}$ of the LRSPP mode is the central parameter for explanation of two nonlinear optical effects in the strip plasmonic waveguides, which were observed experimentally. The first effect is the nonlinear power saturation of the plasmonic mode, and the second effect is the spectral broadening and splitting of the plasmonic mode. The third-order nonlinear susceptibility $\chi^{(3)}_{\mathrm{Au}}$ of the gold layer in the strip plasmonic waveguides has the dominant contribution to the effective third-order nonlinear susceptibility $\chi^{(3)}$ of the long-range surface plasmon polariton mode. This has been verified for three values of gold layer thickness t = 22, 27 and 35 nm. The specific contribution from the gold layer is approximately two orders of magnitude greater than the specific contributions from tantalum pentoxide layers, and silica cladding in the case of 3-ps laser pulses, and at the wavelength 1064 nm [Paper C], and is approximately one order of magnitude greater than the specific contributions from tantalum pentoxide layers, and silica cladding in the case of 200-fs laser pulses, and at the wavelength 1030 nm [Paper A].

It has been shown theoretically and experimentally that the third-order nonlinear susceptibility $\chi^{(3)}_{\mathrm{Au}}$ of the gold layers significantly depends on the layer thickness t. The third-order nonlinear susceptibility $\chi^{(3)}_{\mathrm{Au}}$ of the gold layers increases when the layer thickness t decreases. In other words, thin metal layers provide effective enhancement of the third-order nonlinear susceptibility. The origin of this enhancement is explained by the change in the free electrons motion in the metal layers due to the confinement factor. The collision

frequency of electrons in the metal layer increases when the layer thickness *t* decreases. This leads to the increase of the dielectric permittivity of the metal layer. Consequently, this causes the effective increase of the third-order nonlinear susceptibility of the metal layer. However, the standard Drude breaks down as the metal layer thickness decreases to approximately 10 nm, due to possible nonlocal [41, 103-105], and quantum effects [50, 107-109], and the layer clustering process [39, 40]. On the other side, the long-range surface plasmon polariton mode in the strip plasmonic waveguides breaks down at the metal layer thickness above approximately 50-60 nm, due to the small penetration depth of electromagnetic field in the metal [113-115]. Thus, the effective range of the metal layer thickness in the strip plasmonic waveguides for experimental studies is approximately from 15 nm to 50 nm.

The third-order nonlinear susceptibility of gold also significantly depends on the laser pulse duration [25, 64]. It has been shown experimentally, and the theoretical discussion has been provided to explain this dependence [64]. In particular, the values of the imaginary part of the third-order nonlinear susceptibility of the gold layers with the thickness t = 22, 27, and 35 nm have been obtained from the experiments by using 3-ps optical pulses, and 200-fs optical pulses in the same wavelength region. The comparison of the obtained values shows that the third-order nonlinear susceptibility of gold increases by approximately one order of magnitude as the laser pulse duration increases from 200 fs to 3 ps. The origin of the pulse duration dependency of the third-order nonlinear susceptibility of gold is explained in terms of the electron temporal dynamics [23, 24, 116-119]. A picosecond laser pulse interacts with metal more strongly than a femtosecond laser pulse because of larger temporal overlap with the excited electron gas. Consequently, this leads to higher values of the real and imaginary parts of the third-order nonlinear susceptibility of gold for longer laser pulses. The proposed theoretical approach [64] correctly describe the scaling of the third-order nonlinear susceptibility, when going from 3 ps to 200

fs laser pulses that is an important advance for future numerical models of ultrafast pulses propagating in the strip plasmonic waveguides.

One of the possible developments in this direction is the nonlinear analysis of higher order plasmonic modes in the strip plasmonic waveguides. The presented theoretical model is for the fundamental long-range surface plasmon polariton mode, but other spatial plasmonic modes can also be excited. These higher order plasmonic modes will affect the propagation dynamics by nonlinear cross-phase modulation [34, 120-123].

Another possible development is the design of the strip plasmonic waveguides with particular dispersion properties. It has been shown that the zero-dispersion wavelength of the LRSPP mode in the strip plasmonic waveguides significantly depends on the gold layer thickness. In particular, the zero-dispersion wavelength at the telecom wavelength 1550 nm can be achieved for the strip plasmonic waveguides with the gold layer thickness t = 15 nm. The ZDW value for the plasmonic mode in the strip plasmonic waveguides decreases, when the thickness of the metal layer decreases. Thus, the wavelength range with anomalous-dispersion can be exploited toward excitation of solitons in the designed plasmonic waveguides, for instance, at telecom C-band wavelengths. This has interesting nonlinear applications that promise well for plasmonic systems.

Another possible development is the experimental study of the linear and nonlinear optical properties of the strip plasmonic waveguides with even thinner gold layers (around 10 nm). In this case, a complete hydrodynamic description, including nonlocal effects is required, which is especially important in nonlinear regime [124, 125]. The deviation from the Drude model may lead to higher values of the linear propagation loss of the LRSPP mode in the waveguides. The electron thermalization parameters of gold, in particular τ_{th} and τ_r can also depend on the metal thickness t for thinner gold layers. This, in turn will affect the effective third-order susceptibility for the strip plasmonic waveguides with

the metal layer thickness below 10 nm. The experimental studies of the Drude model breakdown conditions in the metal layers are important for future advances in communication approaches.

Another possible development is the theoretical and experimental studies of nonlinear optical properties of plasmonic waveguides with alternative plasmonic materials. These materials can be transparent conducting oxides (TCOs), and titanium nitride (TiN) [126-130]. For instance, TiN films exhibit a similarly large nonlinear optical response, comparing to Au films, and also are robust, cost-efficient, and compatible with the complementary metal-oxide-semiconductor (CMOS) technology. Thus, titanium nitride is a promising material for nonlinear applications [128].

The presented results on nonlinear optical properties of long-range surface plasmon polaritons in the gold strip waveguides can be exploited for the development and applications of active plasmonic and nanophotonic components.

References

1. M. Kauranin and A. V. Zayats, “Nonlinear plasmonics,” Nat. Photon. **6**, 737-748 (2012).

2. N. Rotenberg, M. Betz, and H. M. van Driel, “Ultrafast all-optical coupling of light to surface plasmon polaritons on plain metal surfaces,” Phys. Rev. Lett. **105**, 017402 (2010).

3. K. F. MacDonald, Z. L. Samson, M. I. Stockman, and N. I. Zheludev, “Ultrafast active plasmonics,” Nat. Photon. **3**, 55 (2009).

4. M. L. Brongersma and V. M. Shalaev, “The case for plasmonics”, Science, **328**, 440 (2010).

5. S. I. Bozhevolnyi, *Plasmonic Nanoguides and Circuits* (Pan Stanford, 2009).

6. A. V. Krasavin and A. V. Zayats, “Active nanophotonic circuitry based on dielectric-loaded plasmonic waveguides”, Adv. Opt. Mater. **3**, 1662 (2015).

7. D. K. Gramotnev and S. I. Bozhevolnyi, “Plasmonics beyond the diffraction limit”, Nat. Photonics, **4**, 2, 83 (2010).

8. V. A. Zenin, A. Andryieuski, R. Malureanu, I. P. Radko, V. S. Volkov, D. K. Gramotnev, A. V. Lavrinenko, and S. I. Bozhevolnyi, Nano Lett. **15**, 12, 8148 (2015), “Boosting local field enhancement by on-chip nanofocusing and impedance-matched plasmonic antennas”, Nano Lett. **15**, 12, 8148 (2015).

9. O. Krupin, H. Asiri, C. Wang, R. N. Tait, and P. Berini, “Biosensing using straight long-range surface plasmon waveguides”, Opt. Express **21**, 1, 698 (2013).

10. P. Berini, “Bulk and surface sensitivities of surface plasmon waveguides”, New J. Phys. **10**, 105010 (2008).

11. I. De Leon and P. Berini, “Amplification of long-range surface plasmons by a dipolar gain medium”, Nat. Photonics **4**, 382 (2010).

12. P. Berini and I. De Leon, “Surface plasmon-polariton amplifiers and lasers”, Nat. Photonics **6**, 16 (2012).

13. F. J. Diaz, G. Li, C. Martijn de Sterke, B. T. Kuhlmey, and S. Palomba, “Kerr effect in hybrid plasmonic waveguides”, J. Opt. Soc. Am. B **33**, 5, 957 (2016).

14. J. Diaz, T. Hatakeyama, J. Rho, Y. Wang, K. O’Brien, X. Zhang, C. Martijn de Sterke, B. T. Kuhlmey, and S. Palomba, “Sensitive method for measuring third order nonlinearities in compact dielectric and hybrid plasmonic waveguides”, Opt. Express **24**, 1, 545 (2016).

15. A. V. Krasavin, S. Randhawa, J.-S. Bouillard, J. Renger, R. Quidant, A. V. Zayats, “Optically-programmable nonlinear photonic component for dielectric-loaded plasmonic circuitry”, Opt. Express **19**, 25, 25222 (2011).

16. A. Degiron and D. R. Smith, “Nonlinear long-range plasmonic waveguides”, Phys. Rev. A **82**, 82, 033812 (2010).

17. J. B. Lassiter, X. Chen, X. Liu, C. Ciracì, T. B. Hoang, S. Larouche, S.-H. Oh, M. H. Mikkelsen, D. R. Smith, “Third-harmonic generation enhancement by film-coupled plasmonic stripe resonators”, ACS Photonics **1**, 1212 (2014).

18. I. De Leon, Z. Shi, A. C. Liapis, R. W. Boyd, “Measurement of the complex nonlinear optical response of a surface plasmon-polariton”, Opt. Lett. **39**, 8, 2274 (2014).

19. N. I. Zheludev, “The road ahead for metamaterials”, Science, **328**, 582 (2010).

20. A. D. Neira, N. Olivier, M. E. Nasir, W. Dickson, G. A. Wurtz, and A. V. Zayats, “Eliminating material constraints for nonlinearity with plasmonic metamaterials”, Nat. Commun. **6**, 7757 (2015).

21. P. Ginzburg, A. Krasavin, and A. Zayats, “Cascaded second-order surface plasmon solitons due to intrinsic metal nonlinearity,” New J. Phys. **15**, 013031 (2013).

22. K. A. O’Donnell and R. Torre, “Characterization of the second-harmonic response of a silver–air interface”, New J. Phys. **7**, 154 (2005).

23. M. Conforti and G. Della Valle, “Derivation of third-order nonlinear susceptibility of thin metal films as a delayed optical response,” Phys. Rev. B **85**, 245423 (2012).

24. A. Marini, M. Conforti, G. Della Valle, H. W. Lee, Tr. X. Tran, W. Chang, M. A. Schmidt, S. Longhi, P. St. J. Russell, and F. Biancalana, “Ultrafast nonlinear dynamics of surface plasmon polaritons in gold nanowires due to the intrinsic nonlinearity of metals,” New J. Phys. **15**, 013033 (2013).

25. R. W. Boyd, Z. Shi, and I. De Leon, “The third-order nonlinear optical susceptibility of gold”, Opt. Commun. **326**, 74 (2014).

26. D. D. Smith, Y. Yoon, R. W. Boyd, J. K. Campbell, L. A. Baker, R. M. Crooks, and M. George, “z-scan measurement of the nonlinear absorption of a thin gold film”, J. Appl. Phys. **86**, 11, 6200 (1999).

27. T. K. Lee, A. D. Bristow, J. Hübner, and H. M. van Driel, “Linear and nonlinear optical properties of Au–polymer metallodielectric Bragg stacks”, J. Opt. Soc. Am. B **23**, 10, 2142 (2006).

28. E. Xenogiannopoulou, P. Aloukos, S. Couris, E. Kaminska, A. Piotrowska, and E. Dynowska, “Third-order nonlinear optical properties of thin sputtered gold films”, Opt. Commun. **275**, 217 (2007).

29. N. Rotenberg, A. D. Bristow, M. Pfeiffer, M. Betz, and H. M. van Driel, “Nonlinear absorption in Au films: Role of thermal effects”, Phys. Rev. B **75**, 155426 (2007).

30. S. A. Maier, *Plasmonics: Fundamentals and Applications* (Springer, 2007).

31. V. Klimov, *Nanoplasmonics* (Pan Stanford, 2014).

32. I. H. Malitson, “Interspecimen comparison of the refractive index of fused silica,” J. Opt. Soc. Am. **55**, 10, 1205 (1965).

33. T. J. Bright, J. I. Watjen, Z. M. Zhang, C. Muratore, A. A. Voevodin, D. I. Koukis, D. B. Tanner, and D. J. Arenas, “Infrared optical properties of amorphous and nanocrystalline Ta_2O_5 thin films,” J. Appl. Phys. **114**, 083515 (2013).

34. G. P. Agrawal, *Nonlinear Fiber Optics* (Elsevier, 2013).

35. G. P. Agrawal, *Fiber-Optic Communication Systems* (Wiley, 2002).

36. D. Marcuse, *Light Transmission Optics* (Van Nostrand Reinhold, 1982).

37. Govind P. Agrawal and M. J. Potasek, “Nonlinear pulse distortion in single-mode optical fibers at the zero-dispersion wavelength”, Phys. Rev. A **33**, 1765 (1986).

38. C. Kittel, *Introduction to Solid State Physics* (Wiley, 2005).

39. J. A. Gordon and R. W. Ziolkowski, “The design and simulated performance of a coated nano-particle laser,” Opt. Express **15**, 5, 2622 (2007).

40. U. Kreibig and M. Vollmer, *Optical Properties of Metal Clusters* (Springer, 1995).

41. S. Raza, S. I. Bozhevolnyi, M. Wubs, and N. A. Mortensen, "Nonlocal optical response in metallic nanostructures," J. Phys. Condens. Matter **27**, 183204 (2015).

42. R. Malureanu and A. Lavrinenko, "Ultra-thin films for plasmonics: a technology overview," Nanotechnol. Rev. **4**, 3 (2015).

43. P. Yeh, *Optical Waves in Layered Media* (Wiley, 1988).

44. A. V. Zayats and S. A. Maier, *Active Plasmonics and Tunable Plasmonic Metamaterials* (Wiley, 2013).

45. I. E. Tamm, *Fundamentals of the Theory of Electricity* (Mir Publishers, 1979).

46. D. Milam, "Review and assessment of measured values of the nonlinear refractive-index coefficient of fused silica," Appl. Opt. **37**, 3, 546 (1998).

47. C. Y. Tai, J. S. Wilkinson, N. M. B. Perney, M. C. Netti, F. Cattaneo, C. E. Finlayson, and J. J. Baumberg, "Determination of nonlinear refractive index in a Ta_2O_5 rib waveguide using self-phase modulation," Opt. Express **12**, 21, 5110 (2004).

48. Z. Lin and L. V. Zhigilei, "Time-resolved diffraction profiles and atomic dynamics in short-pulse laser-induced structural transformations: Molecular dynamics study", Phys. Rev. B **73**, 184113 (2006).

49. C.-K. Sun, F. Vallée, L. H. Acioli, E. P. Ippen, and J. G. Fujimoto, "Femtosecond-tunable measurement of electron thermalization in gold", Phys. Rev. B **50**, 15337 (1994).

50. H. Qian, Y. Xiao, D. Lepage, L. Chen, and Z. Liu, “Quantum electrostatic model for optical properties of nanoscale gold films”, Nanophotonics **4**, 1, 413 (2015).

51. H. Raether, *Surface Plasmons on Smooth and Rough Surfaces and on Gratings* (Springer, 1988).

52. D. J. Griffiths, *Introduction to Electrodynamics* (Prentice-Hall, 1999).

53. A. Baron, T. B. Hoang, C. Fang, M. H. Mikkelsen, and D. R. Smith, “Ultrafast self-action of surface-plasmon polaritons at an air/metal interface,” Phys. Rev. B **91**, 195412 (2015).

54. R. Boyd, *Nonlinear Optics* (Academic Press, 2008).

55. A. Baron, S. Larouche, D. J. Gauthier, and D. R. Smith, “Scaling of the nonlinear response of the surface plasmon polariton at a metal/dielectric interface”, J. Opt. Soc. Am. B **32**, 1, 9 (2015).

56. Q. Lin, O. J. Painter, and G. P. Agrawal, “Nonlinear optical phenomena in silicon waveguides: Modeling and applications,” Opt. Express **15**, 25, 16604 (2007).

57. L. Yin and G. P. Agrawal, “Impact of two-photon absorption on self-phase modulation in silicon waveguides,” Opt. Lett. **32**, 14, 2031 (2007).

58. O. Boyraz, T. Indukuri, and B. Jalali, “Self-phase-modulation induced spectral broadening in silicon waveguides”, Opt. Express **12**, 5, 829 (2004).

59. E. Dulkeith, Y. A. Vlasov, X. Chen, N. C. Panoiu, and R. M. Osgood, Jr., “Self-phase-modulation in submicron silicon-on-insulator photonic wires”, Opt. Express **14**, 12, 5524 (2006).

60. H. K. Tsang, C. S. Wong, T. K. Liang, I. E. Day, S. W. Roberts, A. Harpin, J. Drake, and M. Asghari, "Optical dispersion, two-photon absorption and self-phase modulation in silicon waveguides at 1.5 μ m wavelength", Appl. Phys. Lett. **80**, 416 (2002).

61. Q. Lin, J. Zhang, G. Piredda, R. W. Boyd, P. M. Fauchet, G. P. Agrawal, "Dispersion of silicon nonlinearities in the near infrared region", Appl. Phys. Lett. **91**, 021111 (2007).

62. J. R. Melcher, *Continuum Electromechanics* (MIT Press, 1981).

63. P. Penfield, Jr. and H. A. Haus, *Electrodynamics of Moving Media* (MIT Press, 1967).

64. M. Bache, DTU Fotonik, Technical University of Denmark, 2800 Kongens Lyngby (personal communication, 2016).

65. PhoeniX Software, http://www.phoenixbv.com.

66. M. Feldman, *Nanolithography: The Art of Fabricating Nanoelectronic and Nanophotonic Devices and Systems* (Woodhead Publishing, 2014).

67. S. Landis, *Nano-lithography* (Wiley, 2013).

68. SUSS MicroTec, https://www.suss.com.

69. Nikon Metrology, http://www.nikonmetrology.com.

70. Kurt J. Lesker Company, http://www.lesker.com.

71. Carl Zeiss Company, http://www.zeiss.com.

72. J. Goldstein, *Scanning Electron Microscopy and X-ray Microanalysis* (Springer, 2003).

73. Bruker Company, https://www.bruker.com.

74. P. Eaton and P. West, *Atomic Force Microscopy* (Oxford University Press, 2010).

75. O. Geschke, H. Klank, and P. Telleman, *Microsystem Engineering of Lab-on-a-Chip Devices* (Wiley, 2004).

76. A. Maradudin, *Light Scattering and Nanoscale Surface Roughness* (Springer, 2007).

77. H. Raether, *Surface Plasmons on Smooth and Rough Surfaces and on Gratings* (Springer, 1988).

78. John A. Woollam Company, https://www.jawoollam.com.

79. H. G. Tompkins and E. A. Irene, *Handbook of Ellipsometry* (William Andrew, 2005).

80. A. Boltasseva, *Integrated Optics Components Utilizing Long-Range Surface Plasmon Polaritons* (PhD thesis, Technical University of Denmark, 2004).

81. S. I. Bozhevolnyi, A. Boltasseva, T. Søndergaard, T. Nikolajsen, and K. Leosson, “Photonic bandgap structures for long-range surface plasmon polaritons”, Opt. Commun. **250**, 328 (2005).

82. A. Boltasseva, T. Nikolajsen, K. Leosson, K. Kjaer, M. S. Larsen, and S. I. Bozhevolnyi, “Integrated optical components utilizing long-range surface plasmon polaritons”, J. Lightwave Technol. **23**, 1, 413 (2005).

83. A. Boltasseva, T. Søndergaard, T. Nikolajsen, K. Leosson, S. I. Bozhevolnyi, and J. M. Hvam, "Propagation of long-range surface plasmon polaritons in photonic crystals," J. Opt. Soc. Am. B **22**, 9, 2027 (2005).

84. NKT Photonics Company, http://www.nktphotonics.com.

85. Thorlabs Company, http://www.thorlabs.com.

86. Newport Company, https://www.newport.com.

87. R. Charbonneau, P. Berini, E. Berolo and E. Lisicka-Shrzek, “Experimental observation of plasmon–polariton waves supported by a thin metal film of finite width,” Opt. Lett. **25**, 11, 844 (2000).

88. T. Nikolajsen, K. Leosson, I. Salakhutdinov, S. I. Bozhevolnyi, “Polymer-based surface plasmon polariton stripe waveguides”, Appl. Phys. Lett. **82**, 5, 668 (2003).

89. K. Leosson, T. Nikolajsen, A. Boltasseva, S. I. Bozhevolnyi, “Long-range surface plasmon polariton nanowire waveguides for device applications”, Opt. Express **14**, 1, 314 (2006).

90. R. Hunsperger, *Integrated Optics: Theory and Technology* (Springer, 2002).

91. Yokogawa Meters and Instruments Company, http://tmi.yokogawa.com.

92. T. Nikolajsen, K. Leosson, and S. I. Bozhevolnyi, “In-line extinction modulator based on long-range surface plasmon polaritons,” Opt. Commun. **244,** 455 (2005).

93. A. Boltasseva, S. I. Bozhevolnyi, “Directional couplers using long-range surface plasmon polariton waveguides,” IEEE J. Sel. Topics Quantum Electron. **12**, 6, 1233 (2006).

94. P. Berini, R. Charbonneau, N. Lahoud and G. Mattiussi, “Characterization of long-range surface-plasmon-polariton waveguides,” J. Appl. Phys. 98, 043109 (2005).

95. R. Charbonneau, C. Scales, I. Breukelaar, G. Mattiussi and P. Berini, “Passive integrated optics elements based on long-range surface plasmon polaritons,” J. Lightwave Technol. **24**, 1, 477 (2006).

96. P. Berini, "Plasmon–polariton waves guided by thin lossy metal films of finite width: bound modes of symmetric structures," Phys. Rev. B **61**, 10484 (2000).

97. P. Berini, "Plasmon–polariton modes guided by a metal film of finite width," Opt. Lett. **24**, 15, 1011 (1999).

98. R Buckley and P. Berini, "Figures of merit for 2D surface plasmon waveguides and application to metal stripes," Opt. Express **15**, 19, 12174 (2007).

99. Light Conversion Company, http://www.lightcon.com.

100. P. Berini, “Long-range surface plasmon polaritons,” Adv. Opt. Photon. **1**, 3, 484 (2009).

101. Watec Company, http://www.wateccameras.com.

102. R. Charbonneau, N. Lahoud, G. Mattiussi, and P. Berini, “Demonstration of integrated optics elements based on long-ranging surface plasmon polaritons”, Opt. Express **13**, 3, 977 (2005).

103. N. A. Mortensen, “Nonlocal formalism for nanoplasmonics: Phenomenological and semi-classical considerations”, Phot. Nano. Fund. Appl. **11**, 303 (2013).

104. N. A. Mortensen, S. Raza, M. Wubs, T. Søndergaard, and S. I. Bozhevolnyi, “A generalized non-local optical response theory for plasmonic nanostructures”, Nat. Commun. 5, 3809 (2014).

105. T. Christensen, W. Yan, S. Raza, A.-P. Jauho, N. A. Mortensen, and M. Wubs, “Nonlocal response of metallic nanospheres probed by light, electrons, and atoms”, ACS Nano **8**, 1745 (2014).

106. A. Maradudin, J. Sambles, and W. Barnes, *Modern Plasmonics* (Elsevier, 2014).

107. F. Hache, D. Ricard, and C. Flytzanis, “Optical nonlinearities of small metal particles: surface-mediated resonance and quantum size effects”, J. Opt. Soc. Am. B **3**, 12, 1647 (1986).

108. Z. Liu, Y. Xiao, and H. Qian, “Investigations of the optical properties of nanoscale gold films,” in *Advanced Photonics 2015*, OSA Technical Digest (Optical Society of America, 2015), paper NM4C.1.

109. W. B. Su, C. S. Chang, and T. T. Tsong, “Quantum size effect on ultra-thin metallic films”, J. Phys. D: Appl. Phys. **43**, 013001 (2010).

110. M. Brongersma, *Surface Plasmon Nanophotonics* (Springer, 2007).

111. M. Dressel and G. Gruner, *Electrodynamics of Solids* (Cambridge University Press, 2002).

112. A. V. Zayats, I. I. Smolyaninov, and A. A. Maradudin, “Nano-optics of surface plasmon polaritons”, Phys. Repts. **408**, 131 (2005).

113. L.D. Landau and E.M. Lifshitz, *Electrodynamics of Continuous Media* (Pergamon Press, 1960).

114. J. D. Jackson, *Classical Electrodynamics* (Wiley, 1962).

115. T. Tamir, *Guided-Wave Optoelectronics* (Springer, 1988).

116. A. Marini and F. Biancalana, “Ultrashort self-induced transparency plasmon solitons”, Phys. Rev. Lett. **110**, 243901 (2013).

117. J. K. Chen, D. Y. Tzou, and J. E. Beraun, “A semiclassical two-temperature model for ultrafast laser heating”, Int. J. Heat Mass Transf. **49**, 307 (2006).

118. J. K. Chen, J. E. Beraun, “Numerical study of ultrashort laser pulse interactions with metal films”, Numer. Heat Tr. A-Appl. **40,** 1 (2001).

119. N. Del Fatti, R. Bouffanais, F. Vallée, and C. Flytzanis, “Nonequilibrium electron interactions in metal films”, **81**, 4, 922 (1998).

120. Y. S. Kivshar and G. P. Agrawal, *Optical Solitons: From Fibers to Photonic Crystals* (Elsevier, 2003).

121. G. P. Agrawal, *Applications of Nonlinear Fiber Optics* (Academic Press, 2001).

122. G. P. Agrawal, *Lightwave Technology: Telecommunication Systems* (Wiley, 2001).

123. H. M. Gibbs, *Optical Bistability: Controlling Light with Light* (Academic Press, 1985).

124. P. Ginzburg, A. V. Krasavin, G. A. Wurtz, and A. V. Zayats, “Nonperturbative hydrodynamic model for multiple harmonics generation in metallic nanostructures”, ACS Photonics **2**, 8 (2015).

125. A. V. Krasavin, P. Ginzburg, G. A. Wurtz, and A. V. Zayats, “Nonlocality-driven supercontinuum white light generation in plasmonic nanostructures”, Nat. Comm. **7**, 11497 (2016).

126. G. V. Naik, V. M. Shalaev, and A. Boltasseva, “Alternative plasmonic materials: beyond gold and silver,” Adv. Mater. **25,** 24, 3264 (2013).

127. N. Kinsey, M. Ferrera, C. DeVault, J. Kim, V. M. Shalaev, and A. Boltasseva, "Nanophotonics with Titanium Nitride and Transparent Conducting Oxides," in *Advanced Photonics 2015*, OSA Technical Digest (Optical Society of America, 2015), paper IW1A.4.

128. N. Kinsey, S. Akbar Ali, D. Courtwright, C. DeVault, C. E. Bonner, V. I. Gavrilenko, V. M. Shalaev, D. J. Hagan, E. W. Van Stryland, and A. Boltasseva, “Effective third-order nonlinearities in metallic refractory titanium nitride thin films, ” Opt. Mater. Express **5**, 11, 2395 (2015).

129. M. Z. Alam, I. De Leon, and R. W. Boyd, “Large optical nonlinearity of indium tin oxide in its epsilon-near-zero region,” Science **352**, 795 (2016).

130. L. Caspani, R. P. M. Kaipurath, M. Clerici, M. Ferrera, T. Roger, J. Kim, N. Kinsey, M. Pietrzyk, A. Di Falco, V. M. Shalaev, A. Boltasseva, and D. Faccio, “Enhanced nonlinear refractive index in ε-near-zero materials,” Phys. Rev. Lett. **116**, 233901 (2016).

Paper A

O. Lysenko, N. Olivier, M. Bache, A. V. Zayats, and A. Lavrinenko

Nonlinear dynamics of long-range surface plasmon polaritons in gold strip waveguides

(submitted).

Letter

optica

Nonlinear dynamics of ultrafast long-range surface plasmon polaritons in gold strip waveguides

OLEG LYSENKO,[1,*] NICOLAS OLIVIER,[2] MORTEN BACHE,[1] ANATOLY V. ZAYATS,[2] AND ANDREI LAVRINENKO[1]

[1]*DTU Fotonik, Department of Photonics Engineering, Technical University of Denmark, 2800 Kongens Lyngby, Denmark*
[2]*Department of Physics, King's College London, Strand, London WC2R 2LS, UK*
**Corresponding author: ollyse@fotonik.dtu.dk*

Received XX Month XXXX; revised XX Month, XXXX; accepted XX Month XXXX; posted XX Month XXXX (Doc. ID XXXXX); published XX Month XXXX

We study nonlinear dynamics of ultrafast long-range surface plasmon polaritons in gold strip waveguides. The nonlinear absorption of the plasmons is measured with femtosecond pulses revealing a strong dependence of the imaginary part of the third-order nonlinear susceptibility of gold on the pulse duration and layer thickness. This dependence is consistent with a delayed nonlinear response modeled by a temporal response function when describing the hot-electron temporal dynamics in gold. We report the nonlinear coefficients and scaling laws required for modeling of the ultrafast nonlinear dynamics in nanometer-scale gold waveguides. The results are important for the development of active plasmonic and nanophotonic components.

OCIS codes: *(250.5403) Plasmonics; (230.7370) Waveguides; (190.4400) Nonlinear optics, Materials; (240.6680) Surface plasmons.*

http://dx.doi.org/10.1364/optica.99.099999

Plasmonic nanostructures represent a unique platform for many linear and nonlinear optical applications [1]. A great variety of plasmonic waveguides for integrated optics [2,3], nanofocusing [4,5], sensing [6], lasing and amplification of light [7] has been proposed. In particular, special attention has recently been paid to the nonlinear optical properties of plasmonic waveguides, hybrid plasmonic waveguides, and other elements important for future nanophotonic communication approaches [8-10]. Bulk metals, thin metal layers, and plasmonic metamaterials have been investigated in the nonlinear regime [11].

The nonlinear propagation of surface plasmon polaritons (SPPs) in plasmonic waveguides can be studied in terms of either the second- [12] or the third-order [13] nonlinearity. The latter is particularly important because it is present in all materials. In metals it arises due to hot-electron contributions from changes of the intrinsic electronic temperature after absorption of the incident light. Typically, the electron relaxation time in noble metals is on the few-picosecond scale [13], implying that their nonlinear susceptibility is directly affected by the light pulse duration [14]. The majority of the data on the third-order nonlinear susceptibility of gold were collected near the interband transitions in a wavelength range of 532-630 nm for pulse durations between 100 fs and 1 ns [14]. Most of the results were obtained with the z-scan method, reporting very high values of the third-order susceptibility in the range of 10^{-16}-10^{-15} m^2/V^2 [15-18]. However, the linear losses in plasmonic waveguides, which are also related to the same interband transitions in gold, are very high (~30-40 dB/mm) in this wavelength range [2].

On the other hand, nanophotonic and plasmonic devices are extensively exploited in the infrared (IR) range [2,3]. The propagation losses of long-range SPPs (LRSPPs) in Au-based waveguides can be ~2-5 dB/mm at the telecommunication wavelengths. Meanwhile, the third-order susceptibility of gold, $\chi^{(3)}_{Au}$, in the IR range arises mainly from hot-electron contributions from intraband electron transitions and is much smaller than in the visible range [11]. As such a conventional z-scan method may be not sensitive enough for nonlinear measurements in ultrathin gold layers. Nevertheless, the values of $\chi^{(3)}_{Au}$ can be quite large to affect the signal propagation in a LRSPP waveguide due to the field localization near the metal interfaces and long propagation distance L_{SPP}.

By the virtue of its origin and the SPP's field localization, the effective nonlinear susceptibility of a gold strip waveguide will depend on the pulse duration and thickness of the constituent gold layer. The goal of this Letter is to quantify such dependences adopting experimental and theoretical results on nonlinear propagation of the LRSPP mode conditioned by the third-order nonlinear susceptibility of gold [19,20]. We measure the nonlinear absorption of the LRSPP waveguides, and extract the experimental values of the imaginary part of the third-order susceptibility of gold, $\mathrm{Im}[\chi^{(3)}_{Au}]$, for 200-fs pulses at a wavelength of 1030 nm. Since the same waveguides were also characterized in the same spectral range with 3-ps pulses [19], the data can be directly compared to obtain an experimental dependence of $\mathrm{Im}[\chi^{(3)}_{Au}]$ on the gold layer thickness and pulse durations in the femtosecond-picosecond range. The obtained dependences confirm a significant increase in nonlinearity for picosecond pulses over femtosecond ones due to the better temporal overlap of the longer laser pulse with the transient profile of the excited hot-electron gas. Our data confirm that the delayed thermal response function of gold [13,21] is the key parameter in modeling of the ultrashort LRSPP propagation with a nonlinear Schrödinger equation, having just a single free parameter in the cw value of the nonlinearity. We also report scaling laws describing the enhanced nonlinearity in the nanometer-thin gold waveguides.

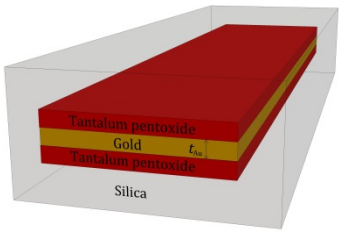

Fig. 1. Sketch (not to scale) of the plasmonic waveguide.

The LRSPP waveguides studied here were fabricated as described in [19]. They contain a thin gold layer of different thickness t_{Au} (22, 27 and 35 nm) sandwiched between tantalum pentoxide adhesion layers and silicon dioxide (silica) cladding (Fig. 1). This symmetric arrangement provides a substantial effective propagation length of LRSPPs of about 0.5-1 mm at a wavelength of 1030 nm depending on t_{Au}.

The experimental setup is described in Supplement 1. 200-fs pulses at a wavelength of 1030 nm were used to couple to LRSPPs. The linear propagation loss of the waveguides increases by a factor of 2 as the gold layer thickness increases from 22 nm to 35 nm, in agreement with what was measured at a wavelength of 1064 nm [19]. At the same time, the end-fire coupling loss per two (in- and out-coupling) facets of the waveguides changes insignificantly. The obtained values for the linear propagation loss per unit length α at 1030 nm are about 10% higher than the corresponding values at 1064 nm [19] as expected for the reduction of material (Ohmic) losses with the wavelength [2]. Although the values of the coupling loss C for the free-space lens coupling are around 7 dB per two facets, i.e., approximately 3 dB higher than the corresponding values for the fiber coupling [19], the free-space coupling method used here is preferred to exclude dispersion effects when operating with femtosecond pulses.

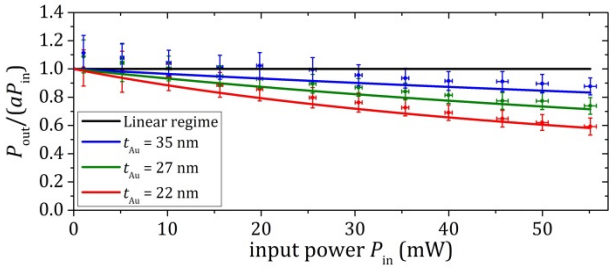

Fig. 2. Experimentally measured nonlinear transmission dependences using 200 fs pulses at 1030 nm in plasmonic waveguides with different gold layer thickness t_{Au}. The black line corresponds to the linear regime and the colored lines are fits to the experimental data.

The nonlinear propagation of the LRSPP mode in the waveguides was characterized by tuning the average input power P_{in} in the range 1-55 mW (see Supplement 1). The electron thermalization rate in metal is much greater than the laser repetition rate of the experiment (200 kHz), implying that each laser pulse interacts individually. The linear and nonlinear losses of the LRSPP mode are traditionally modeled by the equation $\partial_z P = -\alpha P - \beta P^2$, where β is the nonlinear loss parameter. The nonlinear power equation for the LRSPP mode is expressed as $P_{out}/(aP_{in}) = 1/[1 + \beta L_{eff} P_{in} e^{-C/2}/(\sqrt{\pi} T_0 f_{rep})]$ [20], where P_{out} is the average power after the waveguide, $L_{eff} = [1 - \exp(-\alpha L)]/\alpha$ is the effective propagation length, L is the physical length of the waveguides, T_0 is the pulse duration, f_{rep} is the laser repetition rate, and $a = e^{-(\alpha L + C)}$ is the experimental coefficient that contains the linear propagation loss α and coupling loss C. The nonlinear dependences of transmitted power P_{out} with respect to input power P_{in} for the waveguides with the length L = 2 mm, and the gold layer thickness t_{Au} = 22, 27, and 35 nm are shown in Fig. 2. The deviation from the horizontal line $P_{out} = aP_{in}$ is an indication of the two-photon absorption effect represented by the nonlinear parameter β. The nonlinear curve fits are fitted using β as the only free parameter and starting from unity at P_{in}=0 for consistency of the linear and nonlinear regimes.

The only contribution to the nonlinear loss in the waveguides comes from the gold layer because the photon energy at 1030 nm is far below half of the bandgap energy for silica and tantalum pentoxide. Thus, the nonlinear parameter β is directly connected to the imaginary part of the third-order susceptibility of the gold layers as $\beta \approx (3\omega\theta_{Au}\,\mathrm{Im}[\chi^{(3)}_{Au}])/(2\varepsilon_0 c^2 n_0^2 A_{eff})$, where $\omega = 2\pi c/\lambda$ is the light angular frequency, c is the vacuum speed of light, ε_0 is the vacuum permittivity, n_0 is the effective linear refractive index of the LRSPP mode [20], θ_{Au} is the field localization parameter of the gold layer [20], and A_{eff} is the effective area of the LRSPP mode [20].

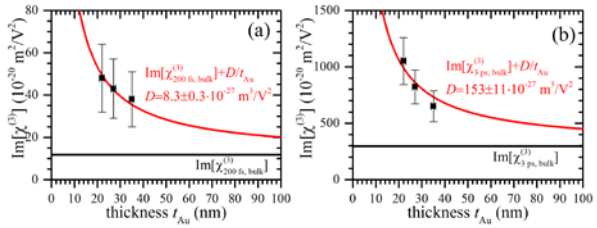

Fig. 3. Experimental data for the imaginary part of the third-order susceptibility vs gold thickness using (a) 200 fs pulses at 1030 nm and (b) 3 ps pulses at 1064 nm [19], fitted to a $1/t_{Au}$ dependence (red lines). The bulk gold value is indicated in each case (black lines).

The layers thickness t_{Au} influences the nonlinear parameter β via the field localization integrals θ_{Au} (whose values increase with t_{Au}) and mode effective areas (whose values decrease with t_{Au}) [20]. After excluding these dependences, the effective enhancement of $\mathrm{Im}[\chi^{(3)}_{Au}]$ for thin gold layers is shown in Fig. 3(a). The fit to experimental data is given by $\mathrm{Im}[\chi^{(3)}_{Au}] = \mathrm{Im}[\chi^{(3)}_{200\ fs,\ bulk}] + D/t_{Au}$ [19,20] where $\mathrm{Im}[\chi^{(3)}_{200\ fs,\ bulk}]$ = 12 × 10^{-20} m^2/V^2 is the value for bulk gold for 200 fs pulses as calculated from Eq. (4) below, and D = 8.3 ± 0.3·10^{-27} m^3/V^2 is the fitting parameter. This confirms the $1/t_{Au}$ dependence [20]. The obtained nonlinear values for 200 fs pulses are an order of magnitude smaller than the ones measured earlier for 3 ps pulses [19], which we show for comparison in Fig. 3(b). Here the fit to experimental data for consistency is recalculated to give D = 153 ± 11·10^{-27} m^3/V^2 by using an updated value of bulk gold susceptibility at 3 ps (again using Eq. (4) below).

The third-order susceptibility for bulk gold for different pulse durations was calculated with the two-temperature model (TTM) of electron temporal dynamics [13, 21]. For pulse durations longer than the electron-electron scattering rate (above 10 fs), the third-order susceptibility of metal originates from the thermo-modulational interaction between the laser pulse and thermalized gas of hot electrons that builds up in metal due to the absorbed power of the laser pulse. The TTM equations can be solved analytically (see Supplement 1). The results in Fig. 4 illustrate how short laser pulses first generate nonthermalized (out of equilibrium) hot electrons, which cannot be described by the electron temperature, which are then converted to thermalized (described by the elevated electronic temperature) electrons. Initially the pulse energy, taken here as a Gaussian

pulse $P(\tau) = P_0 \exp(-\tau^2 / T_0^2)$, is absorbed by the metal, which in our case happens almost instantly, i.e., the mean absorbed power density $P_A \propto P(t)$ as a consequence of being in the IR where the dielectric constant has insignificant dispersion. The absorbed power builds up the non-thermalized electron energy density according to $N(t) = h_{th} * P_A = \int_{-\infty}^{\infty} dt' h_{th}(t-t') P_A(t')$, i.e., the convolution of the mean absorbed power and the "thermalization" temporal response function $h_{th}(t) = \Theta(t)\tau_{th}^{-1} e^{-t/\tau_{th}}$, where $\Theta(t)$ is the Heaviside step function. The rise of the non-thermalized electron density is slightly delayed, caused by losses as they decay to the lattice and thermal electrons with a "total" decay time τ_{th} (300 fs in gold [13]). To model the temperature of the thermalized electrons, it is a good approximation to take the lattice temperature constant, and only model the temperature deviation of the thermal electrons with the "ground state", i.e., the lattice value. This is given by $\Delta T_e(t) \propto h_T * P_A$ as the convolution of the mean absorbed power with the "temperature" temporal response function $h_T(t) = \Theta(t)(\tau_{th} - \tau_r)^{-1}(e^{-t/\tau_{th}} - e^{-t/\tau_r})$, where τ_r is the relaxation time of the thermalized electrons to the lattice (1 ps in gold [13]). We note that $\Delta T_e(t) \propto h_T(t)$ in the short-pulse limit; thus on the leading edge of the laser pulse the rise in temperature is governed by the 300 fs decay time of the non-thermalized electrons while on the trailing edge it is governed by the thermalized electron relaxation time making it dissipate on 6-7 ps timescale. Instead in the long-pulse limit $\Delta T_e(t) \propto P_A(t) \propto P(t)$; thus the "slow" time scales of the electron dynamics become too fast for the slow leading and trailing edges of the laser pulse to experience any effects of the delayed responses and the laser pulse therefore experiences a quasi-instantaneous nonlinear response from the hot electrons.

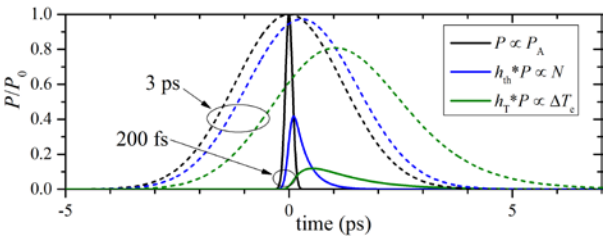

Fig. 4. Results from the two-temperature model of electron temporal dynamics in bulk gold for a 200 fs (full) and 3 ps pulses (dashed).

We apply the TTM to model the cubic nonlinear response of metal via the hot-electron temporal dynamics described by ΔT_e, which depends on the absorbed power and, therefore, is a nonlinear process. To see how this delayed temporal dynamics of ΔT_e affects the nonlinear response of gold, we use the IR wavelengths, far away the strongly dispersive interband transitions. The dynamics is well governed by the following nonlinear Schrödinger equation [13]:

$$(i\partial_\zeta + \hat{D}_\tau + i\tfrac{\alpha}{2})A + (\gamma_{cw} + i\beta_{cw})A[h_T * |A|^2] = 0, \qquad (0)$$

where $\gamma_{cw} \propto \mathrm{Re}(\chi^{(3)}_{cw})$ and $\beta_{cw} \propto \mathrm{Im}(\chi^{(3)}_{cw})$ as we shall see below are the nonlinear parameters in the long-pulse (cw) limit, $\hat{D}_\tau$ accounts for chromatic dispersion, and we have for simplicity neglected self-steepening and contributions from the cladding materials to the nonlinearity. The contribution from nonthermalized electrons to Eq. (1) comes from the response function h_T. Therefore, the nonthermalized electrons are an intermediate stage between the power absorption and appearance of the thermalized electrons, with the latter being the key aspect for the nonlinear response. The field is normalized so $|A|^2 = P$ in watts, and for the loss we need to retain only the imaginary part:

$$(\partial_\zeta + \hat{D}_\tau + \alpha)P + \beta_{cw} P[h_T * P] = 0. \qquad (0)$$

In the cw limit this becomes $\partial_\zeta P = -\alpha P - \beta_{cw} P^2$, with solution $P(\zeta,\tau) = P_0(\tau) e^{-\alpha\zeta}[1 + \beta_{cw} L_{eff} P_0(\tau)]$, where $P_0(\tau)$ is the power at $\zeta = 0$. This is exactly the basic equation we used to fit our data above.

The key step is now to deduce a similar expression for short pulses, especially on the femtosecond scale. The chromatic dispersion can be neglected for the waveguide lengths and pulse durations considered here, so if we then approximate $P[h_T * P] \simeq \rho(T_0)P^2$, Eq. (2) becomes

$$\begin{cases} \partial_\zeta P \simeq -\alpha P - \beta'(T_0) P^2, \\ \beta'(T_0) = \rho(T_0)\beta_{cw}, \\ \rho(T_0) = P_0^{-2} \max(P[h_T * P]), \end{cases} \qquad (0)$$

which is indeed equivalent to the standard equation with a "corrected" nonlinearity $\beta'(T_0)$. The correction factor $\rho(T_0)$ describes the deviation from the cw limit due to the non-instantaneous thermal response. Obviously, it depends strongly on the input pulse duration T_0 and pulse shape, and $\rho(T_0) \to 1$ in the cw limit. Note that since $P[h_T * P] \propto P(t)\Delta T_e(t)$, the correction factor is mainly affected by a temporal overlap between the laser pulse and the excited hot-electron gas. Equation (3) assumes that the temporal shape of $P[h_T * P]$ overlaps with $\rho(T_0)P^2$. We checked that even for very short pulses this assumption is justified, apart from a small femtosecond delay.

The introduction of the correction factor allows us to propose the following equation to predict the measured experimental imaginary nonlinear susceptibility data

$$\mathrm{Im}[\chi^{(3)}(\omega_0, T_0, t_{Au})] = \rho(T_0)(\mathrm{Im}[\chi^{(3)}_{cw,bulk}(\omega_0)] + D_{cw} / t_{Au}), \qquad (0)$$

where t_{Au} is the gold layer thickness in m. $\chi^{(3)}_{cw,bulk}(\omega_0)$ is the cw bulk value at the laser frequency ω_0, calculated e.g., theoretically as in [13] or determined experimentally. In lack of the latter, in what follows we use the theoretical value $\mathrm{Im}[\chi^{(3)}_{cw,bulk}(1030\ \mathrm{nm})] = 430 \times 10^{-20}\ \mathrm{m}^2/\mathrm{V}^2$.

We can now directly compare the values of the nonlinear susceptibility measured here with 200 fs 1030 nm pulses and those of [19] using 3 ps 1064 nm pulses. This is justified by the fact that both the wavelengths are far from the interband transitions, but very close to each other [13]. We calculated the correction factors for Gaussian-shaped input pulses in range from 10 fs to 10 ps, and as a first test of the validity of Eq. (4), we show in Fig. 5(a) that the relation $D = \rho(T_0) D_{cw}$ indeed holds. Here we used the cw fitting parameter as a free parameter and the experimental data are quite well expressed by the theoretical curve for $D_{cw} = 220 \times 10^{-27}\ \mathrm{m}^3/\mathrm{V}^2$ (accurate within 10%). Now Eq. (4) can be used to check the relations between the measurements at the two different pulse durations for each of the 3 waveguide thicknesses, which is shown in Fig. 5(b). We see that for all three values of the gold layer thickness, Eq. (4) represents quantitatively the measured data, thus further justifying the introduction of the correction factor but importantly also validating the theoretical value of the cw bulk nonlinearity. A similar relation as Eq. (4) exists for the real part of the nonlinear susceptibility, governing self-phase modulation effects, and future experiments are needed to find its experimental parameters.

The predicted variation of the imaginary part of the third-order susceptibility of gold monotonically spans over about 4 orders of magnitude as the pulse duration changes from 10 fs to 10 ps. The obtained pulse duration dependences are in agreement with previous studies [14],

where the experimental values of $\chi^{(3)}_{Au}$ for bulk gold were summarized from different experiments. Such a variation of the nonlinearity with respect to the signal pulse duration is due to the nonlinearity having only delayed nonlinear contributions, and this can be one of the principal advantages of free-electron nonlinearities in plasmonic waveguides compared to conventional dielectric nonlinearities for the realization of nanophotonic components.

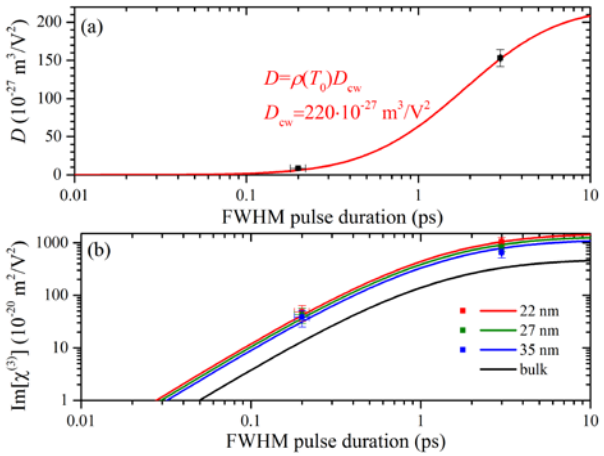

Fig. 5. (a) Pulse duration dependence of the experimental fitting parameters from Fig. 3. The theoretical curve was calculated using $\rho(T_0)$ from Eq. (3) for a Gaussian pulse and taking D_{cw} as a free parameter. (b) The imaginary part of the third-order susceptibility of gold layers with different thicknesses (22, 27, and 35 nm) and bulk gold vs pulse duration on a log-log plot. The experimental data (symbols) were measured at 1030 nm and 200 fs pulses (this work) and at 1064 nm and 3 ps pulses [19]. The theoretical lines use Eq. (4) and the value of D_{cw} determined above in (a).

In summary, we have shown that nonlinear dynamics of the long-range surface plasmon polariton (LRSPP) mode in strip gold waveguides significantly depends on both the metal core thickness and the laser pulse duration. In particular, the origin of the pulse duration dependence has been explained in detail by studying the electron temporal dynamics using the two-temperature model (TTM): a picosecond pulse interacts with metal stronger than a femtosecond pulse because of greater temporal overlaps of the laser pulse with the excited electron gas. Consequently, this leads to higher values of the third-order nonlinearity for longer pulses, as expressed by the correction factor in Eq. (3). The nonlinearity increases for thinner gold films in the 20-40 nm thickness range studied here, but it will be important to investigate in the future the linear and nonlinear optical properties of the waveguides with even thinner gold core layers (t ~10 nm). The standard Drude model breaks down at the metal layer thicknesses below 10 nm due to possible nonlocal [22, 23] and quantum effects [24], even in the absence of the layer clustering process [25], and full hydrodynamic description, including nonlocal effects is required, which is especially important in the nonlinear regime [26, 27]. This may lead to higher linear absorption of plasmonic waveguides. The electron thermalization parameters of gold, in particular τ_{th} and τ_r can also depend on the thickness for thinner metal layers. This, in turn will affect the effective third-order susceptibility for plasmonic waveguides with the metal core thicknesses below 10 nm. Our results validate experimentally the connection between the characteristic nonlinear temperature response function derived in the TTM and how it affects the delayed nonlinear response of an ultrafast LRSPP mode in the framework of a nonlinear Schrödinger equation. The temperature response function is purely based on characteristic time scales of the metal, and we introduced a correction factor to gauge the convolution response giving the central result Eq. (4), which has only two free parameters that can be measured experimentally. Our results are therefore an important step for accurate *a priori* modeling of ultrafast nanoplasmonic devices.

Funding. EPSRC (UK) grants EP/H000917/2, EP/J018457/1 and EP/M013812/1.

Acknowledgments. This work was supported, in part, by EPSRC (UK). A.V.Z. acknowledges support from the Royal Society and the Wolfson Foundation. Data access statement: All the data supporting this research are provided in full in the results section and Supplement 1.

See Supplement 1 for supporting content.

REFERENCES

1. M. L. Brongersma and V. M. Shalaev, Science **328**, 440 (2010).
2. S. I. Bozhevolnyi, *Plasmonic Nanoguides and Circuits* (Pan Stanford, 2009).
3. A. V. Krasavin and A. V. Zayats, Adv. Opt. Mater. **3**, 1662 (2015).
4. D. K. Gramotnev and S. I. Bozhevolnyi, Nat. Photonics **4**, 2, 83 (2010).
5. V. A. Zenin, A. Andryieuski, R. Malureanu, I. P. Radko, V. S. Volkov, D. K. Gramotnev, A. V. Lavrinenko, and S. I. Bozhevolnyi, Nano Lett. **15**, 8148 (2015).
6. O. Krupin, H. Asiri, C. Wang, R. N. Tait, and P. Berini, Opt. Express **21**, 698 (2013).
7. P. Berini and I. De Leon, Nat. Photonics **6**, 16 (2012).
8. F. J. Diaz, G. Li, C. Martijn de Sterke, B. T. Kuhlmey, and S. Palomba, J. Opt. Soc. Am. B **33**, 957 (2016).
9. F. J. Diaz, T. Hatakeyama, J. Rho, Y. Wang, K. O'Brien, X. Zhang, C. Martijn de Sterke, B. T. Kuhlmey, and S. Palomba, Opt. Express **24**, 545 (2016).
10. M. Kauranen and A. V. Zayats, Nat. Photonics **6**, 737 (2012).
11. A. D. Neira, N. Olivier, M. E. Nasir, W. Dickson, G. A. Wurtz, and A. V. Zayats, Nat. Commun. **6**, 7757 (2015).
12. P. Ginzburg, A. V. Krasavin, and A. V. Zayats, New J. Phys. **15**, 013031 (2013).
13. A. Marini, M. Conforti, G. Della Valle, H. W. Lee, Tr. X. Tran, W. Chang, M. A. Schmidt, S. Longhi, P. St. J. Russell, and F. Biancalana, New J. Phys. **15**, 013033 (2013).
14. R. W. Boyd, Z. Shi, and I. De Leon, Opt. Commun. **326**, 74 (2014).
15. D. D. Smith, Y. Yoon, R. W. Boyd, J. K. Campbell, L. A. Baker, R. M. Crooks, and M. George, J. Appl. Phys. **86**, 6200 (1999).
16. T. K. Lee, A. D. Bristow, J. Hübner, and H. M. van Driel, J. Opt. Soc. Am. B **23**, 2142 (2006).
17. E. Xenogiannopoulou, P. Aloukos, S. Couris, E. Kaminska, A. Piotrowska, and E. Dynowska, Opt. Commun. **275**, 217 (2007).
18. N. Rotenberg, A. D. Bristow, M. Pfeiffer, M. Betz, and H. M. van Driel, Phys. Rev. B **75**, 155426 (2007).
19. O. Lysenko, M. Bache, and A. Lavrinenko, Opt. Lett. **41**, 317 (2016).
20. O. Lysenko, M. Bache, and A. Lavrinenko, J. Opt. Soc. Am. B **33**, 1341 (2016).
21. M. Conforti and G. Della Valle, Phys. Rev. B **85**, 245423 (2012).
22. S. Raza, S. I. Bozhevolnyi, M. Wubs, and N. A. Mortensen, J. Phys. Condens. Matter **27**, 183204 (2015).
23. P. Ginzburg and A. V. Zayats, ACS Nano **7**, 5, 4334 (2013).
24. H. Qian, Y. Xiao, D. Lepage, L. Chen, and Z. Liu, Nanophotonics **4**, 413 (2015).
25. U. Kreibig and M. Vollmer, *Optical Properties of Metal Clusters* (Springer, 1995).
26. P. Ginzburg, A. V. Krasavin, G. A. Wurtz, and A. V. Zayats, ACS Photonics **2**, 8 (2015).
27. A. V. Krasavin, P. Ginzburg, G. A. Wurtz, and A. V. Zayats, Nat. Comm. **7**, 11497 (2016).

Supplementary Material

optica

Nonlinear dynamics of long-range surface plasmon polaritons in gold strip waveguides: supplementary material

OLEG LYSENKO,[1,*] NICOLAS OLIVIER,[2] MORTEN BACHE,[1] ANATOLY V. ZAYATS,[2] AND ANDREI LAVRINENKO[1]

[1]DTU Fotonik, Department of Photonics Engineering, Technical University of Denmark, 2800 Kongens Lyngby, Denmark
[2]Department of Physics, King's College London, Strand, London WC2R 2LS, UK
*Corresponding author: ollyse@fotonik.dtu.dk

Published XX Month XXXX

This document provides supplementary information to "Nonlinear dynamics of long-range surface plasmon polaritons in gold strip waveguides," http://dx.doi.org/10.1364/optica.99.099999, concerning the details of the experimental setup, and the two-temperature model of electron temporal dynamics in gold. The obtained experimental and theoretical values of the third-order susceptibility of gold and the linear and nonlinear parameters of the LRSPP mode are presented.

http://dx.doi.org/10.1364/optica.99.099999.s1

1. EXPERIMENTAL SETUP

The experimental setup is shown in Fig. S1. The laser source was the femtosecond laser amplifier PHAROS (Light Conversion), providing ~200 fs FWHM pulses with a tunable repetition rate here set at 200 kHz at a center wavelength of 1030 nm. The average power of the free-space laser beam was tuned by several neutral density (ND) filters, and the linear polarization of the beam was aligned by a half-wave plate and linear polarizer to match the transverse magnetic polarization of the long-range surface plasmon polariton (LRSPP) mode in the plasmonic waveguides. The end-fire coupling method was used to excite the plasmonic modes [1]. An iris diaphragm was placed to eliminate the scattered light and to transmit the plasmonic mode optical flux to the power meter S132C (Thorlabs). The alignment of the samples and the end-fire coupling were controlled by using the digital color camera WAT-221S (Watec). Before the transmission measurements were taken, the LRSPP mode in each waveguide was imaged by the digital camera DCC1240M (Thorlabs) and the transverse magnetic polarization of the plasmonic mode was verified using the half-wave plate and linear polarizer [2]. This polarization check verified coupling to the LRSPP mode in each plasmonic waveguide.

To characterize the linear transmission of the waveguides, the free-space laser beam was tuned to a low average power (approximately 1 mW), and the transmitted power was measured by using the power meter for the plasmonic waveguides with different lengths (2, 3, and 4 mm) and metal layer thicknesses (22, 27, and 35 nm). The insertion loss graphs were used to calculate the linear propagation loss α per unit length and the coupling loss C per two (in-coupling and out-coupling) facets for the waveguides with gold layer thickness t = 22, 27, and 35 nm. For each value of the length and thickness the measurements of five identical plasmonic waveguides were averaged, and the linear fit was calculated by the least squares method. The waveguides with the length L = 2 mm, and the gold layer thickness t = 22, 27, and 35 nm were selected for nonlinear optical characterization.

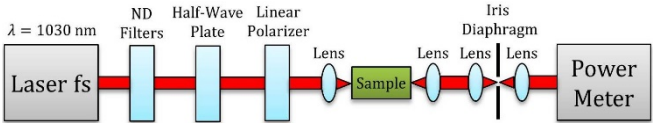

Fig. S1. Experimental setup for nonlinear optical measurements.

The nonlinear propagation of the LRSPP mode in the plasmonic waveguides was measured by tuning the input average power of the free-space laser beam right before the waveguides from 1 mW (5 nJ) to about 55 mW (275 nJ). By using the measured values of the coupling loss C (approximately 3.5 dB per facet), the corresponding values of the pulse energy and peak power inside the waveguides were therefore in the range 1-55 nJ and 5-275 kW, respectively. Any further increase of the average power of the free-space laser beam caused significant heating and melting of the waveguide structures.

2. ELECTRON TEMPORAL DYNAMICS IN GOLD

The experimental values of the imaginary part of the third-order susceptibility $\chi^{(3)}_{\mathrm{Au}}$ of thin gold layers for 200-fs laser pulses are significantly different from the values of $\chi^{(3)}_{\mathrm{Au}}$ obtained previously by using 3-ps laser pulses [3]. Thus, we apply the two-temperature model of electron temporal dynamics in gold [4,5] to explain the experimental results for the imaginary part of $\chi^{(3)}_{\mathrm{Au}}$ and to estimate the real part of $\chi^{(3)}_{\mathrm{Au}}$ for 200-fs laser pulses. We also expand the obtained theoretical dependencies for $\chi^{(3)}_{\mathrm{Au}}$ to see how they change in the wide range from 10 fs to 10 ps.

To introduce the two-temperature model, let us consider an ultrashort optical pulse with the Gaussian electric field profile $E(t) = E_0 e^{-t^2/(2T_0^2)} e^{-i\omega t}$, where E_0 is the electric field amplitude, ω is the light angular frequency, t is the time coordinate, $T_0 = \Delta T / (2\sqrt{\ln(2)})$ is the pulse half-width, and ΔT is the pulse full-width at half maximum (FWHM). The mean absorbed power per unit volume of gold $P_{\mathrm{A}}(t)$ is given by [4]:

$$P_{\mathrm{A}} = \frac{\varepsilon_0 \omega |E_0|^2}{2} \mathrm{Im}[\varepsilon_{\mathrm{Au}}] e^{-t^2/T_0^2} - \frac{t\varepsilon_0 |E_0|^2}{2T_0^2} e^{-t^2/T_0^2} \left(1 + \frac{\omega_{\mathrm{p}}^2(\omega^2 - \gamma^2)}{(\omega^2+\gamma^2)^2}\right), \quad \textbf{(S1)}$$

where $\omega_{\mathrm{p}} = \sqrt{ne^2 / \varepsilon_0 m_{\mathrm{e}}}$ is the plasma frequency for gold, e is the electron charge, ε_0 is the vacuum permittivity, n is the electron density, m_{e} is the electron mass, γ is the collision frequency of electrons for bulk gold, and $\varepsilon_{\mathrm{Au}}$ is the dielectric permittivity for bulk gold. Taking into account that the pulse carrier frequency is far away from the interband transitions in gold, it is straightforward to show that Eq. (S1) can be simplified as $P_{\mathrm{A}} \approx (1/2)\varepsilon_0 \omega |E_0|^2 \mathrm{Im}[\varepsilon_{\mathrm{Au}}] \exp(-t^2/T_0^2)$. Then this expression is used to solve the equations of the electron temporal dynamics [4,5]:

$$\begin{cases} \dfrac{\partial N}{\partial t} = -(\gamma_{\mathrm{e}} + \gamma_{\mathrm{lat}})N + P_{\mathrm{A}}, \\ C_{\mathrm{e}} \dfrac{\partial T_{\mathrm{e}}}{\partial t} = C(T_{\mathrm{lat}} - T_{\mathrm{e}}) + \gamma_{\mathrm{e}} N, \\ C_{\mathrm{lat}} \dfrac{\partial T_{\mathrm{lat}}}{\partial t} = C(T_{\mathrm{e}} - T_{\mathrm{lat}}) + \gamma_{\mathrm{lat}} N, \end{cases} \quad \textbf{(S2)}$$

where $T_{\mathrm{e}}(t)$ is the electronic temperature, $T_{\mathrm{lat}}(t)$ is the lattice temperature, $C_{\mathrm{e}} \approx 2.1 \times 10^4$ J/(m^3·K) is the electronic heat capacity per unit volume of gold [6], $C_{\mathrm{lat}} \approx 2.5 \times 10^6$ J/(m^3·K) is the lattice heat capacity per unit volume of gold [6], $\gamma_{\mathrm{e}} \approx 2$ THz is the electron thermalization rate [7], $\gamma_{\mathrm{lat}} \approx 1$ THz is the lattice thermalization rate [7], $G \approx 20$ PHz is the electron-photon coupling coefficient [6], and $N(t)$ is the energy density stored in the nonthermalized part of the electronic distribution [4]. This system of differential equations can be solved directly, using the initial conditions: $N(0) = 0$ and $T_{\mathrm{e}}(0) = T_{\mathrm{lat}}(0)$. The solution for $N(t)$ is given by:

$$N(t) = Ae^{-(t+4T_0)/\tau_{\mathrm{th}}} \left[\mathrm{erf}\left(\frac{T_0}{2\tau_{\mathrm{th}}} + 4\right) - \mathrm{erf}\left(\frac{T_0}{2\tau_{\mathrm{th}}} - \frac{t}{T_0}\right)\right], \quad \textbf{(S3)}$$

where $\tau_{\mathrm{th}} = 1/(\gamma_{\mathrm{e}} + \gamma_{\mathrm{lat}}) \approx 300$ fs is the characteristic decay time for the energy density of nonthermalized electrons [4], and $A = (\sqrt{\pi}\varepsilon_0/4)\mathrm{Im}[\varepsilon_{\mathrm{Au}}]|E_0|^2 \omega T_0 \exp(T_0(T_0 + 16\tau_{\mathrm{th}})/4\tau_{\mathrm{th}}^2)$ is the time independent constant. The solution for the electronic temperature variation $\Delta T_{\mathrm{e}}(t) = T_{\mathrm{e}}(t) - T_{\mathrm{lat}}(t)$ is given by:

$$\Delta T_{\mathrm{e}}(t) = Be^{-(t+4T_0)/\tau_{\mathrm{th}}} \left\{ \frac{T_0}{\sqrt{\pi}} \left(e^{-\left(T_0/(2\tau_{\mathrm{th}}) - t/T_0\right)^2} - e^{-\left(T_0/(2\tau_{\mathrm{th}})+4\right)^2} \right) + \left[\mathrm{erf}\left(\frac{T_0}{2\tau_{\mathrm{th}}} + 4\right) - \mathrm{erf}\left(\frac{T_0}{2\tau_{\mathrm{th}}} - \frac{t}{T_0}\right)\right] \left(t - \frac{T_0^2}{2\tau_{\mathrm{th}}}\right) \right\}, \quad \textbf{(S4)}$$

where $B = A(\gamma_{\mathrm{e}} C_{\mathrm{lat}} - \gamma_{\mathrm{lat}} C_{\mathrm{e}})/(C_{\mathrm{e}} C_{\mathrm{lat}})$ is the time independent constant. The electronic temperature variation $\Delta T_{\mathrm{e}}(t)$ can be also obtained via the convolution of the mean absorbed power $P_{\mathrm{A}}(t)$ and the response function of gold $h_{\mathrm{T}}(t)$. The latter is expressed as [4,5]:

$$h_{\mathrm{T}}(t) = \frac{\theta(t)}{\tau_{\mathrm{th}} - \tau_{\mathrm{r}}} \left(e^{-t/\tau_{\mathrm{th}}} - e^{-t/\tau_{\mathrm{r}}} \right), \quad \textbf{(S5)}$$

where $\tau_{\mathrm{r}} = C_{\mathrm{e}} C_{\mathrm{lat}} / [G(C_{\mathrm{e}} + C_{\mathrm{lat}})] \approx 1$ ps is the characteristic decay time for thermalized electrons [4,5], and $\theta(t)$ is the Heaviside step function [4]. We also provide the Fourier transform functions of the normalized input pulse intensity $I(t)$, mean absorbed power $P_{\mathrm{A}}(t)$, electronic temperature variation $\Delta T_{\mathrm{e}}(t)$, and nonthermalized electron density $N(t)$ for two particular values of the pulse duration ΔT = 200 fs and 3 ps (Fig. S2).

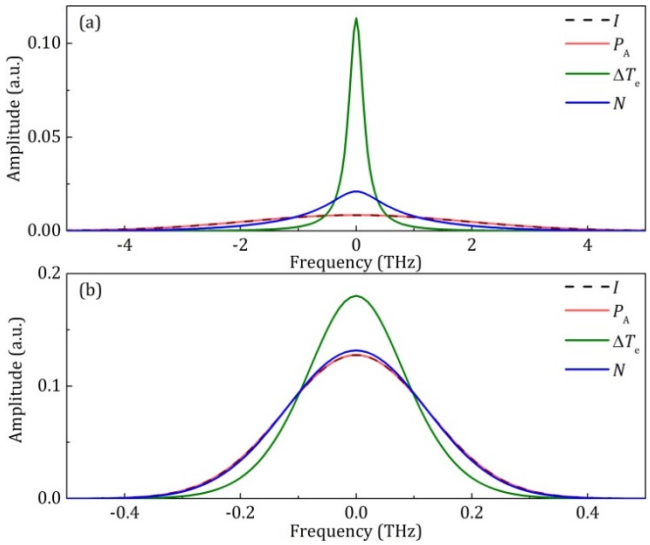

Fig. S2. Modeling of electron temporal dynamics in gold in the Fourier domain for (a) 200-fs laser pulses at 1030 nm and (b) 3-ps laser pulses at 1064 nm.

The electronic temperature deviation ΔT_{e} almost follows the shape of the mean absorbed power P_{A} for 3-ps (and longer) laser pulses, and the Fourier amplitudes for 3-ps laser pulses are larger than the ones for 200-fs laser pulses. Then the obtained

expressions for $\Delta T_e(t)$ and $P_A(t)$ are used to calculate the ratio of the third-order susceptibility $\chi^{(3)}_{Au}$ for bulk gold and gold layers with the thickness t = 22, 27, and 35 nm for different values of the pulse duration ΔT. The obtained pulse duration dependences of the third-order susceptibility of gold explain well the experimental results for the imaginary part of $\chi^{(3)}_{Au}$ for the gold layers with different thicknesses, and also are used to calculate the real part of the third-order susceptibility $\chi^{(3)}_{Au}$, in particular, for 200-fs laser pulses.

3. EXPERIMENTAL AND THEORETICAL RESULTS

The obtained values of the linear propagation loss α, coupling loss C, and coefficient a for the strip plasmonic waveguides with the gold layer thickness t = 22, 27, and 35 nm are shown in Table S1. The experimental values of the nonlinear loss parameter β, and the imaginary part of the third-order susceptibility $\chi^{(3)}_{Au}$ for gold layers with the thickness t = 22, 27, and 35 nm are presented in Table S2. The theoretical values of the third-order susceptibility for gold layers with the thickness t = 22, 27, and 35 nm, and for bulk gold for 200-fs laser pulses are shown in Table S3. The values of the real part of the third-order susceptibility were obtained by the scaling of the known values of the third-order susceptibility from 3-ps laser pulses [3] to 200-fs laser pulses, according to the theoretical pulse duration trends.

Table S1. Experimental values of the propagation loss α, coupling loss C, and parameter a for plasmonic waveguides with different gold layer thicknesses.

t (nm)	α (dB/mm)	C (dB)	a
22	8.7 ± 0.1	6.8 ± 0.4	3.6×10^{-3}
27	11.8 ± 0.2	6.9 ± 0.5	8.6×10^{-4}
35	15.3 ± 0.4	7.0 ± 0.8	2.0×10^{-4}

Table S2. Experimental values of the nonlinear loss parameter β and imaginary part of the third-order susceptibility for gold layers with thickness t = 22, 27, and 35 nm for 200-fs laser pulses at 1030 nm.

t (nm)	β (1/(W·m))	Im[$\chi^{(3)}_{Au}$] (m²/V²)
22	6.2×10^{-3}	$(4.8 \pm 1.6) \times 10^{-19}$
27	5.8×10^{-3}	$(4.3 \pm 1.4) \times 10^{-19}$
35	5.1×10^{-3}	$(3.8 \pm 1.3) \times 10^{-19}$

Table S3. Theoretical values of the third-order susceptibility for bulk gold and gold layers with thickness t = 22, 27, and 35 nm for 200-fs laser pulses at 1030 nm.

t (nm)	Re[$\chi^{(3)}_{Au}$] (m²/V²)	Im[$\chi^{(3)}_{Au}$] (m²/V²)
22	10.8×10^{-18}	4.4×10^{-19}
27	9.2×10^{-18}	3.5×10^{-19}
35	7.5×10^{-18}	2.7×10^{-19}
Bulk gold	1.9×10^{-18}	2.2×10^{-19}

References

1. R. G. Hunsperger, *Integrated Optics: Theory and Technology* (Springer, 2002).
2. R. Charbonneau, P. Berini, E. Berolo and E. Lisicka-Shrzek, "Experimental observation of plasmon–polariton waves supported by a thin metal film of finite width," Opt. Lett. **25**, 11, 844 (2000).
3. O. Lysenko, M. Bache, and A. Lavrinenko, "Third-order susceptibility of gold for ultrathin layers", Opt. Lett. **41**, 2, 317 (2016).
4. A. Marini, M. Conforti, G. Della Valle, H. W. Lee, Tr. X. Tran, W. Chang, M. A. Schmidt, S. Longhi, P. St. J. Russell, and F. Biancalana, "Ultrafast nonlinear dynamics of surface plasmon polaritons in gold nanowires due to the intrinsic nonlinearity of metals", New J. Phys. **15**, 013033 (2013).
5. M. Conforti and G. Della Valle, "Derivation of third-order nonlinear susceptibility of thin metal films as a delayed optical response", Phys. Rev. B **85**, 245423 (2012).
6. Z. Lin and L. V. Zhigilei, "Time-resolved diffraction profiles and atomic dynamics in short-pulse laser-induced structural transformations: Molecular dynamics study", Phys. Rev. B **73**, 184113 (2006).
7. C.-K. Sun, F. Vallée, L. H. Acioli, E. P. Ippen, and J. G. Fujimoto, "Femtosecond-tunable measurement of electron thermalization in gold", Phys. Rev. B **50**, 15337 (1994).

Paper B

O. Lysenko, M. Bache, and A. Lavrinenko

Nonlinear optical model for strip plasmonic waveguides

J. Opt. Soc. Am. B 33, 7, 1341 (2016).

Journal of the Optical Society of America B
OPTICAL PHYSICS

Nonlinear optical model for strip plasmonic waveguides

OLEG LYSENKO,* MORTEN BACHE, AND ANDREI LAVRINENKO

Department of Photonics Engineering, Technical University of Denmark, Oersteds Plads, Building 345 V, Kongens Lyngby 2800, Denmark
**Corresponding author: ollyse@fotonik.dtu.dk*

Received 16 March 2016; revised 9 May 2016; accepted 9 May 2016; posted 11 May 2016 (Doc. ID 261343); published 1 June 2016

This paper presents a theoretical model of nonlinear optical properties for strip plasmonic waveguides. The particular waveguides geometry that we investigate contains a gold core, adhesion layers, and silicon dioxide cladding. It is shown that the third-order susceptibility of the gold core significantly depends on the layer thickness and has the dominant contribution to the effective third-order susceptibility of the long-range plasmon polariton mode. This results in two nonlinear optical effects in plasmonic waveguides, which we experimentally observed and reported in [Opt. Lett. 41, 317 (2016)]. The first effect is the nonlinear power saturation of the plasmonic mode, and the second effect is the spectral broadening of the plasmonic mode. Both nonlinear plasmonic effects can be used for practical applications and their appropriate model will be important for further developments in communication approaches.

OCIS codes: (250.5403) Plasmonics; (230.7370) Waveguides; (190.4400) Nonlinear optics, materials; (240.6680) Surface plasmons.

http://dx.doi.org/10.1364/JOSAB.33.001341

1. INTRODUCTION

The optically controlled optical channel is considered as one of the main tools in enhancing density of communication lines with reduced energy-per-bit consumption. All-optical signal processing is capable of achieving a signal modulation and transmission speeds beyond what is possible by their electronic counterparts. To optically modulate (or switch) signals in plasmonic waveguides (with one or several metal–dielectric interfaces) means that light induces changes in the real or imaginary parts of the dielectric functions of the constituent materials. These changes can occur either in a metal or in a dielectric layer, or in both. Most of the studies in nonlinear plasmonics are connected with the local-field enhancement facilitated by metal nanoparticles [1].

So far the light-induced absorption modulation has been studied with the intrinsic metal nonlinearity [1]. The intrinsic nonlinearity of gold is related to the interband excitation of nonequilibrium electrons and results in small changes of the real part of the permittivity but in significant changes of the imaginary part. The associated relaxation time is on the picosecond scale, making terahertz-frequency modulation of signals in plasmonic gold waveguides possible. The relaxation time of the interband transitions in aluminum is much smaller and can provide even faster modulation speeds [2]. Thus, the optical nonlinearity in metals holds a potential that needs to be explored more. Results can be exploited for rapid optical switching and modulation by using strong excitation via an ultrafast laser pulse. This approach has opened a whole new field of active plasmonic systems [2].

Recent experiments confirm the presence of nonlinear propagation effects in plasmonic waveguides, much like the ones that for decades have been fueling nonlinear fiber optics [3]. We have conducted recently an experiment [4] with strip plasmonic gold waveguides and observed that the loss performance was nonlinear as the power was increased. We attributed this effect to the imaginary part of the nonlinearity of gold. We also saw indications of self-phase modulation (SPM) in picosecond pulses spectra governed by the real part of the third-order susceptibility. Both effects were significantly affected by the nanometer-scale thickness of the gold layers as one can conclude from the restored effective nonlinearity parameters. To our knowledge such a study has not yet been done in plasmonic waveguides. An early study [5] used the cw-like pumping and obtained significant thermal contributions to the nonlinear phase. Also, the real and imaginary components of the third-order susceptibility of thin gold layers were characterized using the z-scan method [6,7]. In another recent experiment Baron *et al.* [8] measured the imaginary component of the third-order susceptibility for bulk gold by studying nonlinear propagation of surface-plasmon polaritons at a single air/metal interface.

The model developed in the present paper provides the theoretical background to our recent experiment, as to understand and ultimately exploit intrinsic metal nonlinearities in

thin metal films. The current vision of possible nonlinear behavior in noble metals is that they occur due to the Fermi smearing process. When a thin metal film is exposed to an ultrafast laser pulse, it absorbs the optical pulse, which leads to rapid heating. The rise in the temperature of the material results in interband transitions and broadens the electronic distribution around the Fermi energy. This eventually causes significant change in the dielectric permittivity of metal [9]. Another possible mechanism is that a strong electric field in ultrashort laser pulses affects the distribution of free electrons. Such direct influence is preferable in terms of exploitation due to the fast electronic response and symmetric time scale of both phases of the nonlinear process: development and relaxation.

In our recent experiment we characterized strip plasmonic waveguides, and this geometry forms the basis of the theory in the present paper. The waveguide layout contains the gold core with the finite microscale width and nanoscale thickness, tantalum pentoxide adhesion layer, and silicon dioxide cladding. This particular waveguide configuration was chosen because it provides effective propagation of a long-range surface plasmon polariton (LRSPP) [10]. The optical properties of the LRSPP mode are utilized in many applications, such as nanofocusing of electromagnetic radiation [11] or photodetectors [12]. The nonlinear effects associated with propagation of a LRSPP in plasmonic waveguides are less investigated. One theoretical approach is related to application of the hydrodynamic model for the free-electron gas [13]. The nonlinear propagation of LRSPP modes can be studied in terms of either the second-order [14] or the third-order nonlinearity [15]. A novel approach in the field of nonlinear optics with metals has been introduced by Conforti and Della Valle in [16], where the third-order susceptibility for gold was derived from the two-temperature model of electron temporal dynamics. In [15] Marini and co-workers reported a consistent nonlinear model for plasmonic modes, formulated in terms of the classical nonlinear fiber optics formalism.

In the present paper we also take into account that all constituent materials (metal, adhesion layer, and cladding) exhibit a nonlinear response. So, in line with the classical nonlinear fiber optics formalism as well as the recent literature [15,16] we consider an *effective nonlinearity* of the LRSPP waveguide mode. We apply the model of the third-order susceptibility of gold [16] to the geometry of the strip plasmonic waveguides and consider losses originated both from the linear and nonlinear parts of the metal dielectric function. The effective nonlinearity of the LRSPP mode leads to two interesting nonlinear effects. The first effect is a nonlinear saturation of the average power of the LRSPP mode. The second effect is nonlinear phase modulation with the spectral broadening of the LRSPP pulse. Since our experiment was conducted with a powerful picosecond laser at 1064 nm, we apply our model for this specified wavelength. We also discuss other important ultrafast laser wavelengths (800 and 1550 nm), in particular, regarding different gold behavior.

The paper has the following structure. Section 2 describes optical properties of the constituent materials: gold, tantalum pentoxide, and silicon dioxide. Section 3 presents the effective index theory for calculation of the LRSPP propagation constant in the strip plasmonic waveguide. Section 4 explains a role of the chromatic dispersion in propagation of the LRSPP mode. Section 5 is devoted to nonlinear parameters of the plasmonic waveguide. Section 6 shows a solution to the pulse propagation equation for the LRSPP mode and explains the obtained nonlinear effects.

2. OPTICAL PROPERTIES OF MATERIALS

We will start the modeling of plasmonic waveguides by considering optical properties of the constituent materials. Dielectric permittivity ϵ_{SiO_2} of silicon dioxide (silica) is described by the following Sellmeier equation [17],

$$\epsilon_{SiO_2} = 1 + \frac{0.6961663\lambda^2}{\lambda^2 - (0.0684043)^2} + \frac{0.4079426\lambda^2}{\lambda^2 - (0.1162414)^2} + \frac{0.8974794\lambda^2}{\lambda^2 - (9.896161)^2}, \quad (1)$$

where λ is the light wavelength in micrometers. Permittivity ϵ_{TPO} of tantalum pentoxide (amorphous dielectric) is given by the following equation [18]:

$$\epsilon_{TPO} = \epsilon_\infty - \frac{\omega_{p,0}^2}{\omega^2 + i\gamma_0\omega} + \sum_{j=1}^{6} \frac{\omega_{p,j}^2}{\omega_j^2 - \omega^2 - i\gamma\omega}. \quad (2)$$

Here $\omega = 2\pi c/\lambda$ is the light angular frequency; c is the vacuum speed of light; $\epsilon_\infty = (A - B/\lambda^2)^2$ is the dielectric permittivity of amorphous Ta_2O_5 from the Cauchy dispersion formula [18] with $A = 2.06$ and $B = 0.025$ μm^2; $\omega_{p,0} = 6490$ cm^{-1} and $\gamma_0 = 6.5 \times 10^{-5}$ cm^{-1} are the Drude plasma frequency and scattering rate for Ta_2O_5; and $\omega_{p,j}$, $\gamma_j (j = 1, 2, 3, 4, 5, 6)$ are the experimental parameters for the Lorentz oscillators taken from [18]. The linear refractive indices are $n_{SiO_2} = \sqrt{\epsilon_{SiO_2}}$ for silica, and $n_{TPO} \approx \sqrt{\mathrm{Re}[\epsilon_{TPO}]}$ for tantalum pentoxide, respectively [Fig. 1(a)]. They have two main features. First, tantalum pentoxide has larger values of the linear refractive index: in particular at 1064 nm, the refractive index n_{SiO_2} for silica is ~1.45, and the refractive index n_{TPO} for tantalum pentoxide is ~2.07. Second, silica has a zero-dispersion wavelength at ~1.27 μm [3], and tantalum pentoxide at ~1.8 μm [18].

Dielectric permittivity ϵ_{Au} of a thin gold layer is based on the classical Drude model [19], but with accounting for an electron confinement factor. For a metal nanosphere the frequency of electron collisions γ_f depends on the radius r [20,21]. In the same way of arguing as in [20], where $1/r$ dependence reflects the ratio of surface area to volume, we can proceed by assuming that for a thin gold stripe with thickness t we can take

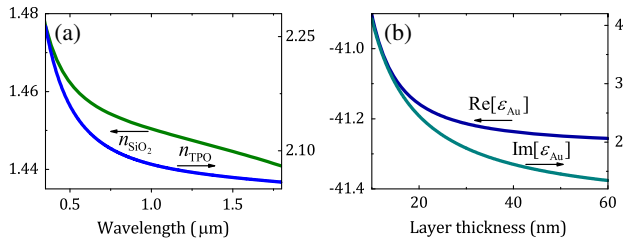

Fig. 1. (a) Linear refractive indices for SiO_2 and Ta_2O_5. (b) Real and imaginary parts of the dielectric permittivity for a gold layer at 1064 nm.

$$\mathrm{Re}[\epsilon_{\mathrm{Au}}] = 1 - \frac{\omega_p^2}{\gamma_f^2 + \omega^2}, \tag{3}$$

$$\mathrm{Im}[\epsilon_{\mathrm{Au}}] = \frac{\gamma_f \omega_p^2}{\omega(\gamma_f^2 + \omega^2)}, \tag{4}$$

$$\gamma_f = \gamma_\infty + \frac{\upsilon_F}{t}, \tag{5}$$

where $\omega_p = \sqrt{ne^2/\epsilon_0 m_e}$ is the plasma frequency for gold, e is the electron charge, ω_0 is the vacuum permittivity, n is the electron density, m_e is the electron mass, $\gamma_\infty = 3.3 \times 10^{13}$ s^{-1} is the frequency of electron collisions for bulk gold, and υ_F is the Fermi velocity of electrons. As the layer thickness t approaches nanoscale values, free electrons start to feel the layer boundaries and the second term in Eq. (5) accounts for this increment of the electron collisions frequency, while the plasma frequency stays the same [19]. The local Drude model may not be applicable for layers with the thicknesses below 10 nm [13,22]. Also there is an intensive clustering process for thin layers [20], and their fabrication especially with thicknesses below 10 nm is still challenging [23]. Therefore our model will focus on plasmonic waveguides with the thickness values above the clustering threshold. Constraining parameter t by 10 nm it is straightforward to show that Eq. (4) can be simplified,

$$\mathrm{Im}[\epsilon_{\mathrm{Au}}] \approx (\mathrm{Im}[\epsilon_{\mathrm{Au}}])_\infty + \frac{\omega_p^2 \upsilon_F}{\omega(\gamma_\infty^2 + \omega^2)t}, \tag{6}$$

where $(\mathrm{Im}[\epsilon_{\mathrm{Au}}])_\infty$ is the imaginary part of the permittivity for bulk gold.

The real and imaginary parts of the dielectric permittivity of a gold layer were calculated at 1064 nm, and for thicknesses t in the range 10–60 nm [Fig. 1(b)]. The real part $\mathrm{Re}[\epsilon_{\mathrm{Au}}]$ is negative and changes insignificantly by only ~0.9%. This is because the frequency of electron collisions γ_f is much less than telecom optical frequencies: $\gamma_f \sim 17.2 \times 10^{13}$ s^{-1} at $t = 10$ nm and decreases to $\sim 5.6 \times 10^{13}$ s^{-1} at $t = 60$ nm. In contrary, imaginary part $\mathrm{Im}[\epsilon_{\mathrm{Au}}]$ changes by an order of magnitude. The obtained values for the linear refractive indices and dielectric permittivities of the constituent materials will be used further for calculation of the plasmonic waveguide dispersion.

3. STRIP PLASMONIC WAVEGUIDES

The designed geometry of strip plasmonic waveguides (Fig. 2) contains the gold core with thickness t, tantalum pentoxide layers with thickness t_1, and thick silica claddings. The waveguide has the microscale width w and millimeter-scale length l. The thickness of the SiO_2 claddings is large enough to cover the LRSPP mode distribution in the yz-plane. The propagation constant β of the plasmonic mode can be calculated by the effective index method [24]. First, the propagation constant β_∞ of the LRSPP mode is derived, assuming an infinitely wide ($w = \infty$) slab waveguide.

By using Maxwell's equations and boundary conditions it is straightforward to show that the dispersion equation for propagation constant β_∞ in the symmetric five-layer system is given by

$$\frac{k_3}{\epsilon_3}\tanh\left(\frac{t}{2}k_3\right) = -\frac{k_2}{\epsilon_2}\frac{\left(\frac{k_2}{\epsilon_2}+\frac{k_1}{\epsilon_1}\right)e^{k_2 t_1} - \left(\frac{k_2}{\epsilon_2}-\frac{k_1}{\epsilon_1}\right)e^{-k_2 t_1}}{\left(\frac{k_2}{\epsilon_2}+\frac{k_1}{\epsilon_1}\right)e^{k_2 t_1} + \left(\frac{k_2}{\epsilon_2}-\frac{k_1}{\epsilon_1}\right)e^{-k_2 t_1}}. \tag{7}$$

Here $k_j = \sqrt{\beta_\infty^2 - \epsilon_j \omega^2/c^2}\,(j = 1, 2, 3)$ are the wave vectors for silica, tantalum pentoxide, and gold, respectively. The dispersion equation is solved numerically for β_∞, and the effective index of the LRSPP mode is $n_{\mathrm{eff}} = \beta_\infty c/\omega$. Then, effective index n_{eff} of the slab waveguide is used to determine the propagation constant β of the plasmonic mode in the finite-width strip waveguide by solving the standard dispersion equation [24]:

$$\sqrt{\frac{\omega^2 n_{\mathrm{eff}}^2}{c^2} - \beta^2}\tan\left(\frac{w}{2}\sqrt{\frac{\omega^2 n_{\mathrm{eff}}^2}{c^2} - \beta^2}\right) = \sqrt{\beta^2 - \frac{\omega^2 n_{\mathrm{SiO_2}}^2}{c^2}}. \tag{8}$$

The normalized propagation constant $\bar{\beta} = \beta c/\omega = n_{\mathrm{eff}1}$ corresponds to the effective refractive index of the LRSPP mode. Equation (8) has several roots, which correspond to different LRSPP spatial modes. The fundamental mode has the largest value of the effective refractive index n_{eff} [25], and the effective refractive indices of other roots are in the range $n_1 < n_{\mathrm{eff}1} < n_{\mathrm{eff}}$. We will focus further on the fundamental mode, which is a transverse magnetic mode with the magnetic field pointed along the y-direction, and the electric field pointed along the z- and x-directions. The real part of the effective refractive index $\mathrm{Re}[n_{\mathrm{eff}1}]$ and imaginary part of the propagation constant $\mathrm{Im}[\beta]$ were calculated in the wavelength range 800–1550 nm, and for thicknesses $t = 22$, 27, and 35 nm (Fig. 3). These specific values of the thickness were selected mainly to follow the recent experimental study [4]. They are above the clustering threshold and small enough to provide low-loss propagation of the LRSPP mode. The imaginary part of the propagation constant defines the linear absorption coefficient $\alpha = 2\,\mathrm{Im}[\beta]$ of the plasmonic mode [22]. As expected, the

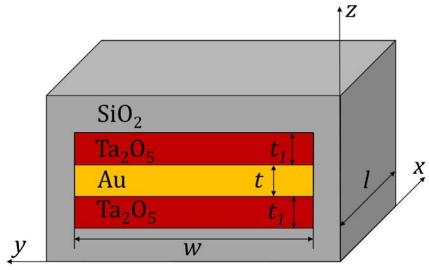

Fig. 2. Geometry of the strip plasmonic waveguide.

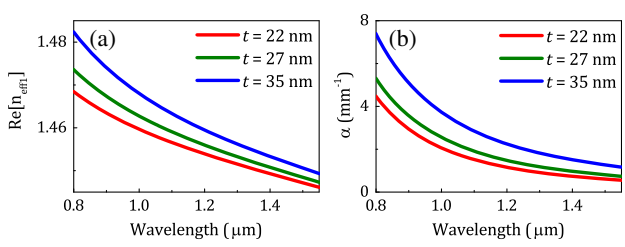

Fig. 3. (a) Effective index and (b) linear absorption coefficient versus wavelength.

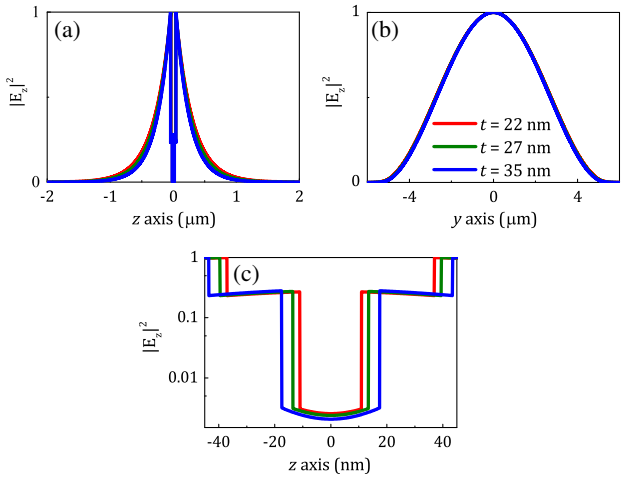

Fig. 4. Intensity distributions in (a) z-axis, (b) y-axis, and (c) zoom on the interfaces.

thinner gold layers have lower attenuation, and the LRSPP mode has a larger propagation distance, respectively. The Ta_2O_5 thickness $t_1 = 26$ nm and the strip width $w = 10$ μm were used in the calculations.

Further we focus on the dominating electric field component E_z. The normalized electric field intensity distribution $|E_z(y, z)|^2$ was calculated for the LRSPP mode in the transverse sections of the waveguide (Fig. 4). In the xy-plane, the distribution function experiences a step-like behavior at the interfaces, both Au\$Ta_2O_5$ and Ta_2O_5\$SiO_2$ [Figs. 4(a) and 4(c)]. Thickness t does not affect the intensity distribution in the z-plane [Fig. 4(b)]. The two-dimensional function $E_z(y, z)$ with a good accuracy can be expressed in terms of a product of the one-dimensional distribution functions: $E_z(y, z) = E_z(y)E_z(z)$. In fact, the value of β_∞ for the infinitely wide slab waveguide differs by less than one percent from the value of β for a finite-width strip waveguide, thus justifying the variables y and z separation in the expression for the two-dimensional distribution function. This property of the distribution function will be used in the further calculation of the field integrals for the constituent materials: gold, tantalum pentoxide, and silica.

4. CHROMATIC DISPERSION

The first and second derivatives of the real part of the propagation constant define the lowest-order chromatic dispersion in plasmonic waveguides. The first derivative $\beta_1 = d\beta/d\omega$ is related to group velocity v_g and group index n_g of the LRSPP mode as $\beta_1 = 1/v_g = n_g/c$ [3]. The second derivative $\beta_2 = d^2\beta/d\omega^2$ [also referred to as the group velocity dispersion (GVD) parameter] is related to the characteristic dispersion length L_D of the plasmonic mode as $L_D = T_0^2/|\beta_2|$, where T_0 is the $1/e$-intensity value of a Gaussian input optical pulse. Group index n_g and GVD parameter β_2 were calculated in the range 800–2000 nm (Fig. 5). The average value of v_g at 1064 nm is ~67% of the vacuum speed of light. The values of the zero-dispersion wavelength of the plasmonic mode are ~1.7, ~1.8, and ~1.93 μm for the gold layer of thicknesses 22, 27, and 35 nm, respectively. The zero-dispersion wavelength at ~1.55 μm can be achieved in plasmonic waveguides with the gold layer thickness 15 nm. The magnitude of β_2 is 10 times larger ($\sim 10^{-4}$ ps^2/mm $= 10^2$ ps^2/km) than typical values for single-mode optical fibers (~10 ps^2/km) [3]. Dispersion length L_D for 3 ps pulses is much larger (~200–1000 mm) than physical length of the waveguide l (~1 mm). This means that the chromatic dispersion has a small effect on the propagation of picosecond optical pulses in the plasmonic waveguide.

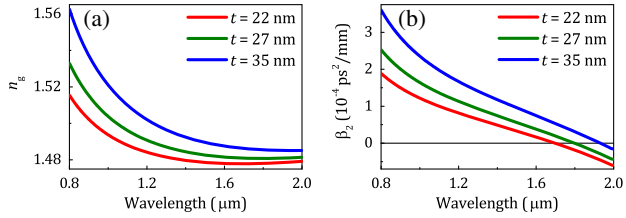

Fig. 5. (a) Group index and (b) GVD parameter versus wavelength.

The situation is different in the case of femtosecond optical pulses, when the dispersion length is comparable with the waveguide length. The chromatic dispersion can significantly affect the propagation of femtosecond optical pulses in plasmonic waveguides, and many interesting phenomena can arise. In this paper we will focus on picosecond optical pulses, when the chromatic dispersion effect has a minor role. The case of femtosecond optical pulses will be discussed elsewhere.

5. NONLINEAR PARAMETERS

For the quantitative analysis of effective nonlinear properties of the LRSPP mode in the waveguide we employed the field integrals in each material section given by the following expressions:

$$\theta_{\mathrm{Au}} = \frac{\int_{-t/2}^{t/2} |E_z|^2 \mathrm{d}z}{\int_{-\infty}^{+\infty} |E_z|^2 \mathrm{d}z}, \tag{9}$$

$$\theta_{\mathrm{Ta_2O_5}} = \frac{2\int_{-t/2}^{t/2+t_1} |E_z|^2 \mathrm{d}z}{\int_{-\infty}^{+\infty} |E_z|^2 \mathrm{d}z}, \tag{10}$$

$$\theta_{\mathrm{SiO_2}} = \frac{2\int_{t/2+t_1}^{+\infty} |E_z|^2 \mathrm{d}z}{\int_{-\infty}^{+\infty} |E_z|^2 \mathrm{d}z} = 1 - \theta_{\mathrm{Au}} - \theta_{\mathrm{Ta_2O_5}}. \tag{11}$$

The initial two-dimensional integrals over the plasmonic mode area in the yz-plane were reduced to one-dimensional integrals over the z-coordinate by applying the variables separation justified above: $E_z(y, z) = E_z(y)E_z(z)$. In fact, the one-dimensional integrals over the y-coordinate have the same values in the numerator and denominator and are canceled due to the waveguide symmetry.

The real and imaginary parts of effective third-order susceptibility $\chi^{(3)}$ of the LRSPP mode are expressed as follows,

$$\mathrm{Re}[\chi^{(3)}] = \theta_{\mathrm{Au}}\,\mathrm{Re}[\chi_3^{(3)}] + \theta_{\mathrm{Ta_2O_5}}\chi_2^{(3)} + \theta_{\mathrm{SiO_2}}\chi_1^{(3)}, \tag{12}$$

$$\mathrm{Im}[\chi^{(3)}] = \theta_{\mathrm{Au}}\,\mathrm{Im}[\chi_3^{(3)}], \tag{13}$$

where $\chi_1^{(3)}$ is the third-order susceptibility for the SiO_2 claddings [26], $\chi_2^{(3)}$ is the third-order susceptibility for the Ta_2O_5 layers [27], and $\chi_3^{(3)}$ is the third-order susceptibility for the Au layer. The third-order susceptibility for bulk gold is given by the following expression [15],

$$\chi_\infty^{(3)} = \frac{1}{2}\epsilon_0 \omega \,\mathrm{Im}[\epsilon_{\mathrm{Au}}]\tau_r\tau_{\mathrm{th}}\left(\frac{\gamma_e}{C_e} - \frac{\gamma_{\mathrm{lat}}}{C_{\mathrm{lat}}}\right)\frac{\partial \epsilon_{\mathrm{inter}}}{\partial T_e}, \tag{14}$$

where C_e and C_{lat} are the electronic and lattice heat capacities per unit volume of gold, γ_e and γ_{lat} are the electron and lattice thermalization rates, $\tau_{th} = 1/(\gamma_e/\gamma_{\mathrm{lat}})$ is the decay time for non-thermalized electrons, $\tau_r = C_e C_{\mathrm{lat}}/[C(C_e + C_{\mathrm{lat}})]$ is the decay time for thermalized electrons, C is the electron–phonon coupling coefficient, and $\partial\epsilon_{\mathrm{inter}}/\partial T_e$ is the complex value of interband thermo-modulational derivative. To calculate the thickness-dependent third-order susceptibility for the gold layer $\chi_3^{(3)}$, one can substitute the thickness-dependent permittivity ϵ_{Au} from Eq. (6) into Eq. (15) and obtain the following expression:

$$\chi_3^{(3)} = \chi_\infty^{(3)}\left(1 + \frac{v_F}{\gamma_\infty t}\right). \tag{15}$$

In the derivation of Eq. (15) we assumed all parameters in the two-temperature model, except $\mathrm{Im}[\epsilon_{\mathrm{Au}}]$, were being thickness independent. For very small thicknesses, the model must be revised by using the nonlocal and quantum approaches [6,13]. The calculated real and imaginary parts of $\chi_3^{(3)}$ for layer thickness t in the range 10–60 nm (Fig. 6) indicate the increment of the third-order susceptibility in ~3 times as the layer thickness decreases from 60 to 10 nm. The horizontal asymptotes in Fig. 6 correspond to the value of third-order susceptibility $\chi_\infty^{(3)}$ for bulk gold at 1064 nm [15]. The real part is $\mathrm{Re}[\chi_\infty^{(3)}] = 4.6 \times 10^{-17}\,\mathrm{m^2/V^2}$, and the imaginary part is $\mathrm{Im}[\chi_3^{(3)}] = 4.8 \times 10^{-18}\,\mathrm{m^2/V^2}$. The real part is ~10 times larger in magnitude than the imaginary part $\mathrm{Im}[\chi_3^{(3)}]$ for the same values of the layer thickness. Figure 6 also shows the thickness limitations. The Drude model [Eqs. (3)–(5)] may be inapplicable for the layer thicknesses below 10–15 nm due to the possible quantum effects [6], nonlocal effects [13], and layer clustering [20]. Conversely, the coupled LRSPP mode collapses at the layer thicknesses above 50–60 nm due to the small penetration depth of the surface electromagnetic waves in metal [22]. Therefore, the effective range of t is ~15–50 nm for experimental studies.

The literature values of $\chi_\infty^{(3)}$ at 1550 nm are mostly the same as at 1064 nm [15], but the linear absorption in the waveguide is somewhat lower [Fig. 3(b)]. The wavelength 1550 nm can be a good option for an experimental study of nonlinear effects in the gold strip waveguides. Moreover, for this wavelength anomalous waveguide GVD can be found, making it possible to excite solitons. For the wavelength 800 nm, although the value of $\mathrm{Re}[\chi_\infty^{(3)}]$ is ~40% larger than at 1064 nm, the value of $\mathrm{Im}[\chi_\infty^{(3)}]$ is ~5 times larger. This means that nonlinear absorption will dominate the nonlinear dynamics.

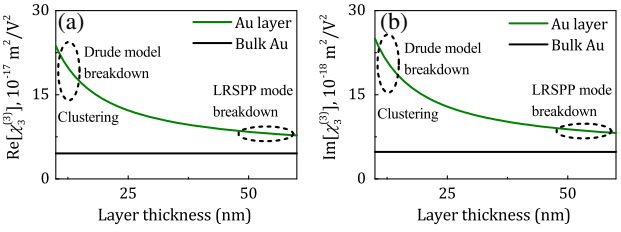

Fig. 6. (a) Real part and (b) imaginary part of the third-order susceptibility for Au layers at 1064 nm.

Effective nonlinear refractive index $n_{2\mathrm{eff}}$, nonlinear absorption coefficient β, and nonlinear parameter γ of the plasmonic mode are expressed by the following expressions [28],

$$n_{2\mathrm{eff}} = \frac{3}{4\epsilon_0 c n_0^2}\,\mathrm{Re}[\chi^{(3)}], \tag{16}$$

$$\beta = \frac{\beta_c}{A_{\mathrm{eff}}} = \frac{3\omega}{2\epsilon_0 c^2 n_0^2 A_{\mathrm{eff}}}\,\mathrm{Im}[\chi^{(3)}], \tag{17}$$

$$\gamma = \frac{\omega}{c}\frac{n_{2\mathrm{eff}}}{A_{\mathrm{eff}}}, \tag{18}$$

where β_c is the conventional definition of the nonlinear absorption coefficient [28], and A_{eff} is the effective area of the plasmonic mode calculated by the following formula [3]:

$$A_{\mathrm{eff}} = \frac{\left(\int_{-\infty}^{+\infty}\int_{-\infty}^{+\infty}|E_z(y,z)|^2\,\mathrm{d}y\mathrm{d}z\right)^2}{\int_{-\infty}^{+\infty}\int_{-\infty}^{+\infty}|E_z(y,z)|^4\,\mathrm{d}y\mathrm{d}z}. \tag{19}$$

The calculated values of the field integrals θ_{Au}, $\theta_{\mathrm{Ta_2O_5}}$, $\theta_{\mathrm{SiO_2}}$, effective linear refractive index $n_{\mathrm{eff}1}$ and third-order susceptibility $\chi_3^{(3)}$ of the LRSPP mode, and linear refractive index n_{Au} of the gold layer for layer thicknesses $t = 22$, 27, and 35 nm are summed up in Table 1. The variation of each parameter was calculated as a function of the thickness variation $\delta_t = 1$ nm. In all the calculations, the same values of the Ta_2O_5 layers thickness $t_1 = 26$ nm, waveguide strip width $w = 10$ μm, and wavelength $\lambda = 1064$ nm were used. The literature values of the dielectrics third-order susceptibilities are $\chi_1^{(3)} = 2.07 \times 10^{-22}\,\mathrm{m^2/V^2}$ for SiO_2, and $\chi_2^{(3)} = 1.12 \times 10^{-20}$ for Ta_2O_5. The field integral values indicate that most of the electric field of the LRSPP mode (around 97%) is situated in the SiO_2 claddings. However, the contribution terms from tantalum pentoxide $\theta_{\mathrm{Ta_2O_5}}\chi_2^{(3)}$ and silica $\theta_{\mathrm{SiO_2}}\chi_1^{(3)}$ to the real part of the third-order susceptibility $\mathrm{Re}[\chi^{(3)}]$ are of the same order of magnitude ($\sim 3 \times 10^{-22}\,\mathrm{m^2/V^2}$ and $\sim 2 \times 10^{-22}\,\mathrm{m^2/V^2}$, respectively). The contribution from the gold layer is ~2 orders of magnitude larger ($\sim 2 \times 10^{-20}\,\mathrm{m^2/V^2}$), and is therefore dominating. The imaginary part of the third-order susceptibility $\mathrm{Im}[\chi^{(3)}]$ is solely determined by the imaginary part of the third-order susceptibility $\mathrm{Im}[\chi_3^{(3)}]$ of the gold layer as the chosen wavelength has a photon energy that is well below half of the optical bandgap of silica and tantalum pentoxide, nullifying their respective imaginary nonlinear susceptibility. Thus, the dominant role of the nonlinearity of the gold layer in the effective nonlinearity of the plasmonic mode is confirmed. This is in accordance with the recent theoretical results published by Baron *et al.* for other plasmonic systems [29].

6. PULSE PROPAGATION EQUATION

Once the mode properties of the strip plasmonic waveguides are known, the propagation dynamics of these modes is well described by the nonlinear Schrödinger equation [3],

$$\frac{\partial A}{\partial x} = i\gamma|A|^2A - \frac{\alpha}{2}A - \frac{\beta}{2}|A|^2A, \tag{20}$$

where $A(x, T)$ is the complex amplitude of an optical pulse, x is the propagation coordinate, T is the time coordinate in the co-moving frame of the input pulse. The first and third terms correspond to the SPM and nonlinear absorption, respectively. The chromatic dispersion has been neglected, which is a good approximation as dispersion length L_D for picosecond optical pulses in a plasmonic waveguide is much larger than its physical length l. The formal solution to Eq. (20) is $A(x, T) = \sqrt{P(x, T)}\exp[i\phi_{\mathrm{NL}}(x, T)]$, where $P(x, T)$ is the pulse power amplitude and $\phi_{\mathrm{NL}}(x, T)$ is the pulse nonlinear phase. Although this has been studied extensively in the literature, we are here dealing with the particular case where dispersion is negligible and where linear and nonlinear absorption is significant, which makes it worth revising the results. Substituting this solution in Eq. (20) gives the following system of differential equations:

$$\begin{cases} \frac{\partial P(x,T)}{\partial x} = -\alpha P(x, T) - \beta|P(x, T)|^2, \\ \frac{\partial \phi_{\mathrm{NL}}(x,T)}{\partial x} = \gamma P(x, T). \end{cases} \tag{21}$$

The system is straightforward to solve for the Gaussian pulse initial conditions: $P(0, T) = P_0\exp(-T^2/T_0^2)$ and $\phi_{\mathrm{NL}}(0, T) = 0$:

$$\begin{cases} P(x, T) = \frac{P_0 e^{-T^2/T_0^2} e^{-\alpha x}}{1+\beta P_0 e^{-T^2/T_0^2}(1-e^{-\alpha x})/\alpha}, \\ \phi_{\mathrm{NL}}(x, T) = \frac{\gamma}{\beta}\ln[1 + \beta P_0 e^{-T^2/T_0^2}(1 - e^{-\alpha x})/\alpha]. \end{cases} \tag{22}$$

These solutions describe how peak power $P(x, T)$ and phase $\phi_{\mathrm{NL}}(x, T)$ of optical pulses change in the time domain upon propagation. For practical purposes, the expression for $P(x, T)$ can be modified to obtain a formula for the average power of light at the output of the plasmonic waveguide, which is the observable and measurable quantity. The equation for the pulse energy $E(x)$ is expressed as

$$E(x) = \int_{-\infty}^{+\infty}|A(x, T)|^2\mathrm{d}T = \int_{-\infty}^{+\infty}\frac{P_0 T_0 e^{-\alpha x}e^{-T^2/T_0^2}}{1 + \beta P_0 e^{-T^2/T_0^2}(1 - e^{-\alpha x})/\alpha}\mathrm{d}(T/T_0). \tag{23}$$

It is straightforward to show that if the integral in Eq. (23) is expanded in the Taylor series up to the second-order term, this equation can be simplified to the following form,

$$E(x) = P_0 T_0 e^{-\alpha x}\left(\sqrt{\pi} - \frac{\sqrt{\pi}\beta P_0}{\sqrt{2}}\frac{1 - e^{-\alpha x}}{\alpha}\right), \tag{24}$$

where $E(x) = \overline{P}(x)/f_{\mathrm{rep}}$ is the pulse energy in terms of average power $\overline{P}(x)$ and laser repetition rate f_{rep}. Peak power P_0 is related to average input power $\overline{P}_0$ as $P_0 = \overline{P}_0/(\sqrt{\pi}T_0 f_{\mathrm{rep}})$. By substituting the expression for the pulse energy and peak power in Eq. (24), and accounting that $\exp(-\alpha x) \ll 1$ at the waveguide output ($x = 1$) due to the large linear attenuation [Fig. 3(b)], the following equation for average output power $\overline{P}(l)$ is obtained:

$$\overline{P}(l) = \overline{P_0}e^{-\alpha l} - \frac{\sqrt{\pi}\beta\overline{P_0}^2}{\sqrt{2}\alpha T_0 f_{\mathrm{rep}}}e^{-\alpha l}. \tag{25}$$

This equation can be used for practical applications since the average input and output power are the directly measurable quantities. It shows that average output power $\overline{P}(l)$ from the plasmonic waveguide of length l depends nonlinearly on the average input power $\overline{P}_0$, and an asymptotic saturation of function $\overline{P}(l)\{\overline{P}_0\}$ is expected at high values of $\overline{P}_0$. The nonlinear trend $\overline{P}(l)\{\overline{P}_0\}$ depends on linear absorption coefficient α, laser repetition rate f_{rep}, pulse duration T_0, nonlinear parameter β, and length l of the waveguide. The calculated power trends for different thicknesses $t = 22$, 27, and 35 nm (Fig. 7) confirm the expected nonlinear behavior. The nonlinear term in Eq. (25) becomes important for values of $\overline{P}_0$ above 0.15–0.2 W. The possible saturation plateau is achievable at values of $\overline{P}_0$ above 0.5 W. The obtained nonlinear functions $\overline{P}(l)\{\overline{P}_0\}$ clearly depend on gold thickness t; the saturation is achieved faster for thinner waveguides. It confirms that gold layer thickness t is a crucial parameter for $\chi^{(3)}$ of the LRSPP mode. The following parameters were used in the calculations: waveguide width $w = 10$ μm and length $l = 3$ mm, Ta_2O_5 thickness $t_1 = 26$ nm, laser peak wavelength $\lambda = 1064$ nm,

Table 1. Parameters of the Waveguide: θ_{Au}, $\theta_{\mathrm{Ta_2O_5}}$, $\theta_{\mathrm{SiO_2}}$, n_{eff1}, n_{Au}, A_{eff}, β, γ, $\chi_3^{(3)}$ for Different Gold Layer Thicknesses

t, nm	35 ± 1	27 ± 1	22 ± 1
θ_{Au}, 10^{-3}	0.1872 ± 0.0055	0.1397 ± 0.0062	0.1084 ± 0.0063
$\theta_{\mathrm{Ta_2O_5}}$	0.0298 ± 0.0004	0.0263 ± 0.0004	0.0239 ± 0.0005
$\theta_{\mathrm{SiO_2}}$	0.9701 ± 0.0005	0.9736 ± 0.0005	0.9760 ± 0.0005
$\mathrm{Re}[n_{\mathrm{eff1}}]$	1.4649 ± 0.0003	1.4603 ± 0.0003	1.4576 ± 0.0003
$\mathrm{Im}[n_{\mathrm{eff1}}]$, 10^{-2}	0.0265 ± 0.0009	0.0179 ± 0.0009	0.0143 ± 0.0009
$\mathrm{Re}[n_{\mathrm{Au}}]$	0.1352 ± 0.0020	0.1570 ± 0.0034	0.1786 ± 0.0050
$\mathrm{Im}[n_{\mathrm{Au}}]$	6.4223 ± 0.0001	6.4208 ± 0.0003	6.4192 ± 0.0004
A_{eff}, μm^2	9.17 ± 0.11	10.24 ± 0.16	11.15 ± 0.20
β, 1/(W·m)	0.139 ± 0.005	0.095 ± 0.005	0.069 ± 0.005
γ, 1/(W·m)	0.77 ± 0.03	0.52 ± 0.03	0.38 ± 0.03
$\mathrm{Re}[\chi_3^{(3)}]$, m^2/V^2	10.03×10^{-17}	11.65×10^{-17}	13.27×10^{-17}
$\mathrm{Im}[\chi_3^{(3)}]$, m^2/V^2	10.58×10^{-18}	12.29×10^{-18}	14.00×10^{-18}

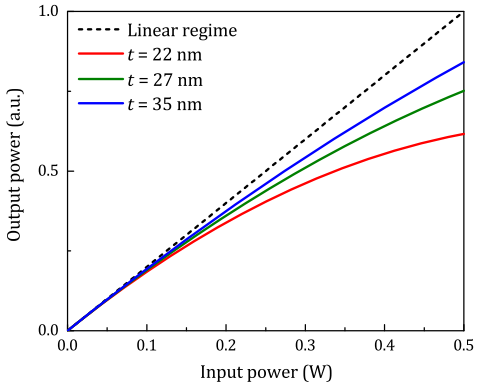

Fig. 7. Nonlinear power trends for different gold layer thicknesses at 1064 nm. Black line corresponds to the linear LRSPP regime.

repetition rate $f_{\text{rep}} = 78$ MHz, and FWHM pulse duration $\Delta T = 2\sqrt{\ln(2)}T_0 \approx 3$ ps.

The second nonlinear effect concerns the LRSPP mode spectral features. The pulse power spectral density (PSD) in W/Hz is given by the squared Fourier transform of pulse amplitude $A(x, T)$ as follows:

$$\text{PSD}(x, \omega) = f_{\text{rep}} \left| \int_{-\infty}^{+\infty} A(x, T) e^{i\omega T} \mathrm{d}T \right|^2. \quad \textbf{(26)}$$

By substituting the expressions for the pulse power amplitude and phase in Eq. (26), the final formula for the PSD is obtained,

$$\text{PSD}(l, \omega) = f_{\text{rep}} \left| \int_{-\infty}^{+\infty} \left(\frac{P_0 e^{-\frac{T^2}{T_0^2}} e^{-\alpha l}}{1 + \beta P_0 e^{-\frac{T^2}{T_0^2}} L_{\text{eff}}} \right)^{1/2} \times e^{\frac{i\chi}{\beta} \ln\left[1 + L_{\text{eff}} \beta P_0 e^{-\frac{T^2}{T_0^2}}\right]} e^{i(\omega - \omega_c)T} \mathrm{d}T \right|^2, \quad \textbf{(27)}$$

where $\omega_c = 2\pi c/\lambda$ is the carrier frequency, which corresponds to the peak wavelength 1064 nm, and $L_{\text{eff}} = (1 - e^{-\alpha l})/\alpha$ is the effective waveguide length. The numerical modeling based on Eq. (27) for the gold layer thickness $t = 22$ nm (Fig. 8) shows the nonlinear spectral broadening and splitting of an input Gaussian pulse, depending on input average power $\overline{P}_0$. The pulse splitting occurs at values of $\overline{P}_0 \sim 0.2$ W. This nonlinear effect was observed in our recent experiment [4]. The further increase of $\overline{P}_0$ leads to the splitting and formation of more SPM peaks. The cases of other thicknesses (27 nm, 35 nm) and wavelengths (800 nm, 1550 nm) are qualitatively the same. The splitting occurs at values of $\overline{P}_0 \sim 0.1$ W at 1550 nm, and $\overline{P}_0 \sim 1.2$ W at 800 nm.

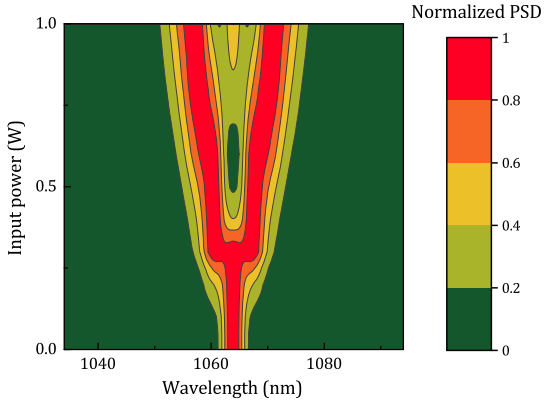

Fig. 8. SPM broadening of the input Gaussian pulse at 1064 nm using $t = 22$ nm.

The obtained spectral features are in accordance with the theoretical results for nonlinear properties of silicon waveguides [30,31]. The principal difference here is that a plasmonic waveguide has much higher linear absorption and shorter physical length than an ordinary silicon waveguide. However, the comparable nonlinear spectral broadening can be achieved. In the case of optical fibers, the required waveguide length can reach hundreds of meters or more to receive the desired nonlinear features. In this sense a plasmonic or silicon waveguide provides the same functionality, and can be integrated on-chip and used for nonlinear purposes even with very short propagation lengths.

7. CONCLUSIONS AND OUTLOOK

In this paper we have presented the theoretical model of nonlinear behavior for plasmonic waveguides. The effective third-order susceptibility $\chi^{(3)}$ of the LRSPP mode is the crucial parameter for explanation of the nonlinear effects in plasmonic strip waveguides—nonlinear power absorption and nonlinear (SPM) of the LRSPP mode. The third-order susceptibility $\chi^{(3)}_{\text{Au}}$ of the gold core has the dominant contribution to $\chi^{(3)}$ of the whole plasmonic mode. It was verified for three values of gold layer thicknesses $t = 22$, 27, and 35 nm. The key point is that the nonlinear properties are thickness dependent, and the third-order susceptibility of gold layers is inversely proportional to the thickness. Thin metal layers enhance the waveguide nonlinearity and provide effective nonlinear propagation of ultrafast optical pulses. In our model, this nonlinear enhancement effectively comes from modeling the electron collision rate with a Fermi velocity term that increases with thinner waveguides due to a $1/t$ dependence. The results confirmed the nonlinear power saturation that was observed in [4] for the average values of the input power $\overline{P}_0$ in the range above 0.15–0.2 W, and for the high repetition rate $f_{\text{rep}} = 78$ MHz picosecond laser pumping at 1064 nm. In the same range an SPM effect was observed, leading to the LRSPP spectral broadening and splitting, again in accordance with our recent experimental results. The deep analogy with classical fiber-based nonlinear optics shows that plasmonic waveguides are potential candidates for nonlinear optics applications on a microscopic length scale.

One of the possible developments in this direction is the nonlinear analysis of higher-order plasmonic modes. The current model is for the fundamental LRSPP mode, but other spatial modes can also be excited. These higher-order modes will affect the dynamics by nonlinear cross-phase modulation [3]. Another development concerns the propagation of even shorter (femtosecond) pulses in the plasmonic waveguides. The chromatic dispersion effect may have a more dominant role than in the present case. The investigation of nonlinear propagation of femtosecond pulses in the plasmonic waveguides will be done

elsewhere. The interaction of the nonlinear and GVD effects leads to many interesting optical phenomena in plasmonic nanostructures with their possible practical realization, for example, in optical communication systems. All further developments will involve a more generalized pulse propagation equation with a strict vectorial approach [32]. Our results indicate that the waveguides investigated here could have anomalous GVD at telecom C-band wavelengths, which means that solitons can be excited using femtosecond Er-fiber lasers. This has interesting nonlinear applications that hold promise for plasmonic systems.

REFERENCES

1. M. Kauranin and A. V. Zayats, "Nonlinear plasmonics," Nat. Photonics **6**, 737–748 (2012).
2. N. Rotenberg, M. Betz, and H. M. van Driel, "Ultrafast all-optical coupling of light to surface plasmon polaritons on plain metal surfaces," Phys. Rev. Lett. **105**, 017402 (2010).
3. G. P. Agrawal, *Nonlinear Fiber Optics* (Elsevier, 2013).
4. O. Lysenko, M. Bache, and A. Lavrinenko, "Third-order susceptibility of gold for ultrathin layers," Opt. Lett. **41**, 317–320 (2016).
5. A. Huck, D. Witthaut, S. Kumar, A. S. Soerensen, and U. L. Andersen, "Large optical nonlinearity of surface plasmon modes on thin gold films," Plasmonics **8**, 1597–1605 (2013).
6. Z. Liu, Y. Xiao, and H. Qian, "Investigations of the optical properties of nanoscale gold films," in *Advanced Photonics*, OSA Technical Digest (Optical Society of America, 2015), paper NM4C.1.
7. E. Xenogiannopoulou, P. Aloukos, S. Couris, E. Kaminska, A. Piotrowska, and E. Dynowska, "Third-order nonlinear optical properties of thin sputtered gold films," Opt. Commun. **275**, 217–222 (2007).
8. A. Baron, T. B. Hoang, C. Fang, M. H. Mikkelsen, and D. R. Smith, "Ultrafast self-action of surface-plasmon polaritons at an air/metal interface," Phys. Rev. B **91**, 195412 (2015).
9. K. F. MacDonald, Z. L. Samson, M. I. Stockman, and N. I. Zheludev, "Ultrafast active plasmonics," Nat. Photonics **3**, 55–58 (2009).
10. P. Berini, "Long-range surface plasmon polaritons," Adv. Opt. Photon. **1**, 484–588 (2009).
11. D. K. Gramotnev and S. I. Bozhevolnyi, "Nanofocusing of electromagnetic radiation," Nat. Photonics **8**, 13–22 (2014).
12. P. Berini, "Surface plasmon photodetectors and their applications," Laser Photon. Rev. **8**, 197–220 (2014).
13. S. Raza, S. I. Bozhevolnyi, M. Wubs, and N. A. Mortensen, "Nonlocal optical response in metallic nanostructures," J. Phys. **27**, 1–17 (2015).
14. P. Ginzburg, A. V. Krasavin, and A. V. Zayats, "Cascaded second-order surface plasmon solitons due to intrinsic metal nonlinearity," New J. Phys. **15**, 013031 (2013).
15. A. Marini, M. Conforti, G. Della Valle, H. W. Lee, Tr. X. Tran, W. Chang, M. A. Schmidt, S. Longhi, P. St. J. Russell, and F. Biancalana, "Ultrafast nonlinear dynamics of surface plasmon polaritons in gold nanowires due to the intrinsic nonlinearity of metals," New J. Phys. **15**, 013033 (2013).
16. M. Conforti and G. Della Valle, "Derivation of third-order nonlinear susceptibility of thin metal films as a delayed optical response," Phys. Rev. B **85**, 245423 (2012).
17. I. H. Malitson, "Interspecimen comparison of the refractive index of fused silica," J. Opt. Soc. Am. **55**, 1205–1209 (1965).
18. T. J. Bright, J. I. Watjen, Z. M. Zhang, C. Muratore, A. A. Voevodin, D. I. Koukis, D. B. Tanner, and D. J. Arenas, "Infrared optical properties of amorphous and nanocrystalline Ta_2O_5 thin films," J. Appl. Phys. **114**, 083515 (2013).
19. V. Klimov, *Nanoplasmonics* (Pan Stanford, 2014).
20. U. Kreibig and M. Vollmer, *Optical Properties of Metal Clusters* (Springer, 1995).
21. J. A. Gordon and R. W. Ziolkowski, "The design and simulated performance of a coated nano-particle laser," Opt. Express **15**, 2622–2653 (2007).
22. S. A. Maier, *Plasmonics: Fundamentals and Applications* (Springer, 2007).
23. R. Malureanu and A. Lavrinenko, "Ultra-thin films for plasmonics: a technology overview," Nanotechnol. Rev. **4**, 1–17 (2015).
24. P. Yeh, *Optical Waves in Layered Media* (Wiley, 1988).
25. R. G. Hunsperger, *Integrated Optics: Theory and Technology* (Springer, 2002).
26. D. Milam, "Review and assessment of measured values of the nonlinear refractive-index coefficient of fused silica," Appl. Opt. **37**, 546–550 (1998).
27. C. Y. Tai, J. S. Wilkinson, N. M. B. Perney, M. C. Netti, F. Cattaneo, C. E. Finlayson, and J. J. Baumberg, "Determination of nonlinear refractive index in a Ta_2O_5 rib waveguide using self-phase modulation," Opt. Express **12**, 5110–5116 (2004).
28. R. W. Boyd, *Nonlinear Optics* (Elsevier, 2008).
29. A. Baron, S. Larouche, D. J. Gauthier, and D. R. Smith, "Scaling of the nonlinear response of the surface plasmon polariton at a metal/dielectric interface," J. Opt. Soc. Am. B **32**, 9–14 (2015).
30. Q. Lin, O. J. Painter, and G. P. Agrawal, "Nonlinear optical phenomena in silicon waveguides: modeling and applications," Opt. Express **15**, 16604–16644 (2007).
31. L. Yin and G. P. Agrawal, "Impact of two-photon absorption on self-phase modulation in silicon waveguides," Opt. Lett. **32**, 2031–2033 (2007).
32. S. Afshar V. and T. M. Monro, "A full vectorial model for pulse propagation in emerging waveguides with subwavelength structures part I: Kerr nonlinearity," Opt. Express **17**, 2298–2318 (2009).

Paper C

O. Lysenko, M. Bache, and A. Lavrinenko

Third-order susceptibility of gold for ultrathin layers

Opt. Lett. 41, 2, 317 (2016).

Optics Letters

Third-order susceptibility of gold for ultrathin layers

Oleg Lysenko,* Morten Bache, and Andrei Lavrinenko

Department of Photonics Engineering, Technical University of Denmark, Oersteds Plads, Building 345 V, Kongens Lyngby 2800, Denmark
**Corresponding author: ollyse@fotonik.dtu.dk*

Received 5 November 2015; revised 29 November 2015; accepted 30 November 2015; posted 2 December 2015 (Doc. ID 253294); published 8 January 2016

This Letter presents an experimental study of nonlinear plasmonic effects in gold-stripe waveguides. The optical characterization is performed by a picosecond laser and reveals two nonlinear effects related to propagation of long-range surface plasmon polaritons: nonlinear power transmission of plasmonic modes and spectral broadening of plasmonic modes. The experimental values of the third-order susceptibility of the gold layers are extracted. They exhibit a clear dependence on layer thickness. © 2016 Optical Society of America

OCIS codes: (250.5403) Plasmonics; (230.7370) Waveguides; (190.4400) Nonlinear optics, materials; (240.6680) Surface plasmons.

http://dx.doi.org/10.1364/OL.41.000317

Plasmonic waveguides possess unique optical properties. They are utilized in many applications, such as components of integrated optics [1], nanofocusing of electromagnetic radiation [2], sensors [3], and photodetectors [4]. The nonlinear optical effects associated with propagation of long-range surface plasmon polaritons (LRSPPs) are investigated much less. There are several theoretical approaches to explain the third-order nonlinear susceptibility $\chi^{(3)}$ of metals in plasmonic waveguides. One approach is related to the hydrodynamic model [5], and excitation of phase-mismatched second-order nonlinearities also invokes an effective cubic nonlinearity [6]. Another approach is related to the thermo-modulational interband derivative [7]. In the latter case, the third-order susceptibility for bulk gold is derived from the two-temperature model [8]. However, there are very few experimental data on $\chi^{(3)}$ in the case of thin metal layers. An overview of some theoretical and experimental results related to $\chi^{(3)}$ of gold has been published recently by Boyd *et al.* [9]. In particular, the real and imaginary components of the third-order susceptibility of thin gold layers have been measured using the z-scan method [10]. Third-harmonic generation from gold nanoparticles over thin gold layers has been reported recently [11]. The enhancement of nonlinear properties can be even more pronounced if the metamaterials concept is involved as shown in [12].

Here we experimentally study propagation of ultrafast picosecond pulses in the LRSPP mode in ultrathin gold layers. The nonlinear propagation effects reveal self-phase modulation (SPM) and nonlinear losses, giving access to the real and imaginary part of $\chi^{(3)}$, respectively. To our knowledge, such a study has not yet been done in plasmonic waveguides; an earlier study [13] used instead cw-like pumping and obtained significant thermal contributions to the nonlinear phase. As adhesion for gold-strip waveguides we chose tantalum pentoxide. Its nonlinear properties are well-known [14], and it provides fewer propagation losses in plasmonic waveguides than metallic adhesion materials, such as titanium [15]. The third-order nonlinearities of all constituent materials [metal, adhesion layer, and cladding (here, silica)] contribute to the *effective* third-order nonlinearity of a plasmonic waveguide mode. Two nonlinear optical effects in the plasmonic waveguides are observed and quantified in the experiment. The first effect is the nonlinear transmission and saturation of the output power of the LRSPP mode. The second effect is the spectral broadening of the LRSPP mode. Both effects are measured for several values of the metal thickness. The third-order susceptibility of gold layers is extracted from experimental data, and the obtained results show the effective enhancement of the nonlinearities for thinner metal layers.

The samples with plasmonic waveguides were fabricated on a silicon wafer with a thick (~6.5 μm) silica layer on top. A standard UV lithography process was applied to pattern a photoresist layer. Then, a metal layer and adhesion layers were deposited using a sputtering machine. A chemical solution (Piranha) was used to remove the photoresist layer afterward. The profile contained four layers: bottom adhesion layer (~26 nm), metal layer (~27 nm), top adhesion layer (~26 nm), and small silicon dioxide layer (~21 nm). The layers were deposited one after another in one sputtering program, and the known deposition times and rates were used to calculate the thickness values. The atomic force microscope Dimension Icon (Bruker) was used to measure the waveguide profile [Fig. 1(a)] and metal layers roughness [Fig. 1(b)]. The inset in Fig. 1(a) shows the deposited multilayer structure. The sharp edges on the waveguide profile are the usual artifacts after the liftoff procedure [16]. The roughness profile on the metal surface shows the spikes with the maximum height values ~2 nm. The root mean square (RMS) value for the roughness of the deposited metal layers is 0.67 nm. Several measurements of 2 μm regions at arbitrary

0146-9592/16/020317-04$15/0$15.00 © 2016 Optical Society of America

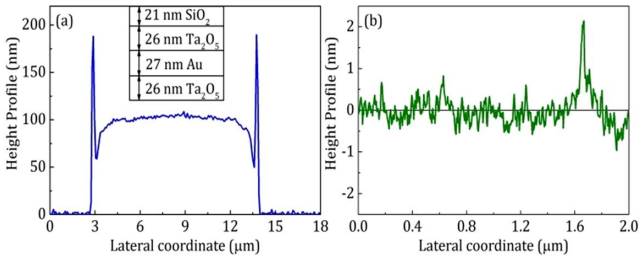

Fig. 1. Atomic force microscope measurements: (a) waveguide profile and layers scheme and (b) metal layer roughness. The inset shows the multilayer waveguide deposited on the silica substrate.

places were performed and confirmed the reported RMS roughness.

To verify the roughness for the inner layers of the waveguide structure (gold and adhesion), a separate test wafer was prepared. A silicon wafer with a thick (~800 nm) layer of silicon dioxide was used as a substrate. A metal layer and an adhesion layer were deposited on top by the same procedure, but in different parts of the wafer. Their surfaces were imaged by the scanning electron microscope LEO (Carl Zeiss). The gold surface [Fig. 2(a)] has many bright dots related to the roughness spikes, and Ta_2O_5 surface [Fig. 2(b)] is smooth and free from any particles. The imaging shows that both layers are continuous and of high quality.

After the sputtering of the waveguides, a 5.5 μm cladding layer of silica was deposited on top using a standard plasma-enhanced chemical vapor deposition method. The cladding thickness and linear refractive index were measured by a multiple-angle reflectometer (FilmTek 4000). The refractive index for deposited silica is 1.456 at 1064 nm. Overall, three wafers with the metal layer thicknesses $t = 22$, 27, and 35 nm were fabricated by the same procedure and used in the experiment. The ready wafers were diced and several samples with lengths 2, 3, and 4 mm were selected for optical characterization. Each sample contained five identical waveguides with 10 μm width, and 100 μm spacing. Thus, the plasmonic waveguides do not interfere with each other and can be investigated independently.

The experimental setup is shown in Fig. 3. The laser source is the picosecond pump source for the SuperK EXTREME (NKT Photonics) with the average output power tunable in the range 0–15 W, repetition rate 78 MHz, pulse duration ~3 ps, and peak wavelength 1064 nm. The free-space laser beam was linearly polarized by a polarizer (Thorlabs), shaped by a Gaussian filter (10LF04-1064, FWHM 3.5 nm, Newport), attenuated by a set of neutral density (ND) filters, and delivered to the sample by a polarization-maintaining fiber (LMA-PM-10, NKT Photonics). The laser beam polarization was aligned to match the fast axis of the polarization-maintaining fiber and transverse magnetic polarization of the LRSPP mode in plasmonic waveguides. The end-fire coupling method was used

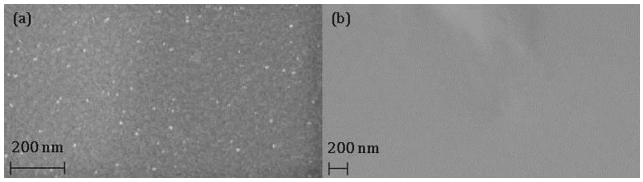

Fig. 2. Scanning electron microscope images: (a) gold surface and (b) tantalum pentoxide surface.

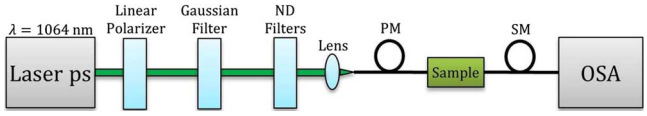

Fig. 3. Experimental setup for nonlinear optical characterization.

to excite plasmonic modes [17]. A single-mode fiber (LMA-10, NKT Photonics) collected and delivered the transmitted optical flux to the optical spectrum analyzer (OSA) AQ6315E (Yokogawa). The end-fire coupling alignment was controlled by an optical microscope. Before the transmission measurements, the LRSPP mode in each waveguide was imaged by a lens (Newport) and camera beam profiler (Thorlabs), and the transverse magnetic polarization of the plasmonic mode was verified by the linear polarizer [18]. This polarization check verifies coupling to the LRSPP mode in each plasmonic waveguide.

First, the linear characterization of the plasmonic waveguides was performed. The laser was tuned to a low average power (<1 mW), and the transmitted power was measured by the OSA for waveguides with different lengths and metal thicknesses. The insertion loss graphs are used to calculate propagation loss α per unit length and coupling loss C per two facets (Table 1). For each value of the length and thickness, the measurements of five identical waveguides are averaged, and the linear fit is calculated by the least squares method. The obtained experimental values show that the linear propagation loss per unit length increases in ~1.8 times as the gold layer thickness increases from 22 to 35 nm. The coupling loss per two facets varies by ~10%, and is completely within the calculation errors. This conclusion is in accordance with the previous measurements of the similar plasmonic waveguides [19]. The obtained values for α are ~2–3 times higher than the results published by Berini *et al.*, and several possible reasons explain this. First, the maximum values of the roughness spikes of the gold layers are ~2 nm, in comparison with ~1 nm in Ref. [19]. Second, the peak wavelength 1550 nm used in Ref. [19] provides lower attenuation of the LRSPP mode in plasmonic waveguides than the peak wavelength, 1064 nm [20]. We expect that the sharp edges on the waveguide profile in Fig. 1(a) do not contribute significantly to the propagation losses as the field intensity of the LRSPP mode is close to zero at the waveguide edges [20].

In order to obtain the necessary amount of measurements, the input power was varied by either changing the ND filters or the output power from the laser. The transmitted power was measured by the OSA for the 3 mm waveguides. The obtained dependencies of transmitted power P_{out} with respect to delivered power P_{in} have nonlinear trends of dependencies $P_{out}(P_{in})$ at high values of input power (Fig. 4). These nonlinear trends depend on the metal layers' thickness. The plasmonic waveguides with thinner metal layers have more pronounced rel-

Table 1. Experimental Values of the Propagation and Coupling Loss for LRSPP with Gold Layers of Different Thicknesses and Fit Coefficients α and b for the Plasmonic Waveguides

t (nm)	α (dB/mm)	C (dB)	a	b (1/W)
22	7.8 ± 0.2	3.2 ± 0.5	$2.26 \cdot 10^{-3}$	$1.54 \cdot 10^{-3}$
27	11.1 ± 0.2	3.3 ± 0.8	$2.49 \cdot 10^{-4}$	$1.38 \cdot 10^{-4}$
35	13.8 ± 0.3	3.5 ± 1.0	$6.53 \cdot 10^{-6}$	$3.09 \cdot 10^{-6}$

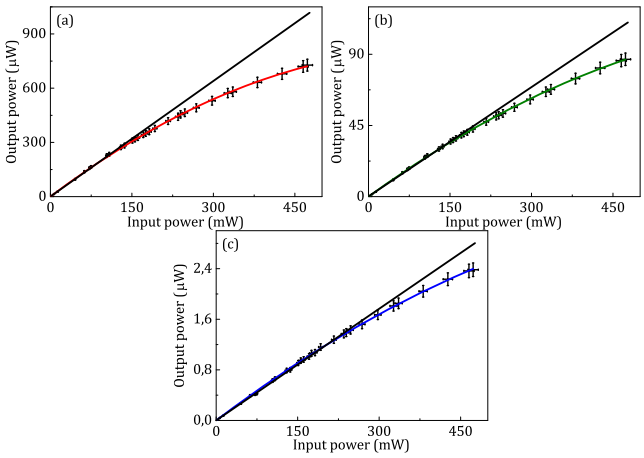

Fig. 4. Nonlinear power transmission for plasmonic waveguides with the gold layer thickness (a) $t = 22$ nm, (b) $t = 27$ nm, and (c) $t = 35$ nm. Black lines on each graph correspond to the fitted linear trend.

ative deviation from the linear power dependences at the same values of P_{in}. The second feature is that these nonlinear trends depend on the metal layers' thickness. The plasmonic waveguides with thinner metal layers have more pronounced relative deviation from the linear power dependences at the same values of the input power. For each value of the metal thickness the measurements of five identical waveguides are averaged and the nonlinear curve fit is calculated a $P_{out} = aP_{in} - bP_{in}^2$, where a and b are the fitting coefficients. Here the input and output powers are corrected for the coupling loss at the end facets. The calculated values for a and b are presented in Table 1. The coefficient a is related to the linear loss parameter α of the LRSPP mode as $a = e^{-\alpha l}$, where l is the waveguide length. The calculated values of α are 8.82 dB/mm, 12.0 dB/mm, and 17.3 dB/mm for the metal thicknesses 22, 27, and 35 nm, respectively. These values are somewhat higher than the values of linear losses at low-power characterization, and the origin of this is at present unclear. The coefficient b is related to nonlinear absorption coefficient β of the plasmonic mode. The nonlinearities of the constituent materials (metal, adhesion, and cladding) in plasmonic waveguides, as well as heating for high powers, contribute to the effective nonlinearity of the LRSPP mode.

In terms of the nonlinear response of the constituent materials, gold has a dominant contribution in the effective third-order susceptibility $\chi_{eff}^{(3)}$ of the plasmonic mode [21]. It is related to the nonlinear coefficient β as $\beta = \beta_c/A_{eff} = (3\omega \mathrm{Im}[\chi_{eff}^{(3)}])/(2\varepsilon_0 c^2 n_0^2 A_{eff})$. Here β_c is the conventional definition of the nonlinear absorption coefficient [22], $\omega = 2\pi c/\lambda$ is the light angular frequency, c is the speed of light in vacuum, ε_0 is the vacuum permittivity, n_0 is the effective linear refractive index, and A_{eff} is the effective area of the LRSPP mode. The nonlinear coefficient b depends on both the nonlinear parameters of the LRSPP mode and the laser parameters. By considering the pulse-propagation equation [23], it is straightforward to show that the ratio $b/a \approx \beta/(\alpha T f_{rep})$, where T is the laser pulse duration, and f_{rep} is the laser repetition rate. We analyzed the structure of our plasmonic waveguides, where the total effective nonlinearity has contributions from all layers, calculated through the overlap integral of the spatial distribution of the plasmonic mode in each layer and using the respective bulk nonlinearities. The values of the field integrals from the gold core θ_{Au} are $\sim 1.1 \times 10^{-4}$, $\sim 1.4 \times 10^{-4}$, and $\sim 1.9 \times 10^{-4}$ for the layers thickness 22, 27, and 35 nm, respectively. And the values of the effective area of the waveguide are ~ 11.2 μm^2, ~ 10.2 μm^2, and ~ 9.2 μm^2, respectively. Through this analysis, which will be presented in detail elsewhere, we found that gold has by far the dominating contribution to the total effective nonlinearity: the contribution from the gold layer is 2 orders of magnitude bigger ($\sim 10^{-20}$ m^2/V^2) than the one from the tantalum pentoxide layer ($\sim 10^{-22}$ m^2/V^2), although the latter has a quite large cubic nonlinearity [14]. The calculated value of the real part of the effective refractive index of the plasmonic mode $\mathrm{Re}[n_{eff}] \approx 1.47$ is much larger than the value of its imaginary part $\mathrm{Im}[n_{eff}] \approx 0.01$. Therefore we can take as a good approximation the following formula for the nonlinear absorption coefficient $\beta \approx (3\omega\theta_{Au}\mathrm{Im}[\chi_{Au}^{(3)}])/(2\varepsilon_0 c^2 n_0^2 A_{eff})$, where $\chi_{Au}^{(3)}$ is the third-order susceptibility of the gold layers, and coefficients a and b are used to extract the imaginary part of $\chi_{Au}^{(3)}$.

The spectra of the transmitted optical flux were measured by the OSA and in the range 1058–1069 nm (Fig. 5). The spectral broadening and splitting are observed, a clear sign of SPM influenced by two-photon absorption from the real and imaginary part of $\chi^{(3)}$, respectively [24]. This was confirmed with numerical simulations of the nonlinear Schrödinger equation, giving almost identical spectra as those in Fig. 5, where the experimental input pulse was used and no free parameters were adopted (all linear and nonlinear parameters were those calculated by our waveguide analysis or measured experimentally). The spectral broadening and splitting in the output spectra differs slightly for each case. We compared the values of the effective spectral widths for the input pulse and output pulses at the splitting level (~0.05), where for simplicity, the side peaks with lower intensities (~0.01–0.03) were neglected. To do an analytical estimate, we approximate the input pulse with a Gaussian one and calculate the nonlinear spectral broadening factor (SBF) from comparing it to a Gaussian fit to the two distinct SPM peaks. The SBF then relates to the effective nonlinear coefficient γ by [23]:

$$\mathrm{SBF} \approx 0.86\gamma P_0 \frac{1 - e^{-\alpha l}}{\alpha}\gamma = \frac{\omega}{c}\frac{n_{2eff}}{A_{eff}}, \quad (3)$$

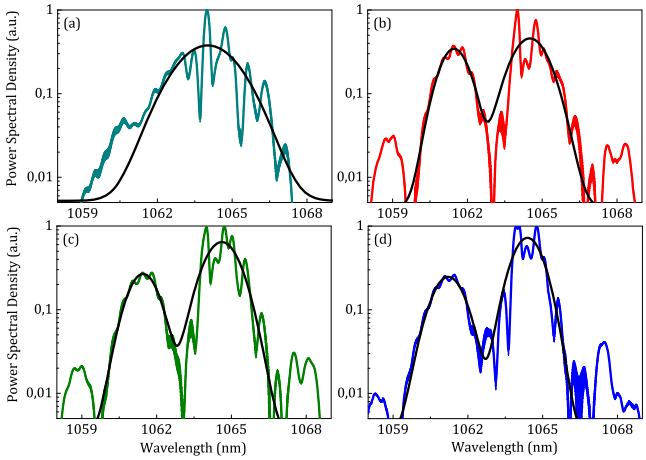

Fig. 5. (a) Input pulse spectrum, and output pulse spectra for plasmonic waveguides at the maximum input power (~480 mW) with the gold layer thickness (b) $t = 22$ nm, (c) $t = 27$ nm, and (d) $t = 35$ nm. Black lines on graph show a Gaussian fit to the measured spectra.

Table 2. Third-Order Susceptibility of Gold Layers with Different Thicknesses

t (nm)	$\mathrm{Re}[\chi^{(3)}_{\mathrm{Au}}]$ ($\mathrm{m^2/V^2}$)	$\mathrm{Im}[\chi^{(3)}_{\mathrm{Au}}]$ ($\mathrm{m^2/V^2}$)
22	$(2.57 \pm 0.84) \cdot 10^{-16}$	$(10.50 \pm 2.08) \cdot 10^{-18}$
27	$(2.18 \pm 0.61) \cdot 10^{-16}$	$(8.22 \pm 1.49) \cdot 10^{-18}$
35	$(1.79 \pm 0.48) \cdot 10^{-16}$	$(6.51 \pm 1.38) \cdot 10^{-18}$

where $\gamma = (\omega n_{2\mathrm{eff}})/(cA_{\mathrm{eff}})$, P_0 is the peak power of an input pulse, $n_{2\mathrm{eff}}$ is the effective intensity-dependent refractive index of the LRSPP mode, and l is the length of a plasmonic waveguide. This result assumes a purely Gaussian input pulse, which is transform-limited (no chirp across the pulse). Although the input pulse in the experiment was not transform-limited and its spectrum had multiple modulated peaks, this expression serves as a rough estimate of the effective waveguide nonlinearity γ in the sample; such an approach is also justified by the close agreement with the numerical simulations. Using the relation between $n_{2\mathrm{eff}}$ and $\mathrm{Re}[\chi^{(3)}_{\mathrm{eff}}]$ the following formula is realized $\gamma \approx (3\omega\theta_{\mathrm{Au}}\mathrm{Re}[\chi^{(3)}_{\mathrm{Au}}])/(4\varepsilon_0 c^2 n_0^2 A_{\mathrm{eff}})$, since as argued above for the nonlinear loss, the dominating contribution comes from gold. . The experimental values of the SBF are used to extract the real part of $[\chi^{(3)}_{\mathrm{Au}}]$ of the gold layers.

The calculated values of the third-order susceptibility for gold layers with different thicknesses, and the calculation errors are presented in Table 2. Both the real and imaginary parts decrease as the layer thickness increases. The values for the third-order susceptibility are plotted in Fig. 6 and the nonlinear curve fit is calculated as $\chi^{(3)}_{\mathrm{Au}} = \chi^{(3)}_{\infty} + C/t$, where $\chi^{(3)}_{\infty}$ is the third-order susceptibility for bulk gold [8], and C is the experimental coefficient. The fitting $1/t$ here is done by analogy with the change of the electrons' collisions frequency in metal nanoparticles with the radius [25]. The calculated values for the real and imaginary parts of the experimental coefficient C are: $\mathrm{Re}[C] = (5.82 \pm 0.15) \times 10^{-24}$ $\mathrm{m^3/V^2}$, and $\mathrm{Im}[C] = (9.34 \pm 1.79) \times 10^{-26}$ $\mathrm{m^3/V^2}$. For comparison we plot also the third-order susceptibility for bulk gold $\chi^{(3)}_{\infty} = (4.56 + 0.48i) \times 10^{-17}$ $\mathrm{m^2/V^2}$ [8].

The experimental values of the real part of $\chi^{(3)}_{\mathrm{Au}}$ are ~4–5 times higher than the real part of $\chi^{(3)}_{\infty}$ for bulk gold. And experimental values of the imaginary part of $\chi^{(3)}_{\mathrm{Au}}$ are ~1.5–2 times higher. Such $\chi^{(3)}_{\mathrm{Au}}$ behavior is in accordance with previous measurements of thin gold layers using the z-scan method [10]. Figure 6 also indicates the thickness limitations. Application of the Drude model to ultrathin gold layers is questionable; also, the possible layer clustering process [26] makes fabrication of such waveguides challenging. On the other side, the LRSPP mode breaks down at the gold layers' thicknesses above 50–60 nm due to the small penetration depth of the electromagnetic field in metal [20].

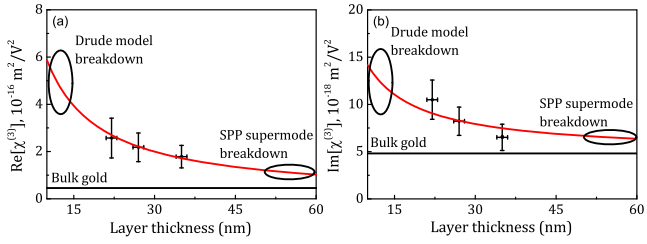

Fig. 6. (a) Real part and (b) imaginary part of the third-order susceptibility for gold layers with different thicknesses.

There are two possible reasons to explain the increase of the third-order susceptibility in gold layers with reduction of their thickness. First, the effective enhancement of the third-order nonlinearity in an ultrathin metal layer can be caused by the change in the free electrons' motion due to the confinement factor. Consequently, their collisions frequency increases, and it leads to the effective increase of the dielectric permittivity of a metal layer. This, in turn, causes the increase of the third-order susceptibility of the metal layer. Second, by considering the ultrafast electrons dynamics in metal [8], it is possible to assume that, for the electrons heated by a laser pulse, the characteristic thermalization rates with other electrons and the metal lattice change with the thickness. It may also lead to the effective enhancement of the third-order susceptibility in a metal layer [8].

Acknowledgment. The authors thank R. Malureanu, G. Wurtz, and A. Zayats for the valuable comments regarding the fabrication process and the fruitful discussions.

REFERENCES

1. A. Maradudin, J. Sambles, and W. Barnes, *Modern Plasmonics* (Elsevier, 2014).
2. D. Gramotnev and S. Bozhevolnyi, Nat. Photonics **8**, 13 (2014).
3. O. Krupin, H. Asiri, C. Wang, R. N. Tait, and P. Berini, Opt. Express **21**, 698 (2013).
4. P. Berini, Laser Photon. Rev. **8**, 197 (2014).
5. M. Scalora, M. Vincenti, D. de Ceglia, V. Roppo, M. Centini, N. Akozbek, and M. Bloemer, Phys. Rev. A **82**, 043828 (2010).
6. P. Ginzburg, A. Krasavin, and A. Zayats, New J. Phys. **15**, 013031 (2013).
7. M. Conforti and G. Della Valle, Phys. Rev. B **85**, 245423 (2012).
8. A. Marini, M. Conforti, G. Della Valle, H. W. Lee, T. X. Tran, W. Chang, M. A. Schmidt, S. Longhi, P. St. J. Russell, and F. Biancalana, New J. Phys. **15**, 013033 (2013).
9. R. Boyd, Z. Shi, and I. De Leon, Opt. Commun. **326**, 74 (2014).
10. E. Xenogiannopoulou, P. Aloukos, S. Couris, E. Kaminska, A. Piotrowska, and E. Dynowska, Opt. Commun. **275**, 217 (2007).
11. G. Hajisalem, D. K. Hore, and R. Gordon, Opt. Mater. Express **5**, 2217 (2015).
12. A. D. Neira, N. Olivier, M. Nasir, W. Dickson, G. Wurtz, and A. Zayats, Nat. Commun. **6**, 7757 (2015).
13. A. Huck, D. Witthaut, S. Kumar, A. Soerensen, and U. L. Andersen, Plasmonics **8**, 1597 (2013).
14. C. Tai, J. S. Wilkinson, N. M. B. Perney, M. Caterina Netti, F. Cattaneo, C. E. Finlayson, and J. J. Baumberg, Opt. Express **12**, 5110 (2004).
15. T. G. Habteyes, S. Dhuey, E. Wood, D. Gargas, S. Cabrini, P. J. Schuck, P. Alivisatos, and S. R. Leone, ACS Nano **6**, 5702 (2012).
16. O. Geschke, H. Klank, and P. Telleman, *Microsystem Engineering of Lab-on-a-Chip Devices* (Wiley, 2004).
17. R. Hunsperger, *Integrated Optics: Theory and Technology* (Springer, 2002).
18. R. Charbonneau, P. Berini, E. Berolo, and E. Lisicka-Shrzek, Opt. Lett. **25**, 844 (2000).
19. P. Berini, R. Charbonneau, N. Lahoud, and G. Mattiussi, J. Appl. Phys. **98**, 043109 (2005).
20. S. Maier, *Plasmonics: Fundamentals and Applications* (Springer, 2007).
21. A. Baron, S. Larouche, D. J. Gauthier, and D. R. Smith, J. Opt. Soc. Am. B **32**, 9 (2015).
22. R. Boyd, *Nonlinear Optics* (Academic, 2008).
23. G. Agrawal, *Nonlinear Fiber Optics* (Academic, 2007).
24. L. Yin and G. P. Agrawal, Opt. Lett. **32**, 2031 (2007).
25. J. A. Gordon and R. W. Ziolkowski, Opt. Express **15**, 2622 (2007).
26. U. Kreibig and M. Vollmer, *Optical Properties of Metal Clusters* (Springer, 1995).

Paper D

O. Lysenko, M. Bache, A. Zayats, and A. Lavrinenko

Effective third-order nonlinearity of plasmonic waveguides for ultrashort laser pulses

Danish Physical Society Annual Conference, Book of Abstracts, p. 27, June 6-7, 2016, Middelfart, Denmark.

Title: Effective third-order nonlinearity of plasmonic waveguides for ultrashort laser pulses

Oleg Lysenko[1,*], Morten Bache[1], Anatoly V. Zayats[2], and Andrei Lavrinenko[1]

[1] DTU Fotonik, Technical University of Denmark, DK-2800, Kongens Lyngby, Denmark
[2] Department of Physics, King's College London, Strand, London WC2R 2LS, UK

[*]Contact Author E-Mail: ollyse@fotonik.dtu.dk

Abstract:

This presentation describes experimental and theoretical studies of the effective third-order susceptibility $\chi^{(3)}$ of the long-range surface plasmon polariton (LRSPP) mode in gold strip waveguides. The investigated plasmonic waveguides were fabricated in house [1], and contain a gold strip core with the layer width 10 μm and thicknesses 22, 27, and 35 nm, tantalum pentoxide adhesion layers, and silica cladding. This particular geometry provides effective propagation of the LRSPP mode in the millimeter range. We performed the nonlinear optical characterization of the waveguides, using a high power femtosecond laser source. The laser source was the femtosecond laser amplifier PHAROS (Light Conversion), providing ~200 fs FWHM pulses with a 200 kHz repetition rate at a center wavelength of 1030 nm. This wavelength was suitable to optimize the linear absorption losses and mode confinement in the plasmonic waveguides [2]. The nonlinear power transmission of the LRSPP mode in the plasmonic waveguides was observed, and the values of the imaginary part of the third-order susceptibility $\chi^{(3)}_{\mathrm{Au}}$ (~10^{-19} m^2/V^2) of the gold layers with different thicknesses were extracted from experimental data. They significantly depend on the laser pulse duration, comparing to the values of the imaginary component of $\chi^{(3)}_{\mathrm{Au}}$ ~10^{-17}-10^{-18} m^2/V^2 obtained previously at 1064 nm and 3-ps laser pulses [1]. To explain the experimental results on the third-order susceptibility of gold at different pulse durations, we apply the two-temperature model of electron temporal dynamics in gold. The theoretical dependence of the real and imaginary parts of $\chi^{(3)}_{\mathrm{Au}}$ with respect to the pulse duration for bulk gold and thin gold layers was obtained in the range 10 fs to 10 ps. It indicates significant adjustability of the real and imaginary parts of $\chi^{(3)}_{\mathrm{Au}}$ over ~4 orders of magnitude in this pulse duration range, and explains well the obtained experimental results. Such tunability of $\chi^{(3)}_{\mathrm{Au}}$ can be one of the principal advantages of plasmonic waveguides on the way towards future plasmonic communication components, comparing to standard communication approaches based on dielectric nonlinearities [3]. We also discuss the thickness dependence of $\chi^{(3)}_{\mathrm{Au}}$. The effective enhancement of $\chi^{(3)}_{\mathrm{Au}}$ for thinner metal layers can be explained by considering the effective change in the electrons motion. When the gold layer thickness approaches the nanoscale, the electrons start to feel the layer boundaries. Their collision frequency increases in several times, and it leads to changes in the real and imaginary parts of the dielectric permittivity of metal. In turn, this causes the effective enhancement of the thermo-modulational interband susceptibility of the metal layer. Therefore, the effective third-order nonlinearity of plasmonic waveguides significantly depends on two parameters: gold core thickness and laser pulse duration. The obtained results can be exploited for the development of future plasmonic communications.

[1] O. Lysenko, M. Bache, and A. Lavrinenko, Opt. Lett. **41**, 2, 317 (2016).
[2] S. Maier, *Plasmonics: Fundamentals and Applications* (Springer, 2007).
[3] G. Agrawal, *Nonlinear Fiber Optics* (Academic Press, 2007).

Paper E

O. Lysenko, M. Bache, R. Malureanu, and A. Lavrinenko

Nonlinear effects in propagation of long-range surface plasmon polaritons in gold strip waveguides

Proceedings of SPIE International Conference Photonics Europe, vol. 9884, 988420, p. 1-12, April 3-7, 2016, Brussels, Belgium.

Nonlinear effects in propagation of long-range surface plasmon polaritons in gold strip waveguides

Oleg Lysenko*, Morten Bache, Radu Malureanu, Andrei Lavrinenko
Department of Photonics Engineering, Technical University of Denmark,
Oersteds Plads, Building 345 V, Kongens Lyngby 2800, Denmark

ABSTRACT

This paper is devoted to experimental and theoretical studies of nonlinear propagation of a long-range surface plasmon polariton (LRSPP) in gold strip waveguides. The plasmonic waveguides are fabricated in house, and contain a gold layer, tantalum pentoxide adhesion layers, and silicon dioxide cladding. The optical characterization was performed using a high power picosecond laser at 1064 nm. The experiments reveal two nonlinear optical effects: nonlinear power transmission and spectral broadening of the LRSPP mode in the waveguides. Both nonlinear optical effects depend on the gold layer thickness. The theoretical model of these effects is based on the third-order susceptibility of the constituent materials. The linear and nonlinear parameters of the LRSPP mode are obtained, and the nonlinear Schrödinger equation is solved. The dispersion length is much larger than the waveguides length, and the chromatic dispersion does not affect the propagation of the plasmonic mode. We find that the third-order susceptibility of the gold layer has a dominant contribution to the effective third-order susceptibility of the LRSPP mode. The real part of the effective third-order susceptibility leads to the observed spectral broadening through the self-phase modulation effect, and its imaginary part determines the nonlinear absorption parameter and leads to the observed nonlinear power transmission. The experimental values of the third-order susceptibility of the gold layers are obtained. They indicate an effective enhancement of the third-order susceptibility for the gold layers, comparing to the bulk gold values. This enhancement is explained in terms of the change of the electrons motion.

Keywords: Plasmonics, nonlinear waveguides, ultrafast nonlinear optics, surface plasmon polaritons

1. INTRODUCTION

Plasmonic waveguides have unique optical properties, and found applications in many areas, such as components of integrated optics [1], nanofocusing of electromagnetic radiation [2], sensors [3], and photodetectors [4]. Meanwhile, nonlinear optical properties of plasmonic waveguides (with one or several metal-dielectric interfaces) are investigated much less. This problem is tricky, because the nonlinear metal properties are not yet well understood. One of the possible theoretical approaches here is based on the hydrodynamic model for the free-electron gas [5]. In other works, the nonlinear propagation of the LRSPP modes in plasmonic waveguides is studied in terms of either the cascaded second-order nonlinearity at a metal-dielectric interface [6] or the third-order nonlinearity of metal and dielectric in plasmonic nanorod structures [7]. In the latter case, the third-order nonlinearity for gold is obtained from the two-temperature model of electrons dynamics [8] and the ideal lossless metal is assumed [7]. An overview of some theoretical and experimental results related to the third-order susceptibility of gold has been published recently by Boyd et al. [9]. The enhancement of nonlinear properties can even overcome the constituent material's constrains if the metamaterials concept is involved [10].

Recent experiments confirm the presence of nonlinear propagation effects in plasmonic waveguides, much like the ones that for decades have been fueling nonlinear fiber optics [11]. We recently conducted an experiment [12] using the same system used in the present paper, namely a strip plasmonic gold waveguide, and we observed that the loss performance was nonlinear as the power was increased, which we attributed to the imaginary part of the nonlinearity of gold, and we also saw indications of self-phase modulation (SPM) in the spectrum. Both effects were significantly affected by the nanometer-scale thickness of the gold layer. To our knowledge such a study has not yet been done in plasmonic waveguides; an early study [13] used instead cw-like pumping and obtained significant thermal contributions to the nonlinear phase. In another recent experiment Baron et al. [14] measured the imaginary component of the third-order

*ollyse@fotonik.dtu.dk

Nanophotonics VI, edited by David L. Andrews, Jean-Michel Nunzi, Andreas Ostendorf, Proc. of SPIE
Vol. 9884, 988420 · © 2016 SPIE · CCC code: 0277-786X/16/$18 · doi: 10.1117/12.2224500

susceptibility for bulk gold by studying nonlinear propagation of surface-plasmon polaritons on a single air/metal interface.

In our experiment, the fabricated plasmonic strip waveguides consist of a gold core, tantalum pentoxide adhesion layers, and silicon dioxide cladding. This configuration provides effective propagation of the LRSPP mode [15]. We take into account that all constituent materials (metal, adhesion layer, and cladding) exhibit a nonlinear response and attribute an effective nonlinearity of the LRSPP waveguide mode, and for the metal part of the waveguide the linear and nonlinear losses are considered as well. This effective nonlinearity of the LRSPP mode leads to two interesting nonlinear effects. The first effect is a nonlinear saturation of the average power of the plasmonic mode. The second effect is a nonlinear phase modulation with spectral broadening of the LRSPP mode. Our theoretical model solves the nonlinear Schrödinger equation for the LRSPP mode, and confirms the observed nonlinear effects.

2. FABRICATION PROCESS

The samples with waveguides were fabricated in house, according to the following procedure. A silicon wafer with a thick (~6.5 μm) layer of SiO_2 on top was used as a substrate. A standard ultraviolet lithography process was applied to pattern a photoresist layer. Then, a gold layer and adhesion layers were deposited using a sputtering machine (Lesker). A chemical solution (Piranha) was used to remove the photoresist layer afterwards. The waveguides profile contained four layers: a bottom Ta_2O_5 layer, Au layer, top Ta_2O_5 layer, and small SiO_2 layer [12]. The layers were deposited one after another in one sputtering program, and the known deposition times and rates were used to calculate the thickness values. It is well-known that the metal layer roughness increases the propagation losses of the LRSPP mode [16]. The atomic force microscope (AFM) Dimension Icon (Bruker) was used to measure the gold layers roughness (Fig. 1a). The roughness profile of the gold surface shows the spikes with the maximum height values ~2 nm. The root mean square (RMS) value for the roughness of the deposited gold layers is 0.67 nm. Several measurements of 2 μm regions at arbitrary places of the gold surface were performed and confirmed the reported RMS roughness.

To verify the quality of the deposited metal and adhesion layers, a separate test wafer was prepared. A silicon wafer with a thick (~800 nm) layer of silicon dioxide was used as a substrate. A gold layer and an adhesion layer were deposited on top by the same procedure, but in different parts of the wafer. Their surfaces were imaged by the scanning electron microscope (SEM) SUPRA (Carl Zeiss). The gold surface (Fig. 1b) has many bright dots related to the roughness spikes. The imaging showed that the both layers are continuous and of high quality.

After the sputtering of the waveguides, a thick (~ 5.5 μm) cladding layer of SiO_2 was deposited on top using a standard plasma-enhanced chemical vapor deposition method. The cladding thickness and linear refractive index were measured by a multiple-angle reflectometer (FilmTek 4000). The refractive index value for deposited silicon dioxide is 1.456 at the wavelength 1064 nm. Overall, three wafers with the gold layer thicknesses t = 22, 27, and 35 nm were fabricated by the same procedure and used in the experiment. The ready wafers were diced and several samples with lengths 2, 3, and 4 mm were selected for optical characterization. Each sample contained five identical waveguides with 10 μm width, and 100 μm spacing. Thus, the waveguides did not interfere with each other and could be investigated independently.

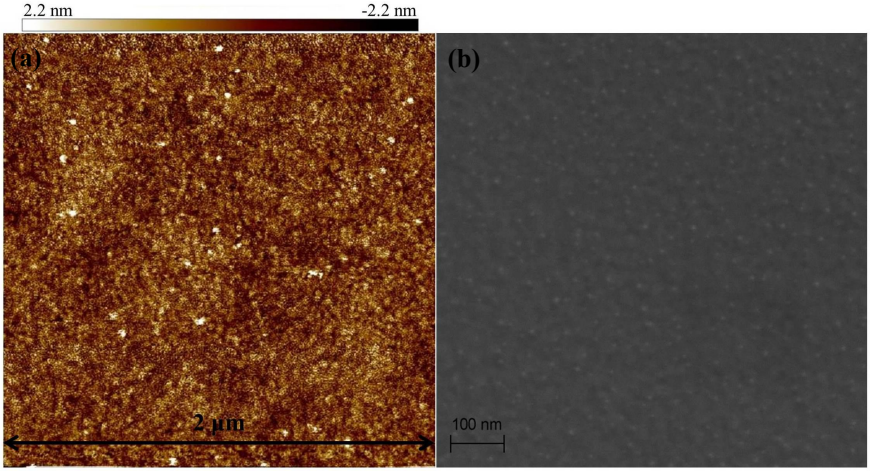

Figure 1. (a) AFM measurement of the gold layers roughness and (b) SEM image of the gold surface.

3. EXPERIMENTAL RESULTS

3.1 Experimental setup

The experimental setup is shown in Fig. 2. The laser source was the picosecond pump source for the SuperK EXTREME (NKT Photonics) with the average output power tunable in the range 0-15 W, repetition rate 78 MHz, pulse duration ~ 3 ps, and peak wavelength 1064 nm. The free-space laser beam was linearly polarized by a polarizer (Thorlabs), shaped by a Gaussian filter (10LF04-1064, FWHM 3.5 nm, Newport), attenuated by a set of neutral-density (ND) attenuation filters, and delivered to the sample by a polarization-maintaining fiber (LMA-PM-10, NKT Photonics). The laser beam polarization was aligned to match the fast axis of the polarization-maintaining fiber and to match the transverse magnetic polarization of the LRSPP mode in plasmonic waveguides. The end-fire coupling method was used to excite plasmonic modes [17]. A single mode fiber (LMA-10, NKT Photonics) collected and delivered the transmitted optical flux to the optical spectrum analyzer (OSA) AQ6315E (Yokogawa). The end-fire coupling alignment was controlled by an optical microscope. Before the transmission measurements, the LRSPP mode in each waveguide was imaged by a lens (Newport) and camera beam profiler (Thorlabs), and the transverse magnetic polarization of the plasmonic mode was verified by the linear polarizer [18]. This polarization check verified coupling to the LRSPP mode in each plasmonic waveguide.

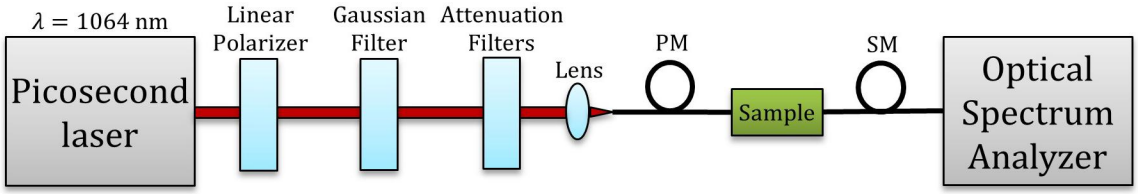

Figure 2. Experimental setup for nonlinear optical characterization.

3.2 Linear characterization

Firstly, the linear characterization of the waveguides was performed. The laser was tuned to a low average power (< 1 mW), and the transmitted power was measured by the OSA for waveguides with different lengths and metal thicknesses. The insertion loss graphs were used to calculate propagation loss α per unit length and coupling loss C per two facets for the plasmonic waveguides with the metal thickness values 22, 27, and 35 nm (Fig. 3). For each value of the length and thickness the measurements of five identical waveguides were averaged, and the linear fit was calculated by the least squares method. The coupling loss was obtained as the intersection of the fitted lines with the vertical axis. The propagation loss was calculated as the slope angle to the fitting lines. The calculated values for α and C, with the calculation errors are presented in Table 1. The obtained experimental values show that the linear propagation loss per unit length increases in ~1.8 times as the gold layer thickness increases from 22 nm to 35 nm. The coupling loss per two facets varies by ~10 %, and is completely within the calculation errors. This conclusion is in accordance with the previous measurements of the similar plasmonic waveguides [19]. The obtained values for α are ~2-3 times higher than the results published by Berini et al., and several possible reasons explain this. First, the maximum values of the roughness spikes of the gold layers are ~2 nm in comparison with ~1 nm in Ref. [19]. Second, the peak wavelength 1550 nm used in Ref. [19] provides lower attenuation of the LRSPP mode in plasmonic waveguides than the peak wavelength 1064 nm [20].

Table 1. Experimental values of the propagation and coupling loss for plasmonic waveguides with different thicknesses.

t (nm)	α (dB/mm)	C (dB)
22	7.8 ± 0.2	3.2 ± 0.5
27	11.1 ± 0.2	3.3 ± 0.8
35	13.8 ± 0.3	3.5 ± 1.0

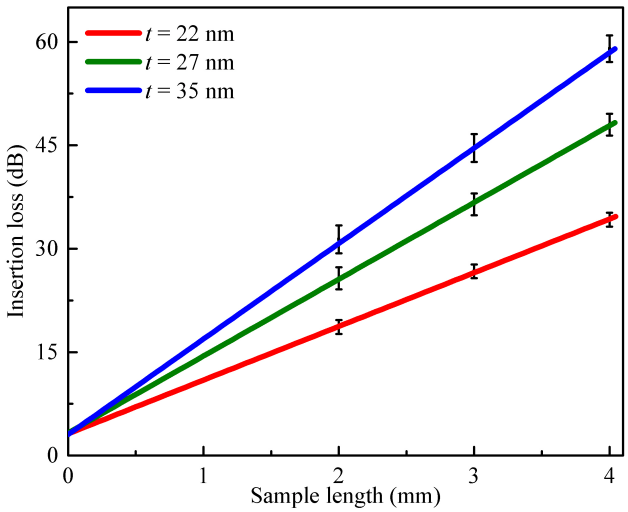

Figure 3. Propagation loss and coupling loss measurements of plasmonic waveguides with different gold layer thicknesses.

3.3 Nonlinear power measurements

Then, the nonlinear characterization of the plasmonic waveguides was performed. In order to obtain the necessary amount of measurements, the input power was varied by either changing the ND attenuation filters or the output power from the laser. The transmitted power was measured by the OSA for the waveguides of length 3 mm and metal thicknesses 22, 27, and 35 nm. The normalized obtained dependencies of the transmitted power P_{out} with respect to the delivered power P_{in} have several interesting features (Fig. 4). The first feature is the nonlinear trends of dependencies $P_{\text{out}}(P_{\text{in}})$ at high values of the input power P_{in}. The second feature is that these nonlinear trends clearly depend on the metal layers thickness. The plasmonic waveguides with thinner metal layers have more pronounced relative deviation from the linear power dependences at the same values of the input power. For each value of the metal thickness the measurements of five identical waveguides are averaged and the nonlinear curve fit was calculated as

$$P_{\text{out}} = aP_{\text{in}} - bP_{\text{in}}^{\,2}, \tag{1}$$

where a and b are the fitting coefficients. Here the input and output powers are corrected for the coupling loss at the end facets. The calculated values for a, and b, with the calculation errors are presented in Table 2. The coefficient a is related to the linear loss parameter α of the LRSPP mode as $a = e^{-\alpha l}$, where l is the waveguide length. The calculated values of α are 8.82 dB/mm, 12.0 dB/mm, and 17.3 dB/mm for the metal thicknesses 22, 27, and 35 nm, accordingly. These values are somewhat higher than the values of linear losses at low power characterization, and the origin of this is at present unclear. The coefficient b is related to nonlinear absorption coefficient β of the plasmonic mode. The nonlinearities of the constituent materials (metal, adhesion, and cladding) in plasmonic waveguides, as well as heating for high powers, contribute to the effective nonlinearity of the LRSPP mode.

Table 2. Fit coefficients a and b for the plasmonic waveguides with different thicknesses.

***t* (nm)**	***a***	***b* (1/W)**
22	$(2.26 \pm 0.01) \cdot 10^{-3}$	$(1.54 \pm 0.02) \cdot 10^{-3}$
27	$(2.49 \pm 0.01) \cdot 10^{-4}$	$(1.38 \pm 0.02) \cdot 10^{-4}$
35	$(6.53 \pm 0.03) \cdot 10^{-6}$	$(3.09 \pm 0.08) \cdot 10^{-6}$

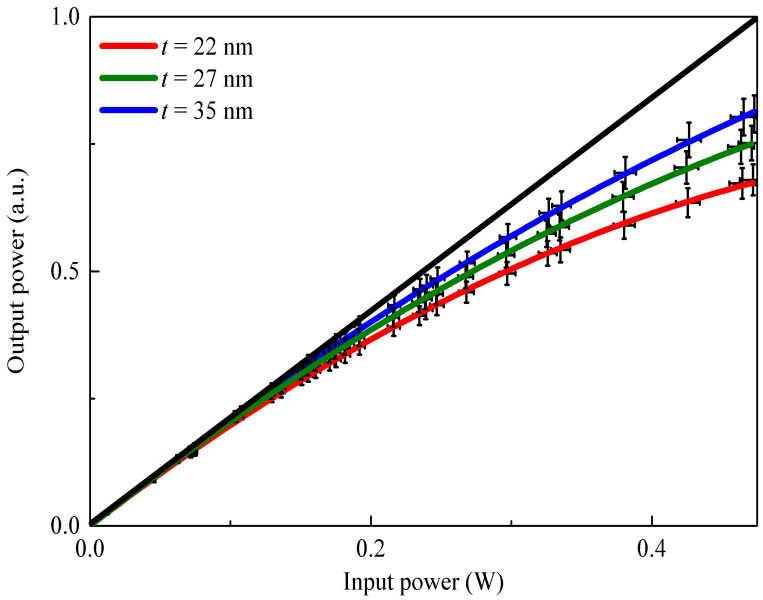

Figure 4. Nonlinear power transmission of plasmonic waveguides with different gold layer thicknesses.

In terms of the nonlinear response of the constituent materials, gold has a dominant contribution to the effective third-order susceptibility $\chi_{\text{eff}}^{(3)}$ of the plasmonic mode [21]. The effective third-order susceptibility of the LRSPP mode is related to the nonlinear absorption coefficient β as follows [22]:

$$\beta = \frac{\beta_c}{A_{\text{eff}}} = \frac{3\omega}{2\varepsilon_0 c^2 n_0^2 A_{\text{eff}}} \text{Im}[\chi_{\text{eff}}^{(3)}], \tag{2}$$

Here β_c is the conventional definition of the nonlinear absorption coefficient [22], $\omega = 2\pi c / \lambda$ is the light angular frequency, c is the speed of light in vacuum, ε_0 is the vacuum permittivity, n_0 is the effective linear refractive index of the LRSPP mode, and A_{eff} is the effective area of the LRSPP mode. The nonlinear coefficient b depends on both the nonlinear parameters of the LRSPP mode and the laser parameters. By considering the pulse propagation equation [11], it is straightforward to show that the ratio $b / a \approx \beta / (\alpha T f_{\text{rep}})$, where T is the laser pulse duration, and f_{rep} is the laser repetition rate. We analyzed the structure of our plasmonic waveguides, where the total effective nonlinearity has contributions from all layers, calculated through the overlap integral of the spatial distribution of the plasmonic mode in each layer and using the respective bulk nonlinearity of each layer. The values of the field integrals from the gold core θ_{Au} are ~$1.1 \cdot 10^{-4}$, ~$1.4 \cdot 10^{-4}$, and ~$1.9 \cdot 10^{-4}$ for the layers thickness 22, 27, and 35 nm correspondingly. And the values of the effective area of the waveguide are ~11.2 μm^2, ~10.2 μm^2, and ~9.2 μm^2 correspondingly. Through this analysis, which will be presented in detail elsewhere, we found that gold has by far the dominating contribution to the total effective nonlinearity: the contribution from the gold layer is two orders of magnitude bigger (~10^{-20} m^2/V^2) than the one from the tantalum pentoxide layer (~10^{-22} m^2/V^2), although the latter has a quite large cubic nonlinearity [23]. The calculated value of the real part of the effective refractive index of the plasmonic mode $\text{Re}[n_{\text{eff}}] \approx 1.47$ is much larger than the value of its imaginary part $\text{Im}[n_{\text{eff}}] \approx 0.01$. Therefore we can take as a good approximation the following formula for the nonlinear absorption coefficient $\beta \approx (3\omega\theta_{\text{Au}} \text{Im}[\chi_{\text{Au}}^{(3)}]) / (2\varepsilon_0 c^2 n_0^2 A_{\text{eff}})$, where $\chi_{\text{Au}}^{(3)}$ is the third-order susceptibility of the gold layers, and the obtained coefficients a and b are used to extract the imaginary part of $\chi_{\text{Au}}^{(3)}$.

3.4 Nonlinear spectral measurements

The spectra of the transmitted optical flux were measured by the OSA and in the wavelength range 1058-1069 nm. They show several interesting features (Fig. 5). Firstly, spectral broadening and splitting are observed, a clear sign of SPM influenced by two-photon absorption from the real and imaginary part of $\chi^{(3)}$, respectively [11]. This was confirmed with numerical simulations of the nonlinear Schrödinger equation, giving almost identical spectra as those in Fig. 5, where the experimental input pulse was used and no free parameters were adopted (all linear and nonlinear parameters were those calculated by our waveguide analysis or measured experimentally). The second feature is that the spectral broadening and splitting in the output spectra differs slightly for each case. We compared the values of the effective spectral widths for the input pulse and output pulses at the splitting level (~0.05), where for simplicity the side peaks with lower intensities (~0.01-0.03) were neglected. To do an analytical estimate, we approximate the input pulse with a Gaussian one and calculate the nonlinear spectral broadening factor (SBF) from comparing it to a Gaussian fit to the two distinct SPM peaks. The SBF then relates to the effective nonlinear coefficient γ by [11]:

$$\mathrm{SBF} \approx 0.86\gamma P_0 \frac{1-e^{-\alpha l}}{\alpha}, \tag{3}$$

where $\gamma = (\omega n_{2\mathrm{eff}})/(cA_{\mathrm{eff}})$, P_0 is the peak power of an input pulse, $n_{2\mathrm{eff}}$ is the effective intensity dependent refractive of the LRSPP mode, and l is the length of a plasmonic waveguide. This result assumes a purely Gaussian input pulse, which is transform limited (no chirp across the pulse). Although the input pulse in the experiment was not transform limited and its spectrum had multiple modulated peaks, this expression serves as a rough estimate of the effective waveguide nonlinearity γ in the sample; such an approach is also justified by the close agreement with the numerical simulations. From the second equation in Eq. (3) and using the relation between $n_{2\mathrm{eff}}$ and $\mathrm{Re}[\chi^{(3)}_{\mathrm{eff}}]$ the following formula is realized $\gamma \approx (3\omega\theta_{\mathrm{Au}}\,\mathrm{Re}[\chi^{(3)}_{\mathrm{Au}}])/(4\varepsilon_0 c^2 n_0^2 A_{\mathrm{eff}})$, since as argued above for the nonlinear loss, the dominating contribution comes from gold. The experimental values of the SBF are used to extract the real part of the third-order susceptibility of the gold layers showing its dependence on the layer thickness.

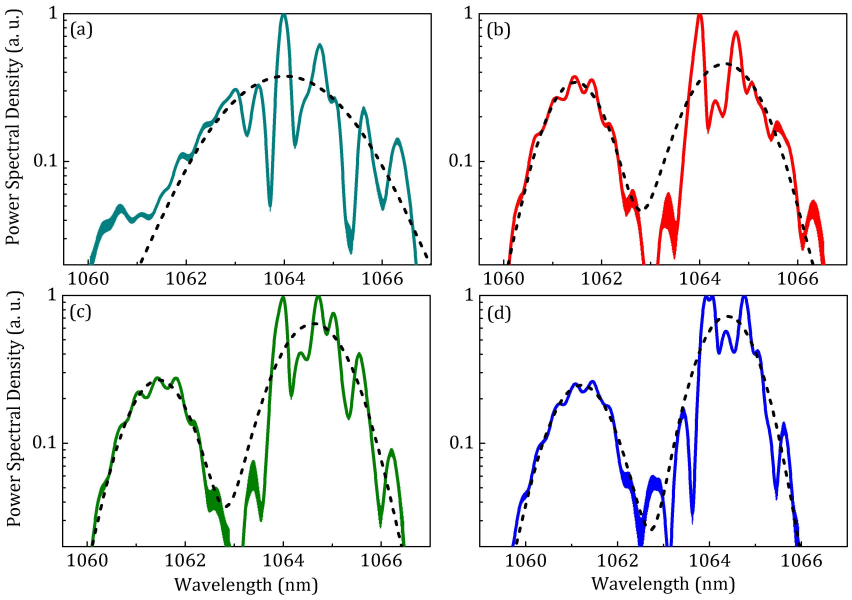

Figure 5. (a) Input pulse spectrum, and output pulse spectra for plasmonic waveguides at the maximum input power (~ 480 mW) with the gold layer thickness (b) t = 22 nm, (c) t = 27 nm, and (d) t = 35 nm. Dashed lines show a Gaussian fit to the measured spectra.

3.5 Third-order nonlinear susceptibility of gold

The calculated values of the real and imaginary parts of the third-order susceptibility for gold layers with different thicknesses, and the calculation errors are presented in Table 3. Both the real and imaginary parts decrease as the layer

thickness increases. The experimental values for the third-order susceptibility are plotted in Fig. 6 and the nonlinear curve fit was calculated as follows:

$$\chi_{\mathrm{Au}}^{(3)} = \chi_{\infty}^{(3)} + \frac{C}{t}, \tag{4}$$

where $\chi_{\infty}^{(3)}$ is the third-order susceptibility for bulk gold [7], t is the gold layer thickness, and C is the experimental coefficient. The fitting $1/t$ here was done by analogy with the change of the electrons collisions frequency in metal nanoparticles with the radius [24]. The calculated values for the real and imaginary parts of the experimental coefficient C are: $\mathrm{Re}[C] = (5.82 \pm 0.15) \cdot 10^{-24}$ m^3/V^2, and $\mathrm{Im}[C] = (9.34 \pm 1.79) \cdot 10^{-26}$ m^3/V^2. For comparison we plot also the third-order susceptibility for bulk gold $\chi_{\infty}^{(3)} = (4.56 + 0.48i) \cdot 10^{-17}$ m^2/V^2 [7]. We here again stress that the obtained values should be taken with caution as they were extracted assuming a transform-limited Gaussian input pulse. Further experiments with cleaner pulse profiles should illuminate this issue.

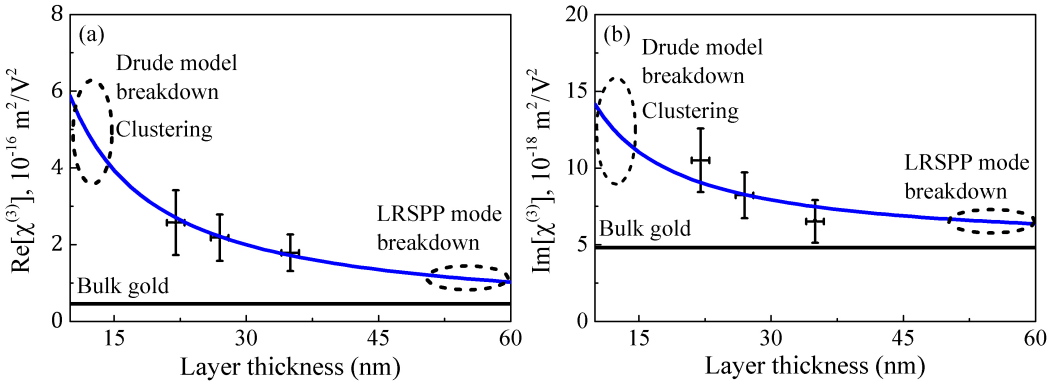

Figure 6. (a) Real part and (b) imaginary part of the third-order susceptibility for gold layers with different thicknesses. Blue curves show the nonlinear curve fit to experimental data, the black lines mark the third-order susceptibility for bulk gold.

Table 3. Third-order susceptibility of gold layers with different thicknesses.

t (nm)	$\mathrm{Re}[\chi_{\mathrm{Au}}^{(3)}]$ (m^2/V^2)	$\mathrm{Im}[\chi_{\mathrm{Au}}^{(3)}]$ (m^2/V^2)
22	$(2.57 \pm 0.84) \cdot 10^{-16}$	$(10.50 \pm 2.08) \cdot 10^{-18}$
27	$(2.18 \pm 0.61) \cdot 10^{-16}$	$(8.22 \pm 1.49) \cdot 10^{-18}$
35	$(1.79 \pm 0.48) \cdot 10^{-16}$	$(6.51 \pm 1.38) \cdot 10^{-18}$

The experimental values of the real part of $\chi_{\mathrm{Au}}^{(3)}$ are ~4-5 times higher than the real part of $\chi_{\infty}^{(3)}$ for bulk gold. And experimental values of the imaginary part of $\chi_{\mathrm{Au}}^{(3)}$ are ~1.5-2 times higher. The obtained dependencies of the third-order susceptibility for the gold layers are in accordance with previous measurements of thin gold layers using the z-scan method [25]. Figure 6 also shows the thickness limitations. The classic Drude model may be inapplicable at the layer thicknesses below 10-15 nm due to possible quantum effects [26], nonlocal effects [27], and layer clustering [28]. Conversely, the coupled LRSPP mode collapses at the layer thicknesses above 50-60 nm due to the small penetration depth of the surface electromagnetic waves in metal [20]. Therefore, the effective range of t is ~15-45 nm for experimental studies.

There are two possible reasons to explain the increase of the third-order susceptibility in gold layers with reduction of their thickness. Firstly, the effective enhancement of the third-order nonlinearity in an ultra-thin metal layer can be caused by the change in the free electrons motion due to the confinement factor. Consequently, their collisions frequency increases, and it leads to the effective increase of the dielectric permittivity of a metal layer. This, in turn, causes the

increase of the third-order susceptibility of the metal layer. Secondly, by considering the ultra-fast electrons dynamics in metal [7], it is possible to assume that, for the electrons heated by a laser pulse, the characteristic thermalization rates with other electrons and the metal lattice change with the thickness. It may also lead to the effective enhancement of the third-order susceptibility in a metal layer [7].
The presented nonlinear optical effects in gold stripe waveguides can be exploited for further developments towards plasmonic communication components.

4. THEORETICAL RESULTS

4.1 Chromatic dispersion effect

The first and second derivatives of the real part of the LRSPP propagation constant β_1 and β_2 define the lowest-order chromatic dispersion in plasmonic waveguides. The first derivative β_1 is related to the group velocity υ_g and group index n_g of the LRSPP mode as $\beta_1 = d\beta / d\omega = 1/\upsilon_g = n_g / c$. The second derivative $\beta_2 = d^2\beta / d\omega^2$ (also referred as the group velocity dispersion (GVD) parameter) is related to the dispersion length L_D of the plasmonic mode as $L_D = T_0^2 / |\beta_2|$, where T_0 is the 1/e-intensity value of a Gaussian input optical pulse. The normalized group velocity υ_g / c and dispersion length L_D were calculated in the range 800-1550 nm (Fig. 7). The average value of υ_g at 1064 nm is ~67 % of the vacuum speed of light. The magnitude of β_2 is somewhat larger (~10^{-4} ps^2/mm=10^2 ps^2/km) than typical values for single-mode optical fibers (~10 ps^2/km) [11]. The dispersion length L_D for 3 ps pulses is much larger (~200-1000 mm) than the physical length of the waveguides l (~1 mm). This means that the chromatic dispersion has a small effect on the propagation of picosecond optical pulses in the plasmonic waveguide.

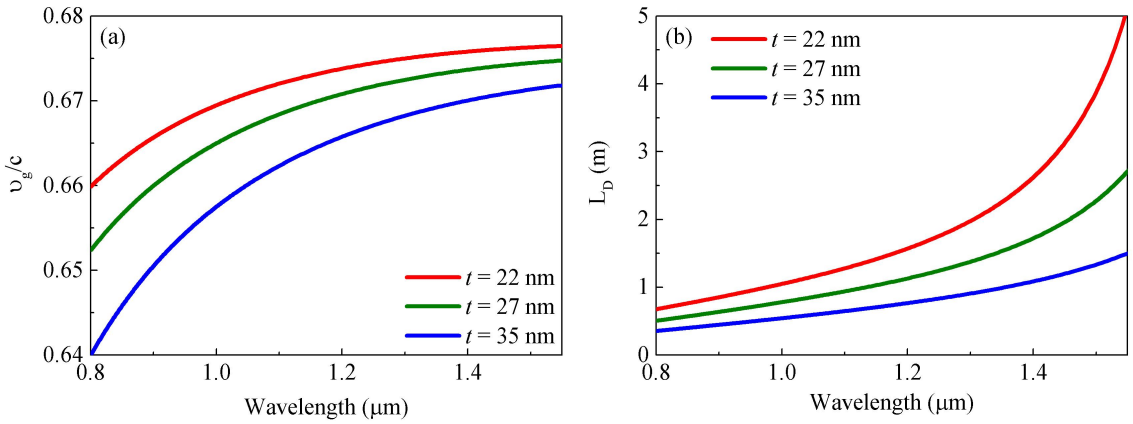

Figure 7. (a) Normalized group velocity and (b) dispersion length vs. wavelength.

4.2 Pulse propagation equation

The propagation dynamics of the LRSPP mode can be well described by the nonlinear Schrödinger equation [11]:

$$\frac{\partial A}{\partial x} = i\gamma |A|^2 A - \frac{\alpha}{2} A - \frac{\beta}{2} |A|^2 A, \tag{5}$$

where $A(x,T)$ is the complex amplitude of an optical pulse, x is the propagation coordinate, T is the time coordinate in the co-moving frame of the input pulse. The first and third term correspond to the self-phase modulation (SPM) and

nonlinear absorption, respectively. The chromatic dispersion has been neglected, which is a good approximation as the dispersion length L_D for picosecond optical pulses of the plasmonic waveguide is much larger than the physical waveguide length l. The formal solution to Eq. (5) is $A(x,T) = \sqrt{P(x,T)}\exp\left[i\phi_{NL}(x,T)\right]$, where $P(x,T)$ is the pulse power amplitude and $\phi_{NL}(x,T)$ is the pulse nonlinear phase. Although this has been studied extensively in the literature, we are here dealing with the particular case where dispersion is negligible and where linear and nonlinear absorption is significant, which makes it worth to revise the results. After substitution this solution to Eq. (5), and solution of the straightforward system of differential equations, the following results are obtained for the pulse power amplitude and pulse nonlinear phase:

$$\begin{cases} P(x,T) = \dfrac{P_0 e^{-\frac{T^2}{T_0^2}} e^{-\alpha x}}{1+\beta P_0 e^{-\frac{T^2}{T_0^2}}(1-e^{-\alpha x})/\alpha}, \\ \phi_{NL}(x,T) = \dfrac{\gamma}{\beta}\ln\left[1+\beta P_0 e^{-\frac{T^2}{T_0^2}}(1-e^{-\alpha x})/\alpha\right]. \end{cases} \quad (6)$$

Here the initial conditions were used: $P(0,T) = P_0\exp(-T^2/T_0^2)$ and $\phi_{NL}(0,T) = 0$. The solutions describe how the peak power $P(x,T)$ and phase $\phi_{NL}(x,T)$ of optical pulses change in the time domain upon propagation. For practical purposes, the expression for $P(x,T)$ can be modified to obtain a formula for the average power of light at the output of the plasmonic waveguide, which is the observable and measurable quantity:

$$\overline{P}(l) = \overline{P}(0)e^{-\alpha l} - \frac{\sqrt{\pi}\beta\overline{P_0}^2}{\sqrt{2}\alpha T_0 f_{rep}}e^{-\alpha l}. \quad (7)$$

This equation shows that the average output power $\overline{P}(l)$ from the plasmonic waveguide of the length l depends nonlinearly on the average input power $\overline{P_0}$, and an asymptotic saturation of the function $\overline{P}(l)\{\overline{P_0}\}$ is expected at high values of $\overline{P_0}$. The nonlinear trend $\overline{P}(l)\{\overline{P_0}\}$ depends on the linear absorption coefficient α, laser repetition rate f_{rep}, pulse duration T_0, nonlinear parameter β, and length l of the waveguide. The experimental power trends for different thicknesses t=22, 27 and 35 nm (Fig. 5) confirm the expected nonlinear behavior. The nonlinear term in Eq. (7) becomes important at the values of $\overline{P_0}$ above 0.15-0.2 W. The possible saturation plateau is achievable at the values of $\overline{P_0}$ above 0.5 W. The obtained nonlinear functions $\overline{P}(l)\{\overline{P_0}\}$ clearly depend on the gold thickness t, the saturation is achieved faster for thinner waveguides. It confirms that the gold layer thickness t is a crucial parameter for $\chi^{(3)}$ of the LRSPP mode.

The second nonlinear effect concerns the LRSPP mode spectral features. The pulse power spectral density (PSD) in units [W/Hz] is given by the squared Fourier transform of pulse amplitude $A(x,T)$ as follows:

$$\mathrm{PSD}(x,\omega) = f_{rep}\left|\int_{-\infty}^{+\infty} A(x,T)e^{i\omega T}dT\right|^2. \quad (8)$$

By substituting the expressions for the pulse power amplitude and phase in Eq. (26), the final formula for the PSD is obtained:

$$\mathrm{PSD}(l,\omega) = f_{\mathrm{rep}} \left| \int_{-\infty}^{+\infty} \sqrt{\frac{P_0 e^{-\frac{T^2}{T_0^2}} e^{-\alpha l}}{1+\beta P_0 e^{-\frac{T^2}{T_0^2}} L_{\mathrm{eff}}}} e^{i\frac{\gamma}{\beta}\ln\left[1+L_{\mathrm{eff}}\beta P_0 e^{-\frac{T^2}{T_0^2}}\right]} e^{i(\omega-\omega_c)T} dT \right|^2 . \quad (9)$$

Here $\omega_c = 2\pi c/\lambda$ is the carrier frequency, which corresponds to the peak wavelength 1064 nm, and $L_{\mathrm{eff}} = (1-e^{-\alpha l})/\alpha$ is the effective waveguide length. The numerical calculations of Eq. (9) for the gold layer thickness t =22 nm (Fig. 8) show the nonlinear spectral broadening and splitting of an input Gaussian pulse, depending on the input average power $\overline{P_0}$. The pulse splitting occurs at the values of $\overline{P_0}$ ~0.2 W. This nonlinear effect was observed in our recent experiment [12]. The further increase of $\overline{P_0}$ leads to the splitting and formation of more SPM peaks.

The obtained spectral features are in accordance with the theoretical results done by Agrawal *et al.* for nonlinear properties of silicon waveguides [29, 30]. The principal difference here is that the plasmonic waveguide has much higher linear absorption and shorter physical length than an ordinary silicon waveguide. However, the comparable nonlinear spectral broadening can be achieved. In the case of optical fibers, the required waveguide length can reach hundreds of meters or more to receive the desired nonlinear features. In this sense a plasmonic or silicon waveguide provides the same functionality, can be integrated on-chip and used for nonlinear purposes even with very short propagation lengths.

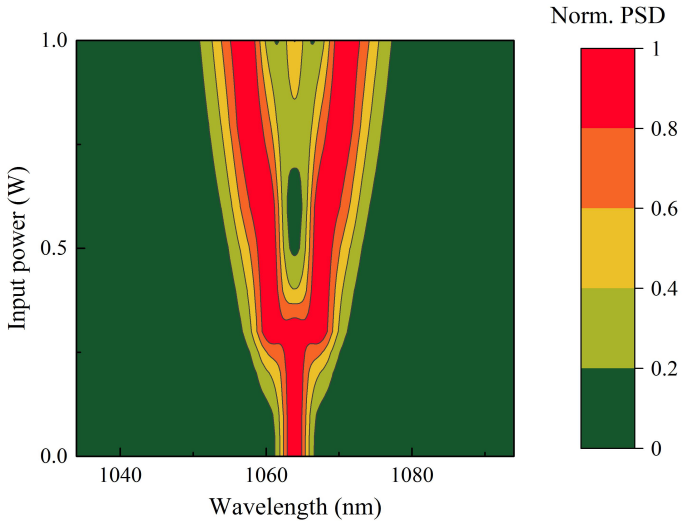

Figure 8. SPM broadening of the Gaussian pulse at 1064 nm, using t = 22 nm.

5. CONCLUSION

In this paper we have summarized the experimental and theoretical results about nonlinear effects in propagation of the LRSPP mode in gold strip waveguides. The third-order nonlinear susceptibility $\chi^{(3)}_{\mathrm{Au}}$ of the gold layers has the dominant contribution to the effective third-order susceptibility of the plasmonic mode. It was verified for three values of gold layer thickness t =22, 27 and 35 nm. The key assumption here is that the nonlinear properties are thickness-dependent and inversely proportional to the thickness. Thin metal layers enhance the waveguides nonlinearity and provide effective nonlinear propagation of ultra-fast picosecond optical pulses. The theoretical model, based on the solution of the nonlinear Schrödinger equation, confirmed the observed nonlinear transmission of the plasmonic modes for the average values of the input power $\overline{P_0}$ in the range above 0.15-0.2 W, and for the high repetition rate (f_{rep} =78 MHz) picosecond pumping at 1064 nm. In the same power range the observed SPM effect leads to the LRSPP spectral broadening and

splitting, again in accordance with our theoretical results. The deep analogy with classical fiber-based nonlinear optics show that plasmonic waveguides are potential candidates for nonlinear optics applications on a microscopic length scale. One of the possible developments in this direction is the nonlinear analysis of higher order plasmonic modes. The current model is for the fundamental LRSPP mode, but other spatial modes can also be excited. These higher order modes will affect the dynamics by nonlinear cross-phase modulation [11]. Another development concerns the propagation of even shorter (femtosecond) pulses in the plasmonic waveguides. The chromatic dispersion effect will have a more dominant role than in the present case. The investigation of nonlinear propagation of femtosecond pulses in the plasmonic waveguides will be done elsewhere. The interaction of the nonlinear and GVD effects leads to many interesting optical phenomena in plasmonic nanostructures with their possible practical realization, for example, in optical communication systems. Our results indicate that the waveguide investigated here could have anomalous GVD at telecom C-band wavelengths, which means that solitons can be excited using femtosecond Er fiber lasers. This has interesting nonlinear applications that promise well for plasmonic systems.

REFERENCES

[1] Maradudin, A., Sambles, J. and Barnes, W., [Modern Plasmonics], Elsevier, Amsterdam, 137-187 (2014).
[2] Zenin, V., Andryieuski, A., Malureanu R., Radko, I., Volkov, V., Gramotnev, D., Lavrinenko, A. and Bozhevolnyi, S., "Boosting local field enhancement by on-chip nanofocusing and impedance-matched plasmonic antennas," Nano Lett. 15(12), 8148-8154 (2015).
[3] Krupin, O., Asiri, H., Wang, C., Tait, R. N. and Berini, P., "Biosensing using straight long-range surface plasmon waveguides," Opt. Express 21(1), 698-709 (2013).
[4] Berini, P., "Surface plasmon photodetectors and their applications," Laser Photon. Rev. 8(2), 197-220 (2014).
[5] Scalora, M., Vincenti, M., de Ceglia, D., Roppo, V., Centini, M., Akozbek, N. and Bloemer, M., "Second- and third-harmonic generation in metal-based structures," Phys. Rev. A 82(043828), 1-14 (2010).
[6] Ginzburg, P., Krasavin, A. and Zayats, A., "Cascaded second-order surface plasmon solitons due to intrinsic metal nonlinearity," New J. Phys. 15(013031), 1-13 (2013).
[7] Marini, A., Conforti, M., Della Valle, G., Lee, H. W., Tran, Tr. X., Chang, W., Schmidt, M. A., Longhi, S., Russell, P. St. J. and Biancalana F., "Ultrafast nonlinear dynamics of surface plasmon polaritons in gold nanowires due to the intrinsic nonlinearity of metals," New J. Phys. 15(013033), 1-19 (2013).
[8] Conforti, M. and Della Valle, G., "Derivation of third-order nonlinear susceptibility of thin metal films as a delayed optical response," Phys. Rev. B 85(245423), 1-4 (2012).
[9] Boyd, R. Shi, Z. and De Leon, I., "The third-order nonlinear optical susceptibility of gold," Opt. Commun. 326, 74-79 (2014).
[10] Neira, A., Olivier, N., Nasir, M., Dickson, W., Wurtz, G. and Zayats, A., "Eliminating material constraints for nonlinearity with plasmonic metamaterials," Nat. Commun., 6(7757), 1-8 (2015).
[11] Agrawal, G. P., [Nonlinear fiber Optics], 5th Edition, Elsevier, Oxford (2013).
[12] Lysenko, O., Bache, M. and Lavrinenko, A., "Third-order susceptibility of gold for ultrathin layers," Opt. Lett. 41(2), 317-320 (2016).
[13] Huck, A., Witthaut, D., Kumar, S., Soerensen, A. and Andersen, U. L., "Large optical nonlinearity of surface plasmon modes on thin gold films," Plasmonics 8(4), 1597-1605 (2013).
[14] Baron, A., Hoang, T. B., Fang, C., Mikkelsen, M. H. and Smith, D. R., "Ultrafast self-action of surface-plasmon polaritons at an air/metal interface," Phys. Rev. B, 91(195412), 1-7 (2015).
[15] Berini, P., "Long-range surface plasmon polaritons ," Adv. Opt. Photon. 1(3), 484-588 (2009).
[16] Maradudin, A., [Light Scattering and Nanoscale Surface Roughness], Springer, New York (2007).
[17] Hunsperger, R., [Integrated Optics: Theory and Technology], Springer, Berlin, (2002).
[18] Charbonneau, R., Berini, P., Berolo, E. and Lisicka-Shrzek, E., "Experimental observation of plasmon–polariton waves supported by a thin metal film of finite width," Opt. Lett. 25(11), 844-846 (2000).
[19] Berini, P., Charbonneau, R., Lahoud, N. and Mattiussi, G., "Characterization of long-range surface-plasmon-polariton waveguides," J. Appl. Phys. 98(043109), 1-12 (2005).
[20] Maier, S., [Plasmonics: Fundamentals and Applications], Springer, New York (2007).
[21] Baron, A., Larouche, S., Gauthier, D. J. and Smith, D. R., "Scaling of the nonlinear response of the surface plasmon polariton at a metal/dielectric interface" J. Opt. Soc. Am. B 32(1), 9-14 (2015).
[22] Boyd, R., [Nonlinear Optics], Academic Press, New York (2008).

[23] Tai, C., Wilkinson, J. S., Perney, N. M. B., Netti, M. C., Cattaneo, F., Finlayson, C. E. and Baumberg, J. J., "Determination of nonlinear refractive index in a Ta_2O_5 rib waveguide using self-phase modulation," Opt. Express 12(21), 5110-5116 (2004).
[24] Gordon, J. A. and Ziolkowski, R. W., "The design and simulated performance of a coated nano-particle laser," Opt. Express 15(5), 2622-2653 (2007).
[25] Xenogiannopoulou, E., Aloukos, P., Couris, S., Kaminska, E., Piotrowska, A. and Dynowska, E., "Third-order nonlinear optical properties of thin sputtered gold films," Opt. Commun. 275, 217-222 (2007).
[26] Xiao, Y. Qian, H. and Liu, Z., "Investigations of the optical properties of nanoscale gold films," Proc. NOMA, NM4C, 1-4 (2015).
[27] Raza, S., Bozhevolnyi, S., Wubs, M. and Mortensen, N. A., "Nonlocal optical response in metallic nanostructures," J. Phys. Condens. Matter., 27(183204), 1-17 (2015).
[28] Kreibig U. and Vollmer, M., [Optical Properties of Metal Clusters], Springer, Berlin (1995).
[29] Yin, L. and Agrawal, G. P., "Impact of two-photon absorption on self-phase modulation in silicon waveguides," Opt. Lett., 32(14), 2031-2033 (2007).
[30] Lin, Q., Painter, O. J. and Agrawal, G. P., "Nonlinear optical phenomena in silicon waveguides: Modeling and applications," Opt. Express, 15(25), 16604-16644 (2007).

Paper F

O. Lysenko, M. Bache, R. Malureanu, and A. Lavrinenko

Modeling of effective third-order nonlinearity for gold strip plasmonic waveguides

Danish Optical Society Annual Conference, Book of Abstracts, p. 4, November 19-20, 2015, Odense, Denmark.

Title: Modeling of effective third-order nonlinearity for gold strip plasmonic waveguides

Oleg Lysenko*, Morten Bache, Radu Malureanu, and Andrei Lavrinenko

DTU Fotonik, Technical University of Denmark, DK-2800, Kongens Lyngby, Denmark

*Contact Author E-Mail: ollyse@fotonik.dtu.dk

Abstract:

This presentation is devoted to the theoretical study of the effective third-order susceptibility $\chi^{(3)}$ of a long-range surface plasmon polariton (LRSPP) mode in gold strip waveguides. The designed plasmonic waveguides contain a gold core with finite microscale width (10 μm) and nanoscale thickness (22-35 nm), tantalum pentoxide adhesion layers above and below the core, and silicon dioxide cladding. We chose this geometry because it provides effective propagation of the LRSPP mode. The effective index method is used to calculate the LRSPP propagation constant, the electric field distributions in the waveguides transverse section, and the dispersion derivatives. It is shown that the dispersion length of picosecond (~3 ps) optical pulses in plasmonic waveguides is much larger (~1-2 m) than the physical length of waveguides (~2-5 mm). Thus, the chromatic dispersion effect has a negligible role in the propagation of optical pulses in the case of picosecond pumping. For practical considerations, a wavelength of 1064 nm was selected for calculations in the model. This wavelength is widely used in laser physics and corresponds to emission of the Nd:YAG laser and Yb-doped fiber lasers. The third-order susceptibilities of all constituent materials (metal, adhesion, and cladding) contribute to the effective $\chi^{(3)}$ of the plasmonic mode. We model the third-order susceptibility of the metal layers by considering the effective change in the electrons motion. When the gold layer thickness approaches the nanoscale, the electrons start to feel the layer boundaries. Their collision frequency increases in ~2-3 times, and it leads to changes in the real and imaginary parts of the dielectric permittivity of metal. In turn, this causes the effective enhancement of the thermo-modulational interband susceptibility of the metal layer. It is shown that the values of the third-order susceptibility of the gold layers increase in ~2-5 times in comparison with the third-order susceptibility value for bulk gold (real part ~10^{-17} m^2/V^2, imaginary part ~10^{-18} m^2/V^2). The nonlinearity enhancement in the metal layers is limited by the Drude model breakdown at the layer thicknesses below 10-15 nm. We show that the third-order susceptibility of the gold layer is dominant to the effective $\chi^{(3)}$ of the LRSPP mode in the designed strip waveguides. The real part of the effective $\chi^{(3)}$ of the LRSPP mode defines the nonlinear parameter and nonlinear length of optical pulses in plasmonic waveguides. In the case of high average power (~200-500 mW) picosecond pumping, the nonlinear length becomes comparable or less than the effective length of plasmonic waveguides (~0.2-0.5 mm), and the third-order nonlinearity affects the propagation of the plasmonic mode. The imaginary part of the effective $\chi^{(3)}$ of the LRSPP mode defines the nonlinear absorption parameter in plasmonic waveguides. We model the propagation of optical pulses in plasmonic waveguides by solving the nonlinear Schrödinger equation and considering a Gaussian shape of the pump laser pulses. The obtained solutions of the pulse propagation equation lead to two nonlinear effects. The first effect is the nonlinear transmission of optical pulses in plasmonic waveguides and the power saturation of the LRSPP mode at high average power (~200-500 mW) picosecond pumping. The second effect is the self-phase modulation of optical pulses in plasmonic waveguides, and the spectral broadening and splitting of the LRSPP mode. A relevant experiment has been performed and confirmed the possibility of practical observation of these nonlinear effects. The results can be used for future applications of plasmonic waveguides in nonlinear optics.

Paper G

A. Lavrinenko and O. Lysenko

Modeling, fabrication and high power optical characterization of plasmonic waveguides

International Conference on Electronics and Nanotechnology (ELNANO),
pp. 245-248, April 21-24, 2015, Kiev, Ukraine.

2015 IEEE 35th International Conference on Electronics and Nanotechnology (ELNANO)

Modeling, Fabrication and High Power Optical Characterization of Plasmonic Waveguides

A. Lavrinenko, O. Lysenko
Department of Photonics Engineering
Technical University of Denmark
Kgs. Lyngby, Denmark
ollyse@fotonik.dtu.dk

***Abstract* — This paper describes modeling, fabrication and high power optical characterization of thin gold films embedded in silicon dioxide. The propagation vector of surface plasmon polaritons has been calculated by the effective index method for the wavelength range of 750-1700 nm and film thickness of 15, 30 and 45 nm. The fabrication process of such plasmonic waveguides with width in the range of 1-100 µm and their quality inspection are described. The results of optical characterization of plasmonic waveguides using a high power laser with the peak power wavelength 1064 nm show significant deviation from the linear propagation regime of surface plasmon polaritons at the average input power of 100 mW and above. Possible reasons for this deviation are heating of the waveguides and subsequent changes in the coupling and propagation losses.**

Keywords — nanophotonics; optical waveguides; plasmons

I. INTRODUCTION

The first experimental observation of surface plasmons in thin gold films embedded in silicon dioxide was published in 2000 [1]. The comprehensive study of long-range surface plasmon polaritons in thin gold films was performed by P. Berini and co-workers and described in [2]. Optical characterization at the wavelength of 1550 nm showed good agreement between theoretical and experimental data. Effect of surface electromagnetic waves propagation in thin metal films can be used for development of integrated optics elements [3, 4, 5]. In some cases, polymer benzocyclobutene is also used as a cladding of plasmonic waveguides instead of silicon dioxide. A review about surface plasmon polaritons is presented in [6].

In the present work, we describe modeling, fabrication and high power optical characterization of thin gold films embedded in silicon dioxide. The effective index method [7] was used for modeling plasmonic waveguides, and calculations of relevant parameters were performed. The modeling is described in section II. The fabrication of prototype samples was performed in a cleanroom and discussed in section III. The optical characterization of plasmonic waveguides was done using a high power laser with the peak power wavelength 1064 nm. The experiment and obtained results are described in section IV.

II. MODELING OF PLASMONIC WAVEGUIDES

Modeling of thin gold films starts from the Maxwell equations, boundary conditions and calculation of dielectric permittivity of gold and silicon dioxide for the wavelength of interest [7, 8].

The dielectric permittivity of silicon dioxide can be assumed constant for simplicity and equal to the following value at the wavelength 1064 nm:

$$\varepsilon_1 = 2.12. \tag{1}$$

The dielectric permittivity of gold is calculated using the Drude model [7, 8] and parameters from [7]:

$$\varepsilon_2 = \mathrm{Re}[\varepsilon_2] + i \cdot \mathrm{Im}[\varepsilon_2], \tag{2}$$

$$\mathrm{Re}[\varepsilon_2] = 1 - \frac{\lambda^2 \cdot {\omega_p}^2 \tau^2}{\lambda^2 + \tau^2 \cdot 4\pi^2 c^2}, \tag{3}$$

$$\mathrm{Im}[\varepsilon_2] = \frac{{\omega_p}^2 \tau \cdot \lambda^3}{2\pi c \cdot \lambda^2 + 8\pi^3 c^3 \tau^2}. \tag{4}$$

Here, $\omega_p = 1.37 \cdot 10^{16}$ rad/s is the plasma frequency of gold, and $\tau = 2.9 \cdot 10^{-14}$ s is the relaxation time of gold, c is the speed of light in vacuum, and λ is the wavelength of interest.

A thin gold film can be modeled as an infinitely wide slab with thickness t and dielectric permittivity ε_2, embedded in medium with dielectric permittivity ε_1 (Fig. 1). Surface electromagnetic waves can propagate along the top and bottom boundaries of the slab and form coupled electromagnetic oscillations, one of which is called a long-range surface plasmon polariton. Another coupled oscillation is called a short-range surface plasmon polariton, and is known as more important for the localized plasmon resonances [9]. The propagation vector β for the long-range mode of surface plasmon polaritons in this configuration can be found from the dispersion equation [8, 10]:

$$\tanh\left(\frac{t}{2} \cdot \sqrt{\beta^2 - \varepsilon_2 \frac{4\pi^2}{\lambda^2}}\right) + \frac{\varepsilon_2}{\varepsilon_1} \cdot \frac{\sqrt{\beta^2 - \varepsilon_1 \frac{4\pi^2}{\lambda^2}}}{\sqrt{\beta^2 - \varepsilon_2 \frac{4\pi^2}{\lambda^2}}} = 0. \tag{5}$$

This equation was solved numerically for β for the thickness values of 15, 30 and 45 nm and for the wavelength range of 750-1700 nm. The real part of the propagation vector $\mathrm{Re}[\beta]$ is shown in Fig. 2. The calculation step is 50 nm, and the obtained points are connected by straight lines. The real part of β decays over the wavelength range and differs very little for selected values of the slab thickness. The obtained results show that the effective refractive index of plasmonic

978-1-4673-6534-5/15/$31.00 ©2015 IEEE

waveguides does not have significant dependence on the waveguide thickness for the wavelength range of interest.

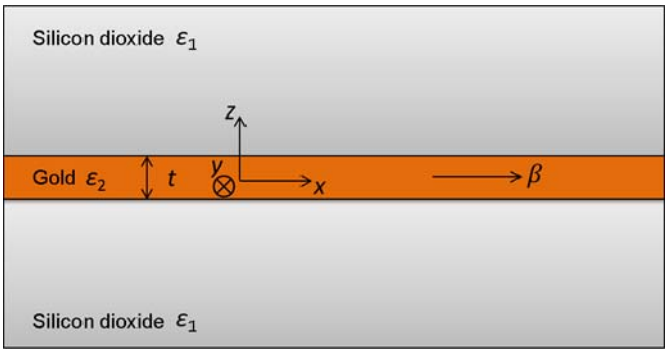

Fig. 1. Thin gold film as a slab embedded in silicon dioxide.

The imaginary part of the propagation vector Im[β] is shown on Fig. 3. The calculation step is 50 nm, and the obtained points are connected by straight lines. The imaginary part of the propagation vector monotonically decays over the wavelength range, and differs significantly for selected values of the slab thickness. It is about one order of magnitude smaller for the thickness of 15 nm than that for the thickness of 45 nm. The imaginary part of β is responsible for absorption and propagation losses in a plasmonic waveguide. Thinner plasmonic waveguides have less losses and, thus, longer propagation length of surface plasmon polaritons. The long range mode of surface plasmon polaritons can propagate over several millimeters and can be observed and studied experimentally for the selected thickness and wavelength range [7].

The obtained results and literature data [2, 7, 10] were used for the design and fabrication of plasmonic waveguide structures. The effective penetration depth for surface electromagnetic waves in gold is around 21-22 nm for the selected wavelength range and effective penetration depth in silicon dioxide is around the wavelength value. Thus, the gold film thickness should be around 50 nm or thinner and covered by several micrometers of dielectric from top and bottom side to observe the propagation of long-range surface plasmon polaritons.

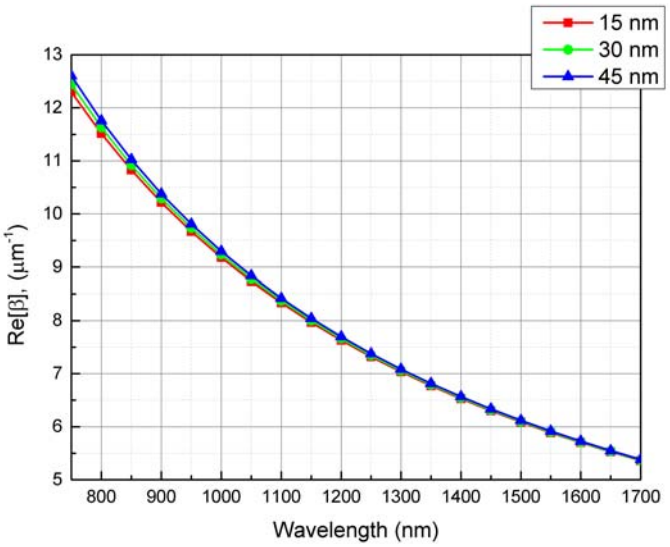

Fig. 2. Real part of propagation vector as a function of wavelength.

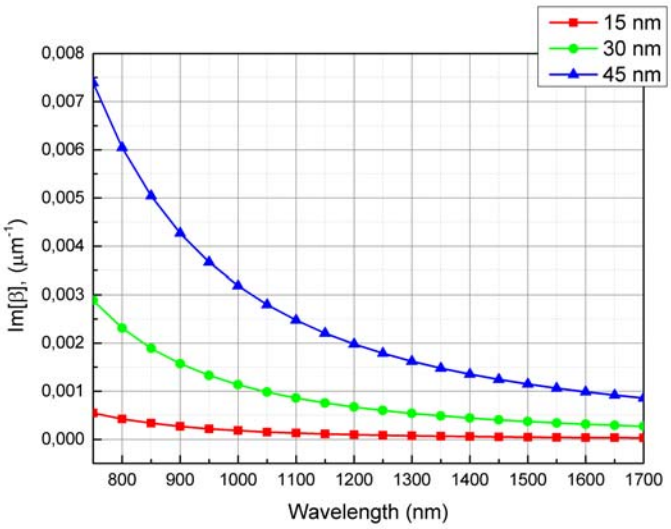

Fig. 3. Imaginary part of propagation vector as a function of wavelength.

III. FABRICATION

The prototype samples with plasmonic waveguides were fabricated in a cleanroom. A photolithography mask was designed in CleWin layout editor and ordered from a commercial supplier. A silicon wafer with pre-made 6.5 μm of the silicon dioxide cladding was used as a substrate. Standard ultraviolet lithography process was applied, and gold films were deposited on top of silicon dioxide afterwards using a sputtering machine. A chemical solution Piranha was used to remove the photoresist layer. A top cladding of silicon dioxide was deposited using the plasma-enhanced chemical vapor deposition method. The quality of plasmonic waveguides was checked using a scanning electron microscope. An image with several waveguides of different width obtained by the microscope is shown in Fig. 4. The waveguides are bright lines with widths 1, 2, 3, 4, 5, 6, and 7 μm. One fabricated wafer contained two groups of waveguides: thin waveguides and wide waveguides. Thin waveguides had width in the range of 1-10 μm, with width step of 1 μm. Wide waveguides had width in the range of 10-100 μm, with width step of 10 μm. The distance between neighbor waveguides was 100 μm. This value is much bigger than typical penetration depth of surface electromagnetic waves in silicon dioxide, and each plasmonic waveguide could be investigated standalone, without influence on another neighbor waveguides. The difference between the nominal and fabricated widths of plasmonic waveguides was within the range of 1 μm. The thickness of waveguides was measured using a Dektak XT profilometer and was around 35 nm. The thickness and refractive index of silicon dioxide were measured using a Filmtek 4000. The total thickness of silicon dioxide layer was around 11.5 μm, thus the thickness of deposited top cladding was around 5 μm. The refractive index of silicon dioxide was 1.456 at the wavelength of 1064 nm.

The fabricated wafer was diced, and 15 rectangular slices with plasmonic waveguides of different width and length were collected in the chessboard (Fig. 5). The width of rectangular slices was 1.5 cm, and the length was 2, 3, 4, 5 and 6 mm. The top raw contains slices with 5 identical groups of wide plasmonic waveguides, each group has waveguides with the

width in the range of 10-100 μm and the groups are separated by the distance of 500 μm. The total number of waveguides in each slice is 5 × 10 = 50. The middle raw contains slices with 10 identical groups of thin waveguides, each group has waveguides with the widths of 1-10 μm and the groups are separated by the distance of 150 μm. The total number of waveguides in each slice was 10 × 10 = 100.

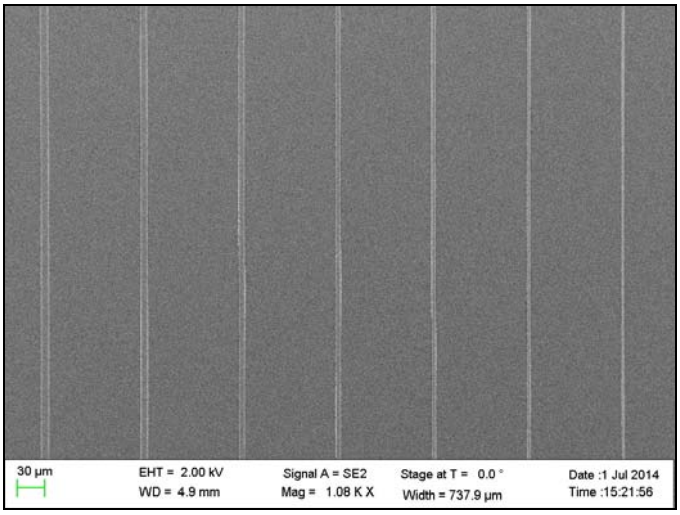

Fig. 4. Scanning electron microscope image of plasmonic waveguides.

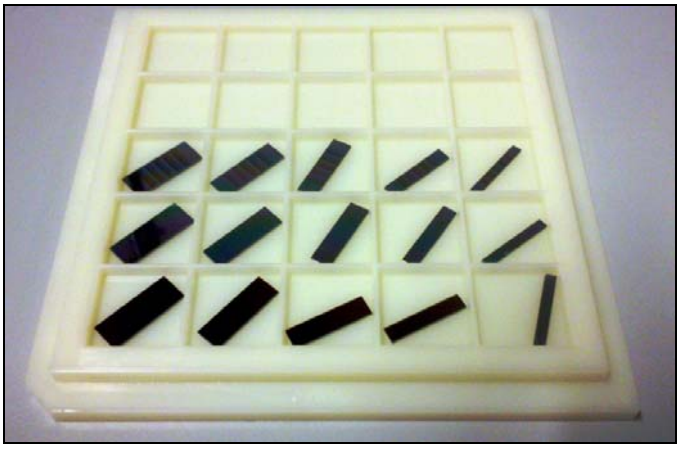

Fig. 5. Chessboard with fabricated samples.

The bottom raw contains slices with a thin gold film covering the whole surface of slices. The rectangular samples from the top raw containing wide waveguides were selected for optical characterization.

IV. Experiment

The experimental setup to characterize the samples is shown on Fig. 6. The laser source is picosecond SuperK EXTREME (NKT Photonics) with the maximum average power 15 W, repetition rate 78 MHz and peak power wavelength 1064 nm. A laser beam propagated in the step-index optical fiber to the fiber port, passed polarizers and coupled again to the polarization maintaining fiber. Two linear polarizers were used to tune the beam power without changing the laser operational current, and to keep the fixed linear polarization of output light. The first polarizer rotated to tune its polarization direction with respect to the second polarizer direction, and, thus, the beam power was tuned from zero to a half of the maximum value. The output beam polarization was maintained to match the transverse magnetic mode of surface plasmon polaritons in waveguides. The samples were placed by one on the moving platform and two positioners were used to implement the end-fire light coupling to plasmonic waveguides. A single mode fiber was used to collect and deliver the transmitted flux to the optical spectrum analyzer AQ6315E (Yokogawa). The samples motion and fibers alignment were controlled by the optical microscope Axiotech vario (Carl Zeiss). The polarization maintaining fiber is a photonic crystal fiber with the core diameter 10 μm. The single mode fiber is a photonic crystal fiber with the core diameter 10 μm. Plasmonic waveguides with the width of 10 μm were selected for investigation to have the most coupling efficiency. The results of transmission measurement for plasmonic waveguides of different lengths and at the average power in the range below 1 mW were reported in [11]. The new results of high power optical characterization are shown on Fig. 7.

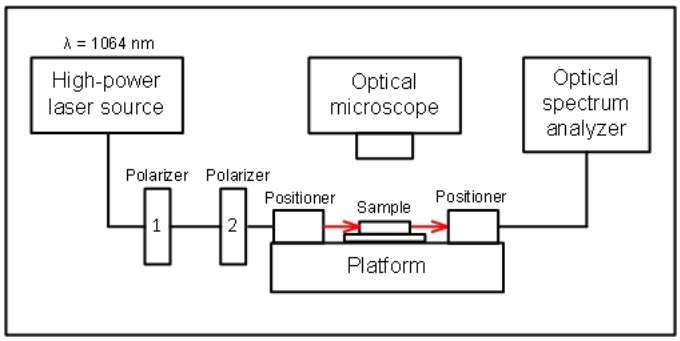

Fig. 6. Experimental setup for high power optical characterization.

The horizontal axis corresponds to the laser reference power measured without samples by the fiber to fiber direct coupling method. The polarization maintaining fiber was placed in front of the single mode fiber, and transmitted power was measured by the optical spectrum analyzer. Thus, the first polarizer was calibrated according to its polarization direction and values of transmitted power. The maximum possible power used in the experiment was limited by damage threshold of the first polarizer and also by coupling efficiency of the polarization maintaining fiber. The reference power was tuned in the range from 0 to about 320 mW. The horizontal error bars include calibration error of the first polarizer and statistical error of the optical spectrum analyzer. Ten consequent measurements were performed to obtain each point of the reference power. The vertical axis shows transmitted power though five plasmonic waveguides with the length 3 mm and width 10 μm. The vertical error bars include calibration error of the first polarizer and statistical error of the optical spectrum analyzer. Ten consequent measurements were performed to obtain each point of the transmitted power. The experimental data show monotonic increase of transmitted power with increase of the reference power. However, the trend for each plasmonic waveguide is somewhat different from expected linear dependence. The waveguides were nominally identical, but were situated in different places within one rectangular slice,

and had different end-fire coupling efficiency with the optical fibers. The difference in coupling efficiency could be one of the possible reasons to explain trend deviations. The transmitted power discrepancy between plasmonic waveguides becomes even higher as the reference power increases, thus a power dependence of the coupling losses is observed. The second possible reason of the unusual power trends is propagation losses in plasmonic waveguides. The light propagating in plasmonic waveguides is absorbed in gold and silicon dioxide and, for high power regime, heating of waveguides can effectively change the optical parameters of materials. As the reference power increases, the change in propagation losses becomes significant and results in deviation from the linear trend for individual waveguides. The obtained power trends show that this deviation from the linear propagation regime becomes important for the reference power values in the range of 100 mW and above. For the reference power values in the range below 100 mW, the propagation regime in plasmonic waveguides can be assumed linear and the power discrepancy between waveguides is mainly due to different end-fire coupling efficiency.

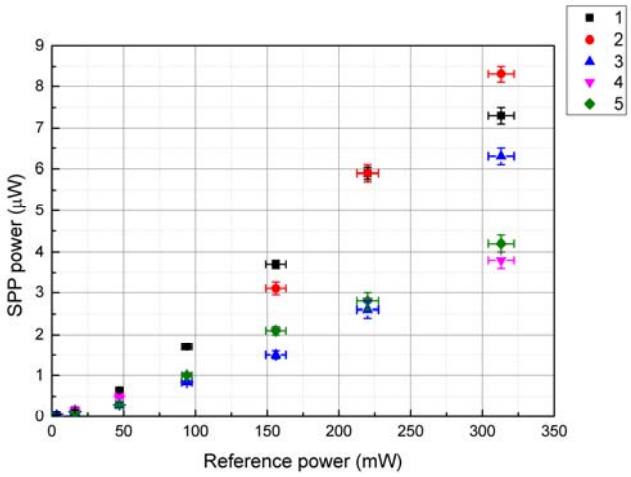

Fig. 7. Power output from waveguides as a function of reference power.

CONCLUSION

We have described modeling, fabrication and high power optical characterization of plasmonic waveguides based on thin gold films embedded in silicon dioxide. The effective index method was applied to calculate the propagation vector of long-range surface plasmon polaritons. The real and imaginary parts of the calculated propagation vector monotonically decrease as the light wavelength increases. The real part of the propagation vector Re[β] does not change significantly as the thickness of plasmonic waveguides changes from 15 nm to 45 nm, and the imaginary part of the propagation vector Im[β] increases by around one order of magnitude as the thickness of plasmonic waveguides changes from 15 nm to 45 nm.

The fabrication process of the samples with plasmonic waveguides was described in detail and the quality inspection of waveguides by the scanning electron microscope was discussed. The fabrication error for the width of plasmonic waveguides was within the range of 1 μm.

The optical characterization of plasmonic waveguides with the width 10 μm, length 3 mm, and thickness 35 nm was performed at high power. The obtained power trends for five waveguides of the same nominal geometry showed a deviation from the linear propagation regime for values of the reference power in the range of 100 mW and above. The differences in coupling loss and heating of waveguides by a high power laser beam could be possible reasons of the power deviation. The quantitative analysis of this phenomenon will be the subject of the further research in this direction.

ACKNOWLEDGMENT

The authors would like to thank Morten Bache and Radu Malureanu for the help and discussions during the work.

REFERENCES

[1] R. Charbonneau, P. Berini, E. Berolo and E. Lisicka-Shrzek, "Experimental observation of plasmon–polariton waves supported by a thin metal film of finite width," Optics Letters, vol. 25, no. 11, pp. 844-846, June 2000.

[2] P. Berini, R. Charbonneau, N. Lahoud and G. Mattiussi, "Characterization of long-range surface-plasmon-polariton waveguides," Journal of Applied Physics, vol. 98, 043109, August 2005.

[3] A.Boltasseva, T. Nikolajsen, K. Leosson, K. Kjaer, M. Larsen and S. Bozhevolnyi, "Integrated optical components utilizing long-range surface plasmon polaritons," Journal of Lightwave Technology, vol. 23, no. 1, pp. 413-422, January 2005.

[4] A. Boltasseva, S. Bozhevolnyi, "Directional couplers using long-range surface plasmon polariton waveguides," IEEE Journal of Selected Topics in Quantum Electronics, vol. 12, no. 6, pp. 1233-1241, November/December 2006.

[5] R. Charbonneau, C. Scales, I. Breukelaar, G. Mattiussi and P. Berini, "Passive integrated optics elements based on long-range surface plasmon polaritons," Journal of Lightwave Technology, v. 24, no. 1, pp. 477-494, January 2006.

[6] P. Berini, "Long-range surface plasmon polaritons", Advances in Optics and Photonics, vol. 1, issue 3, pp. 484-588, September 2009.

[7] M. Zalkovskij, Surface plasmons in nanostructures, M.S. thesis, pp. 11-34, University of Copenhangen, January 2009.

[8] S. Maier, Plasmonics: fundamentals and applications, pp. 21-34, Springer, New York, May 2007.

[9] A. Maradudin, J. Sambles, W. Barnes, Modern Plasmonics, pp. 137-187, Elsevier, Amsterdam, August 2014.

[10] V. Klimov, Nanoplasmonics, pp. 63-85, Pan Stanford, Singapore, September 2014.

[11] M. Bache, A. Lavrinenko, O. Lysenko and R. Malureanu, "Nanoplasmonic solution for nonlinear optics", DTU Sustain Conference, Technical University of Denmark, December 2014.

Paper H

M. Bache, A. Lavrinenko, O. Lysenko, and R. Malureanu

Nanoplasmonic solution for nonlinear optics

DTU Sustain Conference, Book of Abstracts, p. 106, December 17, 2014, Kongens Lyngby, Denmark.

Nanoplasmonic solution for nonlinear optics

M. Bache, A. Lavrinenko, O. Lysenko*, R. Malureanu
DTU Fotonik
*Corresponding author email: ollyse@fotonik.dtu.dk

Nonlinear optical properties of dielectric waveguides are well known and are widely used in modern telecommunication systems [1]. However, the fundamental law of diffraction imposes physical limitation for integration of dielectric photonics and semiconductor electronics [2]. A possible way to combine the high speed of a photonic device with the compact size of an electronic device is to produce a nanoplasmonic device based on metal waveguides. The successful solutions can be used for future sustainable technologies. In meantime, nonlinear optics of metal waveguides is not fully understood and is being under investigation in recent years [3].

The purpose of our research is to study nonlinear optical properties of gold waveguides embedded into dielectric medium (silicon dioxide) using picosecond laser spectroscopy. The work includes modeling of optical properties of gold waveguides, fabrication of prototype samples, and optical characterization of samples using a picosecond laser source.

The prototype samples of gold waveguides embedded into silicon dioxide were fabricated at DTU Danchip. A silicon wafer with pre-made 6.5 µm layer of silicon dioxide was used as a substrate and gold waveguides (films) with the thickness of 35 nm were deposited using the sputter-system (Lesker). The waveguides have different width in the range of 1 µm to 100 µm. A cladding layer of silicon dioxide of about 5 µm was deposited on top of the gold waveguides using the plasma-enhanced chemical vapor deposition (PECVD) method. The quality of samples was inspected using the optical microscope, scanning electron microscope, atomic force microscope, and ellipsometer. The ready wafer was diced into several rectangular sliced with the fixed width of 15 mm and the different length from 2 mm to 6 mm for optical characterization in the laboratory.

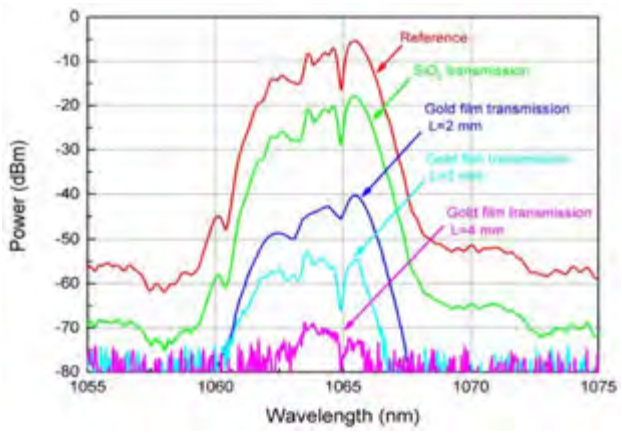

Picture 1. Transmission spectra measurements

The samples were characterized using the picosecond laser source (NKT Photonics) with the peak wavelength of 1064 nm. The relevant spectra are shown on picture 1. The red curve corresponds to the reference measurement of the laser spectrum. The green curve is the transmission spectrum for the silicon dioxide cladding. The blue, cyan and magenta curves correspond to the transmission spectra for the gold waveguides with the width of 10 µm and length of 2, 3, and 4 mm. The polarization of laser beam was tuned to match the transverse magnetic mode of surface plasmon polaritons in the gold waveguides.

The propagation loss per unit length and coupling loss for the gold waveguides were calculated. The average propagation loss was 14 dB/mm and the average coupling loss was 6 dB. The obtained results showed a capability of the prototype samples to guide surface plasmon polaritons and their potential for the further investigation of nonlinear properties.

References

[1] G. Agrawal, “Nonlinear fiber optics”, fifth edition, Academic Press (2013).
[2] M. Brongersma, V. Shalaev, “The case for plasmonics”, Science, 328, 440 (2010).
[3] M. Kauranen, A. Zayats, “Nonlinear plasmonics”, Nature Photonics, 6, 373 (2012).